Heterojunction Quantum Dot Solar Cells

by

Navid Mohammad Sadeghi Jahed

A thesis
presented to the University of Waterloo
in fulfillment of the
thesis requirement for the degree of
Doctor of Philosophy
in
Electrical and Computer Engineering

Waterloo, Ontario, Canada, 2016

I hereby declare that I am the sole author of this thesis. This is a true copy of the thesis, including any required final revisions, as accepted by my examiners.

I understand that my thesis may be made electronically available to the public.

Abstract

The advent of new materials and application of nanotechnology has opened an alternative avenue for fabrication of advanced solar cell devices. Before application of nanotechnology can become a reality in the photovoltaic industry, a number of advances must be accomplished in terms of reducing material and process cost. This thesis explores the development and fabrication of new materials and processes, and employs them in the fabrication of heterojunction quantum dot (QD) solar cells in a cost effective approach.

In this research work, an air stable, highly conductive ($\rho = 2.94 \times 10^{-4}$ Ω.cm) and transparent (≥85% in visible range) aluminum doped zinc oxide (AZO) thin film was developed using radio frequency (RF) sputtering technique at low deposition temperature of 250 °C. The developed AZO film possesses one of the lowest reported resistivity AZO films using this technique. The effect of deposition parameters on electrical, optical and structural properties of the film was investigated. Wide band gap semiconductor zinc oxide (ZnO) films were also developed using the same technique to be used as photo electrode in the device structure. Sputtered ZnO thin films with high electron mobility (30 $cm^2V^{-1}s^{-1}$) is achieved at a deposition temperature of 250 °C to eliminate charge collection losses in the solar cell device. The developed AZO and ZnO thin films are a suitable substitute for the expensive indium tin oxide (ITO) and low carrier mobility titanium oxide (TiO_2) films respectively.

To increase the junction area in the final device, a novel and scalable method was developed for fabrication of upright ordered arrays of ZnO nanowires (NWs) combining top-down etching of ZnO film and silica sphere nanomasking in fluorine-based plasma. The electrical properties of the resulted NWs can be controlled using this approach. The effect of plasma etching parameters and surface treatments on the structural and surface properties of the ZnO NWs were investigated.

A high throughput drop-casting process was next developed using colloidal quantum dots (CQDs) for the formation of light absorbing quantum dot film (QD-film) to replace the widely used input-intensive spin-coating technique. The QD-film provides controllability over thin film properties via tuning the properties of the CQDs building blocks. Crack-free QD-films were formed with single-step drop casting of CQDs from solution (solution-phase ligand-exchange) and Layer-by-layer (L-B-L) replacement of long ligands with short charge transport-compatible ones (solid-phase ligand-exchange).

Charge carrier dynamics were also studied at the CQDs and ZnO interface using photoluminescence decay analyses in order to optimize the selection of CQDs for efficient electron transfer which leads to a better working device. For the first time, the electron transfer in a ZnO/CQD/MoO_3 structure was studied to

eliminate the effect of other non-radiative pathways and determine the true electron transfer at the CQD/ZnO interface. Effect of CQD size and ligands on the transfer efficiency was discussed. The device concepts and theoretical treatment of QD-film/ZnO were also highlighted to gain insight on the CQD and ZnO optical and electrical parameters affecting the performance of the QD solar cell device.

The developed materials and processes were employed for the fabrication of planar and nanowire heterojunction QD solar cell devices. For planar structure power conversion efficiency of η=2.3% at 100 mW/cm^2 solar irradiance were achieved.

Acknowledgements

First and foremost, I would like to thank my parents, Mohtaram and Safar. My parents have sacrificed a lot to raise me up and to tolerate the hardship of me being away when they were in need. I would like to thank my siblings, Neda and Nima, for their moral support and encouragement. This thesis belongs to my family at least as much as it does to me.

I would like to thank my graduate advisor, Professor Siva Sivoththaman. He has been a continual source of ideas and support throughout my graduate studies, while giving me the freedom to explore my own ideas. His patience, enthusiasm, endless pursuit of excellence and dedication to research have given me the motivation to work hard and seek perfection in life and my doctoral research.

I am truly grateful to all my PhD defense committee members, Professor Hany Aziz, Professor Chris Backhouse and Professor Zhongchao Tan, for their time and effort to improve the quality of this thesis and providing valuable comments.

I would like to thank my external examiner, Professor Karin Hinzer, for reviewing my thesis and providing valuable comments and suggestions.

I would like to thank Mr. Joseph Street, CAPDS lab manager, for his valuable technical assistance and dedication to CAPDS lab. I would like to thank Dr. Bahareh Sadeghimakki, research associate in CAPDS lab, for her support and advises during my PhD research. I would like to thank all CAPDS lab members and fellow students that I had the privilege of working with, Dr. Roohen S. Tarighat, Dr. Behzad Esfandiarpour, Maziar Moradi, Zhen Gao, Yaxin Zheng, Dr. Christopher Baldus-Jeursen Nasim Bakhshi-Zadeh, Mohsen Mahmoudysepehr and Dr. Bita Janfeshan.

Many people influenced my graduate experience, I am grateful to all my friends in Waterloo who made my PhD enjoyable experience and full of unforgettable memories.

Dedication

I wish to dedicate this thesis to my parents.

Table of Contents

List of Figures

List of Tables

Acronyms

AM1.5	Air mass 1.5 solar spectrum
Al	Aluminum
Au	Gold
AZO	Aluminum doped zinc oxide
CQD	Colloidal quantum dot
CdSe	Cadmium selenide
CIS	Copper indium sulfide
DLE	Deep level emission
EBL	Electron beam lithography
EBL	Electron blocking layer
EDT	Ethanedithiol
E_F	Fermi level
EPLED	Elastomeric polymer light-emitting device
EQE	External quantum efficiency
ETL	Electron transport layer
FAST	Fluorescence analysis software
FESEM	Field emission scanning electron microscopy
FF	Fill factor
FTO	Fluorine doped tin oxide
FTIR	Fourier transform infrared
FWHM	Full width half maximum
HBL	Hole blocking layer
HRSEM	High resolution scanning electron microscopy
HRTEM	High resolution transmission electron microscopy
HTL	Hole transport layer
HOMO	Highest occupied molecular orbital
ICP	Inductively coupled plasma
IQE	Internal quantum efficiency
ITO	Indium tin oxide
I-V	Current-voltage characteristic
J_{sc}	Short-circuit current
J-V	Current density-voltage characteristic
L-B-L	Layer-by-layer
LED	Light emitting diode
LUMO	Lowest unoccupied molecular orbital
MEG	Multiple exciton generation
MoO_3	Molybdenum trioxide
MPA	Mercaptopropionic acid
NBE	Near band edge emission
NCs	Nanocrystals
NSL	Nanosphere lithography
NWs	Nanowires

OA	Oleic acid
ODA	Octadecylamine
PbS	Lead sulfide
PCE	Power conversion efficiency
PL	Photoluminescence
PLQY	Photoluminescence quantum yield
PV	Photovoltaics
QDs	Quantum dots
QD-film	Quantum dot film
QY	Quantum yield
RF	Radio frequency
RIE	Reactive ion etching
R_s	Series resistance
R_{sh}	Shunt resistance
R_{sh}	Sheet resistance
RT	Room temperature
SCs	Solar cells
SEM	Scanning electron microscopy
TEM	Transmission electron microscopy
TCSPC	Time correlated single photon counting
TCO	Transparent conductive oxide
TiO_2	Titanium oxide
TRPL	Time resolved photoluminescence
VFP	Vertical field power
V_{oc}	Open-circuit voltage
XRD	X-ray diffraction spectroscopy
ZnO	Zinc oxide

Chapter 1
Introduction

1.1 Colloidal quantum dots as “semiconductor ink”

Within the last few decades, the price of electronic devices and gadgets has consistently decreased. This cost reduction have made electronic devices available for daily use, opening a large consumer market. Owing to this cost reduction, many futuristic ideas that were once only considered science fictions (such as wearable electronics, electronic clothes, electronic papers, flexible electronic) have become serious research topics, and in many cases, are steps away from becoming reality. This cost reduction is mainly fueled by the progress and advancement in the fabrication of electronic devices.

A complicated set of factors determines the final cost in the fabrication of an electronic device. Among them, material cost (mainly semiconductor substrate) and processing costs (such as lithography, vacuum, thermal budget) are considered to be the main factors.

One way to reduce material and processing cost is to fabricate electronic devices with solution processing of materials (i.e., using new materials to substitute expensive silicon). This approach for fabrication of electronic devices has been the focus of intense research during last two decades, and is considered a path towards additive manufacturing of devices. To fabricate an electronic device using only solution processing, solution processes for compatible materials (inks) must be developed for every layers used in semiconductor technology. A few of these layers include: insulator layers, metallic layers and semiconductor layers.

Solution process-compatible “semiconductor inks” based on colloidal quantum dots (CQDs) are candidates for fabrication of semiconductor thin films [1]. Colloidal quantum dots are small semiconductor nanoparticles (a few nanometers in size) that are dispersed in solution. Since their advent in early 90s’, knowledge of solution process syntheses of colloidal quantum dots, have dramatically improved. It is now possible to inexpensively synthesize high throughput colloidal quantum dots with high photoluminescence quantum yield (PLQY) approaching 100%. Colloidal quantum dots dispersed in solution can be applied to a variety of substrates. The solvent is removed via evaporation, and the remaining colloidal quantum dots form a densely packed array of semiconductor nano-crystals on the substrate. This arrangement is referred as “nanocrystal solids” or “quantum dot/quantum film”. Nanocrystal solids represent a new form of condensed matter that benefits from the quantum features of its nanoparticle building blocks, which enable tuning of its material properties. In quantum dot film, quantum dots are coupled together to have efficient

charge carrier transport in the QD-film, without sacrificing the highly desired quantum size effect tuning offered by the use of colloidal quantum dots [2]. The overall properties of quantum films are not only governed by the quantum confinement effect in their QD building blocks, but also by the position of the particles, their coupling and packing density, surface traps, polymer ligands and other factors.

The concept of nanocrystal solids, formed by fabricating quantum film from semiconductor ink (CQDs dispersed in solution), is still in its infancy. Knowledge of CQDs' assembly and understanding of its underlying physics and operation mechanisms are also limited. So far, most of the focus have been on traditionally well studied CQDs such as PbS, PbSe, CdS, CdSe, CdTe.

1.2 Third generation photovoltaics based on nanotechnology and new materials

One of humanity's greatest challenges in the 21st century is the search for sources of energy that can substitute fossil fuel. The exponentially growing demand for energy and concerns over the pollution associated with the burning fossil fuel has increased the need for new energy sources. Solar energy has become an attractive source of clean energy and an acceptable substitute for the dwindling fossil fuel supplies. Harnessing this free, clean and abundant solar energy by photovoltaic devices is an attractive, sustainable alternative to fossil fuel. However, despite all of its attraction and advantages, annual energy generation from photovoltaic devices is much lower than other energy resources (less than 0.1%) [3].

The main issue preventing photovoltaic devices from dominating the mainstream energy generation industry is their higher energy production cost compared to their other fossil fuel-based rivals. This energy production cost stems from a complicated assortment of factors including material cost, fabrication cost, installation cost to battery and maintenance cost. Therefore, photovoltaic devices with higher energy efficiencies are favored. As more energy is delivered from fixed-size solar panels assembled with high efficiency PV cells, the resulting price/kWh decreases, compensating for their initial high costs.

Like other semiconductor industries, the solar cell industry is currently dominated by silicon-based photovoltaic devices. These first generation devices are formed from single p-n junctions based on crystalline silicon. Electronic grade pure crystalline silicon is an expensive material. Fabrication of silicon-based devices require high processing costs (Such as lithography and thermal budget). Despite these high fabrication and material cost, the power conversion efficiency of commercial single-junction photovoltaic devices are limited to only 12% to 19%, with a laboratory record of approximately 25% [3]. This is due to mismatch between the bandgap energy of silicon (~ 1.1 eV) and the solar spectrum. While photons with lower energies than the bandgap energy of silicon are not absorbed, the energy of the photons with energies

exceeding the bandgap of silicon is also rapidly lost due to phonon thermalization. One way to resolve this problem is stacking semiconductors with different bandgap energies to maximize the absorption overlap with the solar spectrum. This configuration is realized in multi-junction solar cells and tandem solar cells [4]. The fabrication of multi-junction photovoltaic devices is a complicated, time-consuming and expensive process. Furthermore, issues such as lattice mismatch, proper bandgap energies, and process compatibility contribute to technical and fabrication limitations in selection of materials. In order to achieve maximum efficiency, there must be current matching between each layer of a tandem solar cell, such that only materials with specific bandgap values may be used. However, these required bandgap energies might be unavailable from materials existing in nature.

To avoid the high material and processing expenses associated with first generation solar cells, second generation solar cell technologies use cheaper materials (such as polycrystalline, multicrystalline silicon, silicon spheres and organic solar cells) and inexpensive fabrication techniques (such as solution processing, low temperature deposition). However, this cost reduction in material and fabrication processing is counterbalanced by a substantial decrease in power conversion efficiencies. As a result, the fundamental energy/cost problem of solar cell devices is not resolved.

Third generation solar cell technologies employ nanotechnology and new materials to overcome the high cost of power generation in the solar cell industry. New materials systems such as wide band gap semiconductors, transparent conductive oxides and nano materials (nanowires and quantum dots) are the building blocks of third generation PV devices. Nanotechnology provides new concepts and paths that overcome the theoretical limits associated with PV power conversion efficiency. As well, it provides a means for fabrication and material processing at a low cost [5]. In short, third generation PV technology provides high efficiency PV devices fabricated at low cost.

"Semiconductor inks" based on colloidal quantum dots have the potential to reduce material, process and fabrication costs by providing solution process alternatives for fabrication of photovoltaic devices. Solution processed "quantum dot films" can address the inherent problems associated with multi-junction solar cells. The energy levels in colloidal quantum dots can be tailored by controlling the size of the nanoparticles. This also addresses the issue of availability of natural materials with bandgap energies that meet the needs of multi-junction solar cells. Furthermore, lattice matching can be relaxed in the formation of multi-junction "quantum dot films" because only one type of CQDs, albeit of different sizes (energy bandgaps), is used for each layer. The concept and subsequent research of third generation solar cells based on colloidal quantum dots is not well understood, and theoretical and experimental frameworks are not

established. In order to build a better background for feasible experiment and application, more research and development is required in these fields.

Transparent conductive oxides (TCOs) and wide band gap semiconductors are among the most widely used new material systems in advanced optoelectronic devices and third generation solar cells. So far, indium tin oxide (ITO) is the most commonly used TCO in this type of devices. The resistivity of ITO can be easily lowered to values ($\rho \sim 10^{-4} \Omega.cm$) that allow them to replace metallic contacts. However, ITO is not a suitable TCO for third generation photovoltaic technology. Indium is not an abundant element on earth, and TCOs based on ITO are expensive. Thin films of ITO have low optical transparency in the near infrared and infrared regions. This opposes the requirements of third generation and advanced photovoltaics, where high transparency in the infrared region is an important requirement of a good TCO. In particular, third generation solar cells based on colloidal quantum dots and stacked multiple junctions are designed to maximize absorption across the solar spectrum. These designs require TCOs with high transparency in the visible, near infrared and infrared regions.

TCOs based on zinc oxide have gained attention as a potential replacement for the commonly used ITO in optoelectronic devices. Zinc is more abundant in nature and it can be easily produced with high purity. Therefore, zinc oxide offers a cheaper, nontoxic, bio-compatible, chemically stable replacement for ITO. TCOs prepared by sputtering of aluminum doped zinc oxide (Al: ZnO or AZO) are of particular interest. Sputtering offers a low temperature, robust deposition method with repeatability, uniformity and large area fabrication adaptability. The optical and electrical properties of AZO is tunable by adjusting sputtering parameters (power, pressure and temperature) for high optical transparency in the visible and infrared region, as well as high conductivity. In addition to satisfying the optical transparency requirements of third generation photovoltaic technology, sputtered AZO is an affordable TCO with high conductivity. Therefore, sputtered AZO is a suitable alternative to ITO.

Sputtering of ZnO results in a wide band gap semiconductor that can replace commonly used titanium oxide (TiO_2) in advanced optoelectronic devices. The electron mobility in optimized ZnO thin films is orders of magnitude (10-100 times) higher than TiO_2 thin films. In general, materials with high carrier mobility are attractive for solar cell applications because high carrier mobility reduces the collection loss, and consequently resulting PV devices with higher power conversion efficiency. In the PV device structures where ZnO thin film acts as an active layer, it is equally important to control its mobility and carrier concentration. In third generation heterojunction quantum dot solar cells (HQDSCs), adjusting the carrier concentration in ZnO thin film, maximizes the width of the space charge region in the absorber quantum

film layer [6]. In sputtered ZnO thin films, carrier concentration and mobility of the film is tuned by controlling deposition parameters (power, pressure and temperature).

Nanowire and nanopillar arrays are among the most widely used nanomaterials in third generation photovoltaic devices. Application of nanopillars in PV devices, increases the junction area (high surface to volume ratio). This allows solar cell devices to deliver more energy for a fixed area. Arrays of nanowires also provide orthogonality between light absorption and charge collection paths. In solar cell devices, separation of optical and electrical paths make it possible to engineer the device for both maximum light absorption and carrier collection. The former is done by adjusting the length of nanowires, while, the latter is achieved through tuning nanowire interspacing. Despite these advantages, application of nanowires is very limited in photovoltaic devices. Nanowires are fabricated via two main technology streams: Bottom-up (growth) and top-down methods. Nanowires made from bottom-up techniques are often prone to low geometrical control and random orientation, which limits the performance of the photovoltaic device. Bottom-up techniques are also unfavorable for solar cell applications because of the adverse effects of the metallic (gold, silver) seed layers/ catalysts used in the growth process. These metals act as the recombination centers, which adversely affect the performance of solar cell devices. On the other hand, top-down techniques allow the advantage of higher control over nanowire geometry and orientation. Electron-beam lithography (EBL) is the most studied and widely used top-down method for nanowire fabrication. However, e-beam lithography is expensive and time consuming. Making it an unsuitable choice for the PV industry. Nano sphere lithography (NSL) provides a practical, inexpensive and scalable alternative method for top-down fabrication of nanowires. The development of scalable techniques for nanowires fabrication is among the primary goals of third generation PV technologies.

1.3 Motivation and research objectives

In recent years, progresses in nanotechnology and the advent of new materials have inspired novel design and device structures. Among these new device structures QD-heterojunction solar cells based on solution process colloidal quantum dots (CQDs) and QD-film are very promising and gaining a lot of attention. QD-heterojunction solar cells aim to benefit from quantum confinement advantages as well as solution process fabrication compatibility provided by CQDs to increase the power conversion efficiency and reduce fabrication cost. In the structure of these type of devices often indium tin oxide, which is an expensive material, is used as TCO. So far, the commonly used technique for deposition of QD-film in fabrication of these devices has been based on input-intensive spin-coating technique. In this regard, this study explores new materials system and processes compatible with advanced optoelectronic and third generation PV

devices. The developed materials and processes are employed for fabrication of QD-heterojunction solar cell devices. New material systems investigated in this report include: TCOs and wide band gap semiconductor based on aluminum doped zinc oxide and zinc oxide, and semiconductor ink and quantum films based on colloidal quantum dots. Herein, the report also presents a simple and innovative process for up-down fabrication of ZnO nanowires using nano-sphere masking and reactive ion etching (RIE). The application of these new materials and processes allows fabrication of solution processed and semi-transparent photovoltaic devices. As a proof of concept, planar and nanowire QD-heterojunction solar cells based on CQDs have been fabricated with these materials and developed processes.

The following objectives have been considered in this work:

1. Development of transparent conductive oxide (TCO) based on aluminum doped zinc oxide (AZO): Aluminum-doped zinc oxide provides an affordable alternative to ITO. In this research, we have developed a stable, transparent conductive oxide thin film deposited using RF sputtering of AZO. The AZO thin film is characterized by Hall effect measurement, optical transmission, photoluminescence, transmission electron microscopy (TEM) and X-ray diffraction spectroscopy (XRD) measurements. The optical properties of the film is optimized for high transparency in the visible and near infrared regions of light spectrum, while the resistivity is lowered to a record value of $\rho = 2.94 \times 10^{-4}$ Ω.cm at low deposition temperature of 250 °C. This high quality TCO, can replace expensive ITO in 3rd generation photovoltaic and advanced optoelectronic devices.

2. Development of a wide band gap semiconductor based on ZnO: zinc oxide is a wide band gap semiconductor whose application in 3rd generation photovoltaic devices has been less explored compared to the commonly used titanium oxide. The crystalline zinc oxide has similar properties to the more commonly used crystalline titanium oxide. Zinc oxide is an attractive replacement for TiO_2 because of its reportedly higher electron mobility (10-100 times). Herein, we present RF sputtered ZnO thin films with tunable optical and electrical properties that are optimized for advanced optoelectronic applications.

3. Development of silica sphere nanomask and top-down fabrication of ZnO nano-wires:

   Amino functionalized silica microspheres are used to form a nanomask (densely packed, ordered monolayer of silica nanospheres) on the surface of zinc oxide. Through dry etching, this nanomask is then used for top-down fabrication of ZnO nano-wires. This process can replace the electron-beam lithography step in fabrication of ZnO nanowires and is compatible with PV device fabrication.

4. Exploring drop-casting method as an alternative technique for deposition of "quantum dot film": Spin-coating is the commonly used method for deposition of QDs. However, spin-coating is very input-intensive and results in a considerable material waste. In this research, drop-casting is used for the formation of densely packed array of colloidal quantum dots on a ZnO coated glass substrate. The quantum dots' long, insulating ligands are replaced with short length and charge transport-compatible ligands via the solid-phase ligand-exchange. In an alternative approach, quantum dot film is deposited in a single-step drop-casting of short, polar and charge transport-compatible CQDs solution.
5. Investigating charge transfer dynamics in quantum dot-ZnO interface. Time resolved photoluminescence (TRPL) method is used to measure the exciton life time in QDs. The effect of size, ligand on the charge carrier transfer efficiency is explored.
6. Studying device physics concepts to gain insight on the QD and ZnO opt electric properties which affects the performance of quantum dot solar cell devices.
7. Integration and characterization of electronic devices: Planar and nanowire based PV devices are fabricated using materials and processes developed during this research.

1.4 Organization of this Thesis

Chapter 2 provides an essential background review of the fabrication, technical and physical fundamentals associated with colloidal quantum dots and their application in advanced optoelectronic devices. This background review is divided into four subsections covering the topics of quantum solids, transparent conductive oxides (TCOs) and wide band gap semiconductors, top-down approaches for zinc oxide nanowire fabrication and devices based on CQDs.

Chapter 3 describes the experimental details of AZO and ZnO thin film fabrication (using RF magnetron sputtering) and characterization (electrical, optical and structural). This section presents a summary of the development process of ambient stable AZO and ZnO thin films. This chapter also discusses the control of deposition conditions (power, pressure and temperature) as a method for controlling carrier concentration and Hall mobility in sputtered ZnO/AZO thin films.

Chapter 4 focuses on the development of affordable ZnO nanowires using nano sphere masking (with amino functionalized silica nano spheres as nanomask) and RIE. This section contains experimental details on the formation of silica sphere monolayer nano mask on ZnO coated glass substrates. Herein, RIE etching

conditions (pressure, power and gas ratios) are optimized for high etching selectivity between nano mask (silica spheres) and ZnO substrate.

Chapter 5 describes experimental details taken towards the formation of "quantum dot solids" or "quantum film". We have explored the possibility of using drop-casting of non-polar colloidal quantum dots to form a quantum dot film on the hydrophilic surface of ZnO. Unlike commonly used spin-coating technique, drop-casting is not input-intensive and almost all of the QDs are used in the formation of "quantum dot film". To enhance the conductivity of the quantum film, the CdSe QD's insulating long length ligands are replaced with shorter, carrier conduction-compatible ligands through a solid-phase (ethanedithiol) and solution-phase (mercaptopropionic acid) ligand exchange processes. A layer-by-layer drop-casting process is developed for deposition of charge carrier transport-compatible QD-film from non-polar CQDs in solution. Quantum dot film is also prepared with single-step drop-casting of polar quantum dots with short ligands on ZnO surface.

Chapter 6 presents the charge transfer dynamics in quantum dot-ZnO interface. Time resolved photoluminescence (TRPL) method is used to measure the exciton life time in QDs. The effect of size and ligand on the charge carrier transfer efficiency is explored.

Chapter 7 discusses the theoretical concepts on charge carrier transport in quantum film and devices' operation mechanism. In this chapter, we have tried to correlate characteristics of colloidal quantum dots in solution to electrical and optical properties of quantum dot film. The operation of QD-heterojunction is explained by Schottky diode equation approximation. The challenges in controlling the electrical and optical properties of quantum dot film via tuning NCs' size is highlighted.

Chapter 8 outlines the different advanced solar cell designs built using the materials developed in the previous sections (AZO, ZnO, ZnO nanowires and colloidal quantum dot films). The design considerations and advantages of nanowire heterojunction (QD-ZnO nanowire structure) devices over planar device are highlighted. The AZO-ZnO interface is assessed for an ohmic contact.

Chapter 9 reports the experimental steps taken towards fabrication, integration and characterization of the advanced quantum dot solar cell devices proposed and studied in this research. We explored the possibility of fabricating planar and nanowire heterojunction quantum dot solar cells with the materials developed throughout this research. This section details the preparation of shadow masks, details for the deposition of metal contacts, preparation of molybdenum (III) oxide layers and development of a sealed measurement pack for air-unstable quantum dot solar cell devices. Finally, this section highlights the characteristics of our planar and nanowire QD heterojunction solar cell devices.

Chapter 10 summarizes the findings made during this study and provides suggestions for future work.

Chapter 2
Literature review

2.1 From colloidal quantum dots (CQDs) to quantum dot film

There are many different ways for fabrication of quantum dots: Stransky-Krastanov quantum dots (S-K dots) grown by molecular beam epitaxy (MBE) [7], chemical bath deposition (CBC) [8], successive ion adsorption and reaction (SILAR) [9] and solution processed quantum dots (colloidal quantum dots), to name a few. Among these methods, only colloidal quantum dots are suitable for large scale production. As large scale production (is essential for the fabrication of photovoltaic devices) colloidal quantum dots can provide a proper platform for development of solution-processed and flexible optoelectronic devices.

In 1993, Murray *et al*. developed the first known method for solution processed synthesis of colloidal quantum dots using rapid decomposition of metal-organic complexes at temperatures close to the solvent's boiling point [10]. Since then, various synthesis methods such as: photochemical decomposition [11], thermolysis [12], hydrothermal synthesis [13], solvothermal synthesis [14], sol-gel processing [15], hot-injection method [16], coprecipitation [17] and microemulsion method [18] have been developed for colloidal quantum dots (CQDs) fabrication. The motivation behind of all these methods is to develop a scalable technique for syntheses of CQDs which allows precise control of size, shape, composition and morphology of the colloidal nanoparticles. This has led to emergence of "colloidal quantum dots", a broad topic, which has been reviewed in detail many times in literature [19-21]. Since size control and monodispersity is one of the ultimate goals of these studies, this report will elaborate on nucleation and growth mechanisms for the formation of CQDs. This is followed by reviewing techniques to alter CQDs properties and methods for formation of densely packed, ordered arrays of quantum dots (which can be considered as a new form of condensed matter, and is referred in this report as quantum film/quantum dot film or quantum solid). Finally, we will have an overview of devices which employ colloidal quantum dots and quantum film as their building blocks.

2.1.1 Underlying mechanisms for nucleation and growth of CQDs

Understanding the growth mechanism of solution processed synthesis is critical for tight control of CQDs size and monodispersity. Synthesis of CQDs involves two steps: (a) nucleation, (b) growth of the nuclei. Nucleation happens very rapidly and its rate is affected by temperature, degree of supersaturation of the solution and interfacial tension. Nucleation stops naturally when the precursors are consumed, and

concentration is reduced below a critical level. Nucleation can also be terminated artificially by a rapid drop of temperature of the solvent which happens after injection of the precursors (often at room temperature) into coordinating / non-coordinating solvents at elevated temperatures. This is called the hot-injection method [22].

In contrast to the fast nucleation, growth is a much slower process. There are two widely accepted models to describe the underlying growth mechanism:

- Large particles grow slower than smaller particles, simply because much more material are needed to grow. This phase of growth is referred as the size focusing phase, where the number of particles are constant and their size distribution is narrow [23]. According to this model, a narrow size distribution can be achieved if the nucleation of new particles is terminated while particles are growing.
- Small particles are more prone to dissolve than larger particles, resulting in the continued growth of larger particles while smaller particles are dissolving. This phenomena is known as Ostwald ripening. This phase is referred as the size defocusing phase.

In a typical synthesis scenario, the size focusing phase occurs at the beginning of the growth, right after the termination of nucleation. After a critical size is reached, the size defocusing phase (Ostwald ripening) takes over, and the number of particles decreases (smaller particles dissolve and become consumed by larger ones), resulting in the size distribution increase.

The resulting nanoparticles have a high surface to volume ratio, and are very reactive and prone to oxidation. To stabilize CQDs, their surface is passivated by organic surfactants or ligands. These ligands can affect optical and electrical properties while determining chemical properties (solubility, reactivity) of the colloidal nanoparticles.

2.1.2 Hot-injection and non-injection synthesis methods

The thermal decomposition method is an inexpensive method for synthesis of CQDs that can provide control over the nanoparticle size and shape. There are two common ways to separate nucleation and growth steps during thermal decomposition:

- Hot-injection method, where precursors are injected into high temperature solvent (often surfactant polymer). The injection of precursors initiates nucleation, which is rapidly followed by termination of nucleation due to temperature drop of the solvent. After this stage two growth

phases (size focusing and then size defocusing) prevail. Control over injection temperature is critical since it affects the decomposition of precursors (Figure 2.1).

- Non-injection method (or heat up method), where all precursors and solvents (ligands) are heated up together in the reaction flask. The nucleation happens after reaching a critical temperature, terminates when precursors are consumed. This is followed by the size focusing growth step (Figure 2.2).

The continuous non-injection method is believed to have several advantages over the hot-injection method, such as better control over reaction parameters and efficient mixing of solvent ligand and reagents [24].

The growth can be terminated by a temperature drop (with the aid of water bath or other cooling tool), where resulting CQDs which are dispersed in the surfactant solvent. In order to obtain a monodispersed CQDs solution, nanoparticles should be extracted from the CQD-surfactant solvent mixture and re-dispersed in an appropriate solvent. This is done by performing sequential dispersion and precipitation (with the help of centrifuging) of the CQDs in appropriate solvents, followed by filtering of the nanoparticles. The overall process is referred to as purification. CQDs are very sensitive to purification and may lose their photo-luminescence quantum yield (PLQY) due to partial loss of their surfactants [25].

2.1.3 Methods for controlling properties of CQDs

The optical, electrical and chemical properties of CQDs can be controlled with different techniques. Common methods used for controlling CQDs properties will be discussed herein.

2.1.3.1 Size and shape

The energy band gap of materials can be tuned using the quantum confinement effect. The quantum confinement effect depends heavily on material geometry. Confinement can be in one dimension (quantum wells), two dimensions (nanowires) or in three dimensions (quantum dots). Below a critical dimension (Bohr radius) the quantum confinement effects prevail. In this regime, the behavior of the QD's energy band gap is predicted by quantum confinement theory. By decreasing the size of the quantum dot, larger energy band gaps are obtained. Figure 2.3 represents the predicted values of energy band gap from quantum confinement theory, as well as

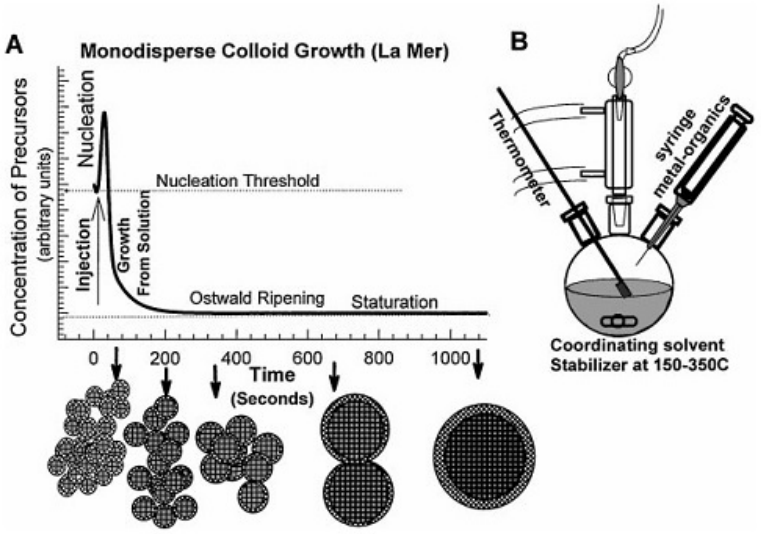

Figure 2.1: (a) Illustration of different steps in hot-injection method, (b) Schematic of three neck reaction flask for synthesis of colloidal nanoparticles [19].

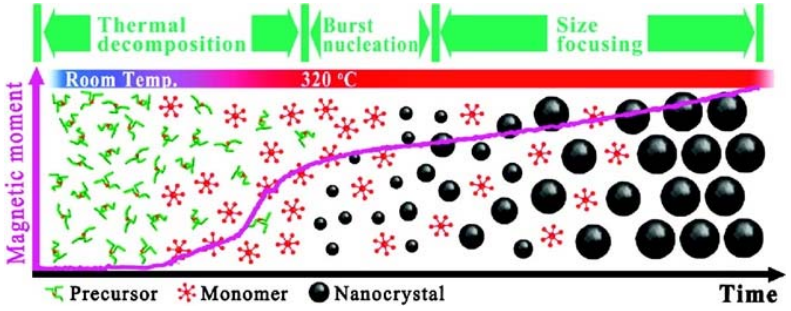

Figure 2.2: Typical synthesis scenario for non-injection or heat up method. In this method all the reactants and solvents are mixed and heat up together inside of the reaction flask. Heating will initiate the nucleation, which will be followed by growth step [26].

experimental values for spherical CdSe and InP quantum dots. As indicated by the diagrams, the theoretical values are very close to experimental values. The wavelength of emission peak in PL spectra or the wavelength of absorption peak in absorption spectra are used for calculation of QDs' optical energy band gap. One practical method for indirect estimation of QDs' size (in comparison to direct electron microscopy techniques such as TEM) is to use the energy band gap-size diagram and optical energy band gap values to find the QDs' size.

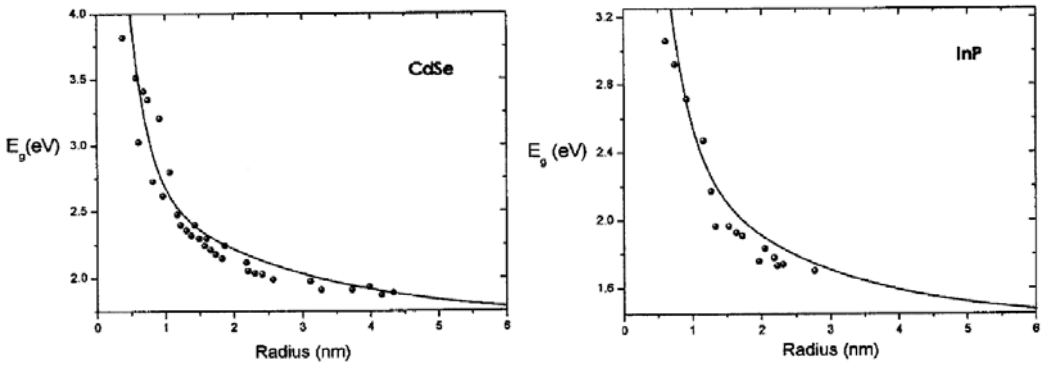

Figure 2.3: Comparison between calculated and measured band gap energies for two different QDs. The experimental data are plotted with symbols and the theoretical predictions with a solid line [27].

Colloidal quantum dots with different sizes can be achieved by terminating the growth process at a specific time. It has been shown that the size and shape of CQDs (such as disk, sphere, tetrapod) can be controlled by adjusting the ratio of precursors and/or surfactant solvents for both core and core/shell nanocrystals [16, 28, 29]. For example, in the case of copper indium sulfide (CIS) CQDs, synthesis methods have been developed to control the structure of nanocrystals. Recently, CIS nanocrystals with tetragonal chalcopyrite or wurtzite structures have been achieved by tuning the composition of surfactants [30, 31].

2.1.3.2 Surfactants/ligands

Ligands are primarily used to stabilize and passivate CQDs in solution. However, ligands can also strongly affect electrical, physical and chemical properties of nanoparticles. Ligands are widely used for surface functionalization and surface modification of colloidal nanoparticles to engineer their interaction with the environment. Talapin *et al.* and Sperling *et al.* have reviewed the different ligands and methods used for passivation and functionalization of colloidal nanoparticles [21, 32].

In 2014, Brown *et al.* reported the effects of different ligands on the energy level modification of lead sulfide (PbS) CQDs [33]. As depicted in Figure 2.4, it is possible to adjust the position of the conduction band and valence band with respect to the reference (vacuum or energy of the hydrogen atom). The relative location of the Fermi level is also affected by different ligands, indicating that carrier concentration of the resultant quantum film is also altered. This study shows that ligand induced surface dipoles can be utilized to control absolute energy levels of CQDs and adjust the energy levels of resulted QD-film.

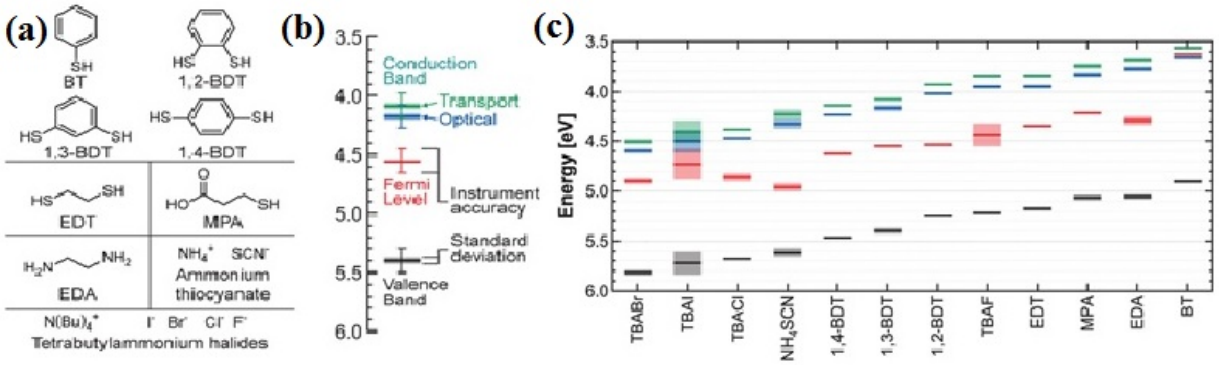

Figure 2.4: (a) Chemical structures of the ligands employed in Brown *et al.'s* study. (b) Energy level diagram of 1,3-BDT-exchanged PbS CQDs. (c) Modification of the absolute energy levels by exchanging the original oleic acid (OA) ligand with different ligands. The original PbS CQDs are ligated with oleic acid and have absorption peaks at λ= 963 nm [33].

While ligands or surfactants are primarily used to passivate the surface of CQDs, they also determine the monodispersity and solubility of nanocrystals in proper solvent after purification.

In general, there are two types of organic solvents:

- Non-polar solvents: solvents with dielectric constants less than 15 are generally considered non-polar solvents. Common non-polar organic solvents include: hexane, toluene, benzene, chloroform.
- Polar solvents: solvents with dielectric constants above 15 are generally considered polar solvents. Polar solvents that have hydrogen bonds (O-H or N-H) in their structure are called polar protic solvents. Example of this family of solvents include: water, ethanol, methanol and isopropanol. On the other hand, polar solvents that do not possess a hydrogen bond are referred as polar aprotic solvents. Acetone and acetonitrile are two commonly used polar aprotic solvents.

In order to obtain a stable monodispersed CQD solution in the selected solvent, the surfactant/ligand of CQDs must be compatible with the solvent. Non-polar ligands such as: trioctylphosphine (TOP), trioctylphosphine oxide (TOPO), oleic acid (OA), octadecylamine (ODA) and dodecanethiol (DDT) allow CQDs to be soluble in non-polar organic solvents like hexane, toluene and chloroform. On the other hand, polar ligands such as mercaptopropanoic acid (MPA) are suitable candidates for polar solvents such as water and methanol. CQDs with non-polar surfactants will agglomerate in polar solvents like water, while CQDs with polar surfactants tend to agglomerate in non-polar solvents.

Due to their high surface to volume ratio, many properties of CQDs are governed or affected by their surface properties. For example, CQDs are very reactive and can easily react with oxygen in the atmosphere. The photoluminescence quantum yield (PLQY) of CQDs is also affected strongly by traps and nonradioactive recombination centers on the surface of the nanocrystals. Ligands are used not only to passivate these traps/recombination centers and enhance PLQY of colloidal nanoparticles, but also to protect the colloidal nanocrystals from oxidation and degradation. As a matter of fact, ligands with longer lengths (longer chains) like OA and TOPO are favored over short length ligands because they provide better passivation, stability, higher PLQY and longer shelf life time for the CQDs [34]. For this reason, most commercial vendors prepare CQDs with long non-polar ligands, like OA, TOPO and ODA, in non-polar solvents.

Surface adsorption of CQDs is also governed by the properties of their surfactants. Commonly used non-polar ligands like TOPO, which are used to stabilize CQDs in non-polar organic solvents, form hydrophobic nanoparticles. These hydrophobic nanoparticles most likely do not adsorb onto the hydrophilic surfaces (such as surfaces of ZnO, TiO_2) [34].

This problem can be solved by "surface engineering" the CQDs. There are two widely used methods to "surface engineering" of CQDs:

- Application of bi-functional surfactants/molecules and linkers: One end of these molecules possesses a hydrophilic properties (allowing them to attach to the hydrophilic surface) while the other end is hydrophobic (attaching to the surfactant of CQD) [35, 36].
- Ligand-exchange: In this method, the original hydrophobic ligand of CQDs are exchanged with another proper hydrophilic ligand to facilitate adsorption onto hydrophilic surfaces such as ZnO or TiO_2 [37]. This process takes place in solution and results in CQDs with reduced PLQY. A variation of the solution phase ligand-exchange is the solid-phase ligand-exchange, where quantum film is placed in a solution with the ligand to be exchanged [38].

CQDs have also been fabricated in aqueous solutions, which accordingly results in a hydrophilic CQD suspension. Synthesis of CQDs in non-polar ligands are more favored because they produce CQDs with higher PLQY and better stability.

2.1.3.3 Core/shell CQDs

Another way for surface passivation of CQDs is through the growth of thin inorganic layers around the core quantum dot to form a core/shell structure. In contrast to passivation with organic surfactants, inorganic

passivation by growth of core/shell structure provides a more efficient (higher PLQY) and durable passivation. Organic materials used for passivation degrade over time and are much more sensitive to heating and surrounding environmental conditions.

In its nature, core/shell structure are heterojunctions. Consequently, all of the factors that must be considered in the formation of bulk materials heterojunctions such as: crystal structure, lattice mismatch, energy band alignments, stress at the interface and strain also affect "nano-heterojunctions" in core/shell quantum dots.

Considering energy band alignments, heterojunctions are categorized into three types (Figure 2.5):

- Straddling gap (type I): in type I heterojunctions, the bandgap of one semiconductor is contained in the bandgap of the other. The discontinuities of the energy bands are in such a way that both carriers (electrons and holes) need energy to cross from the material with the smaller band gap to the material with the higher band gap. Type I nano-heterojunctions are quite common in core/shell CQDs such as CdSe/ZnS, CdS/ZnS, CIS/ZnS, CIS/CdS or PbS/CdS [39, 40].
- Staggered gap (type II): in type II heterojunctions, the energy bandgap of two materials overlap. The discontinuities of the energy bands are in such a way that one carrier type traveling from material A (right material in Figure 2.5) to material B (left material in Figure 2.5) gains energy, while the other carrier type loses energy. An example of type II nano-heterojunctions in CQDs is CdTe/CdSe, CdSe/ZnTe, Znse/CdS and CdSe/CdS [41-43].
- Broken gap (type III): in type III heterojunctions, there is no overlap between the band gaps of the materials. The interfacial carrier transfer resembles type II, but is more pronounced.

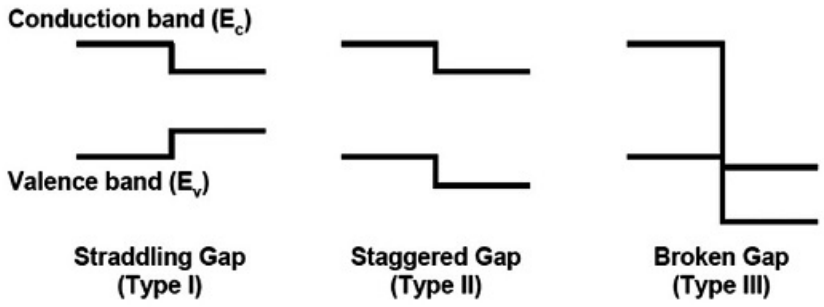

Figure 2.5: Three type of semiconductor heterojunctions categorized by energy band alignment [42].

Common type I core/shell CQDs is CdSe/ZnS where the surface of CdSe core is passivated with high band gap material ZnS. The similar crystal structures of CdSe and ZnS (zinc blend) and close lattice matching between the two materials allows for perfect surface passivation, thereby increasing PLQY.

Nano-heterojunctions also benefit from quantum confinement effect. It is possible to have type I and type II nano-heterojunction for the same material system by either changing size of core, thickness of shell or geometry (shape) of the nanoparticles. Eshet et al. recently studied the transition from Type I to Type II nano-heterojunction in CdSe/CdS core/shell colloidal nano-rods by controlling parameters affecting quantum confinement [43].

In type II CQDs, spatial separation of carriers (electrons and holes) is possible by properly aligning the band gap of the core with the conduction energy band (spatial localization of the hole inside core) or valence energy band of the shell (localization of electrons inside the shell). Kim *et al.* showed that this can lead to localization of one carrier and decrease on e-h overlap, thus increasing exciton radiative lifetimes in CdTe/CdSe and CdSe/ZnTe core/shell CQDs [41].

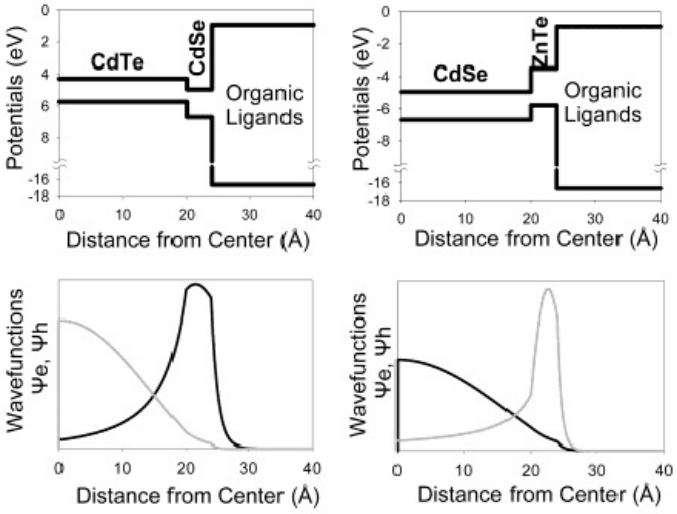

Figure 2.6: Energy diagrams (top) and modeled radial wave functions for electron (gray) and holes (black) for CdTe/CdSe and CdSe/ZnTe core/shell CQDs [39].

2.1.3.4 Alloying and doping

Alloying

Traditionally, the energy band gaps of materials have been tuned by controlling the compositional weight of the constituent semiconductors (controlling stoichiometry) through alloying. Vegard's law regarding

energy band gap and composition of material has been used to tune the energy band gap of materials by adjusting their composition [44]. For CQDs and nanoparticles, alloying can be combined with quantum confinement effect to tune the energy band gaps of the nanoparticles. Tuning the band gap through a combined methodology of stoichiometry control and quantum confinement effect enables absorption and emission wavelengths that is not otherwise possible for the original material [45].

The stoichiometry in CQDs' synthesis can be tuned by controlling the ratio and reactivity of precursors. Pan *et al.* has developed a non-injection method for synthesis of $CdSe_xTe_{1-x}$ CQDs for applications in solution junction CQD solar cells [46].

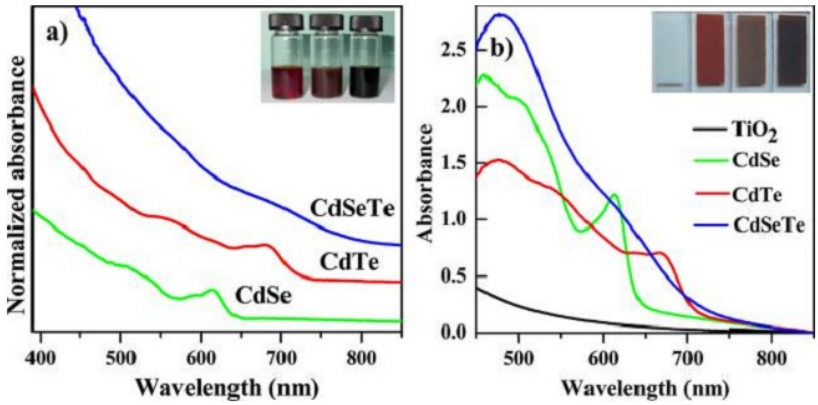

Figure 2.7: Absorbance spectra of binary (CdSe and CdTe) and ternary (CdSeTe) CQDs in (a) solution form, (b) QD-films on TiO_2 substrate [45].

Doping

Bulk semiconductors are electronically doped by "substantial impurity doping technique". Electronic doping of quantum dots and nanoparticles still remains a challenge. Three main techniques have been used to dope nanocrystals":

- Impurity doping of nanocrystals and QDs: Doping of nanocrystals based on deliberate introduction of substantial impurity has demonstrated very limited success. The nanoparticles tend to purify themselves (self-purification) and segregate the dopants out of the core to the surface of the nanoparticle [47]. There have been some successful reports on doping the CQDs using impurity doping technique. Bismuth has been successfully used as an impurity dopant to turn originally p-type PbS CQDs into n-type quantum dot [48]. Silver has also been used to dope PbS CQDs and convert p-type CQDs to n-type nanocrystals [49].

- Doping using surfactants/ligands and surface treatments: Talapin *et al.* and Johnson *et al.* have successfully controlled the doping in PbSe and PbS colloidal quantum dots by surface treatment and use of different passivation techniques [50, 51].These two initial observations paved the path for the idea of doping CQDs and QD-film by surface treatment and choice of ligands. In this regard, the doping of QD-film can be explained by the preference of different ligands to passivate different types of traps (electron-capturing and hole-capturing). Un-passivated surface atoms are either in the form of anions or cations. Cations trapping electrons to form electron-capturing defects, and act as acceptors. On the other hand, by trapping holes, anions form hole-capturing defects and act as donors. The overall doping density would be the difference in the number of hole-capturing traps (donors) and electron-capturing traps (acceptors) [47].

Quantum dot films show stable p-type characteristics. This is because n-type QD-films are unstable and rapidly oxidize in the presence of oxygen and turn to p-type. Consequently, QD-films in their stable form show p-type characteristics. Achieving stable n-type QD-film still remains a challenge. However, Ning *et al.* reported a major breakthrough in their successful realization of air stable n-type PbS QD-film in 2014 [38].

- Incorporation of another nanoparticle/CQD in colloidal quantum dot film: Ko *et al.* has observed 100-fold increase in conductivity of nanocrystal films prepared with 1:1 ratio of PbTe: Ag_2Te nanocrystals over PbTe-only nanocrystal films [52].

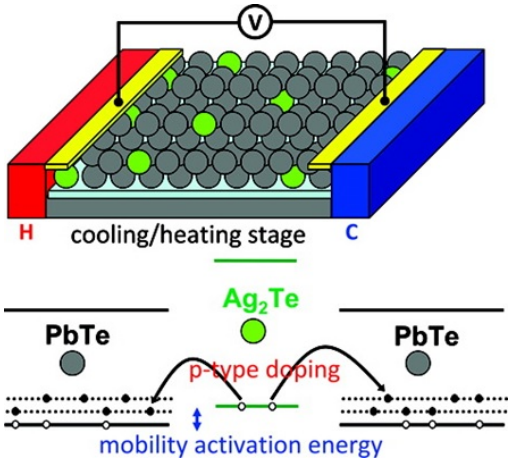

Figure 2.8: Temperature-dependent thermopower and conductivity measurement of nanocrystal solid made from a mixture of PbTe: Ag_2Te (Top), Schematic energy diagram, showing electrons in Ag_2Te nanoparticles filling the trap states of neighboring PbTe nanocrystals (bottom) [52].

As depicted in Figure 2.8, the energy bands of Ag_2Te have a staggered alignment with the host PbTe. Because of this alignment, electrons from Ag_2Te move to fill the trap states of neighboring PbTe nanocrystals, leaving mobile holes in Ag_2Te that contributes into the conductivity of p-type PbTe: Ag_2Te nanocrystal film. This observation suggests that the incorporation of another nanocrystal in the host QD-film can be used to tune the overall doping on the nanocrystal film. So far, the application of this technique has been very limited.

2.1.4 Methods for quantum dot film formation from CQDs

Colloidal quantum dots can be brought together to form an ordered, densely packed array of nanocrystals, which is referred as: “nanocrystal solids”, “quantum dot/quantum solids” or “quantum dot/quantum film”. Nanocrystal solids represent a new form of condensed matter that benefits from the quantum features of its nanoparticle building blocks to tune material properties. The overall properties of the quantum dot film is not only governed by the quantum confinement effect in its nanoparticle building blocks, but also with the position of particles, their coupling and packing density. While the former is affected by selection of material, size of nanoparticles, shape and type of CQDs the latter is sensitive to the method used for the formation of the ordered nanoparticle arrays or quantum dot film.

Herein, we review three major emerged methods (drop-casting, spin-coating, dip-coating) used for formation of nanocrystal solids in small-scale laboratory applications. Industrial methods for large-scale application has not yet received much attention.

2.1.4.1 Drop-casting

In drop-casting, a drop of CQD solution is deposited onto the surface of substrate and left to dry without any physical disturbance. This method is the simplest method for formation of quantum dot film. Drop-casting can be performed on hot substrates to accelerate the evaporation process. Hot substrate drop-casting is often performed with CQDs that are dispersed in solvents with high boiling points. However, the elevated temperature can change the morphology of the CQDs, decompose the surfactants or oxidize the CQDs, causing an unwanted decrease in PLQY [53].

2.1.4.2 Spin-coating

In spin-coating, CQD solution is deposited on the surface of the substrate, mounted on a spinner, and the substrate is spun at typical speeds of 1000-5000 rpm. The centrifugal force spreads the solution across the substrate surface and forms a uniform quantum dot film. To achieve a desired thickness, a layer-by-layer approach is pursued. Deposition and spinning is repeated several times until the desired thickness is reached.

Colloidal quantum dot solutions prepared in solvents with low boiling points such as toluene and hexane are preferred for the spin-coating technique because they allow for quick evaporation during spinning, resulting in high quality quantum dot film [54]. The disadvantage of the spin-coating method is its wastefulness. Thus, this technique is not suitable for industrial applications.

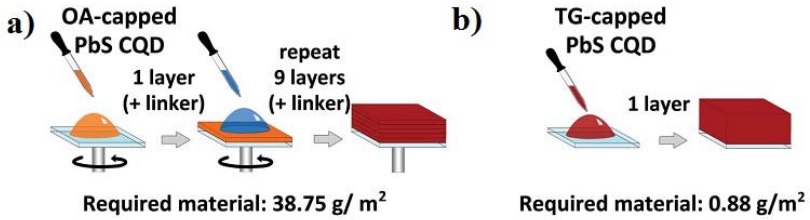

Figure 2.9: a) Standard layer-by-layer spin-coating process with estimation of required active material (PbS CQDs), b) Single-step drop-casting process and the estimation of required active material for the same thickness [52].

2.1.4.3 Dip-coating

In dip-coating, the substrate is dipped into the solution of CQDs and withdrawn at a constant speed. Based on the viscosity and surface tension of the solvent, a thin layer of nanocrystals is formed on the substrate.

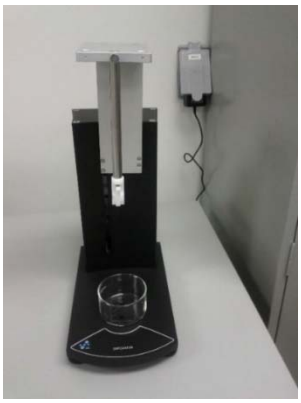

Figure 2.10: Image of automatic system for dip-coating in CAPDS lab.

For this technique, low boiling point solvent is preferred to enhance the evaporation rate of the solvent from the surface of the substrate. Both dip-coating and spin-coating techniques produce QD-films with comparable uniformity. However, dip-coating is less input-intensive than spin-coating. [55]. Often dip-coating is performed with the aid of any robotic system (Figure 2.10).

2.1.5 Minibands in artificial crystals and quantum dot films

A single quantum dot has discrete energy levels. These discrete energy levels are indicated by $1S_e$, $1P_e$, $1D_e$, $2S_e$, ... for electrons and, in a similar way, $1S_h$, $1P_h$, $1D_h$, $2S_e$, ... for holes. Energy band gap for a quantum dot is referred to $E_{gQD}=1S_e - 1S_h$.

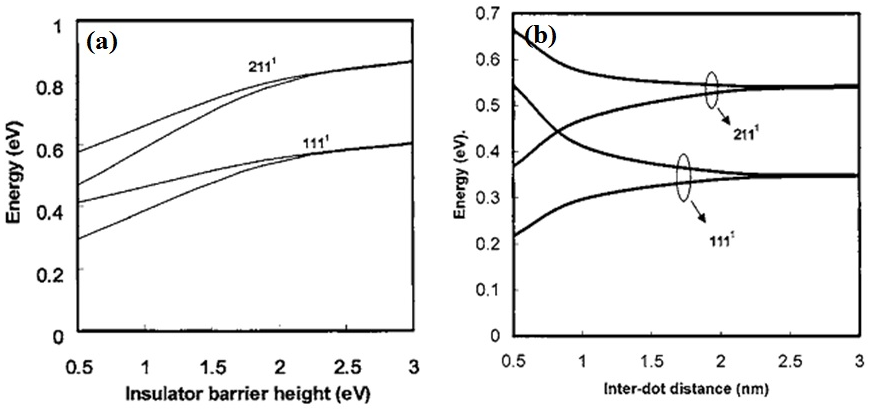

Figure 2.11: Minibands in a silicon nanocrystal film. This nanocrystal film is composed of cubic silicon quantum dots. The dot size is $2\times2\times2$ nm^3. The energy bands are denoted by three quantum number n_x, n_y and n_z. (a) The effect of dielectric barrier height on bandwidth and energy level. The dielectric effective mass is $0.4m_0$ and the interdot distance is 1 nm in all three coordinate direction. The reference energy is taken from the conduction band edge of silicon. (b) The effect of interdot distance on bandwidth and energy level. The calculation parameters are the same as (a) except barrier height which was 0.5 eV [56].

When quantum dots are brought together in a closely packed structure, wave functions of the quantum dots start to overlap with each other and an artificial crystal or a superlattice is formed. Similar to bulk crystal material, this artificial crystal has a periodic potential which is formed by quantum dots, as opposed to atoms in a bulk crystal [57, 58]. As the distance between quantum dots reduces, the wave functions' overlap significantly increases and as a consequence, the discrete energy levels split to minibands (Figure 2.11). The formation of minibands is very similar to formation of energy bands in condensed matter which leads to formation of conduction band and valence band in solid state materials. In fact, minibands in artificial crystals/superlattices of QDs are identical to energy bands in condensed matter [59]. In quantum dot film, quantum dots are coupled together and proximity is increased to have efficient charge carrier transport in the QD-film, without sacrificing the highly desired quantum size effect tuning offered by the use of (colloidal) quantum dots [2].

2.2 Transparent conductive oxides (TCOs) and wide band gap semiconductors

Wide band gap transparent conductive oxides (TCOs) offer high transparency in the visible range, owing to a large intrinsic band gap (~3 eV), and tunable conductivity. Conductivity in TCOs are adjustable over a wide range, from nearly insulating to highly conductive, mainly due to defect (non-stoichiometry) or dopant controlled n-type carrier concentration [56]. Common TCOs are based on tin oxide (SnO_2), indium oxide (In_2O_3), indium tin oxide (ITO), fluorine doped tin oxide (FTO) and zinc oxide (ZnO) ; among these, ITO is the most widely used TCO material.

2.2.1 Intrinsic limit for conductivity of transparent conductive oxides

Although different models have been proposed for carrier transport in TCOs [60], the underlying physics and transport mechanism in TCOs are not fully understood [61, 62]. In these materials, electrons and holes are separated by a large energy gap (~3 eV), where the conduction band is often filled with degenerated electron gas with a density of $10^{19} - 10^{21}$ cm^{-3}. In this free electron gas system, the conductivity will be limited by the scattering of electrons. The total conductivity of TCOs will then be limited by the superposition of all of the possible scattering mechanisms which do not obstruct the transmission of light. Bellingham *et al.*, have showed that ionic scattering of electrons with positive charges (originated from ionized dopants) determines the intrinsic limit for conductivity in TCOs [63]. Bellingham's low resistivity limit and experimental data are depicted in Figure 2.12.

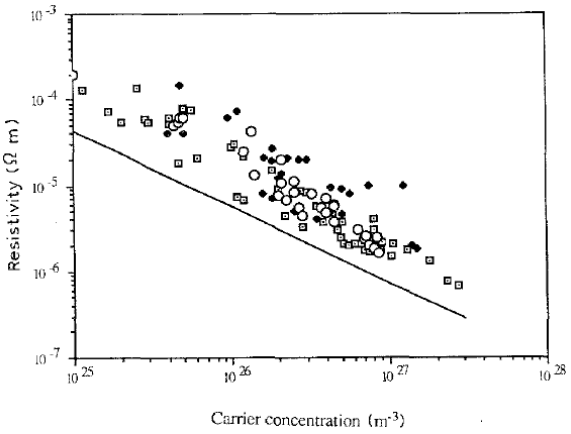

Figure 2.12: Bellingham's low resistivity limit and experimental data for three oxide systems (indium oxide: square, zinc oxide: filled square and tin oxide: circles) [63].

2.2.2 Transparent conductive oxide for 3rd generation photovoltaic cells

Lowering down the resistivity of TCOs while maintaining the highest level of optical transparency is a challenging task. So far, indium tin oxide (ITO) has been the most commonly used TCO due to the fact that its resistivity can be easily lowered to values ($\rho \sim 10^{-4}$ Ω.cm) that allows them to replace metal contacts. However, elemental indium is not abundant on earth. As a result, TCOs based on ITO are expensive and are un-suitable for 3rd generation photovoltaic cells, where low cost is one of the main goals.

For over a decade, TCOs based on zinc oxide have been noted as viable replacement for ITO in optoelectronic devices. The driving force behind this interest comes from zinc's abundance in nature and the ease of producing high purity (99.99%) zinc. Therefore, zinc oxide is a cheaper (more than 10 times), nontoxic, bio-compatible, chemically stable replacement for ITO. Moreover, ZnO films are less absorbent in ultra violet (UV) range and can be doped by commonly available group III elements (boron, aluminum, gallium or indium).

ZnO and impurity-doped ZnO are being incorporated in a wide range of optoelectronic devices such as: solar cells, LEDs, front panel displays and TFTs. TCOs based on ZnO films can be prepared in crystalline, polycrystalline and amorphous forms. ZnO and aluminum doped zinc oxide (Al:ZnO or AZO) thin films are prepared by a variety of techniques such as: evaporation, pulsed laser deposition, chemical deposition, metal organic chemical vapor deposition (MOCVD), spray pyrolysis and magnetron sputtering. Among these techniques, magnetron sputtering is of particular interest, because it offers low temperature deposition, robust process, repeatability, uniformity and large area fabrication adaptability.

Sputtered aluminum doped zinc oxide (Al:ZnO or AZO) is often used as a transparent front contact and back reflector for light trapping in first generation solar cell technology [64]. AZO is also widely used as a transparent electrode in second generation thin film solar cells [65]. Sputtered AZO is a degenerated, semi metallic and highly conductive TCO. Over the past decade, the resistivity of sputtered AZO has been reduced to match ITO ($\rho \sim 10^{-4}$ Ω.cm). Under controlled laboratory conditions, the resistivity of impurity-doped zinc oxide TCOs has been reduced to the range of 10^{-5} Ω.cm; this is accomplished by increasing the carrier concentration up to 1.5×10^{21} cm^{-3} [66, 67]. Although the high carrier concentration is desirable in terms of better electrical properties (i.e. better conductivity), it is unfavorable with regards to optical transmission, particularly in the higher wavelength range. Due to free electrons oscillation above a specific wavelength (plasma frequency), high number of free carriers increases light reflection. This effect is prominent in near infrared and infrared regions, and causes a decrease in light transmission in those regions. In TCO materials, conductivity ($\sigma = en\mu$) is in the range of 10^4 $(\Omega.cm)^{-1}$. Thus higher electron mobility (μ)

in TCO materials allows films with lower carrier concentration (n) to be conductive. TCO films with low carrier concentration and high electron mobility have higher optical transmission compared to similar films (films with same conductivity) with high carrier concentration and lower mobility. In thin film solar cell applications and some third generation solar cell applications where a high transmission in the range of 400 nm-1300 nm is required, it is desirable to exert control over carrier concentration and mobility, such that reflection from free electrons oscillation above the plasma frequency is prevented.

2.2.3 Wide band gap semiconductor for 3rd generation photovoltaic cells

The use of wide band gap semiconductors such as titanium oxide (TiO_2) and zinc oxide (ZnO) provides modern opto-electronics with benefits from their coupled high transparency (for optical coupling) and carrier conductivity. Applications ranges from electron transport layer (ETL), hole transport layer (HTL), window layer, anti-reflection coating and others. [61, 68-70].

Titanium oxide (TiO_2) thin films and TiO_2 based nanostructures (nano pillars, nano-wires, nano particles) are the most commonly studied and used wide band gap semiconductors. Titanium oxide was used by Gratzel *et al.* to realize the first solution junction quantum dot sensitized solar cell [70]. In this structure, titanium oxide nanowires were used to form quantum dot sensitized photo electrodes. TiO_2 nanowires provide high effective junction area as well as orthogonality between electrical and optical path in PV devices. TiO_2 nano-particles and nano-wires have been utilized by Sargent's group for realization of the first bulk quantum dot heterojunction solar cell [71, 72].

The application of zinc oxide in 3rd generation photovoltaic devices is less explored compared to titanium oxide. Crystalline zinc oxide has similar properties to crystalline titanium oxide [73]. Single crystal zinc oxide has band gap of 3.4 eV (direct), refractive index of 2.008 and possesses a wurtzite crystal structure [74]. Meanwhile, crystalline titanium oxide has a band gap of 3.05 eV (for rutile) and tetragonal/ orthorhombic crystal structure (for rutile, Anatase and brookite TiO_2), as well as refractive index of 2.488 (Anatase) [75].

Despite the similarities, zinc oxide is more attractive than TiO_2 due to its possibility for achieving higher electron mobility (10-100 times) in zinc oxide thin films [76]. Higher mobility in the photo electrode can reduce the collection loss, consequently resulting in higher power conversion efficiency.

In device structures where ZnO acts as an active layer, it is equally important to control mobility and carrier concentrations in the ZnO layer. For example, in third generation heterojunction quantum dot solar cells (HQDSCs), where the active layer is the junction between a quantum dot layer and ZnO layer, control

over carrier concentration in the ZnO layer is of crucial importance [77]. In HQDSCs, light absorption happens in the QD layer. The carrier mobility is usually low outside of the depletion region in the QD layer. Control over carrier concentration in ZnO layer is necessary to produce a fully depleted device, which offers better depletion region carrier mobility and better exciton dissociation [78].

2.3 Top-down approaches for zinc oxide nanowires fabrication

Since their advent in the 1990s, arrays of nanowires/ nanopillars have been used in many electronic and optoelectronic device applications. Their popularity is primarily due to the high aspect ratio (surface to volume) they provide [22]. Through providing orthogonality of electrical and optical path, these nano-structures can bypass the essential compromise between minority carrier lifetime/exciton diffusion length and absorber layer thickness when used in photovoltaic devices. Separation of optical and electrical paths means that it is possible to engineer the device for maximum light absorption through controlling the nanowires'/ nanopillars' length (for high thickness of absorber layer), while simultaneously maximizing carrier collection by controlling the interspacing between nanowires/nanopillars [79]. Furthermore, it is possible to optimize the nanowire/nanopillar array for strong light trapping and enhanced light absorption [80, 81].

It has been also demonstrated that it is possible to fabricate nanowires/nanopillars with compositional regimes/regions that are inaccessible in bulk material. This has been accomplished for InGaN nanowires through exploiting the one dimensional nature of nanowire synthesis [82]. When in the quantum confinement regime (dimensions are below Bohr's radius), the band gap of nanowire increases by decreasing its diameter. Combining these two effects (new compositional regimes and quantum confinement) can produce nanowire/nanopillar arrays with tunable band gap and material properties that are beneficial for high efficiency solar cells.

Over the past two decades, different methods and techniques have been developed to fabricate and synthesize nanowires/nanopillars. The fabrication methods can be categorized into two broad categories:

(1) Bottom-up techniques: vapor-liquid-solid (VLS), hydrothermal and others.

(2) Top-down techniques: such as electron beam lithography (EBL), nano imprint, deep reactive ion etching (DRIE) and metal assisted chemical etching.

The problem with bottom-up techniques is the adverse effect of metallic (such as gold, silver) seed layer/ catalyst, which acts as the recombination center, resulting in degrading the performance of solar cell devices

[83]. In addition, the resulting nanowires produced from bottom-up techniques are often prone to low geometrical control and random orientation, which limits the performance of the photovoltaic devices they are used in [80].

Top-down techniques have the advantage of allowing higher control over nanowire geometry (diameter, shape and spacing) and orientation. In top-down methods, if the material is not in the confinement regime, it is possible to extend the electrical properties (like carrier concentration and carrier mobility) of the bulk material to their nanowires. Among top-down methods, electron beam lithography is most studied and commonly used in practice. However, EBL method is not a good candidate for solar cell technology, because it is expensive and time consuming; as a result, it is only limited to fabrication of high tech. optoelectronic devices where cost is not the primary concern. In order to flourish, third generation solar cell technologies need innovative yet affordable masking techniques, such as utilization of nanowires/ nanopillars. One proposed solution is natural lithography, which exploits chemically synthesized nanoparticles (of different shapes) as masks for patterning the underlying substrate [84, 85]. Additionally, nano sphere lithography (NSL) can provide a practical, inexpensive and a scalable alternative method for top-down fabrication of nanowires/ nanopillars [86]. In this study, we explored the possibility of using amino functionalized silica nanospheres as the nanomask in top-down fabrication of zinc oxide nanowires using the reactive ion etching technique.

2.3.1 Basics of reactive ion etching (RIE)

Zinc oxide (ZnO) is very sensitive to both acidic and basic environments; as a result, achieving nano-patterns on ZnO using wet etching is difficult [87]. However, plasma assisted dry etching, can provide essential directionality for meaningful anisotropic etching of ZnO. In this regard, reactive ion etching (RIE) is the primary option for directional etching of ZnO.

Reactive ion etching (RIE) combines chemical etching of the species generated in plasma with physical etching caused by bombardment of ions. Figure 2.13 represents the schematic of an RIE system which uses a planar inductively coupled plasma (ICP) coil. The frequency of the RF power in our RIE system in CAPDS (center for advanced photovoltaic devices and displays) lab is set at 13.56 MHz.

In general, the main steps during an RIE process are (Figure 2.14):

1. Generation of active species
2. Formation of a DC bias to assist acceleration of ions
3. Diffusion of the reactants to the surface of the substrate being etched

4. Adsorption of the reactants by the surface
5. Reaction of the species with the material being etched and formation of volatile products
6. Deposition of the volatile products on the surface
7. Diffusion to the bulk gas and pump out

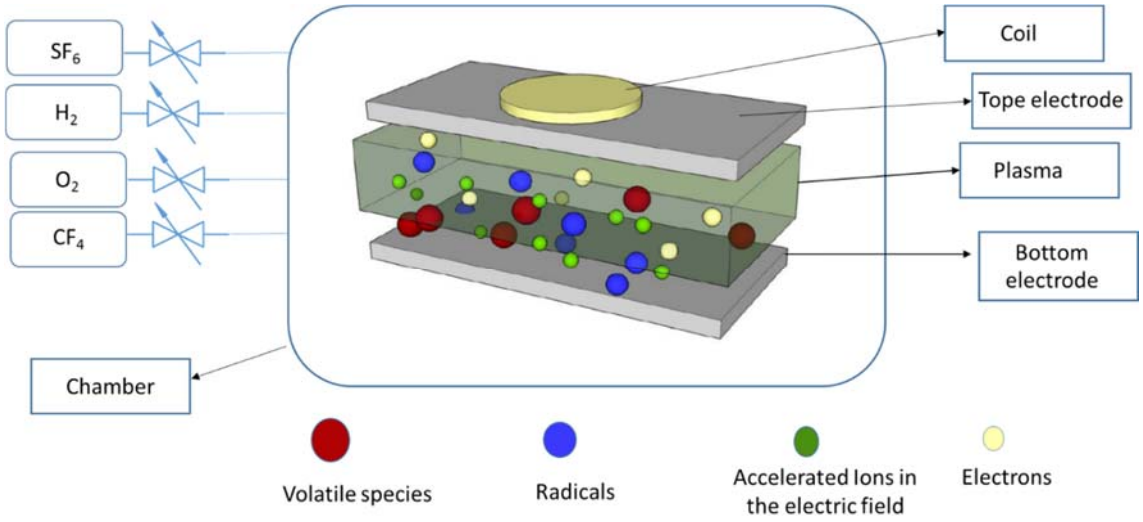

Figure 2.13: Schematic showing generation of etchant species in plasma. The coil is connected to the ICP power generator and the top and bottom electrodes are connected to RF power generator.

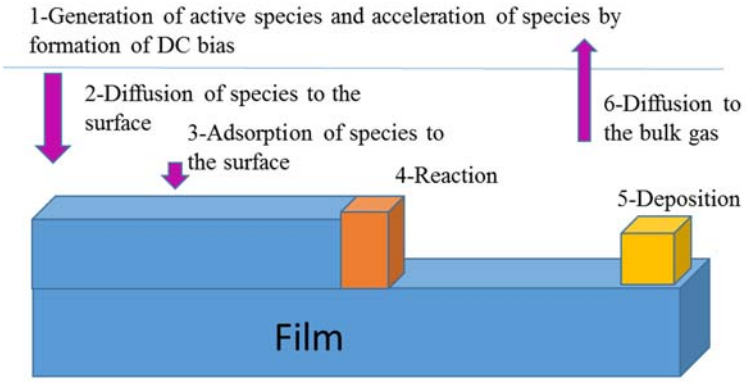

Figure 2.14: Main steps occurring during RIE process.

2.3.2 Etchant gases for reactive ion etching of ZnO

Owing to their high bond energy, plasma etching of wide band gap materials has traditionally been a challenging task. The use of ICP is necessary to achieve meaningful etch rates in wide band gap materials [88, 89].

Different gases have been used for RIE etching of ZnO, such as: Cl_2/Ar, Cl_2/H_2/Ar, BCl_3/Cl_2/Ar, CH_4/H_2/Ar and $BCl_3/CH_4/H_2$, CF_4/Ar, SF_6/Ar. In general, the most common etchant gases used for RIE etching of zinc oxide can be categorized into three families [89, 90]:

(1) Cl_2-based chemistries: Chlorine based chemistries are better candidates for etching of ZnO than fluorine based chemistries since $ZnCl_2$ (Chlorine-based etch product) is more volatile than ZnF_2.

(2) BCl_3-based chemistries

(3) CH_4-based gases and related chemistries: Methane and methane based chemicals are proper candidates for the etching of ZnO. The CH_x produces volatile metallurgical zinc compounds such as $(CH_3)Zn$. As a comparison, the vapor pressure of $(CH_3)Zn$ is 301 Torr at 20 °C, while $ZnCl_2$ has a much lower vapor pressure of 1 Torr at 428 °C.

Table 2-1: CH_4-based and related chemistry ICP etch results [86].

Chemistry	Etch rate (A/min)	Press. (mTorr)	Flow rate (sccm)	ICP power (W)	RF power (W)	Bias (V)	Temp. (°C)	ZnO type
CHF_3/H_2	190	10	50/25	1500	100	_	20	Undoped epi
CF_4/H_2	245	10	50/25	1500	100	_	20	Undoped epi
CH_4/H_2	988	10	30/15	1500	100	_	20	Undoped epi
CH_4/H_2	1200	10	50/25	1500	100	_	20	Undoped epi
CH_4/H_2/Ar	250-2000	10	30/8/16	1500	0-200	0-80	20	Undoped epi
CH_4/H_2/Ar	550-1500	10	30/8/16	500-2500	150	190-15	20	Undoped epi
CH_4/H_2/Ar	100-3000	1	3/8/5	500	50-300	91-294	_	Eaglepicher,bulk
CH_4/H_2/Ar	1000-2800	5	25/5/20	700	150	_	25	Undoped epi

The etching results of ZnO with CH_4-based chemistries is summarized in Table 2-1. Argon is added into the gas mixture for better stabilization of the plasma [89]. Photoluminescence (PL) studies of the etched samples have revealed the possibility of defect passivation by hydrogen. It has also been reported that the

$CH_4/H_2/Ar$ gas mixture is a better etchant than Cl_2/Ar in terms of producing higher PL and minimizing damage to the etched surface [91, 92].

The gases connected to the Trion RIE system in our lab are: SF_6, H_2, O_2 and CF_4. Based on considering of the above mentioned facts, there is care in ensuring a proper ratio of CF_4/H_2 for the etching of ZnO.

2.4 Devices based on CQDs

Colloidal nanocrystals and quantum dots have been used in the fabrication of a variety of electronic devices. Examples include: photo-resistors, diodes, light-emitting diodes, photovoltaic devices, memory units and thermo-electric devices. Herein, we will briefly highlight progresses and advancements in the fabrication of quantum dot light emitting devices (QD-LEDs) and quantum dot solar cells (QD-SCs). We will also high light some advanced concepts in quantum dot solar cells and discuss application of colloidal quantum dots in these third generation solar cells.

2.4.1 Quantum dot light emitting devices (QD-LEDs)

Quantum dots have been used as light emitters in the fabrication of colloidal quantum dot-light emitting diodes (CQD-LEDs) [93].

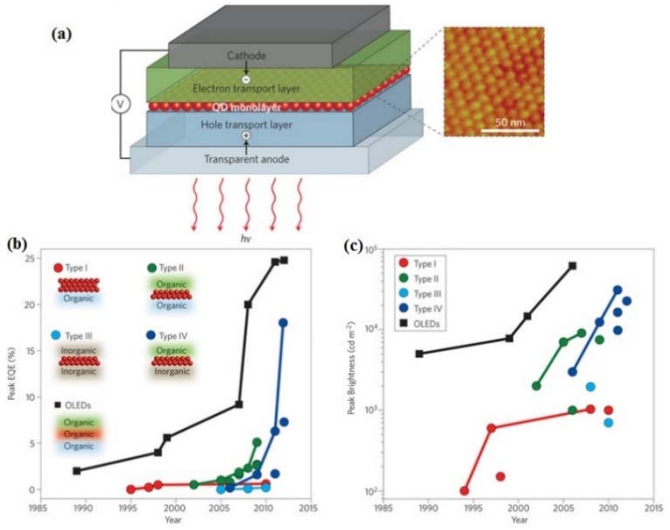

Figure 2.15: (a) The general QD-LED structure, comprised of a monolayer of QDs sandwiched between a hole-transport layer (HTL) and an electron-transport layer (ETL). Progression of orange/red-emitting QD-LED performance over time in terms of peak EQE (b) and peak brightness (c). The insets in (b) show illustrations of different types of emerged QD-LED structures [94]

In a typical CQD-LED, a thin layer of quantum dots (quantum dot film) is sandwiched between a hole-transport layer (HTL) and an electron-transport layer (ETL). ETL and HTL layers allow for the injection of carriers into the light emitting quantum dot layer. ETL and HTL layers can be organic or inorganic materials [94] . A hybrid structure, where one transport layers is organic and the other is inorganic, can also be realized. Incorporating CQDs in light emitting diodes produces devices with high color purity and emission color tunability (varying the size of QDs) from UV to near-IR. Devices using different types of CQDs, organic materials and device configuration have been reported in literature. For example, Shirasaki *et al.* reviewed emerged configuration and device structure of QD-LEDs in their 2013 publication [94].

2.4.2 Quantum dot solar cells (QD-SCs)

One of the challenges current photovoltaic technology faces is replacing the dominant, relatively expensive single crystalline silicon technology with efficient and inexpensive photovoltaic materials. Colloidal semiconductor nanocrystals can be considered a promising alternative material for photovoltaic applications. Nanocrystals provide adjustable optical and electrical properties (through quantum confinement and nanomaterial engineering), and allow for inexpensive solution processed fabrication methods (such as like ink-jet printing, spin-coating and dip-coating). This section reviews emerging solar cell device structures and configurations that utilize colloidal quantum dots as the active layer.

2.4.2.1 Solution junction quantum dot solar cells

Colloidal quantum dots have been utilized to replace dyes (absorber material) in dye-sensitized solar cells (DSSCs) or Gratzel cell. These solution junction quantum dot devices are referred as colloidal quantum dot sensitized solar cells (CQD-SSCs). The first CQD-SSC was reported by Zaban *et al.* in 1997, where InP CQDs were used as sensitizers [95]. In 2007, Leschkies *et al.* reported a CQD-SSC with a power conversion efficiency of 0.4% under AM1.5 simulated solar illumination [96]. In this device, vertically oriented ZnO nanowires sensitized with CdSe colloidal quantum dots were infiltrated with an iodine-based liquid electrolyte. Many different types of quantum dots, electrolyte and electrodes have been studied to form different configurations of CQD-SSCs. Kamat and Emin *et al.* have reviewed this family of quantum dot solar cells comprehensively [97, 98].

2.4.2.2 Hybrid (organic-inorganic) quantum dot solar cells

Hybrid solar cells are formed by bringing organic and inorganic semiconductor materials together. Hybrid-quantum dot solar cells make use of quantum dots by coupling them to an organic semiconductor material. Earlier studies of hybrid-quantum dot solar cells were done by Alivisatos group [99, 100]. The first hybrid-

quantum dot solar cell were reported by Greenham *et al.* in 1996 from Alivisatos group where CdSe/CdS CQDs were coupled to the conjugated polymer poly (2-methoxy,5-(2'-ethyl)-hexyloxy-p-phenylenevinylene) (MEH-PPV) [99]. This device configuration attempted formation of a discrete, separate nano-crystalline phase within the polymer; this was done by increasing the relative amount of CdS/CdSe quantum dots in the composite to above the percolation threshold. This model is analogous to bulk heterojunction organic solar cells, but with a nanocrystal semiconductor phase instead of high electron affinity polymer. In fact, the first hybrid-quantum dot solar cell was configured in a bulk device structure. Greenham's devices showed poor power conversion efficiencies in the order of 0.1% under AM1.5 simulated solar illumination. Many different types of quantum dots, organic materials and so on, have been studied to form different hybrid-quantum dot solar cells. Kamat and Emin *et al.* have provided an in-depth review of this family of quantum dot solar cells [97, 98].

2.4.2.3 All-inorganic quantum dot solar cells

2.4.2.3.1 Quantum dot-Schottky solar cell

Nanocrystal solids have been used to form Schottky junctions with appropriate metals. Air-stable quantum dot solids are often p-type semiconductors. These QDs have been used in formation of QD-Schottky solar cells. In these devices, a quantum dot film is sandwiched between the metal (Schottky junction) and a transparent conductive oxide. The transparent conductive oxide provides an ohmic contact to the quantum dot film [101]. The internal electric field of the quantum dot film, separates electron-hole pairs; electron flow is directed towards metal while holes flow is towards transparent conductive oxide.

The first quantum dot-Schottky solar cell was reported by Johnston *et al.* in 2008 [102]. PbS CQDs with oleate ligands were used in the fabrication of the QD-Schottky device (Figure 2.16). Prior to spin-coating CQDs onto ITO coated glass, solution-phase ligand-exchange was performed to replace the original oleate ligands (~ 2 nm) with much shorter butylamine ligands (~0.5 nm). The PbS-butylamine CQDs were dispersed in octane and spin-coated onto ITO-coated glass to form a uniform layer of PbS-butylamine quantum dot film. A Schottky junction was formed between Al and PbS-butylamine quantum dot film. A maximum power conversion efficiency of 1.8% was achieved under AM1.5 simulated solar illumination at 100 mW cm^{-2}. This Schottky solar cell had a V_{oc} of 0.33 V, a J_{sc} of 12.3 mA/cm^2 and a fill factor (FF) of 49%.

A PbSe-based CQD-Schottky solar cell was developed by Luther *et al.* in 2008. By using sandwiching the PbSe CQDs, between ITO and metal, Luther's device achieved a power conversion efficiency of 2.1%

under AM1.5 simulated solar illumination (Figure 2.17). In the fabrication process of this device, solid-phase ligand-exchange was used to replace the long oleate ligands of the PbSe CQDs with much shorter ethanedithiol ligands (EDT treatment). This Schottky solar cell had a V_{oc} of 0.239 V, a high J_{sc} of 24 mA/cm^2

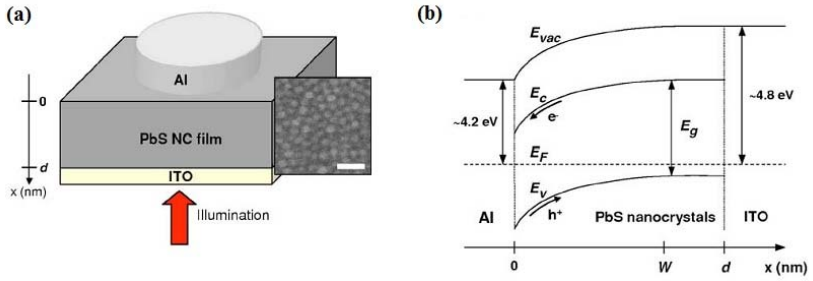

Figure 2.16: (a) architecture of the ITO/PbS/AL CQD-Schottky device. The inset shows an SEM image of PbS-quantum dot film active layer. The scale bar for the depicted SEM image of the active layer is 20 nm. (b) The energy band model for the PbS CQD Schottky device [104].

and a FF of 40.3%.

There have been many efforts to improve the efficiency of QD-Schottky devices. QD-Schottky devices generally suffer from three fundamental limitations [101]:

1. In QD-Schottky devices, light enters the device from the glass side and couples into the TCO/QD junction (ohmic junction), where light absorption starts. As a result, the highest density of photogenerated electrons are far away from the electron-collecting Schottky contact. These electrons must travel the entire thickness of the quantum dot film to reach to metal electrode, and are likely to be lost via recombination.

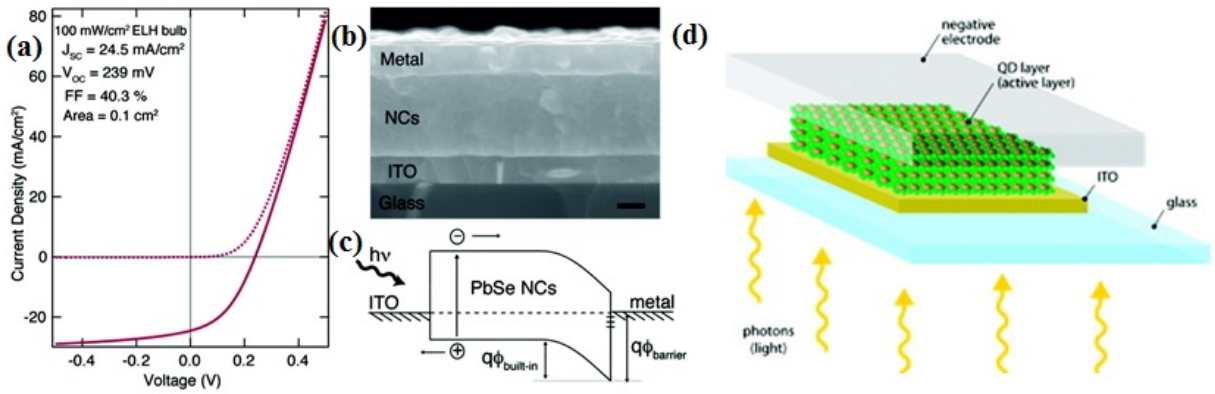

Figure 2.17: (a) I-V characteristic of a PbSe quantum dot solar cell in the dark and under AM1.5 simulated solar illumination, (b) cross sectional SEM of the device, (c) proposed equilibrium band diagram, (d) Schematic of the device [105].

2. The barrier height for an ideal Schottky junction is limited to ~0.67 E_g. At the metal quantum dot film interface, Fermi level pinning happens due to defects states, thus lowering achievable open circuit voltage.

3. There is no effective barrier to prevent hole injections into the metal electrode (electron-collecting electrode in the QD-Schottky device). This causes electron and hole recombination in the metal electrode, limiting the shunt resistance of the solar cell device.

An inverted QD-Schottky solar cell device was reported by Dung Mai *et al.* in 2014 [103]. In this device, the QD-Schottky junction is moved from the back (QD-metal) to the front (QD-TCO) of the device (inverted QD-Schottky solar cell). The surface of the FTO (fluorine-doped tin oxide) is treated with polyethylenimine (PEI) to form an electron transport layer, as well as modify the work function of the FTO. The work function of PEI-coated FTO, is reported to be 3.6 eV, which is comparable with Ca or Mg work-functions. The inverted QD-Schottky solar cell is formed by sandwiching PbS between a low work-function TCO (PEI treated FTO) and a high work function metal (Au). During fabrication of this device, solid-phase ligand-exchange was used to replace the original long oleate ligands of the PbSe CQDs with ethanedithiol ligands (EDT treatment). The device reached a power conversion efficiency of 3.8% at AM1.5 simulated solar illumination and showed a high V_{oc} of 0.64 V, a J_{sc} of 13.6 mA/cm^2 and a FF of 43.3%.

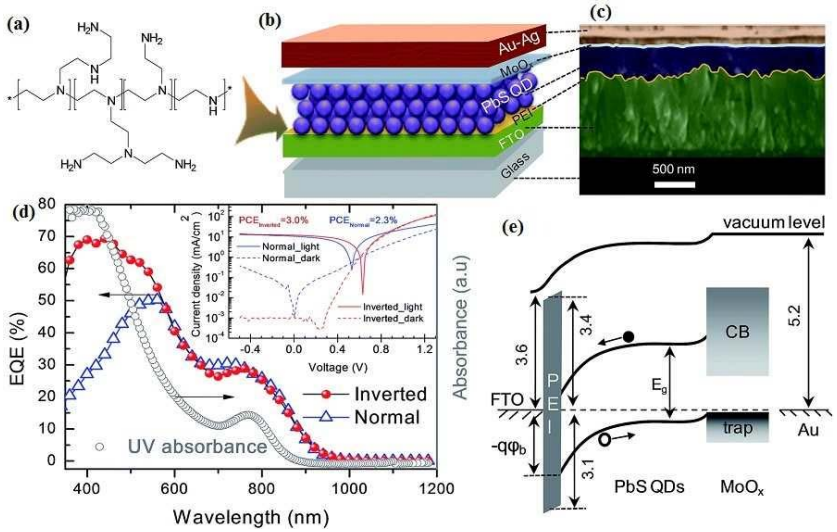

Figure 2.18: a) Chemical structure of polyethylenimine (PEI) molecule, (b) schematic of an inverted QD-Schottky solar cell device structure, (c) Cross-sectional field emission scanning electron microscope (FESEM) of an inverted QD-Schottky solar cell, (d) The EQE of an inverted and a normal Schottky solar cell with a 200 nm thick PbS QD layer. The structure of a normal Schottky cell is ITO/PbS CQD/LiF-Al, (e) The proposed energy band diagram for the inverted Schottky device under open-circuit conditions.

2.4.2.3.2 Quantum dot-heterojunction solar cells

QD-heterojunctions are formed by bringing a quantum dot film together with a semiconductor thin film. As quantum dot films are generally p-type, an n-type transparent semiconductor is typically used for the other side of p-n QD-heterojunctions. The band gap of materials is specifically selected and aligned to have a type II (staggered) heterojunction between the two materials. Type II heterojunctions allows for better exciton dissociation and carrier separation. The selection of material and its composition, as well as tuning its quantum confinement effect (via NCs size control), are used to adjust the band gap of the two materials to achieve the best possible quantum dot-heterojunction solar cell. Since the restriction on material selection is relaxed by the quantum confinement effect and control over material composition, a broader range of materials can be used for the construction of QD-heterojunction solar cells.

Herein, we briefly review different types of QD-heterojunction solar cells, with emphasis on structures based on wide band gap transparent semiconductors (such as ZnO and TiO_2) and CQDs.

Planar QD-heterojunction solar cell

In 2009, Leschkies *et al.* reported a QD-heterojunction solar cell device [77]. Fabricated with PbSe QDs film, this device achieved power conversion efficiency of 1.6% under AM1.5 simulated solar illumination (Figure 2.19). The PbSe colloidal quantum dots were deposited by dip-coating on to ZnO, and solid-phase ligand-exchange was used to replace the bulky oleic acid ligands on the PbSe quantum dots with EDT ligands (EDT treatment). An electron blocking layer (α-NDP) was used to prevent electron injection into the metal electrode (Au) and eliminate electron-hole recombination. This QD-heterojunction solar cell displayed a V_{oc} of 0.45 V, a J_{sc} of 12-15 mA/cm^2 and a FF of 27%.

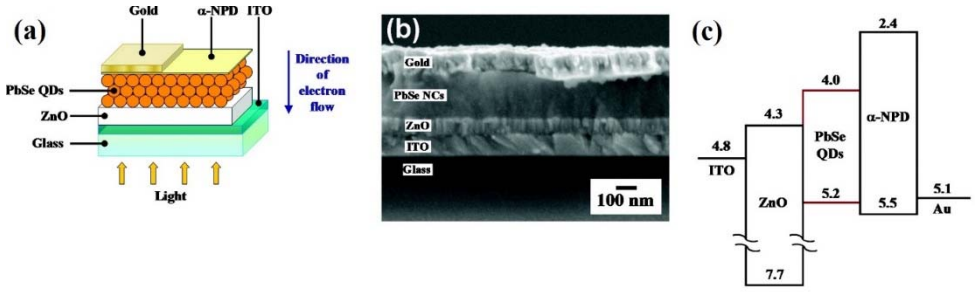

Figure 2.19: (a) Schematic of the PbSe QD-heterojunction solar cell. (b) Cross-sectional scanning electron micrograph (SEM) of the PbSe-heterojunction solar cell illustrated in (a). (c) Proposed energy band diagram of an ITO/ZnO/PbSe QDs/α-NPD/gold stack. Energies are in eV and with respect to vacuum [77]. α-NDP: [N, N'-bis (1-naphthalnyl)-N, N'-bis (1-phenylbenzidine)].

Bulk QD-heterojunction solar cell

The first solution processed depleted bulk QD-heterojunction solar cell was reported by Barkhouse *et al.* in 2011 [71]. In this device, a nanostructured bulk active layer is deposited with a thickness that is sufficient to absorb all of the incident light in the absorption wavelength corresponding to QDs' size (Figure 2.20). Barkhouse *et al.* proposed that the increased surface and active layer thickness in this structure increases light absorption and helps charge collection in the active layer, resulting in the efficiency of bulk QD-heterojunction devices surpassing the efficiency of planer QD-heterojunction devices.

The architecture breaks the photon absorption/carrier extraction compromise inherent in planar devices. The TiO_2 electrodes are fabricated by spin-coating colloidal TiO_2 nanocrystals. A porous TiO_2 (from 150-250 nm in size nanocrystals) layer was formed on top of the previously deposited dense layer of TiO_2 (from 10-30 nm in size nanocrystals). The porous TiO_2 layer was infiltrated with PbS quantum dots. Solid-phase ligand-exchange was used to replace the PbS QDs' bulky oleic acid (OA) ligands with shorter mercaptopropionic acid (MPA) ligands.

The planar device achieved a power conversion efficiency of 5.1% under AM1.5 simulated solar illumination and had a V_{oc} of 0.51 V, a J_{sc} of 16.2 mA/cm^2 and a FF of 51%. Meanwhile, bulk device achieved a power conversion efficiency of 5.5% under AM1.5 simulated solar illumination and had a V_{oc} of 0.48 V, a J_{sc} of 20.6 mA/cm^2 and a FF of 56%.

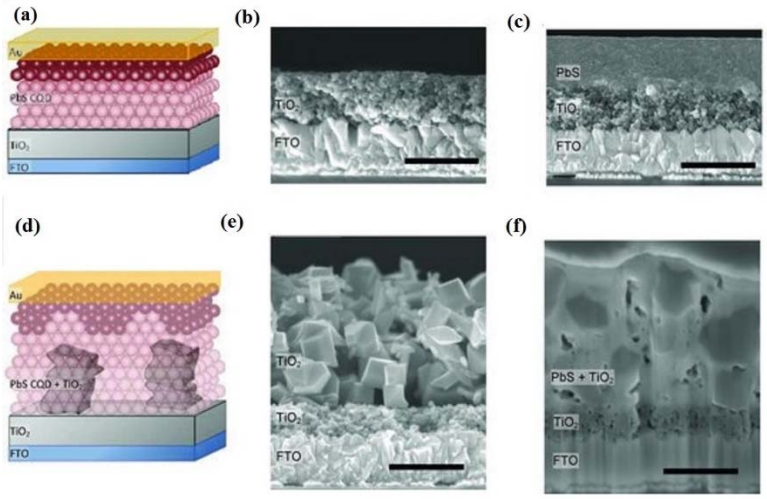

Figure 2.20: Schematic drawings of the cross-section of (a) depleted heterojunction (DH) and (c) depleted bulk heterojunction (DBH) devices. The color gradient indicates the charge depleted portion of the device. (b) and (e) cross sectional scanning electron microscopy (SEM) images of the TiO_2 and nanoporous TiO_2 structure, (c) PbS CQDs on the TiO_2, (f) PbS CQDs are in-filtered in the nanoporous matrix. In each case the scale bar is 1 μm [71].

2.4.3 Emerging advanced third generation solar cells based on QDs and CQDs

2.4.3.1 Multi-junction solar cells

One approach to reduce the thermalization loss and increase efficiency of photovoltaic devices has been to use a stack of cascaded multiple p–n junctions. This stack of multiple p-n junctions are separated by tunnel junctions and are placed in descending band gap values along the direction of the incident light. The descending band gap values allows higher energy photons to be absorbed in the higher band gap semiconductors and lower energy photons in the lower band gap semiconductors; this reduces the overall heat loss. Such cells are generally called tandem or multi-junction solar cells [104].

In practice, multi-junction solar cells are typically implemented in III-arsenide and phosphide systems with 2-4 band gaps, taking advantage of the tunability of band gap energies and lattice constants with the compositions of III-V compounds. A typical structure of a triple junction solar cell with current world record efficiency is shown in Figure 2.21 (a). In this solar cell, the top cell is made of gallium indium phosphide (GaInP) (E_g= 1.89 eV), the middle cell is Gallium Arsenide (GaAs) (E_g = 1.42 eV) and the bottom cell is Germanium (Ge) (E_g = 0.67 eV) with tunnel junctions in between, to match the currents between each cells [105]. As demonstrated in the quantum efficiency plot of Figure 2.21 (b), the three layers absorb different portions of the solar spectrum, depicting excellent coverage of the sun's spectrum.

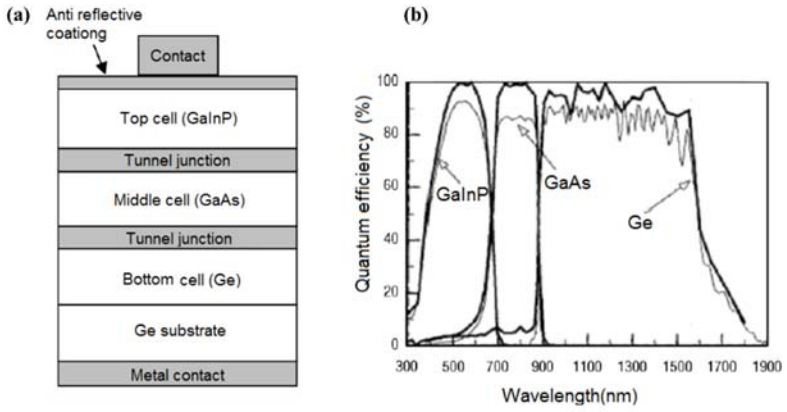

Figure 2.21: (a) A typical structure of a triple junction solar cell. Bottom cell, middle cell and top cell are individual p-n junction solar cells based on Ge, GeAs and GaInP respectively. (b) Quantum efficiency curve of the cell [105].

The first tandem solar cell with colloidal quantum dots was reported by Wang *et al.* in 2011 [106]. This device employs CQDs with different band gap (1.6 eV and 1 eV) via size tuning of PbS CQDs to form a multifunction solar cell. In this structure, a graded recombination layer (GRL) is used to provide a

progression of work functions from the hole-accepting electrode in the bottom cell to the electron-accepting electrode in the top cell, allowing matched electron and hole currents to meet and recombine. The GRL layer is composed of molybdenum trioxide (MoO_3), indium tin oxide (ITO) and aluminum doped zinc oxide (AZO) (see Figure 2.22 (a) and (b)). Wang's tandem solar cell has an open-circuit voltage of 1.06 V, equal to the sum of the two constituent single-junction devices, a J_{sc} of 8.3 mA/cm^2, a FF of 48% and a solar power conversion efficiency of up to 4.2% under AM1.5 simulated solar illumination [106].

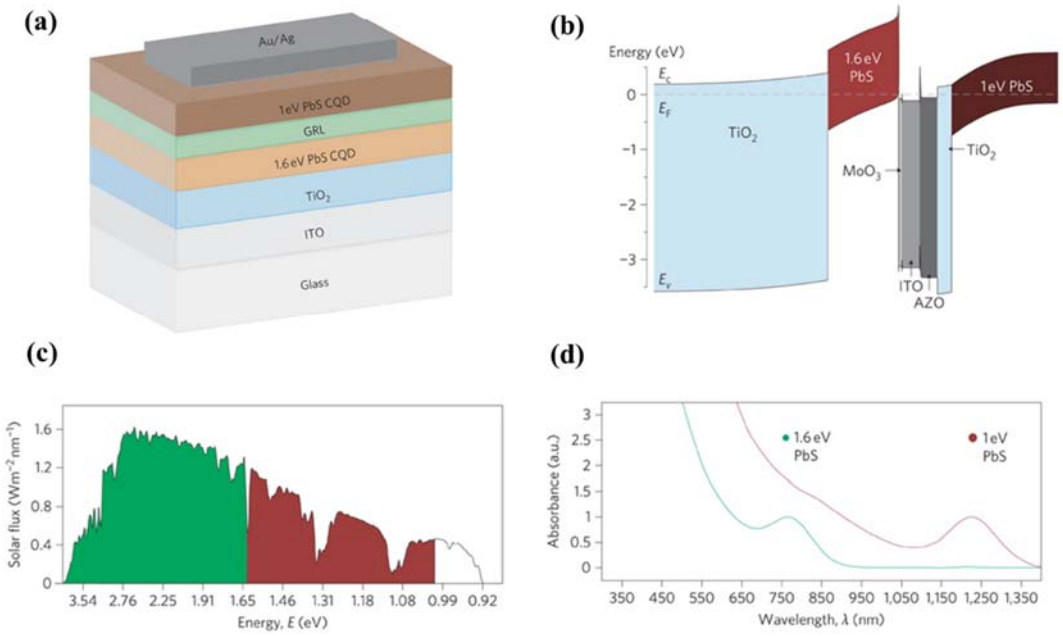

Figure 2.22: (a) CQD tandem device architecture, (b) spatial band diagrams for CQD tandem cells at equilibrium, (c) spectral utilization for CQD tandem solar cell, (d) Absorbance of PbS CQDs with quantum-confined bandgaps of 1.6 eV (green) and 1.0 eV (red) [102].

2.4.3.2 Multi-exciton generation (MEG) solar cells

The creation of more than one electron-hole pair per high energy absorbed photon (multi-exciton generation or MEG) has been recognized for over 50 years in bulk semiconductors; it has been observed in the photocurrent of bulk p–n junctions such as Si, Ge, PbS, PbSe, PbTe, and InSb [107, 108]. However, MEG in bulk semiconductors is rather inefficient because of competing decay channels for the photogenerated electron-hole pairs, such as phonon-assisted cooling, which is extremely fast.

In contrast to bulk semiconductors which show low MEG quantum efficiency, Klimov *et al.* in 2005 [109] demonstrated that in semiconductor QDs the MEG can be very efficient and the threshold photon

energy for the process to generate two electron–hole pairs per photon can approach values as low as twice the threshold energy for absorption (the absolute minimum to satisfy energy conservation); this effect allows the threshold to occur in the visible (VIS) or near infra-red (NIR) spectral region. Figure 2.23 depicts the overall process of MEG in QDs. As a result of hot electrons cooling rate reduction, the efficiency of MEG process can be enhanced.

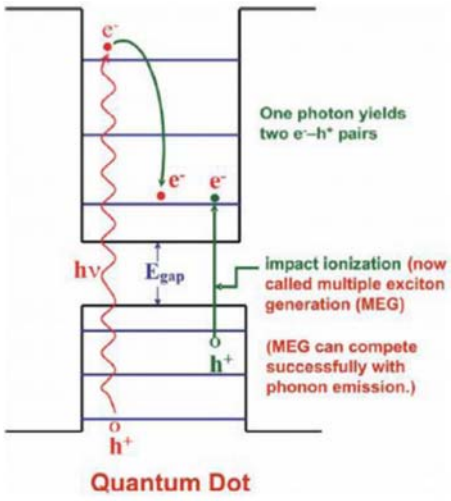

Figure 2.23: Multiple exciton generation (MEG) in a quantum dot [110].

The first third generation colloidal quantum dot solar cell device utilizing MEG concept is realized by Semonin *et al.* in 2011[111]. In this depleted heterojunction colloidal quantum dot solar cell structure, PbSe CQDs with different energy band gap were employed as absorber layer. PbSe quantum dot films are treated with ethanedithiol (EDT), hydrazine, methylamine and ethanol for fabrication of different CQD heterojunction solar cells. Films treated with EDT showed a reduced MEG efficiency whereas films treated with hydrazine, methylamine, and ethanol preserved (to varying degrees) the MEG-enhanced photon-to-exciton quantum yield measured in colloidal dispersions. Semonin *et al.* has reported an increase in the photocurrent arising from MEG in lead selenide (PbSe) QD, as manifested by an external quantum efficiency (EQE) that peaked at 114 ± 1% in the best device measured. The associated internal quantum efficiency (IQE; corrected for reflection and absorption losses) for the same device was 130% [111]. The architecture of the CQD heterojunction device and EQE and IQE spectra's are represented in Figure 2.24.

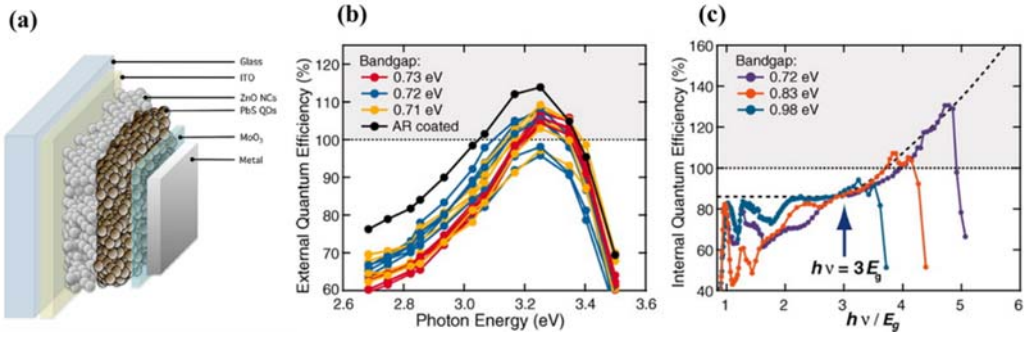

Figure 2.24: (a) The structure for PbSe CQD-heterojunction solar cell, (b) EQE peaks for 18 independent devices made with QD bandgaps of 0.71 eV (yellow), 0.72 eV (blue), and 0.73 eV (red), as well as a device with an antireflective coating (black), (c) collected IQE curves versus the ratio of photon energy to bandgap [111, 112].

2.4.3.3 Intermediate band solar cells

Another leading concept that can be obtained with quantum dots for high efficiency cells is the impurity level PV (IPV) or intermediate band (IB) solar cell. The idea in intermediate band solar cells is to present sub band gap density of states to allow sub band gap absorption. In such systems beside the normal absorption (VB→CB), the low energy photons are absorbed through two step absorption: VB→IB, IB→CB.

The IPV concept can be exploited by two-step generation via impurity states within the band gap to utilize sub-band gap photons and therefore enhance solar cell performance (see Figure 2.25 (a))[113].The challenge is to find a suitable host wide band gap semiconductor combined with a sufficiently radiatively efficient impurity. The IB solar cell is characterized by the existence of a narrow band within the main band gap (See Figure 2.25 (b)). The states of closely spaced QDs, when finely tuned, yield an intermediate band. Three transitions, available in both systems, enable the device to better match to the solar spectrum.

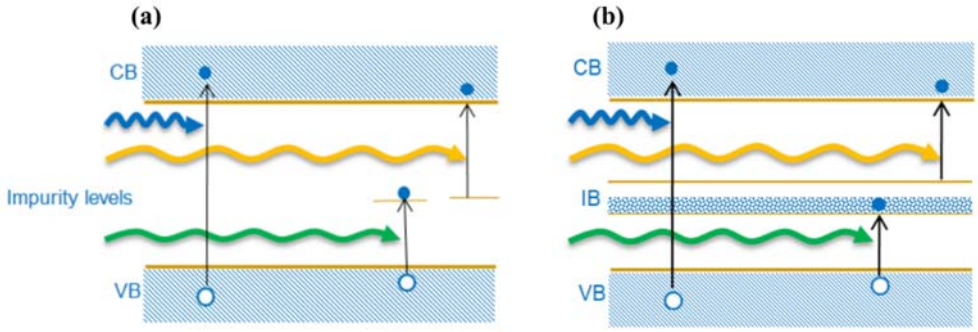

Figure 2.25: Schematic diagram showing absorption of above-band gap and sub-band gap photons through (a) impurity level, (b) intermediate band; showing the valence band (VB), intermediate band (IB), and conduction band (CB), transitions between these bands (A).

Yu *et al.* using a combined high energy oxygen implantation and laser recrystallization process in the ZnCdTe system demonstrated the first successful intermediate band solar cell [114].

One way to form intermediate bands is through incorporation of quantum wells (QWs) or QDs with narrower band gap in the original PV material [115]. Walker *et al.* has studied the effect of number of InAs QD layer, placed in the middle subcell of a triple-junction InGaP/InGaAs/Ge photovoltaic device, on the performance of multi-junction solar cell [116]. Limited experimental works has been carried out using QDs to form intermediate band solar cells. Martí *et al.* reported intermediate band solar cell using InAs quantum dots embedded in GaAs host semiconductor [117].

Intermediate band solar cell employing colloidal quantum dots was proposed by Vörös *et al.* in 2015 [118]. In this work it has been argued that intragap states present in the isolated colloidal CdSe quantum dots with reconstructed surfaces combine to form an IB in arrays of CQDs, which is well separated from the valence and conduction band edges [118].

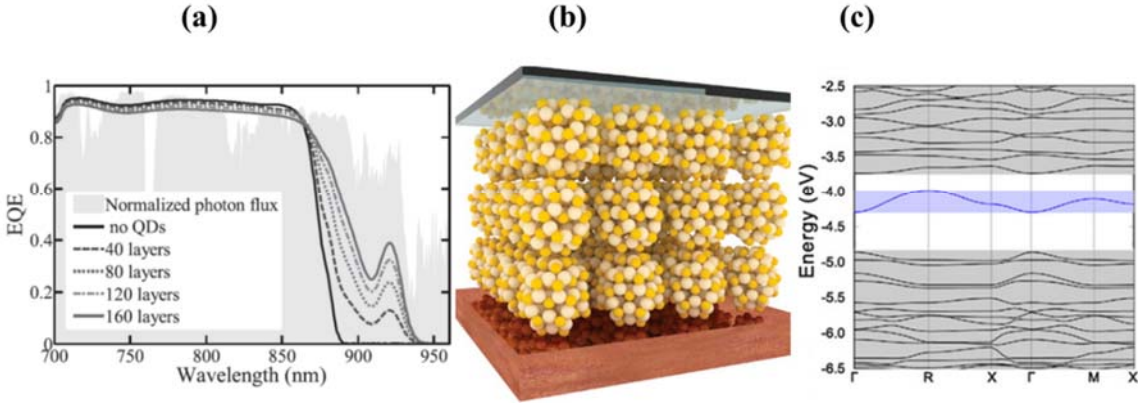

Figure 2.26: (a) Increase in the middle sub-cell quantum efficiency due to the addition of QD layers described with 7 meV of effective band offsets for the wetting layer [116], (b) Cluster of CQDs proposed for the formation of intermediate bands in solar cells [118], (c) simulated energy bands for CdSe CQDs [114].

2.4.3.4 Spectrum conversion/shifting (Up/Down Conversion and Down-shifting)

One of the effective methods to address the energy losses due to lattice thermalization loss and sub-band gap transmission loss is spectral modification through down-shifting (DS), down-conversion (DC) as well as up-conversion (UC) of photons. First generation single-junction semiconductor solar cells are just able to convert energy of photons slightly above the energy band gap of the material (silicon). In these devices, low-energy photons are not absorbed while high-energy photons are excited well above the conduction band edge (produce hot electrons) where they are mostly lost due to interaction with phonons (thermalization). Down-shifting is aimed at absorbing these high-energy photons and shifting them to lower energies, through

a relaxation process, to a lower energy state (see Figure 2.27 (a)). The fundamental mechanism of down-conversion is the absorption of high energy photon, with relaxation into intermediate states within the band gap, emitting two lower energy photons (see Figure 2.27 (b)). Up-conversion is to generate one higher energy visible or NIR photon from at least two lower energy photons [119]. The typical mechanism of up-conversion involves absorption of sub-band gap light into an intermediate state, followed by further absorption of a second photon to the conduction band edge. The excited charge carrier then relaxes back to the valence band edge, emitting a single higher energy photon (see Figure 2.27 (c)).

Spectral modification aims at converting the solar spectrum via luminescence to match the absorption properties of the PV devices. Spectral modification can be treated as an optical process alone and dissociated from the actual operating physics of the PV devices. Photon conversion materials can be applied to the existing first and second-generation PV devices. In this regard, colloidal quantum dots are attractive candidates for spectral modification.

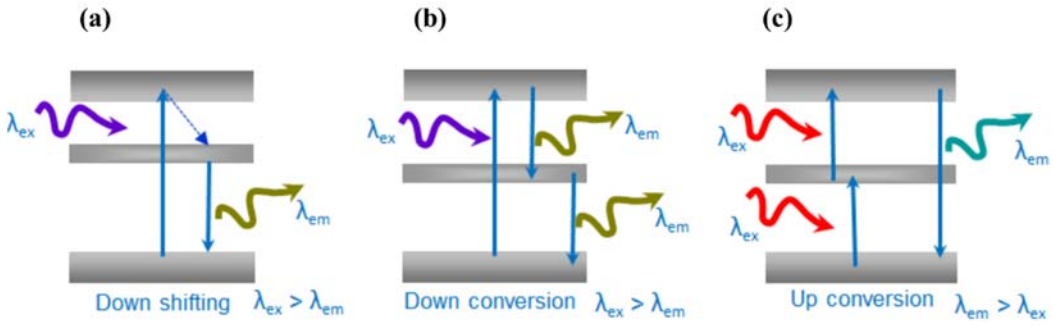

Figure 2.27: Fundamental mechanisms for a) down-shifting, b) down-conversion and c) up-conversion.

There are few reports on successful employment of colloidal quantum dots on PV devices for spectral modification. In 2014, Sadeghimakki *et al.* reported the occurrence of luminescence down-conversion (LDC) mechanism in CdSe/ZnS colloidal quantum dots deployed on silicon solar cells [120]. In the same year, Gardelis *et al.* reported a significant down-conversion in a silicon solar cell using CIS/ZnS colloidal quantum dots [121].

A luminescence up-conversion effect in colloidal double quantum dots is reported by Deutsch *et al.* in 2013 [122]. In this double dot quantum dot, CdTe and CdSe dots are capped together with CdS shell. The CdTe quantum dot absorbs the low energy photons and the CdSe QD emits the up-converted high energy photons. Two possible mechanism has been proposed for up-conversion in double dot QDs (see Figure 2.29 (c)): (a) Direct intraband hole absorption mechanism of up-conversion: (1) a hot hole formed due to intraband

absorption, (2) hole crosses above the barrier to the second dot; (b) Auger-mediated up-conversion: (1) a second intraband absorption event happens, (2) this second intraband absorption event is followed by Auger recombination, leading to a formation of a hot hole, (3) this hot hole crosses above the barrier to the second dot [122].

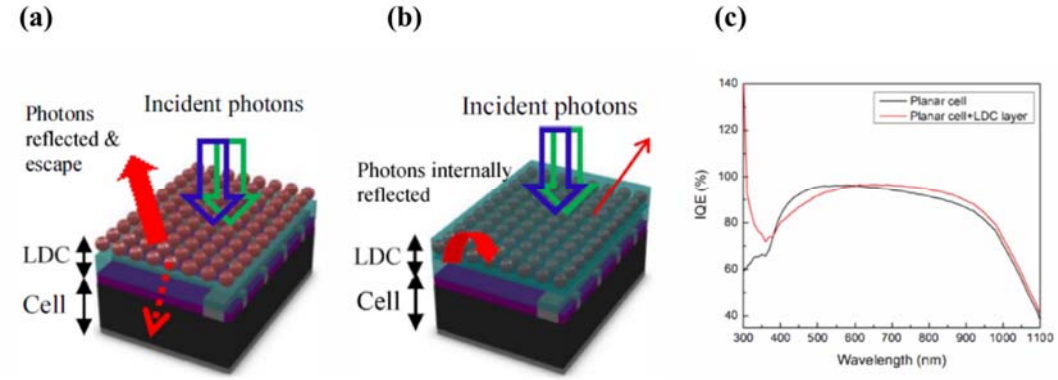

Figure 2.28: Schematic diagrams of cells with (a) a QD layer, (b) QD layer capped with spin on glass (SOG) layer used as luminescence down-conversion (LDC) layers, (c) IQE of a planar cell with an LDC layer [120].

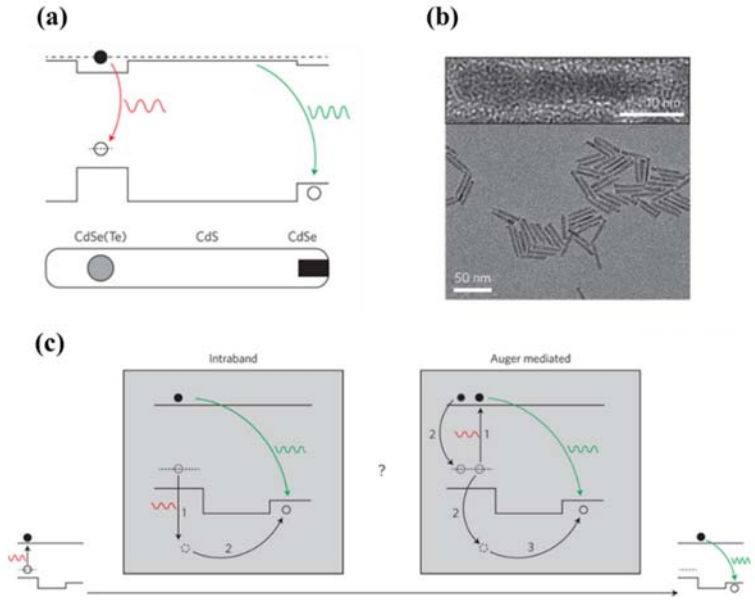

Figure 2.29: (a) Schematic depiction of dual emitting quantum dot, (b) TEM image of the QDs, (c) Proposed mechanism for up-conversion in double dot QDs [122].

2.5 Summary

Colloidal quantum dots can be deployed by solution processed deposition techniques to form a thin nanocrystal layer which in this thesis has been referred as “quantum dot film”. The electrical and optical quality of this “quantum dot film” is determined considerably by the quality of each individual quantum dots. Thus, the properties and structural quality of individual quantum dots drastically affects the performance of final quantum dot solar cell device. The synthesis steps and underlying mechanism in solution processed synthesis of nanocrystals is briefly reviewed to provide an insight on the solution process synthesis of nanoparticles. We highlighted some of the methods used to control the electrical and optical properties of nanocrystals. Common solution processed deposition techniques used for quantum dot film formation is discussed.

A brief overview on transparent conductive oxides (TCOs) and their profound application in optoelectronic devices is provided. Our review has been focused particularly on aluminum doped zinc oxide (AZO) as TCO and zinc oxide (ZnO) as wide band gap semiconductor for their abundance in nature and lower cost. A brief overview on the role of arrays of nanowires/ nanopillars in advanced solar cell devices and their fabrication is presented. Nano sphere masking is introduced as an alternative and simple method to replace electron beam lithography (EBL). Different gas compositions for reactive ion etching of ZnO is reviewed.

Some of the advanced solar cell architectures and electronic devices which employ quantum dots as their active/passive layer is reviewed. Although the concept of quantum dot film and quantum dot heterojunction solar cell is in its early stages but there have been appreciable progresses in understanding the challenges and accordingly, development of new solar cell architectures to address them.

Chapter 3
Development of ZnO-based highly transparent and conductive metal oxide

Based on what we discussed in Chapter 2, there is a high demand for inexpensive TCOs for applications in 3rd generation photovoltaics. For providing higher mobility and lower carrier density in TCOs for applications in advanced optoelectronic devices and in particular in colloidal QD solar cells there is a need to develop appropriate materials at low cost. RF-sputtered AZO and semiconductor ZnO films are considered as good candidates to be replaced with ITO and TiO_2 layers for formation of photo electrode and wide band gap semiconductor in QD solar cell devices. This chapter summarizes efforts to control transparency, carrier concentration, and Hall mobility in sputtered Al:ZnO and ZnO thin films via control of deposition conditions including power, pressure and temperature.

3.1 Experimental details

Zinc oxide and Al doped zinc oxide films were deposited onto corning glass wafers (Eagle XG) and (100) p-type silicon via radio frequency magnetron sputtering using an Intel Vac. sputtering tool, in the process detailed below. Ceramic, 3-inch diameter discs of Al_2O_3: ZnO (2 wt. %) with 99.999% purity, purchased from Angstrom sciences are used as Al:ZnO target. Similar ceramic discs of ZnO with 99.999% purity are installed on another gun inside the chamber, to be used as ZnO target. Target selection is enabled by the sputtering tool's ability to switch between the guns. Standard RCA cleaning procedures were used to clean the samples prior to loading into the chamber. The samples are placed parallel to the targets, in four sample holders at a distance of 50 ± 3 mm. To improve the uniformity (> 94%), a mechanical system was designed to provide both revolution (for 4 sample holders) and rotation (for each individual sample holder) motion to the sample holders' batch [123]. The sample holder batch is capable of 40 revolutions per minute, while each individual sample holder is capable of 14 rotation per minute. Prior to deposition, the chamber is left over night to reach background pressure of 4×10^{-7} Torr before each deposition. The non-reactive deposition is carried out in inert Ar gas. The deposition pressure was varied between 0.5 mTorr and 10 mTorr. During the deposition, the pressure is stabilized by controlling the gas flow rate with mass flow controllers. The deposition power is varied in the range of 80 W to 300 W. The deposition temperature is controlled by a thermocouple placed in the vicinity of the sample holders. The temperature controller is recalibrated to match the temperature readings from a reference temperature logger, which is temporarily placed on the

back of the substrates during the process, for more accurate readings. The temperature is stabilized inside the chamber by preheating the chamber at deposition temperature for 1 hour. Prior to every deposition, in order to clean up the target surfaces, a two minutes of pre deposition (with closed shutter) is performed at 100 W, followed by a 1 minute warm up at deposition power. The deposition is performed with a stabilized plasma for up to 120 minutes.

The sheet resistance of the samples presented in this report were measured with a four point probe system immediately after unloading from the chamber. The samples were patterned by a UV lithography mask aligner system (OAI: optical associates incorporation) and wet etched in a solution of 10% HCl in water. The thickness of the samples were measured using a stylus-type profilometer (Dektak 150). The transmission of light on the corning glass-prepared samples were measured using PerkinElmer UV/VIS/NIR Lamda 1050 spectrometer, with air as the reference. The open source PUMA software was used to verify the thickness of ZnO films coated on glass substrates and attain index of refraction. PUMA software uses the transmission spectra of the samples to calculate refractive indices and thickness of the films [124, 125]. The software used in this work is freely available through the PUMA project web page (http://www.ime.usp.br/_egbirgin/puma/). Finally, the interface of the AZO-Si heterojunction was studied by high resolution transmission electron microscopy (HRTEM, FEI Titan 80-300 HB, FEI Co.).

Photoluminescence (PL) spectra of ZnO samples were acquired using a fluorescence spectrometer (Edinburgh Instruments, FLS980) at room temperature, with excitation at 310 nm from a 900 W Xe lamp. In this measurement, a long pass optical filter with lower cut off wave length at 340 nm is placed before monochromator in emission arm. The filter helps to suppress the measurement artifacts caused by formation of excitation harmonics (artifact forms at λ= 620 nm). The carrier concentration and mobility of the films were characterized by Hall effect experiment in a Van der Pauw configuration with Ecopia HMs-300 setup in a magnetic field of 0.54 T at room temperature. Samples were diced from the center of 4 inch coated glass wafers. Prior to every Hall measurement experiment, the I-V characteristic of the samples prepared in Van der Pauw configuration, was studied to make sure that the contact is ohmic. The Hall measurement current is adjusted accordingly for every sample to have a meaningful Hall measurement experiment.

3.2 Towards highly conductive TCO by RF sputtering of Al:ZnO

Al:ZnO films can be sputtered from Al_2O_3:ZnO targets with various Al_2O_3/ZnO weight ratios, or target doping concentration (TDC). Ceramic Al_2O_3: ZnO targets with TDCs of 0.5%, 1%, 2% and 4% are available. Al_2O_3:ZnO targets with 2% TDC are of particular interest since they result in thin films with the

lowest thickness-dependent resistivity [126]. Moreover, lowest reported resistivities are achieved by targets with 2% TDC [127].

Deposition pressure is the sputtering parameter that strongly effects electrical properties of the AZO thin film. Generally, at higher pressures, deposition rate is lower because of smaller mean free paths in particles. The deposition rate in dynamic sputtering systems (with rotation and/or revolution motions) is several times lower than stationary systems.

Table 3-1 summarizes the electrical properties of AZO samples prepared from Al_2O_3: ZnO targets with 2% TDC at different pressures and powers. It is apparent that at a fixed power, deposition rate decreases with increasing pressure. Sheet resistance of the samples are measured immediately after unloading them from the chamber. After samples are left outside of the chamber at room temperature for some time, films deposited at higher pressures show instability in electrical properties. Degradation in sheet resistances, is particularly apparent for the films deposited at 10 mTorr and 150 W, 200 W at room temperature. This effect is reflected in Hall measurement results, which is performed up to one week after samples are unloaded from the chamber and stored at room temperature. Degradation is more prominent for the samples that are prepared at higher pressures and higher powers. As reported by Minami *et al.* this effect is mainly due to diffusion of atmospheric oxygen in the AZnO/ZnO thin film and is prominent in thinner films and humid ambient [128]. Atmospheric oxygen diffusion causes a decrease in carrier concentration and in mobility, both of which are responsible for electrical degradation of films and increase in resistivity [129]. For AZO films deposited at pressures below 5 mTorr, this effect becomes less significant. As seen in Table 3-1, the films deposited at a low pressure of 0.5 mTorr show very stable electrical properties when left outside of chamber. Their measured sheet resistance (R_{sh}) following deposition, is very close to the value calculated from Hall measurement results ($\rho = R_{sh} \times \text{thickness}$).

To verify the effect of the deposition temperature on the stability of films deposited at high pressure, the deposition process with the least stable conditions (150W and 10 mTorr) was repeated at 250 °C. The sheet resistance of this film ($R_{sh} = 58$ Ω/sq at 180 nm) was more stable over time. The instability of electrical properties for the films deposited at higher pressure, relaxed when films were sputtered at the deposition temperature of 250 °C. In AZO films, carrier concentration stems from impurity dopants (Al) and non-stoichiometry (mainly in the form of oxygen vacancy). As a result, oxygen diffusion decreases the number of free carriers from oxygen vacancies. For the films deposited at high pressure, aluminum dopants are not activated and oxygen vacancy is the main source of free carrier concentration. At high deposition

temperatures (250 °C), aluminum dopants are activated and as a result, oxygen diffusion has less effect on the electrical stability of the film.

At higher pressures, and when the power is increased above 150 W, there is arcing in the plasma, which causes re-deposition of AZO from coated films of the sample holder onto the sample. This re-deposition results in the appearance of black spots on the samples and can be eliminated when the deposition pressure is lowered to 0.5 mTorr. At a low pressure of 0.5 mTorr and proper power of 150 W, resistivity as low as $\rho = 1.5 \times 10^{-3}$ Ω.cm is achieved. In order to further decrease the resistivity, the deposition temperature is increased up to 250 °C.

The effect of deposition temperature on electronic transport parameters of AZO thin films is summarized in Table 3-2. A steady decrease in resistivity can be seen as temperature is increased. This corresponds to an increasing trend in both mobility and carrier concentration with respect to temperature. AZO films with resistivity as low as $\rho = 2.94 \times 10^{-4}$ Ω.cm was achieved. The optical transmissions of the films are represented in Figure 3.5. Transmission of light in the visible range is above 85% for all of the films. As seen from the Figure 3.5, increasing the deposition temperature produces a continuous decrease in light transmission in the infrared region. This decrease in light transmission in infrared region is mainly attributed to an increase in carrier concentration. High number of free carriers increases light reflection (due to free electrons oscillation above plasma frequency) and decreases light transmission.

To calculate the mean crystallite size (d), the Scherrer formula [130] is used as follow:

$$d = \frac{K\lambda}{\beta cos\theta} \qquad (3\text{–}1)$$

where K represents shape factor, (normally 0.9) , λ is the X-ray wavelength (Cu Kα, 0.15406 nm), β is the value of the full width at half maximum (FWHM) of diffraction peak, and θ corresponds to the Bragg diffraction angle. Table 3-3 summarizes the crystallite size calculated for two main peaks (002) and (103).

Both samples have a similar peak intensity for their main crystal peak (103), which indicates that the crystal structure is not degraded. However, grain size increases when deposition temperature increased. Comparing the FWHM for the two films, shows that the thin film formed at high temperature has slightly better quality, indicated by the decrease in FWHM.

To further elaborate on the effects of Al addition on ZnO structure, a thin film of ZnO was prepared with the same deposition parameters as AZO, at 250 °C. Figure 3.2 shows the diffraction pattern of AZO and

ZnO prepared at high temperature. It can be seen that the doping of Al in ZnO changes the dominant crystal orientation from (002) in ZnO to (103) in AZO. Additionally, when considering the FWHM (0.3936° for

Table 3-1: Variation of electronic transport parameters: sheet resistance (R_{sh}), resistivity (ρ), carrier concentration (Ne) and Hall mobility (μ) of the AZO films sputtered on glass substrate at room temperature with different deposition power and pressure.

	RF power (W)	Rate of deposition (A°/min)	R_{Sh}* (Ω/sq)	Film resistivity ρ (Ω.cm)	Carrier concentration N_e (cm^{-3})	Hall mobility μ ($cm^2V^{-1}s^{-1}$)	Time (min.)	Thickness (nm)
Pressure: 10 mTorr† Ar flow=165 sccm	200	36.67	504	6.18×10^{-03}	$1.34\times10^{+20}$	7.563	60	220
	150	21.7	79	2.24×10^{-01}	$1.79\times10^{+20}$	1.55×10^{-01}	60	130
	120	6.61	1505	2.95×10^{-01}	$4.829\times10^{+20}$	4.38×10^{-02}	120	80
Pressure: 5 mTorr Ar flow=120 sccm	240	70	130	2.24×10^{-02}	$6.19\times10^{+19}$	4.496	60	420
	150	41.7	249	4.70×10^{-02}	$6.60\times10^{+19}$	2.018	60	250
	80	18.3	287	3.09×10^{-03}	$9.30\times10^{+19}$	2.17×10^{-01}	60	110
Pressure: 2 mTorr Ar flow=80 sccm	300	125	51.6	3.33×10^{-02}	$1.817\times10^{+20}$	1.032	60	750
	200	49.3	18.8	1.33×10^{-01}	$1.19\times10^{+19}$	3.956	150	740
	100	36.7	263	3.62×10^{-03}	$1.75\times10^{+20}$	9.834	60	220
Pressure: 0.5 mTorr Ar flow=50 sccm	200	79.2	25.2	2.017×10^{-03}	$3.75\times10^{+20}$	8.182	120	950
	150	56.7	27.2	1.52×10^{-03}	$5.51\times10^{+20}$	7.57	120	680
	100	36.25	43.4	1.9×10^{-03}	$2.67\times10^{+20}$	8.805	120	435

*, Sheet resistance of all of the samples are measured right after deposition whereas Hall experiment is performed after a week.
†, AZO thin films prepared at 10 mtorr were un-stable in air.

Table 3-2: Variation of electronic transport parameters: sheet resistance (R_{sh}), resistivity (ρ), carrier concentration (Ne) and Hall mobility (μ) and etching rate (10% HCl in water) of AZO films sputtered at 0.5 mTorr and 150 W with different deposition temperature.

Temperature (C°)	R_{Sh} (Ω/sq)	Film resistivity ρ (Ω.cm)	Carrier concentration N_e (cm^{-3})	Hall mobility μ ($cm^2V^{-1}s^{-1}$)	Thickness (nm)	Index of refraction (n) at 550nm	Etching rate in 10%HCl (A^0/S)
250	3.7	2.94×10^{-04}	$1.07\times10^{+21}$	19.9	780	1.86	11.1
200	8.3	6.13×10^{-04}	$8.1\times10^{+20}$	12.7	775	1.85	11.4
180	8.6	6.67×10^{-04}	$5.57\times10^{+20}$	16.4	775	1.85	12.9
160	11.8	7.21×10^{-04}	$8.17\times10^{+20}$	11	770	1.85	14.0
140	12.5	9.23×10^{-04}	$5.42\times10^{+20}$	12.5	765	1.84	15.3
120	16.6	1.14×10^{-03}	$5.91\times10^{+20}$	9.46	760	1.89	16.9
90	23	1.51×10^{-03}	$6.68\times10^{+20}$	6.35	725	1.86	20.7
60	25.8	1.71×10^{-03}	$6.71\times10^{+20}$	5.43	710	1.86	23.7
RT	27.2	1.52×10^{-03}	$5.51\times10^{+20}$	7.57	680	1.85	29.0

ZnO at (002) and 0.72° for AZO at (103)), it can be seen that the quality of the film decreases when Al is slightly incorporated in the developed thin film.

Table 3-3: Calculated lattice parameters, (002)/(103) peak ratio and crystallite size for AZO deposited at room temperature and 250 °C.

Peaks	Sample	2θ (degree)	Crystallite size (nm)	d-spacing (nm)
(002)	AZO-RT	34.2067	15.36	0.262138
	AZO-250°C	34.4880	56.36	0.2600064
(103)	AZO-RT	62.669	11.92	0.148125
	AZO-250°C	63.0093	12.94	0.147407

Scherrer equation shows that ZnO has also higher crystallite size of 21.13 nm compared to AZO, with a size of 11.08 nm. Therefore, it can be concluded that, incorporation of Al in ZnO degrades the structural quality of the film by introducing defects. Al influences the dynamics of ZnO grain growth by enhancing the formation of nano-crystallites in grain boundaries [131]. Increasing deposition temperature eliminates these negative effects and improve the crystal quality of the film.

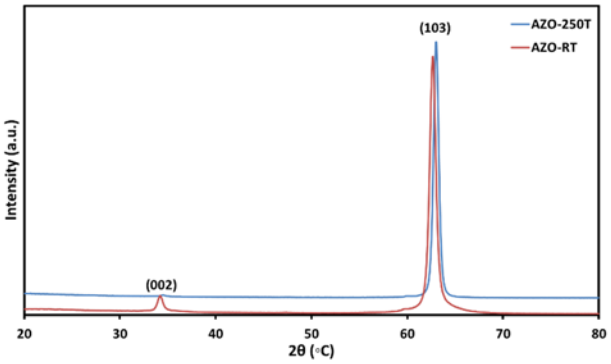

Figure 3.1: XRD analysis of AZO film deposited at pressure 0.5 mTorr, power 150 W and different temperature (room temperature and 250 °C).

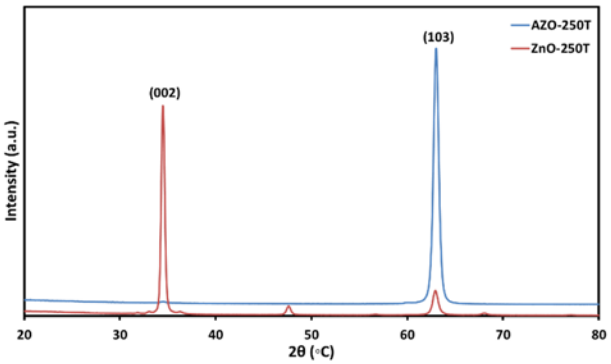

Figure 3.2: Comparison of X-ray diffraction pattern AZO with ZnO at the same deposition condition (pressure 0.5 mT, power 150 W, temperature 250 °C).

The cross section TEM micrograph of AZO thin films deposited on Si substrate is presented in Figure 3.3. The TEM micrograph clearly shows the columnar structure of the sputtered AZO thin film. These columnar grains consist of several tilted crystallites. The size of these crystallites is shown in Table 3-3.

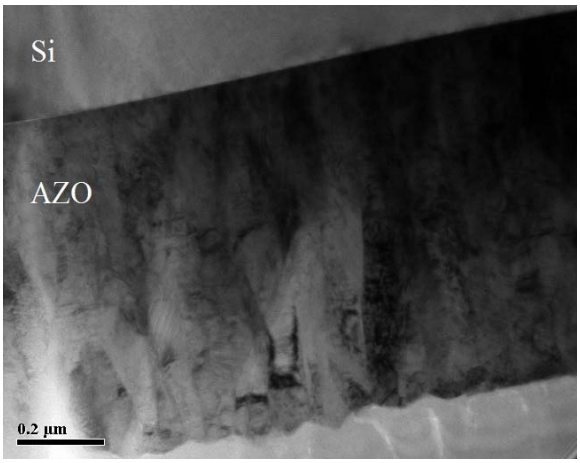

Figure 3.3: Cross section TEM micrograph of AZO film sputtered on silicon substrate.

An HRTEM micrograph of the AZO-Si interface is depicted in Figure 3.4. The bright region corresponds to a thin SiO_x layer (1-2.5 nm), formed between AZO and Si substrate probably due to the existence of oxygen during deposition [131, 132] .

Near band edge photoluminescence (NBE) is an important signature of every material. NBE photoluminescence originates from radiative recombination of excitons with binding energy close or equal to band gap energy of material. We have used PL to look at the stability of the developed layers at different deposition temperatures. PL spectra of ZnO and AZO films deposited on both glass and silicon substrate has been studied. There are several mechanisms responsible for the occurrence of near band edge peaks, such as free exciton emission (FX), bound exciton (BX), donor-acceptor pair (DAP) and others. All of these mechanisms have excitonic behavior and are temperature dependent. Zinc oxide has a large exciton binding energy (~ 60 meV), making it possible to have free exciton emission up to room temperature [133]. To enable NBE emission at room temperature it is important to suppress non-radiative processes, which corresponds with better crystalline quality. As a result, the presence of NBE emission is an indication of better crystalline quality. In addition to NBE emission, zinc oxide also has deep level emissions (DLE) in the range of 405 nm to 750 nm. The origin of broad band DLEs is unconfirmed, but it is believed that defects in the form of zinc vacancy/interstitial and oxygen vacancy/interstitial are the main cause for these so called defect related emissions.

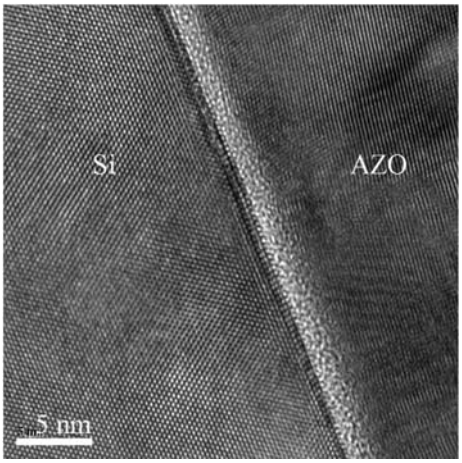

Figure 3.4: HRTEM image of AZO-Si interface. The bright region corresponds to a thin SiO_x layer (1-2.5 nm) formed due to existence of oxygen during deposition.

Figure 3.6 and Figure 3.7 shows room temperature photo-luminescence spectra of AZO films on silicon and glass substrates, deposited at 150 W and 0.5 mTorr, respectively, at different deposition temperatures. Sputtered AZO on Si substrate deposited at room temperature (pale blue line in Figure 3.6) exhibits NBE peaks at 367 nm and 396 nm with DLE peaks at 426 nm, 468 nm (blue), 653 nm and 740 nm (red). The peak at 620 nm is the artifact of the measurement system, caused by the second harmonic of the excitation source (at 310 nm) and does not indicate photoluminescence emission of the samples. As seen from Figure 3.6, increasing the deposition temperature, causes the position of NBE and DLE peaks to gradually change. At a deposition temperature of 250 °C, NBE emission peaks are located at 363 nm and 390 nm whereas DLE peaks are located at 426 nm, 485 nm (blue spectrum range), 595 nm (orange spectrum rage), 678 nm and 731 nm (red spectrum range).

Ahn *et al.* calculated the defects' energy levels responsible for DLEs in zinc oxide materials [134]. It was found that DLE peak at 426 nm can be attributed to zinc vacancies and peak at 595 nm and 615 nm can be attributed to oxygen interstitials. Interestingly, this is produced by the joint behavior of DLE pairs at 653 nm and 740 nm for the sample prepared at room temperature, and 678 nm and 731 nm in the sample prepared at 250 °C. As shown by Alvi *et al.* these peaks can be attributed to oxygen vacancies situated ~ 1.65 eV below the conduction band [135]. DLE peaks at 468 nm and 485 nm can be attributed to negatively charged zinc interstitials situated ~ 2.5-2.6 eV below the conduction band [136]. These changes in defect types, which are induced by increasing the deposition temperature, indicate tremendous structural changes in the thin film of AZO. Increasing deposition temperature results in a steady increase in photoluminescence emission, as seen in Figure 3.6. The ratio of highest NBE emission to highest DLE (I_{NBE}/I_{DLE}) is of particular

interest. This ratio steadily increases from ~1.7 for room temperature deposition to ~3 for deposition at 250 °C ($Max\ I_{DLE}\ at\ 485\ nm$).This shows that the crystalline quality of the sample improves when increasing deposition temperature.

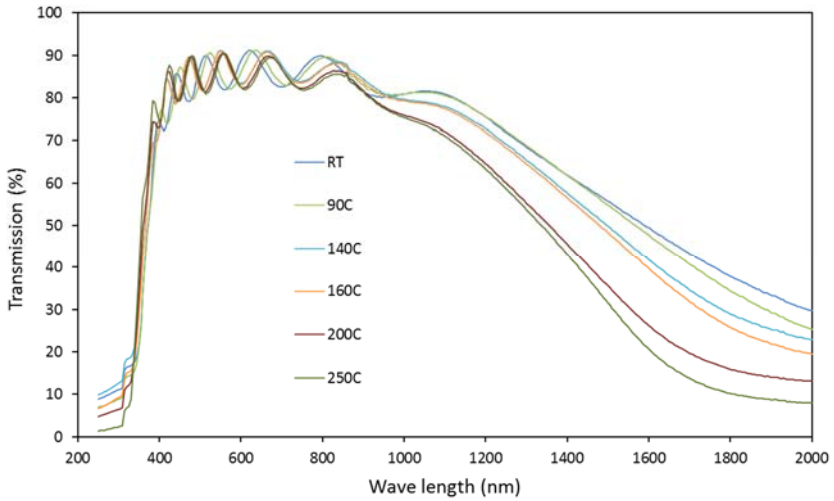

Figure 3.5: Change in light transmission of AZO film deposited at pressure=0.5 mTorr, power=150 W with respect to deposition temperature.

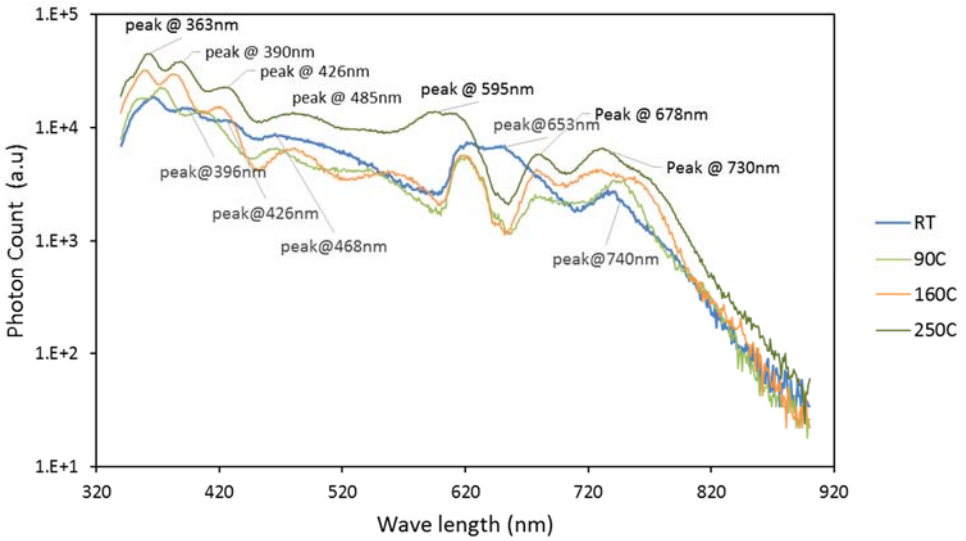

Figure 3.6: Room temperature photo-luminescence spectra of AZO films deposited at 150 W and 0.5 mTorr on Si at different deposition temperatures (logarithmic scale). Excitation wave length is 310 nm. The emission peaks for sample prepared at substrate temperatures of RT and 250° C are presented.

The effect of deposition temperature on the photoluminescence of AZO samples prepared on glass is more drastic. As depicted in Figure 3.7, the photoluminescence intensity increases by two orders of magnitude for samples prepared at a substrate temperature of 160 °C. A congruous behavior is observed in electronic transport parameters (Table 3-2), where, at a substrate temperature of 160 °C, there is an apex in carrier concentration accompanied by a decrease in Hall mobility.

The changes in the position of emission peaks and in photoluminescence intensity indicate that the samples experience a tremendous structural change at deposition temperatures between 140 °C-160 °C [137]. The I_{NBE}/I_{DLE} ratio for samples prepared on glass substrate at RT, 160 °C and 250 °C is 0.58, 2.04 and 2.93 respectively, indicating an improvement in crystalline quality. All of the samples, regardless of the substrate, show a strong near band edge photoluminescence emission (NBE) at deposition temperatures above 160 °C.

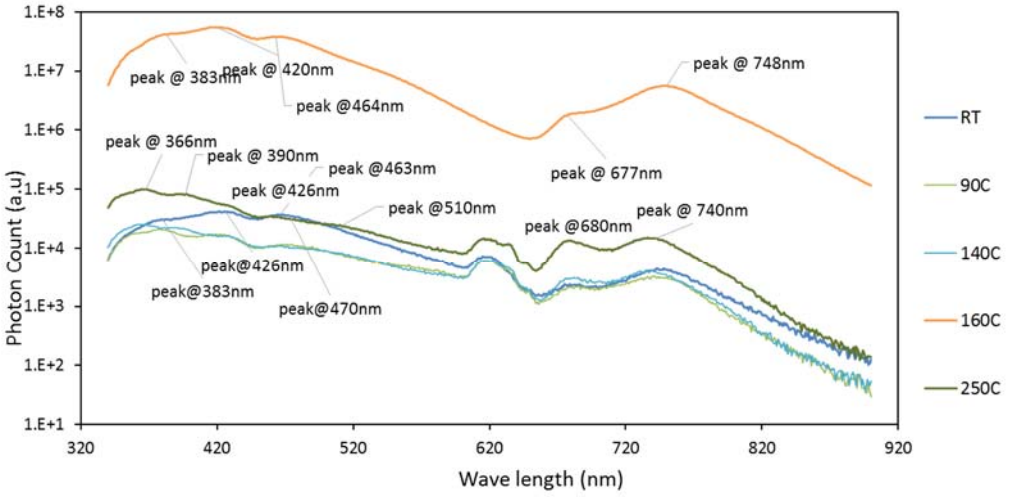

Figure 3.7: Room temperature photo-luminescence spectra evolution of AZO films deposited at 150 W and 0.5 mTorr on glass, different deposition temperatures are depicted on a logarithmic scale. Excitation wave length is 310 nm. The emission peaks for samples prepared at substrate temperatures of RT, 160 °C and 250 °C are presented.

3.3 Towards ZnO thin film for 3rd generation photovoltaic devices

Table 3-4 summarizes the electrical properties of zinc oxide samples prepared from ZnO target using different chamber pressures and deposition powers. Like sputtered aluminum doped zinc oxide, sputtered ZnO films show sensitivity to atmospheric oxygen when exposed to air. The degradation in electrical properties due to atmospheric oxygen diffusion is more significant in ZnO samples than AZO. Even ZnO films deposited at low pressures show electrical degradation immediately upon exposure to air.

Table 3-4: Variation of electronic transport parameters: sheet resistance (R_{sh}), resistivity (ρ), carrier concentration (Ne) and Hall mobility (μ) of the ZnO films sputtered on glass substrate at room temperature with different deposition power and pressure.

	RF power (W)	Rate of deposition (A°/min)	R_{Sh}^{*}(Ω/sq)	Film resistivity ρ (Ω.cm)	Carrier concentration N_e (cm^{-3})	Hall mobility μ ($cm^2V^{-1}s^{-1}$)	Time (min.)	Thickness (nm)
Pressure: 10 mTorr Ar flow=165 sccm	200	35.8	510	$2.6\times10^{+02}$	$1.11\times10^{+16}$	2.31	120	430
	150	17.9	412.6	4.51	$3.16\times10^{+16}$	41	120	215
	120	6.25	4310	5.1	$1.45\times10^{+18}$	8.4×10^{-01}	120	75
Pressure: 5 mTorr Ar flow=120 sccm	200	57	9850	27	$2.28\times10^{+17}$	1.1	60	340
	150	43	284	$1.6\times10^{+02}$	$6.70\times10^{+16}$	5.52×10^{-01}	75	325
	100	21	12800	$4.3\times10^{+03}$	$1.30\times10^{+16}$	1.12×10^{-01}	60	126
Pressure: 2 mTorr Ar flow=80 sccm	200	125	61300	$1.58\times10^{+03}$	$3.55\times10^{+16}$	1.1×10^{-01}	120	620
	150	39.5	2900	2.10×10^{-01}	$1.70\times10^{+17}$	16.71	120	475
	100	36.1	$1.3\times10^{+05}$	74	$5.9\times10^{+17}$	14.30	65	235
Pressure: 0.5 mTorr Ar flow=50 sccm	200	75	180.3	1.5	$2.3\times10^{+18}$	1.41	90	680
	150	60	90000	11.8	$2.1\times10^{+17}$	2.2	120	720
	100	35	144	$7.00\times10^{-01**}$	$9.5\times10^{+17**}$	9.4^{**}	100	360

*, Sheet resistance of all of the samples are measured right after deposition whereas Hall experiment is performed after a week.
**, Hall measurement for this sample is done a few hours after unloading it from chamber.

Table 3-5 summarizes the effect of deposition temperature on the electronic transport parameters of ZnO films sputtered at 150 W and 0.5 mTorr. Deposition temperature has a drastic effect on ZnO film's electrical properties, which is reflected in the decrease of film sheet resistance when substrate temperature is increased (measured immediately after unloading the samples from the chamber). Apart from the films deposited at substrate temperatures of 250 °C and 200 °C, all of the ZnO film samples degraded gradually in the course of a few weeks when exposed to air. Increasing the substrate temperature up to 250 °C allows the realization of ZnO films with resistivity as low as $\rho=3.7\times10^{-2}$ Ω.cm and acceptable stability in ambient air and at room temperature. As depicted in Figure 3.8 (next page), lower carrier concentration and high electron mobility of these films allows to have high conductivity while the light transmission in infrared region is increased. High light reflection in infrared region prevails due to high number of free carriers and reduces the light transmission for highly doped wideband gap materials. All of the ZnO samples show light transmission higher that 85% in the visible range. The changes in the carrier concentration is consistent with changes in transmission spectra in the infrared range. The changes seen in ZnO mobility are more significant in comparison to the changes seen in AZO.

Table 3-5: Variation of electronic transport parameters: sheet resistance (R_{sh}), resistivity (ρ), carrier concentration (Ne) and Hall mobility (μ) and etching rate (10% HCl in water) of ZnO films sputtered at 0.5 mTorr and 150 W with different deposition temperature.

Temperature (C°)	R_{Sh}*(Ω/sq)	Film resistivity ρ (Ω.cm)	Carrier concentration N_e (cm^{-3})	Hall mobility μ ($cm^2V^{-1}s^{-1}$)	Thickness (nm)	Index of refraction (n) at 550nm	Etching rate in 10%HCl (A°/S)
250**	448	3.7×10^{-02}	$5.62\times10^{+18}$	30	740	1.86	528.57
200	1880	1.90×10^{-01}	$4.40\times10^{+18}$	13.1	500	1.85	552.22
180	2450	8.70×10^{-01}	$1.01\times10^{+18}$	7.1	480	1.85	533.3
160	3100	4.23	$2.41\times10^{+18}$	11	470	1.85	587.5
140	3636	1.56	$1.78\times10^{+18}$	6.8	460	1.84	657.14
120	5220	1.39	$8.31\times10^{+17}$	5.4	440	1.89	733.3
90	6520	6.2	$1.86\times10^{+17}$	5.1	435	1.86	876
60	7610	6.5	$2.00\times10^{+17}$	4.5	430	1.86	860
RT**	90000	11.8	$2.1\times10^{+17}$	2.2	720	1.85	1440

*, Sheet resistance of all of the samples are measured right after deposition whereas Hall experiment is performed after a week.
**, Deposition time for these film is 120 minute and for the rest of the films is 75 minute.

Figure 3.9 shows the diffraction pattern of developed ZnO sputtered at 0.5 mTorr, 150 W, room temperature and 250 °C. It shows that (002) is the main crystal orientation for both thin films. Crystallite sizes calculated from Scherrer's equation, and measured d-spacings are summarized in Table 3-6.

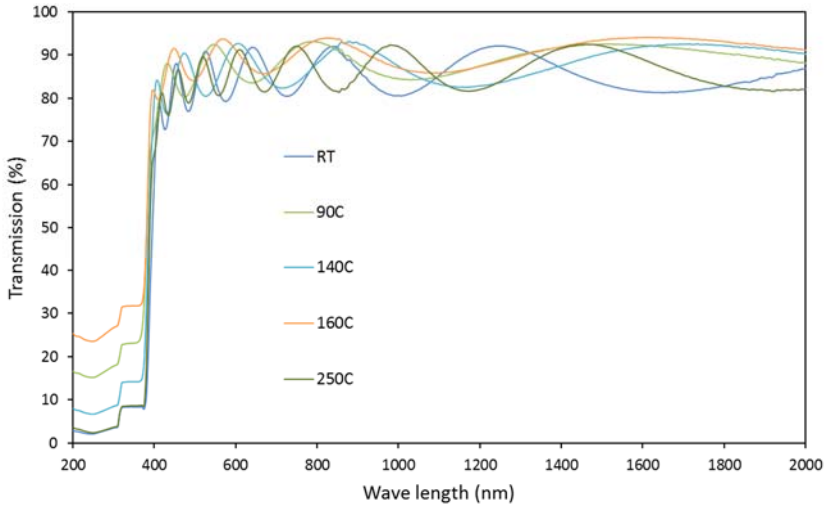

Figure 3.8: Change in light transmission of ZnO film deposited at a pressure of 0.5 mTorr and power of 150 W with respect to deposition temperature. Deposition time for samples sputtered at 250 °C and RT is 120 minutes; the other films are deposited over 75 minutes.

Table 3-6: Calculated lattice parameters, (002)/(103) peak ratio and crystallite size for ZnO deposited at RT and 250 °C.

Peaks	Sample	2θ (degree)	Crystallite size (nm)	d-spacing (nm)
(002)	ZnO-RT	34.2888	14.08	0.261529
	ZnO-250 °C	34.4861	21.13	0.260077
(103)	ZnO-RT	62.6685	37.8	0.148249
	ZnO-250 °C	62.9327	17.2	0.147690

The XRD patterns show that increasing deposition temperature improves the quality of crystals. This is made evident by the sharp increase in the intensity of (002). Additionally, there is a small decrease in the d-spacing, indicating a more compact structure. It is also revealed that, when the deposition temperature is increased, the FWHM for (002) decreases from 0.59° to 0.39°. This indicates an improvement in the structure's crystal quality with regards to decreased crystal imperfections, stress, and grain boundaries [138]. Furthermore, the increase in crystallite size confirms the enhancement of crystal quality. Larger crystalline size means less grain boundaries, which act as a barrier for the electrical performance of ZnO film [60, 139].

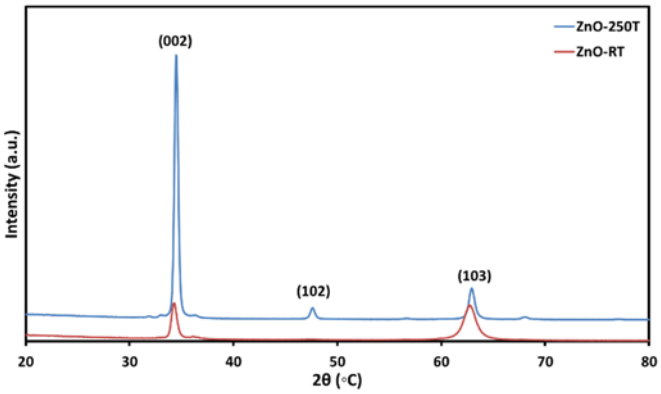

Figure 3.9: XRD analysis of ZnO film deposited at pressure 0.5 mTorr, power 150 W and different temperature (room temperature and 250 °C).

Figure 3.10 and Figure 3.11 represent room temperature photoluminescence spectra of ZnO samples deposited on silicon and glass substrate, respectively. The samples were deposited at different temperatures. The overall PL intensity of ZnO thin films are higher than that of AZO films, for both silicon and glass substrates. This was expected, since ZnO thin films generally show better crystalline quality than aluminum-doped zinc oxide thin films. The defect states caused by aluminum dopants can provide a non-radiative recombination path to suppress the overall PL intensity [140]. The PL spectra in Figure 3.10 and Figure 3.11 indicate that for ZnO samples prepared on either silicon or glass, a drastic structural change of material

starts upon increasing the deposition temperature. At temperatures of approximately around 140 °C-160 °C, the overall PL intensity increases one order of magnitude. Similar to the AZO deposited on silicon at room temperature, ZnO thin film prepared on silicon substrate at room temperature have a considerable NBE intensity. The $^{I_{NBE}}/_{I_{DLE}}$ ratio steadily increases for ZnO samples deposited on silicon substrates; room temperature sample show a ratio of 2.71, which increases to 3.43 for the sample deposited at 250 °C.

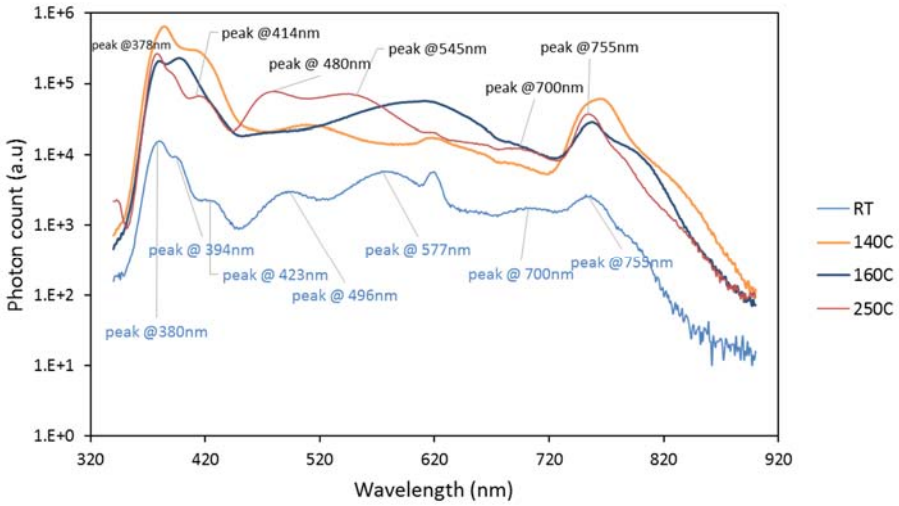

Figure 3.10: Room temperature photo luminescence spectra evolution of ZnO films deposited at 150 W and 0.5 mTorr on a Si substrate; different deposition temperatures are shown on a logarithmic scale. Excitation wave length is 310 nm. The image depicts emission peaks for samples prepared at 250 °C and room temperature.

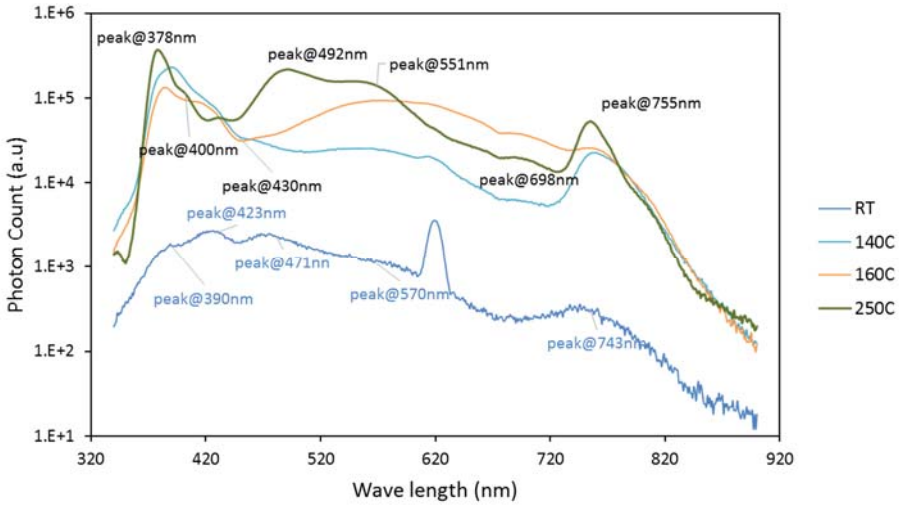

Figure 3.11: Room temperature photo luminescence spectra evolution of ZnO films deposited at 150 W and 0.5 mTorr on glass substrate; different deposition temperatures are displayed on a logarithmic scale. Excitation wave length is 310 nm. The emission peaks for samples prepared at 250 °C and room temperature are shown.

In contrast to samples prepared on silicon substrate, which had noticeable NBE peaks, both ZnO and AZO samples prepared on glass show suppressed PL intensity for near band edge emissions (NBE). The I_{NBE}/I_{DLE} ratio for ZnO sputtered on glass substrate increases from 0.68 for room temperature deposition, to 1.7 for deposition at 250 °C. Like aluminum doped ZnO thin films, all of the zinc oxide samples, prepared at deposition temperatures above 140 °C show noticeable NBEs, regardless of type of substrate.

3.4 Summary

In this section, the electrical and optical properties of RF sputtered ZnO and AZO films prepared at different deposition conditions were studied. AZO with resistivity as low as $\rho=1.52\times10^{-3}$ Ω.cm and stable electrical properties was obtained using room temperature deposition. By increasing the deposition temperature to 250 °C, the resistivity of AZO films was lowered to $\rho=2.94\times10^{-4}$ Ω.cm. This is one of the lowest reported resistivity for AZO films using this technique at relatively low temperature of 250 °C. The films showed acceptably high light transmission both in visible and near infrared ranges. The photoluminescence of AZO on silicon and glass substrate at different deposition temperatures was studied. It was found that AZO undergoes a tremendous structural change that affects the NBE emission intensity and location of DLE peaks. According to the photoluminescence signature of AZO, samples prepared with substrate temperatures above 140 °C show distinct NBE emission peaks.

The effect of deposition condition including power and pressure on the electrical/optical properties of ZnO film was also studied. Sputtered ZnO thin film with sheet resistance of 144 ohm/square was achieved. The film shows high sensitivity to diffused atmospheric oxygen. ZnO thin films with stable electronic transport parameters were only achieved at relatively high deposition temperatures of 200 °C- 250 °C. The effect of substrate temperature on the photoluminescence spectra of sputtered ZnO samples was studied. Regardless of substrate type, all deposited ZnO and AZO samples, sputtered at a power of 150 W and a pressure of 0.5 mTorr, show noticeable NBE emission peaks when the substrate temperatures were above 140 °C.

Chapter 4
Technology development for top-down formation of ZnO nanowires

Wide-band gap metal oxide nanowires (NWs) is a promising structure providing a transparent medium with high surface area for the QD absorbers. It also provides a directional path for the carriers to use in nanowire heterojunction devices [96]. Wide bandgap materials in the form of nanoparticles, nanotubes [141, 142], and NW structures [143, 144] has been used as photo-electrode.

One of the common methods to form ZnO NWs is hydrothermal growth method. Upright ZnO NWs with a relatively high aspect ratio and perfect crystalline structure has been synthesized using this method. However, as we discussed in chapter 2, it is hard to control the size and ordering of the hydrothermally grown NWs. Moreover, this method provides NWs with good optical, but poor electrical properties.

Simple and scalable process technologies that can better control the geometrical structure (mainly the size and spacing between the individual wires) and electrical properties of the NW arrays, is required to be used in NW heterojunction device targeted in this PhD work. To further control the structural and electrical properties of the wires, a novel, low cost, and scalable approach was used for ZnO NW formation by combining nanosphere lithography and etching in fluorine-based plasma.

CH_4 and CF_4 based gases are common etchants for dry etching of ZnO (see Table 2-1). Etching in fluorine-based plasma is a promising technique for pattern transfer to ZnO film. Fluorine is relatively easier to handle than the toxic and corrosive chloride and bromide gases that have mostly been used for ZnO etching [145]. The wires were formed on a pre-sputtered ZnO layer with sheet resistance of ~ 450Ω/□, carrier concentration of 5.6×10^{18} cm^{-3} and average transparency of 85% in visible range (discussed in chapter 3, see Table 3-5).

In this chapter we report on the fabrication of upright and ordered arrays of ZnO NWs with controlled doping levels and long range ordering (>10 μm) combining silica nanosphere lithography and RIE top-down etching in a Trion Reactive Ion Etching (RIE) system. For plasma generation, the cathode was driven with the radio-frequency power at 13.56 MHz (see Figure 2.13). The schematic of etching sequences is shown in Figure 4.1.

The structural properties of the nanowires were studied using scanning electron microscopy (SEM) (Philips XL30) and extreme high-resolution SEM (XHRSEM) (FEI Magellan 400). The optical properties

of the NWs were studied using photoluminescence (PL). Defect study on the nanowires was also performed using photoluminescence.

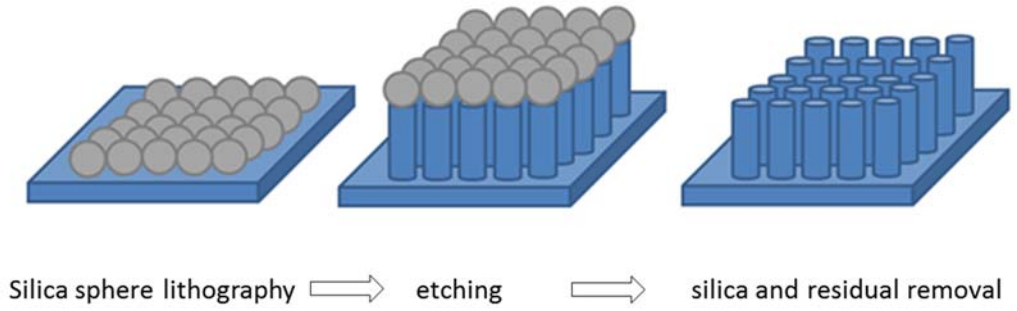

Figure 4.1: Schematic of etching sequences in nanosphere masking.

4.1 Preparation of nanomask with amino functionalized silica spheres

Different type of materials have been used as nanospheres mask. Metallic nanoparticles can readily solve the selectivity problem in RIE process. However, their application as nanospheres mask is avoided for solar cell applications. This is due to the fact that metals (like gold and silver) are often considered to form deep trap levels/ carrier recombination center in silicon and other solar cell semiconductors, deteriorating the performance of the final device [146]. To avoid cross contamination, generally such metals are not allowed into RIE systems and clean rooms. Silica and polymeric nanospheres have been successfully synthesized with different diameters and used as nanosphere masks. Silica nanospheres are more favored, since, unlike the polymeric nanospheres, they don't produce polymeric residuals on the substrate and relieve the burden of cleaning sensitive surfaces of ZnO.

Different methods have been practiced to form monolayers of nano spheres on the surface of substrate to be etched (which often traditionally has been silicon): spin-coating, dip-coating, roll to roll coating and Langmuir-Blodgett (LB) method, are a few to name. Spin-coating is a simple and affordable method which can be used for formation of the monolayer nanosphere mask. In this study, we have used spin-coating technique to form monolayers of amino functionalized silica spheres on the surface of RF sputtered zinc oxide thin film.

Amino (NH_2) functionalized silica (SiO_2) spheres were purchased from Bangs laboratories, Inco. The diameters of silica spheres were ranging from 320 nm to ~1µm with a standard deviation 10%-15%.

We have focused our experiments, mainly on silica spheres of 500 nm in diameter. Table 4-1 summarizes the properties of the silica spheres purchased from Bangs laboratories [147].

Table 4-1: Properties of the silica spheres purchased from Bangs laboratories [147].

Composition	SiO_2, nonporous
Surface groups	NH_2
Refractive index	~ 1.43-1.46 (at 589 nm)
Density	2.0 g/cm^3
Glass Transition Temperature	>>1000 °C*

*Reported value for bulk Silica

4.1.1 Experimental details for silica nanosphere mask formation on ZnO

Amino functionalized silica nanospheres purchased from Bangs laboratories came in a dry powder form. The hydrophilic particles (Si-NH_2) require polar solvents like water, ethanol, methanol and isopropanol alcohol (IPA) for uniform mono-dispersion. In this study, we have used methanol as the solvent for silica nanospheres. The hydrophilicity of the amino functionalized nanoparticles assists their adsorption on a hydrophilic surface of ZnO.

Zinc oxide thin films (~800 nm thick) were prepared on glass substrates in the same way as described in chapter 3 of this report. ZnO coated wafers were diced to 22 mm by 22 mm squares. Prior to spin-coating, samples were further rinsed with acetone and IPA. To promote wettability of ZnO surface and for further cleaning, samples are immersed in methanol and sonicated for 10 minutes in bath sonicator. Colloidal solutions were prepared by dispersing amino functionalized silica sphere powder in 20 ml methanol. The solution is then vigorously vortexed for 2 minutes, followed by 20 minutes sonication in a sonic bath to get a monodispersed colloidal solution. Solutions with different concentration have been prepared to study the effect of colloid concentration on the formation of monolayer mask. The colloidal solution was kept in the refrigerator to avoid agglomeration of the nano particles. Colloidal solution was spin-cast onto ZnO coated substrates. Spinning parameters (time, speed and concentration of colloidal solution) have been tuned for monolayer ordered (crystalline) nanospheres. The acceleration of the spinner was set to 500 rpm/minute.

4.1.2 Formation of uniform silica nanosphere mask on ZnO

The first set of samples was prepared by drop-casting of 100 gr/cm^3 silica nano-spheres in methanol on ZnO coated substrate. The area of the samples was fully covered with the solution and then spun at 2000 rpm/min and 4000 rpm/min for 30 seconds. Studying SEM micrograph (Figure 4.2) of these samples revealed the

following facts: (a) for both samples prepared at 2000 rpm/min and 4000 rpm/min we have a double layer of silica nanospheres formed on the ZnO surface (Figure 4.2 (a), (b)). Increasing the spinning speed from 2000 rpm/min to 4000 rpm/min does not have an enormous effect on reducing the double layer of silica nanospheres to monolayer one.

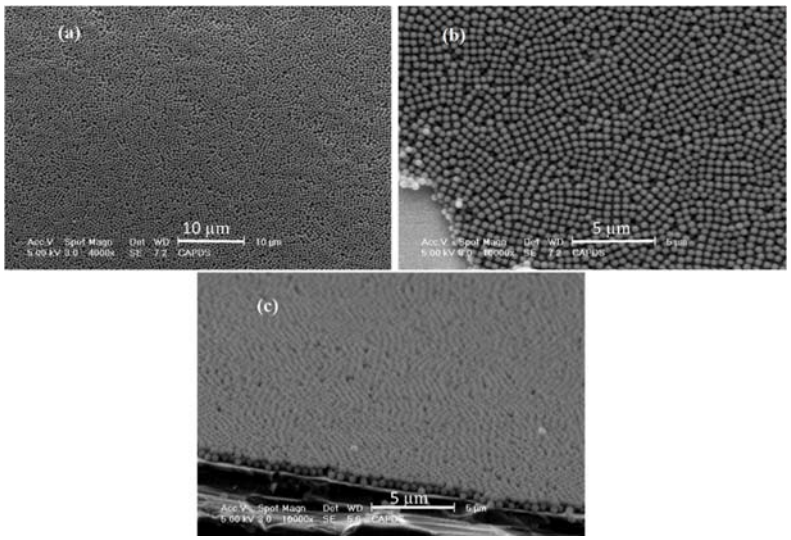

Figure 4.2: Top view SEM micrograph of samples prepared at 2000 rpm/min (a) and 4000 rpm/min from 100 mg/cm3 silica nanospheres in methanol (b). Cross sectional SEM image of sample prepared at 4000 rpm/min is depicted in (c).

A nearly periodic pattern of monolayer silica nanospheres were formed on a ZnO film using 50 mg/mL of 500 nm amino-functionalized silica nanospheres in methanol, after spin coating at 4000 rpm for 30 s. The SEM micrograph in Figure 4.3 (a) demonstrates a long range (>10µm) arrangement of silica polycrystal. Figure 4.3 (b), (c) show the closer view of the silica self-assembled layer.

In a process variation, we added few drops of Triton X-100 containing organic linkers to the silica solution to improve the assembly of silica nanospheres over a large area. Due to the presence of organic linker, oxygen plasma was used to remove the organic components. Silica spheres were separated from each other after a moderate etching at 50 mTorr, using 50 W ICP power, CF_4:O_2 flow rate of 10/5 for 200s. Figure 4.4 (a) and (b) show the silica ordering before and after the plasma treatment respectively. Clean, defect-free silica templates with long-range arrangement (>50 µm) was obtained using this method.

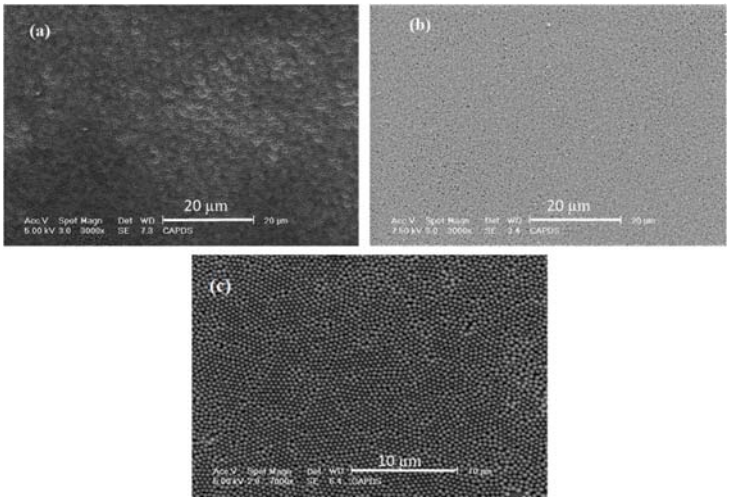

Figure 4.3: Top view SEM photograph of (a) long range (>10µm) monolayer arrangement of silica nanospheres (b), (c) higher magnification of Top view SEM of monolayer silica nanosphere polycrystal.

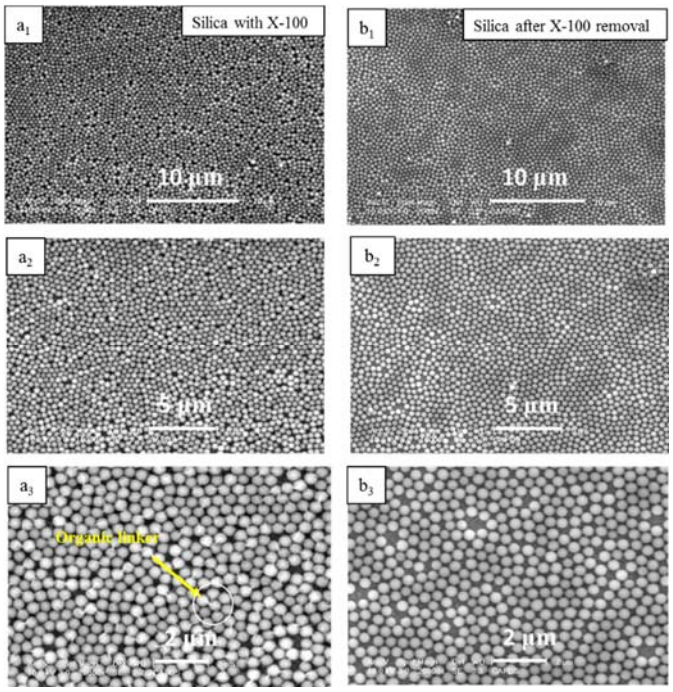

Figure 4.4: Top view SEM images representing long range ordering of the silica template (a) with X-100, and (b) after plasma dry etching of organic linkers.

4.2 Preparation of zinc oxide nanowires/nanopillars with RIE

After the silica mask formation, etching was performed in an RIE reactor at 1 mTorr, inductively coupled plasma (ICP) power of 200 W, self-bias voltage of 600 V with RIE vertical field (VF) power of 245 W and

CF_4/H_2 gas ratio of 1/12. The SEM micrographs in Figure 4.5 (a), (b) and Figure 4.5 (c), (d) show ordered arrays of ZnO NWs formed after 600 second of etching, before and after silica removal, respectively. Silica spheres were removed using sonication for 20 min in methanol.

Figure 4.6 show the high resolution SEM (HRSEM) image of the NWs obtained by etching of the ZnO at 3mTorr, ICP power of 200 W, self-bias voltage of 500 V (VF power 225 W) in CF_4/H_2 plasma with a gas ratio of 1/12. NWs with base of 500 nm (same as silica microsphere size), tips of 300 nm, and height of 250

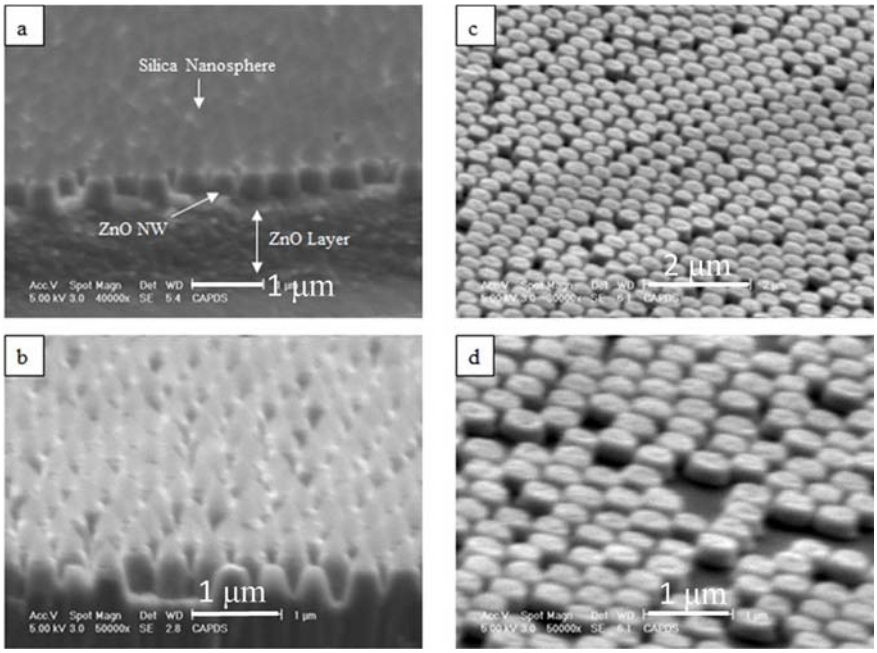

Figure 4.5: (a), (b) Cross section and (c), (d) tilted view SEM images of ZnO nanowires etched in a CF_4/H_2 plasma with a gas ratio of 1/12, at 1 mTorr, ICP power of 200 W, RIE-power of 245 W after 600 second etching.

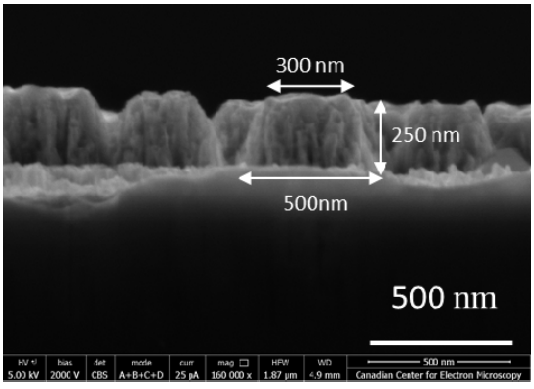

Figure 4.6: Cross sectional HRSEM image of the ZnO NWs obtained at 3 mTorr, ICP power of 200 W, self-bias voltage of 500 V (VF power of 225 W) in CF_4/H_2 plasma with a gas ratio of 1/12.

nm were obtained. The tapered structures of the NWs indicate that there is not a high degree ZnO etch selectivity over silica mask using this plasma chemistry. The plasma condition needs to be adjusted to provide the best etching selectivity and anisotropy.

4.2.1 Long range arrangement of fabricated ZnO NWs

Arrays of ZnO NWs with long range arrangement (>10μm) were obtained using etching at specified condition above. Figure 4.7 shows the tilted and top view of the fabricated ZnO NWs. In addition to long-range ordering, the size of the NWs can be adapted using different size silica nanospheres. The spacing between the adjacent NWs can also be engineered by etching silica templates using the etching chemistry selective to silica as described in section 4.1.2 above.

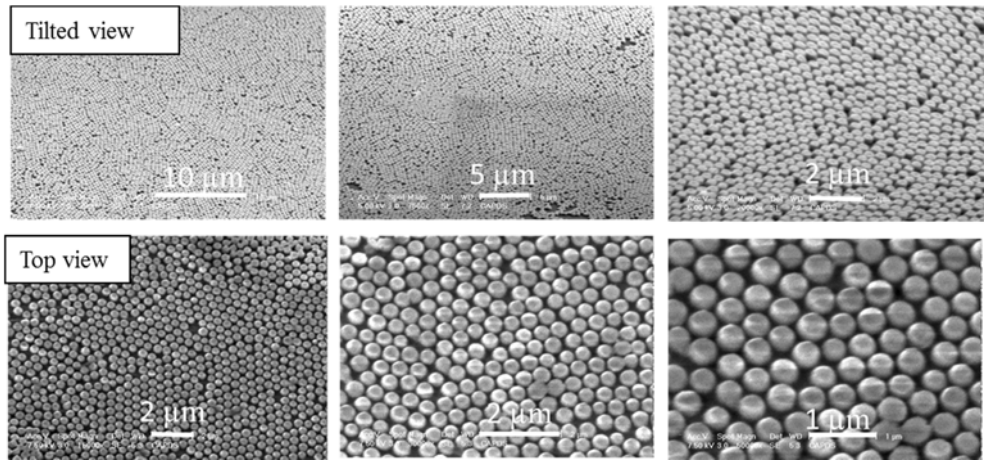

Figure 4.7: Tilted and top view of the fabricated ZnO NWs with long range ordering (>10 μm).

4.2.2 RIE etching mechanism of ZnO used for NW formation

As mentioned above, etching performed for 600 s at pressure of 1 mTorr, ICP power of 200 W, VF power of 245 W in CF_4/H_2 plasma with gas ratio of 1/12. Plasma reactions are as follows;

$CF_4+e \longrightarrow CF_3+F+e$
$CF_3+e \longrightarrow CF_2+F+e$
$CF_4+e \longrightarrow CF_3+F^-$
$H_2+e \longrightarrow H^++H+2e$
$CF_x+H \longrightarrow CHF_x$
$Zn+yCF_x \longrightarrow Zn(CF_x)_y$ (Volatile species)
$Zn+yCHFX \longrightarrow Zn(CHF_x)_y$ (Volatile species)
$Zn+2F \longrightarrow ZnF_2$ (Non-volatile species)
$n(CF_x)+surface \longrightarrow (CF_x)n$ (Polymerization)

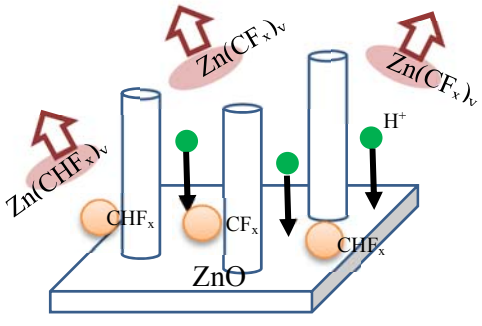

Figure 4.8: RIE etching mechanism for ZnO NW formation.

Based on reaction specified above, the etching mechanism include i) breaking of zinc and oxygen bond in ZnO, ii) reaction of Zn with active CF_x, and CHF_x radicals by ion-bombardment, iii) formation of volatile zinc compounds ($Zn(CF_x)_y$, $Zn(CHF_x)_y$), iv) removal of etch volatile by-products from the surface by energetic H^+ ions under a negative substrate potential (see Figure 4.8).

In this RIE process, low CF_4 concentration (< 8%) and low pressure (<3 mTorr) result in higher ZnO etch selectivity over silica masks, which allow silica masks remain longer during the etching cycle. Anisotropic etching of ZnO with vertical sidewalls can also be controlled by optimum ratio of CF_4/H_2. Using < 8% CF_4 in the gas mixture, the number of active CF_x radicals in the plasma is sufficient to balance the etching rate and sidewall passivation. At low pressure regime (<3 mTorr), the lower etching capacity lowers downs the etching rate. However, at pressures higher than 3 mTorr, etching rate increases at a risk of etching the silica mask. Increase in self-bias voltage (RF-power) enhances etching rate by increasing the broken bonds in ZnO layer and the degree of sputter desorption of by products, exposing a fresh surface to the reactive species. ICP power also enhances the plasma reaction. For an effective etching, the rate of formation of volatile zinc compounds needs to be higher than nonvolatile ZnF_2 zinc fluoride species.

4.2.3 Effect of plasma condition on the structure of etched ZnO NWs

4.2.3.1 Effect of plasma pressure

To examine the effect of plasma pressure on the ZnO NW structures, etching was performed at three different pressures; 1, 3 and 5 mTorr (see Figure 4.9).

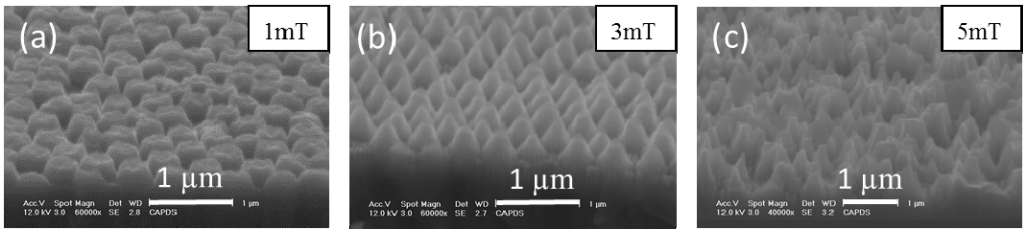

Figure 4.9: ZnO NWs formed using ICP power of 200 W, RIE self-bias voltage of 600 V with a CF_4:H_2 ratio of 1/12 for 600 s at plasma pressures of (a) 1 mTorr, (b) 3 mTorr, and (c) 5 mTorr.

The ZnO layer was etched for 600 s using ICP power of 200 W, RIE self-bias voltage of 600 V with the power of 350 W for 1 mTorr and 423 W for 3 and 5 mTorr using a CF_4:H_2 ratio of 1/12.

As discussed in the previous section, at low pressure regime (<3 mTorr), the lower etching capacity reduces the etching rate. However a pressure <3 mTorr results in higher ZnO etch selectivity over silica masks, which allow silica masks remain longer during the etching cycle. At pressures higher than 3 mTorr,

etching rate increases at a risk of etching the silica mask. Anisotropic etching of ZnO with vertical sidewalls is also be controlled by pressure. Lower pressure results in more anisotropy and vertical sidewalls.

4.2.3.2 Effect of plasma power

In the next set of experiments, the self-bias voltage increased from 550 V to 800 V when other plasma parameters remained unchanged as described above; 1 mTorr, ICP 200 W, 600 s, CF_4/H_2 1/12. Figure 4.10 shows longer ZnO NWs were formed when the VF power increased from 230 W to 470 W. Higher VF power enhances etching rate by increasing the broken bonds in ZnO layer and the degree of sputter desorption of by products, exposing a fresh surface to the reactive species.

At VF plasma power of 280 W and higher, silica self-masking resulting in formation of ZnO nanopillars (see Figure 4.10 (b)). It is occurring due to the increased etching rate of silica and redepositing of silica nanomasks on ZnO layer.

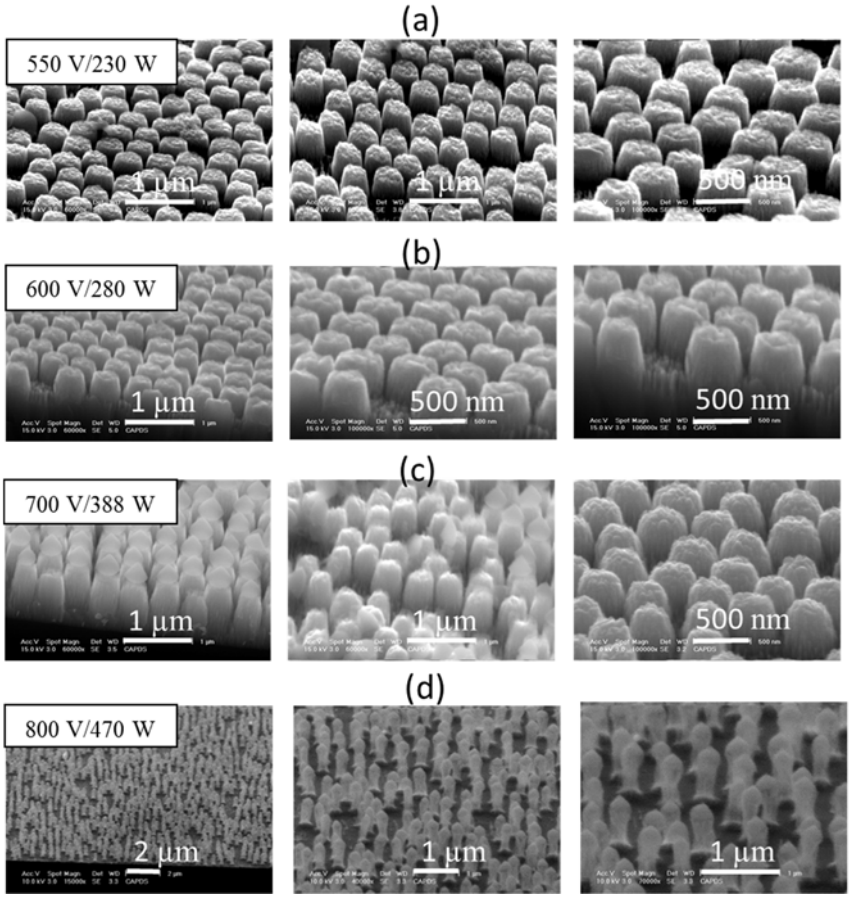

Figure 4.10: ZnO NWs formed at 1 mTorr, ICP power of 200 W, with a CF_4:H_2 ratio of 1/12 for 600 s at VF power of (a) 230 W, (b) 280 W, (c) 388 W, and (d) 470 W.

At high power regime, slight increase in pressure (~3 mTorr) improves the ZnO etching selectivity over silica mask resulting in formation of NWs with higher aspect ratio. Etch rate of 1.3 nm/s was achieved when VF power of 380 W was used.

As mentioned earlier, ICP power also enhances the plasma reaction and as a result improves the ZnO etching rate due to ion enhanced etching. We increased the ICP power from 0 to 300 W, when other plasma parameters were fixed as reported earlier (1 mTorr, RIE 600 V/280 W, 600 s, CF_4/H_2 1/12). As the ICP power is increased, the etch rate also is increased indicating that the plasma density is an important factor in the etching of ZnO. Figure 4.11 presents that at ICP powers <200w the etching rate decreases by a factor of two. The shapes of resulted NWs are quite the same when even no ICP power is used, especially when higher RIE power at slightly higher pressure (~3 mTorr) is being used. The etching rate increases by the increase of ICP power although the rate is not increasing linearly. The ICP power of 200 W is sufficient for achieving an effective etching rate.

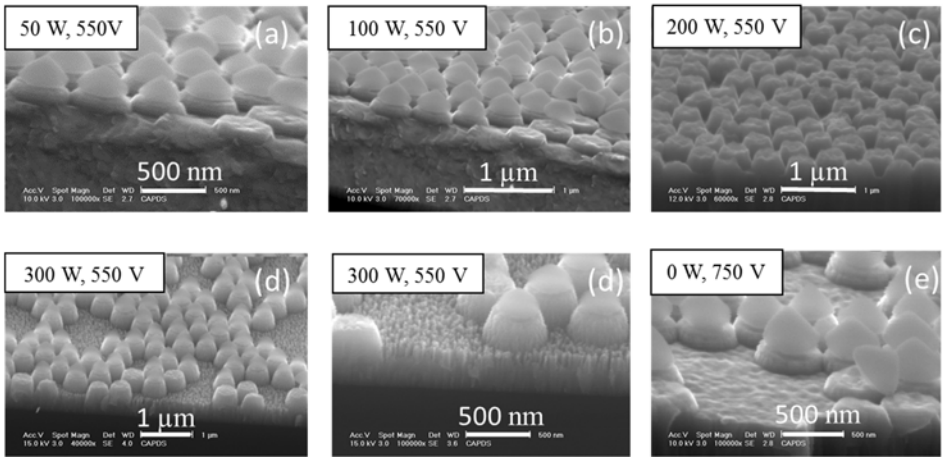

Figure 4.11: ZnO NWs formed by etching at 1 mTorr, RIE self-bias voltage of 550 V (180 W), with a CF_4:H_2 ratio of 1/12 for 600 s at ICP power of (a) 50 W, (b) 100 W, c) 200 W, and d) 300 W. e) NWs formed at higher RIE self-bias voltage 750 V (350 W) using no ICP power.

4.2.3.3 Effect of CF_4 concentration

As described earlier, in this RIE process, high ZnO etch selectivity over silica masks and anisotropic etching of ZnO with vertical sidewalls can be also controlled by optimum ratio of CF_4/H_2. Using less than 8% CF_4 in the gas mixture, the number of active CF_x radicals in the plasma is sufficient to balance the etching rate and sidewall passivation.

Figure 4.12 a, b compares the ZnO NWs obtained using CF_4/H_2 gas ratio of 1/12 (CF_4 concentration of 8%) and 0.6/12 (CF_4 concentration of 5%), respectively. The latter resulted in better anisotropy and vertical

sidewalls. Lower CF_4 concentration and relatively higher H_2 flow rate results in more etching selectivity of ZnO to silica, as a result the silica masks remain longer during etching. H_2 also passivates defects in the depth of ZnO, away from the film surface.

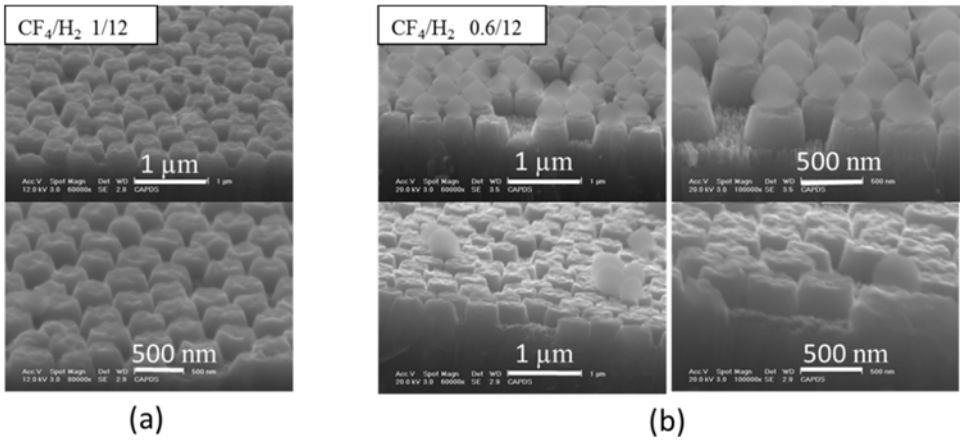

Figure 4.12: ZnO NWs formed at 1 mTorr, ICP power of 200 W, RIE self-bias voltage of 600 V etched for 600 s using (a) CF_4:H_2 gas ratio of 1/12 (CF_4 concentration of 8%) and (b) 0.6/12 (CF_4 concentration of 5%).

Using higher CF_4 concentration (>8%) results poor ZnO etch selectivity over silica masks. As demonstrated in Figure 4.13 (a) silica mask were fully removed during 600 s etching using CF_4/H_2 gas ratio of 1/4 (CF_4 concentration of 25%) and resulted in ZnO nanodomes. CF_4/H_2 gas ratio of 4/1, where higher CF_4 flow rate than H_2 is being used, resulted in reverse selectivity; silica etched away before ZnO NWs were formed.

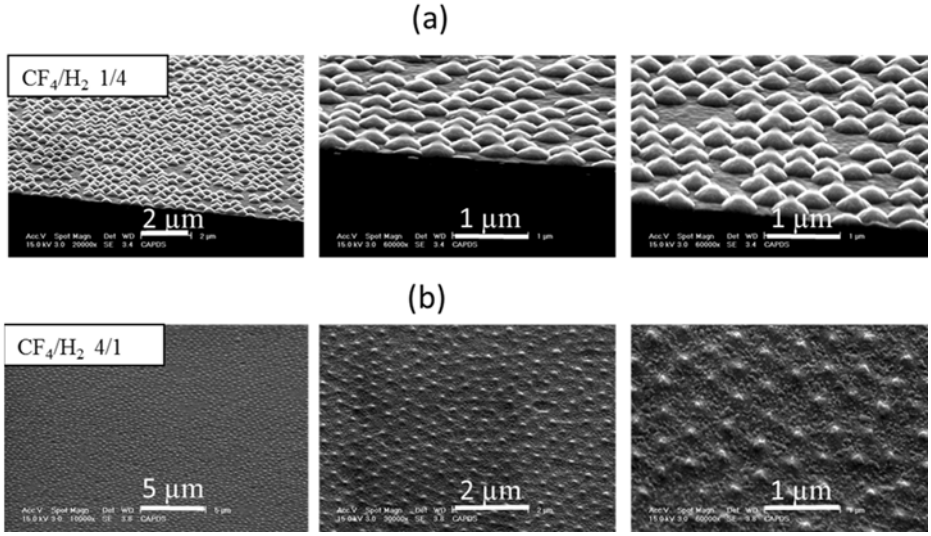

Figure 4.13: ZnO NWs formed at 1mTorr, ICP power of 200 W, RIE self-bias voltage of 600 V for 600 s using a) CF_4:H_2 gas ratio of (a) 1:4 (CF_4 concentration of 25%) and (b) 4:1 (CF_4 concentration of 400%).

4.2.3.4 Effect of etching time

The effect of etching cycle was examined to determine the shape of the resulting ZnO NWs. The etching was performed at 1 mTorr, ICP power of 200 W, self-bias voltage of 600 V with VF power of 280 W, using CF_4:H_2 gas ratio of 1/12. Ordered arrays of short ZnO NWs were obtained after 600 s etching (see Figure 4.14 (a)). Longer ZnO NWs with tapered sidewalls were obtained as the etching time was increased (see Figure 4.14 (b)). Silica masks etches away at longer etching cycles. The cone-like ZnO structures were formed as a result of etching for 1200s (see Figure 4.14 (c)).

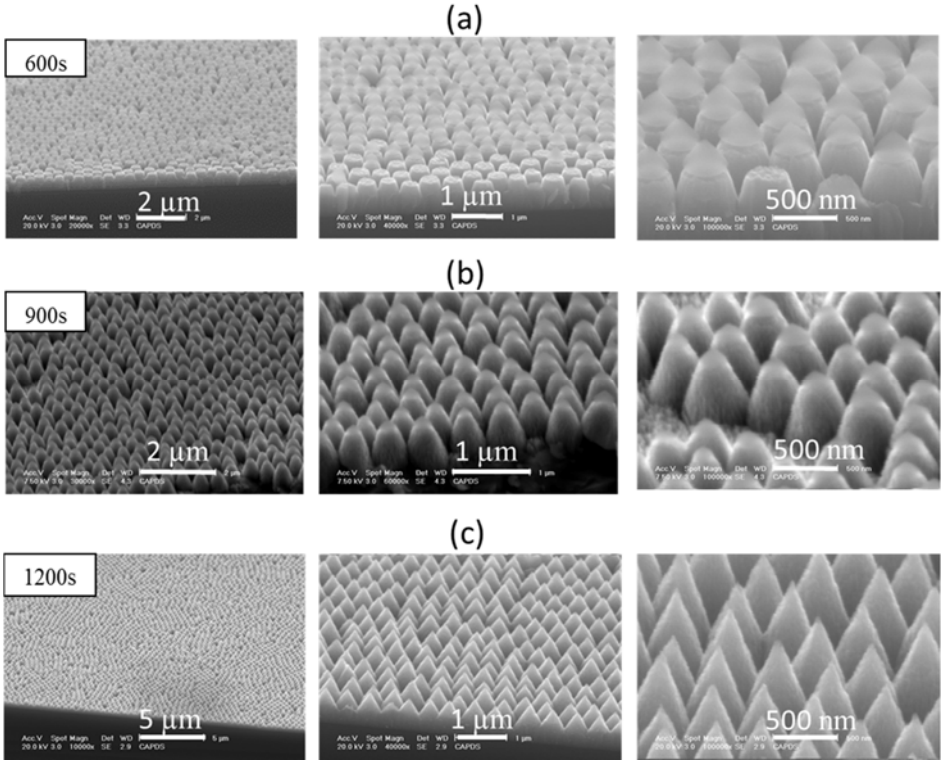

Figure 4.14: ZnO NWs formed at 1mTorr, ICP power of 200 W, RIE self-bias voltage of 600 V (280 W) with a CF_4:H_2 ratio of 1/12 at etching cycles of (a) 600, (b) 900 s, and (c) 1200 s.

4.2.4 Wet chemical treatment of ZnO NWs

As-etched ZnO NWs were cleaned using BHF and 0.1% HCl (in water) solutions in order to remove the RIE damages. These damages if remain; create surface trap states which act as potential barriers in carrier transfer into NWs, resulting poor collection efficiency in QD-based PV devices where NWs are used as photo-electrode. In this section we study how the wet-cleaning process affects the structural properties of the wires. In section 4.3 the optical properties of the as-etched wires and cleaned wires will be compared and discussed.

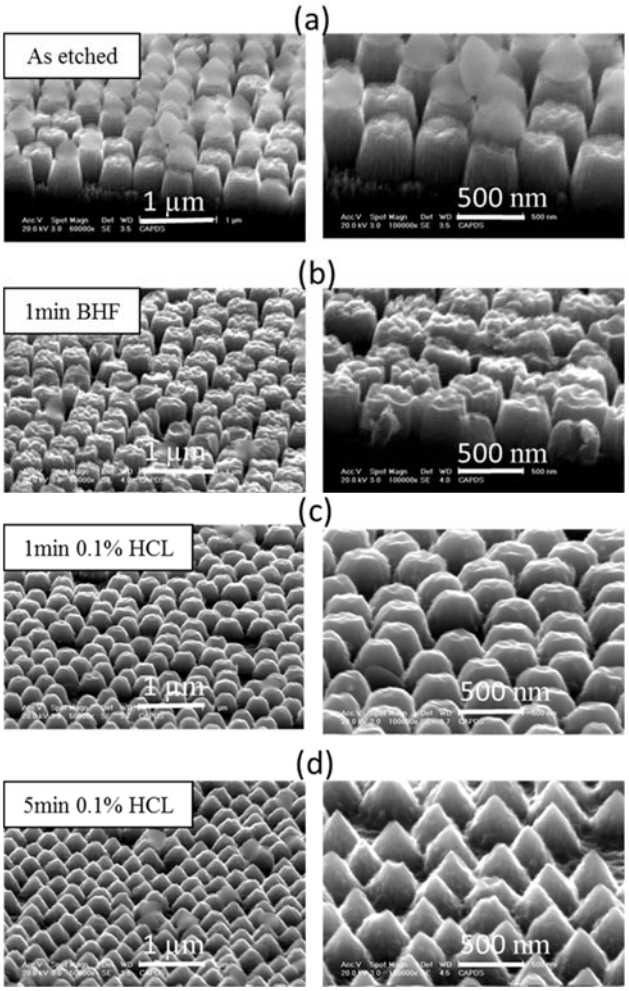

Figure 4.15: ZnO NWs (a) before and after wet chemical treatments; (b) 1 min dip in BHF, (c) 1min dip in 0.1% HCl, and (d) 5 min dip in 0.1% HCl.

As depicted in Figure 4.15 (a), (b), by a single dipping of the etched ZnO NWs in buffered hydrofluoric acid (BHF) for 1min, the silica masks were removed and the structure of the wires remained unchanged. BHF also removes any other oxide compounds deposited on the surface of NWs and the defects created on the surface of the NWs during etching. The brittle nanopillars also were removed from the sample due to the forces applied from the polar solution.

Hydrochloric acid (HCl) is known as the etchant of the ZnO layers. A 0.1% diluted solution of HCl was used for removing defects from the NWs by ZnO etching in a control way with minimal change on the shape of the NWs. Figure 4.15 (c) depicts 1 min etching of the NWs in 0.1% HCl does not affect the shape of the wires. The surface of the wires also looks less defective and brighter. Conic-like structures were formed after exposing NWs to this solution for longer time (~5 min) (see Figure 4.15 (d)).

4.2.5 Hydrogen plasma treatment of ZnO NWs

The surface of the ZnO NWs were treated with Hydrogen plasma subsequent to the etching. In-situe plasma treatment were applied on the NWs in the RIE chamber. After ZnO etching step, the chamber was outgassed for 10 min. ZnO NWs were treated with H_2 plasma by applying 20 sccm hydrogen gas for 100s under ICP power of 50 W. In another process, we increased the plasma power by using 100 W ICP and 10 W VF powers. No considerable change observed on the NW structure after these treatments. H_2 passivates defects in ZnO away from the film surface. We studied and discussed the optical properties of the H_2-plasma treated NWs in the next section.

4.3 Study of surface states in ZnO NWs due to RIE etching

Photoluminescence was used as a tool to study defects created in the ZnO NWs due to RIE damages. Figure 4.16 (a) and Figure 4.16 (b) demonstrate the PL spectra obtained for ZnO film (RT) and etched ZnO NWs under excitation at 320 nm and 380 nm respectively. The peak emissions at 420 nm and 460 nm appeared in ZnO film and wires are the emissions from deep trap levels associated with the native defects such as zinc and oxygen interstitials and vacancies [148-151]. Some researchers have also attributed the peak at 420 nm to near band edge emissions (NBE) [152]. The broad peak emission at 500 nm in the NWs can be attributed to the surface trap states originating from RIE damages and the lattice imperfection sites [153, 154]. The photoluminescence emission spectra of zinc oxide is excitation dependent [155].

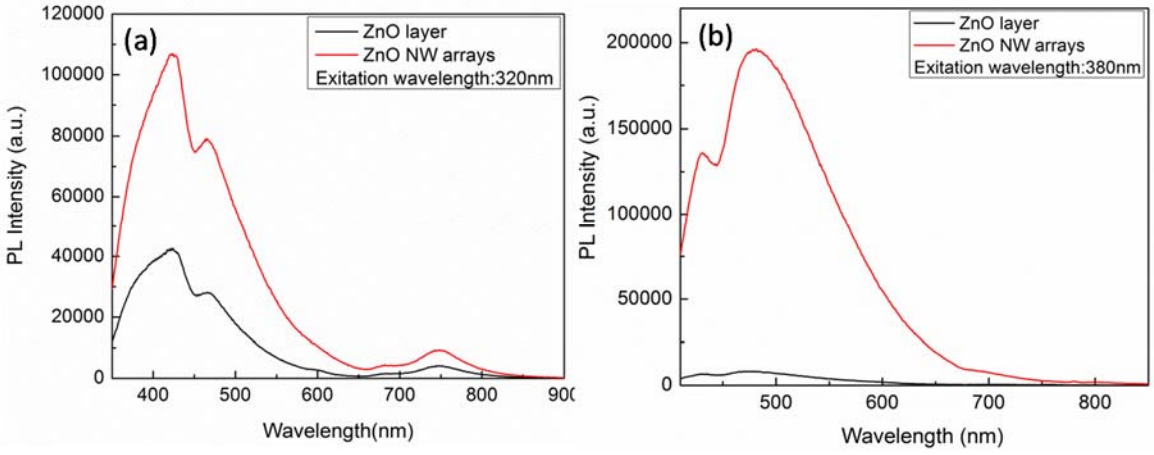

Figure 4.16: PL spectra of ZnO film (RT) and etched ZnO NW arrays under excitation wavelength at (a) 320 nm and (b) 380 nm.

4.3.1 Effect of wet chemical treatment on surface states of ZnO NWs

In order to remove the defects created from the RIE damages, different wet chemical treatments were applied on the nanowires. Effect of these wet process treatment on photoluminescence of ZnO NWs was studied. Figure 4.17 (a), (b) show the PL and normalized PL spectra of ZnO NW arrays, excited at 320 nm, before and after wet cleaning. The normalized spectra are obtained by dividing the spectra by maximum intensity value and then scaling spectra to desired value (multiplying the spectra to a desired value such as 410 in this image). The results show that the peak at 420 nm is remained unchanged. The peak at 460 nm is red-shifted to 480 nm after ZnO NW arrays formation. This can be attributed to creation of some new states in the ZnO NWs due the plasma reactions. It also can be due to band structure modification of the ZnO during etching by creating deep trap states in the NWs. As discussed in previous chapter, the ZnO layer is polycrystalline, as a result the high power plasma condition used for NW formation can create surface defect sites in the resulting NWs. The results from wet cleaning process show that the states created by etching in the NWs were recovered using a moderate etching of ZnO and oxide components in 0.1% HCl and buffered BHF. The improvement also achieved by 15 min ultra-sonication of the nanowires in methanol. This cleaning process helps with removing trap states due to polymeric contaminations. Using a moderate wet process resulted in NWs with emission spectra very similar to starting ZnO layer indicating recovery of some NWs trap sites after wet chemical treatment.

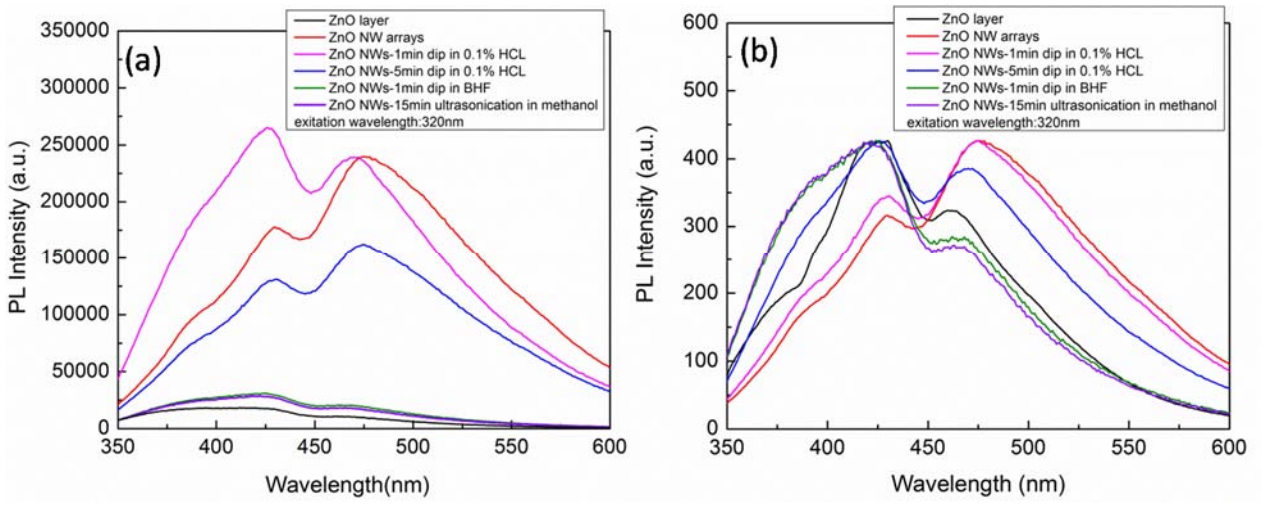

Figure 4.17: (a) PL and (b) normalized PL spectra of ZnO NW arrays before and after wet cleaning. Samples excited at excitation wavelength of 320 nm.

To study how the surface properties of the NWs were changed after cleaning, samples were excited at 380 nm. Figure 4.18 shows that the emission peak at 500 nm decreased after 1min cleaning in BHF indicating removal of a portion of defects from NWs' surfaces by wet chemical treatment. The same trend also was observed for the wires cleaned in 0.1% HCl. This finding was further elaborated in charge carrier transfer dynamic study between QD/NW presented in chapter 6.

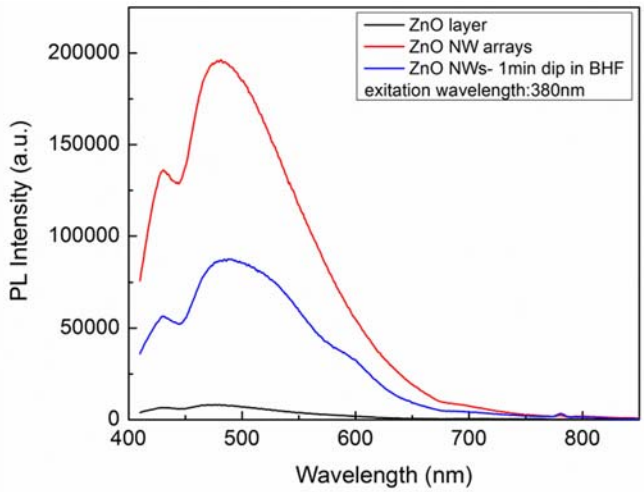

Figure 4.18: PL spectra of ZnO NW arrays before and after wet cleaning in BHF. Samples excited 380 nm.

4.3.2 Effect of hydrogen plasma treatment on surface states of ZnO NWs

As discussed in previous section, the NWs were treated in hydrogen plasma after formation. Different hydrogen plasma conditions were applied on the nanowires. Figure 4.19 presents steady state PL spectra of ZnO NW arrays before and after hydrogen plasma treatments.

Samples are optically excited at wavelength of 320 nm and 380 nm to study any possible modification in trap states by the treatment. The results indicate that the defect-related 480 nm and 500 nm peaks are blue shifted and lowered down respectively using moderate H_2 plasma conditions. Plasma power of 50 W and lower terminates the dangling bonds and passivate a percentage of defects, hence improves the quality of the resulting NWs without causing any change in the geometrical structure of the NWs.

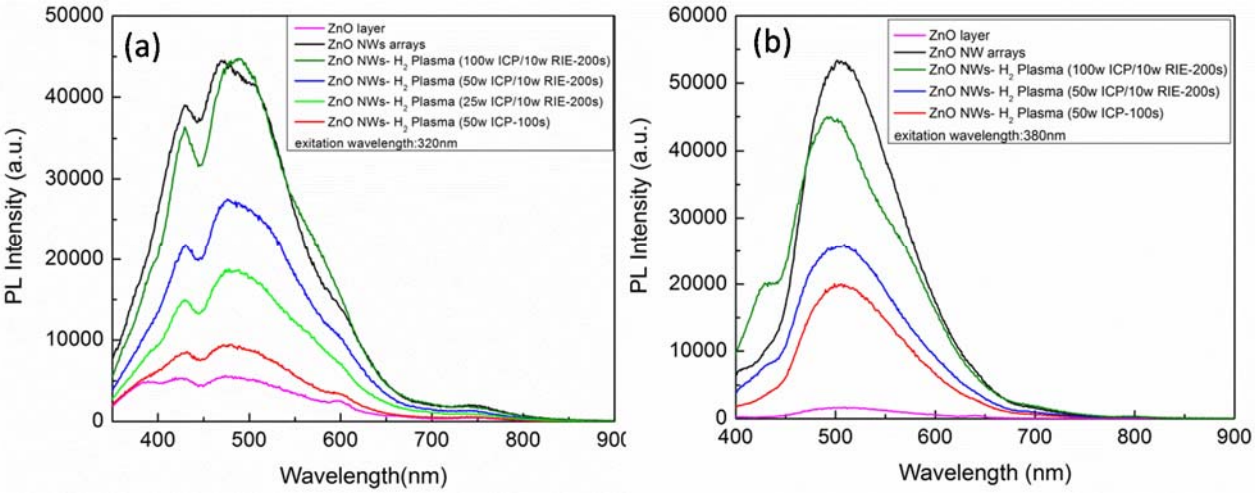

Figure 4.19: PL spectra of ZnO NW arrays before and after hydrogen plasma treatments. Samples excited at (a) 320 nm and (b) 380 nm excitation wavelengths.

4.4 Summary

In this section, we developed a scalable method for fabrication of ZnO nanowires combining RIE etching and silica sphere nanomasking. Amino functionalized silica spheres with different sizes were employed as nanomask to develop ZnO NWs with different diameter. Herein, we utilized less corrosive CF_4 and H_2 gas mixtures to etch ZnO film through nanomasks using different plasma conditions. The etching rate, anisotropy, and the selectivity of the etching process was controlled with adjusting the plasma parameters. Using higher plasma power with low CF_4 concentration at low pressure resulted in NWs with vertical side walls. Fine tuning of the recipe would allow controlling the spacing between nanopillars. The effect of post treatments, such as hydrogen plasma treatment and wet etching, on the surface trap states was also investigated.

Chapter 5
Formation of ordered arrays of QDs (quantum solids)

In chapter 2, we briefly discussed the advantages of colloidal quantum dots and their potential application for solution processed, vacuum-less semiconductor technology in the form of QD-film.

We also briefly highlighted the common methods for the formation of ordered array of quantum dots. The widely used spin-coating method is very input-intensive and wastes huge amounts of quantum dots. Spin-coating utilizes less than 0.1% of the QDs and results in a huge material waste. This is a considerable limitation for industrial applications and scaling up of the deposition method. Finding alternative high yield methods for deposition of quantum dots is a crucial step for adapting quantum dot technology into cost-sensitive optoelectronic industry. In this chapter we explore drop-casting as one of possible alternative methods.

Pre-requirement of spin-coating and dip-coating methods is the high surface adhesion of CQDs on to the surface of the substrate to be deposited. Surfactants such as trioctylphosphine (TOP), trioctylphosphine oxide (TOPO), oleic acid (OA), octadecylamine (ODA) are non-polar ligands for CQDs and provide hydrophobic nanoparticles. These hydrophobic nanoparticles do not like hydrophilic surface of ZnO. As discussed in chapter2, there are two methods to address this problem:

1. Application of bi-functional surfactants: The big drawback of this technique is that it increases the effective length of the polymer between ZnO and CQDs. This adversely affects charge transfer dynamics between CQDs and ZnO. For applications in solar cell devices, this results in power conversion efficiency losses (high series resistance).
2. Ligand-exchange (solution-phase): The problem with ligand-exchange is the reduction of PLQY in CQDs after ligand-exchange process. PLQY drops after ligand-exchange because of formation of trap states on the surface of CQDs. The presence of these surface trap states affect the electrical properties of nanocrystal film. In solar cell applications this translates to lower power conversion efficiency (limited shunt resistance).

Compared to dip-coating and spin-coating, drop-casting method is not bound to surface property of QDs and substrate. Drop-casting method is not input-intensive and avoids wasting of CQDs. The advantage of drop-casting of non-polar, hydrophobic ligated quantum dots on hydrophilic surfaces like ZnO is that there is little attraction force between quantum dots and the surface of the ZnO coated substrate, allowing quantum

dots to freely move on the surface and find proper sites to settle. This freedom in the movement would allow quantum dots to find proper locations and form an ordered array upon drop-casting and during dry out of the solvent. The CQDs upon drying are adhered to the surface. The long length and non-polar ligand (such as DDT, OA and TOPO) is then replaced with shorter ligands like ethanedithiol (EDT) and mercaptopropionic acid (MPA) by the solid-phase ligand-exchange for better charge transfer (between CQDs and ZnO surface) and, particularly, better carrier transport (higher mobility in quantum dot film). The advantage of the solid-phase ligand-exchange over solution-phase one is that PLQY is profoundly preserved in QDs after the solid-phase ligand-exchange.

In this study, we have used drop-casting method to form carrier transport-compatible CdSe QD-film on ZnO substrate. In this study two different approach has been explored for deposition of conductive QD-film: (a) layer-by-layer drop-casting of non-polar QDs based on solid-phase ligand exchange with ethanedithiol (EDT) and mercaptopropionic acid (MPA); (b) single-step drop-casting of transport-compatible polar quantum dots (MPA).

5.1 Formation of CdSe QD-film with drop-casting of non-polar QDs capped with long ligands

The CdSe QD-film is prepared by drop-casting of CdSe-OA colloidal quantum dots dissolved in non-polar organic solvents such as: toluene, chloroform, and hexane on the ZnO coated glass substrates. The drop-casting is performed on leveled stage, in the glove box and inside closed ambient of a desiccator (Figure 5.1). The leveled stage reduces the effect of gravity while the closed ambient of desiccator eliminates the turbulences caused by ambient gases. Around 200 µl of CQD solution is drop-casted to cover the surface of the samples (22 mm×22 mm). The thickness of the QD-film can be controlled by controlling the CQDs' concentration in the non-polar organic solvent. The higher the concentration, the higher is the thickness. Table 5-1 summarizes the thickness values for different CdSe CQD concentration by dispensing 200 µL of the solution. The thicknesses are measured with Dektak profilometer after annealing the samples on a hot plate at 200 °C. The measured values represent the thickness at the middle of the sample away from the edges. Near the edges, the CdSe-OA quantum dots are adsorbed by exposed area of the glass substrate and the thickness tends to be higher than the middle of the sample.

Figure 5.2 represents cross sectional HRSEM CdSe QD-film prepared by drop-casting of 1 mg/ml of CdSe-OA in chloroform on top of ZnO coated silicon substrate. A ruler is used to measure the thickness (~ 91 nm).

Figure 5.1: Set-up (leveled stage inside desiccator) used for drop-casting deposition of quantum dots.

Table 5-1: Dependency of CdSe QD-film thickness with respect to CQD concentration. The dispensing volume is 200 µL.

Concentration	Thickness
0.8 mg/mL	70 nm ± 10 nm
1 mg/mL	85 nm ± 10 nm
5 mg/mL	450 nm ± 30nm
20 mg/mL	2 µm ± 100nm

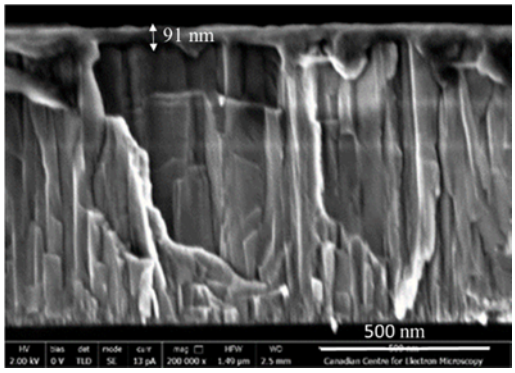

Figure 5.2: Cross sectional HRSEM micrograph of CdSe quantum dot film on top of ZnO thin film. The QD-film is prepared by drop-casting of 1mg/ml of CdSe-OA in chloroform. Image processing software (ImageJ) is used to measure the thickness. The measured thickness of QD-film in the image using ImageJ software is 91 nm.

The resulted QD-film has long length polymers as ligands, though, it is relatively an insulator material. The solid-phase ligand-exchange has been performed on the CdSe-OA QD-film to replace long length OA ligands with much shorter EDT ones. The sample is immersed in a solution of 1mmol EDT in acetonitrile for 1 minute and then washed with acetonitrile and left to dry. The Fourier transform infrared (FTIR) spectra of the CdSe-OA QD-film deposited on AZO-ZnO (~ 50 nm) coated glass before and after EDT treatment is depicted in Figure 5.3. The decrease in C-H bond peak (at 2900 cm^{-1}) is an indication that long carbon-chain of OA ligand is replaced with shorter carbon-chain of EDT ligand.

SEM micrograph of the surface of the resulted QD-film is depicted in Figure 5.4. The QD-film is prepared by drop-casting of 200µL from 20 mg/ml CdSe solution in chloroform. The CdSe-OA colloidal quantum dots form a uniform, flawless and crack free QD-film (Figure 5.4 (a)). After the solid-phase ligand-

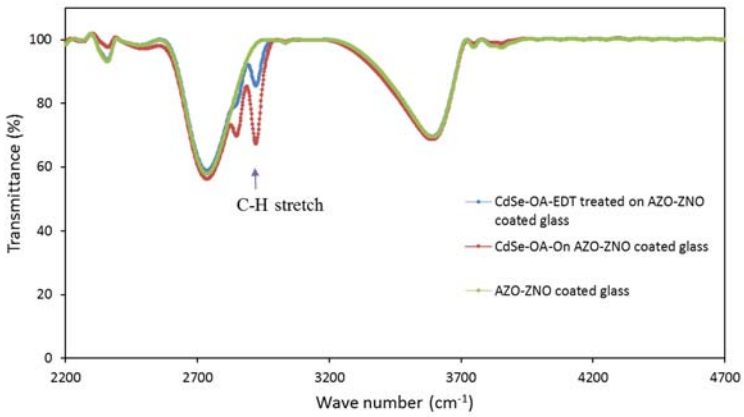

Figure 5.3: The Fourier transform infrared (FTIR) micrograph of CdSe-OA (red line), CdSe-OA after EDT treatment (blue line) on AZO-ZnO coated glass substrate (green line). The FTIR spectra shows a clear decrease in intensity of C-H bound (at 2900 cm^{-1}) which is an indication that OA ligands are replaced with shorter EDT ligands.

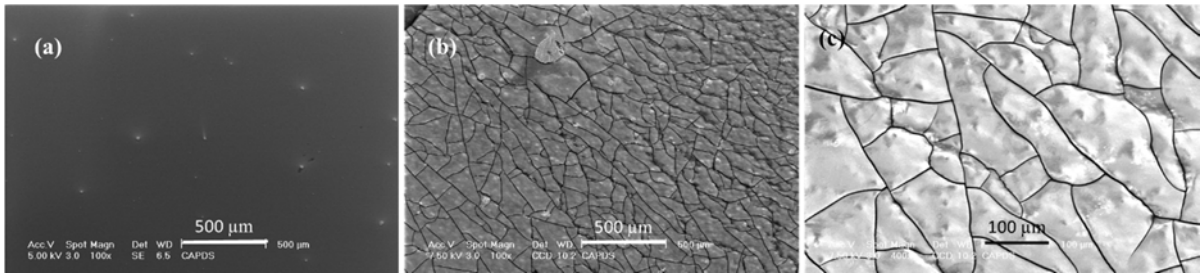

Figure 5.4: (a) QD-film prepared by drop-casting of 200 µL from 20 mg/ml of CdSe-OA colloidal quantum dots in chloroform on ZnO coated glass; (b) QD-film after solid-phase ligand-exchange, the cracks are formed because of volume loss due to replacement of OA ligands with shorter EDT ligands; (c) Closer view of the cracks in QD-film.

exchange, the resulted CdSe QD-film has cracks and flaws (Figure 5.4 (b), (c)). These cracks are the result of volume loss due to replacement of long OA ligands with shorter EDT ones. These cracks are undesirable and will cause shorting in the electronic device.

5.1.1 Formation of thin QD-film with less cracks by solid-phase ligand-exchange

During solid-phase ligand-exchange procedure, short length EDT molecules replace the long length OA molecules. The substitution starts from the surface of QD-film and takes a while until the EDT molecules diffuse deep inside of the QD-film to replace the OA ligands. This volume loss makes a built in stress in the

QD-film and causes the film to crack. The thicker the film is, the higher is the built in stress. Therefore, thicker films are prone to have bigger and more cracks. It is expected for thinner films to have less cracks.

The thickness of the drop-casted film can be controlled by controlling the concentration of CQDs in the solution. The concentration of CQDs is lowered by adding non-polar solvent (chloroform) to the stock solution. Figure 5.5(a) and Figure 5.5(b) represent the SEM micrographs of QD-films with different thicknesses. As it is apparent in the SEM image of thinner QD-film (Figure 5.5(b)), we still have cracks in the thinner film. However, these cracks are narrower and shorter in length. It has been also noted that the cracks are often happening around the agglomerated QDs sites (Figure 5.5(c)). It is most likely that the presence of these agglomerated QDs sites, initiates the formation of cracks. Therefore, the film with more agglomerated QDs is prone to have more cracks.

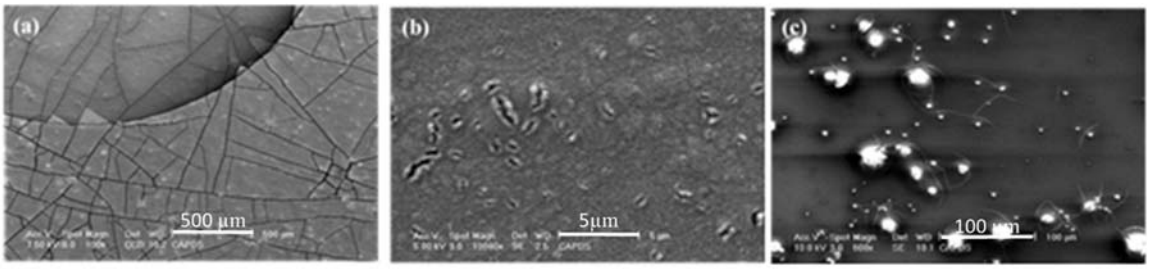

Figure 5.5: (a) CdSe-QD-film prepared by drop-casting of CdSe colloidal quantum dots in chloroform, the thickness of the QD-film is ~2.2 µm. The top left circle is the metal pad. (b) Higher magnification of a thinner CdSe QD-film (~ 85 nm) after treatment. The bright spots in the picture are agglomerated QDs, (c) The cracks are formed around the agglomerated QDs sites.

To address this problem (the formation of cracks in EDT treated CdSe QD-film), we bath sonicated the CQDs solution prior to use. Then, the sonicated CQDs solutions have been filtered using a 450 nanometer size particle filter upon drop-casting onto the samples. With this technique, QD-film with much less cracks is achieved (Figure 5.6 (a)). This method (diluting CQDs solution) is applicable for the formation of thinner QD-films (lower thickness regimes range < 100 nm).

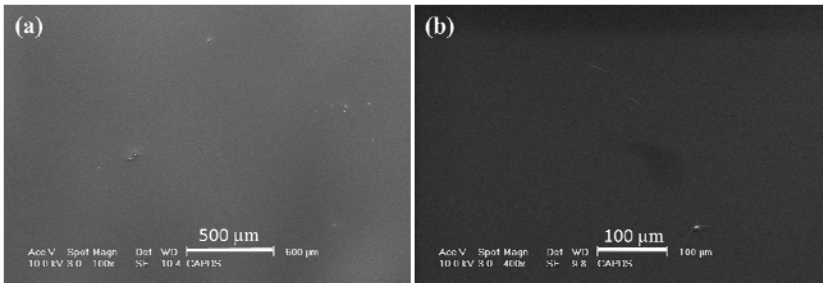

Figure 5.6: (a) SEM micrograph of crack free CdSe QD-film (thickness ~220 nm) drop-casted from CQDs in chloroform (~2.5 mg/ml) after EDT treatment, (b) Higher magnification image of the same QD-film.

5.1.2 Formation of thick QD-film through layer-by-layer deposition

Possibility of multilayer deposition to increase the thickness of the QD-film is also explored. A thinner CdSe QD-film is formed by an identical drop-casting procedure explained before (by drop-casting of 1 mg/ml). This film is then EDT treated. The second layer is formed on top of resulted CdSe QD-film. The CdSe-OA colloidal quantum dots fill the cracks. This cycle is repeated till the desired thickness is achieved. The final multilayer film still have some limited cracks (Figure 5.7(b), (c)). This multilayer method is applicable for the formation of thicker QD-films.

In a similar way, solid-phase ligand exchange has been used to replace the original OA ligands in CdSe-OA QD-film with polar MPA ligands. MPA is more polar than EDT and provides better attachment to ZnO. The sample is immersed in a solution of MPA in methanol (10% volume) for 1 minute and then left to dry. The methods developed for EDT treatment of CdSe QD-film and layer-by-layer deposition technique are identically applicable for MPA treatment as well.

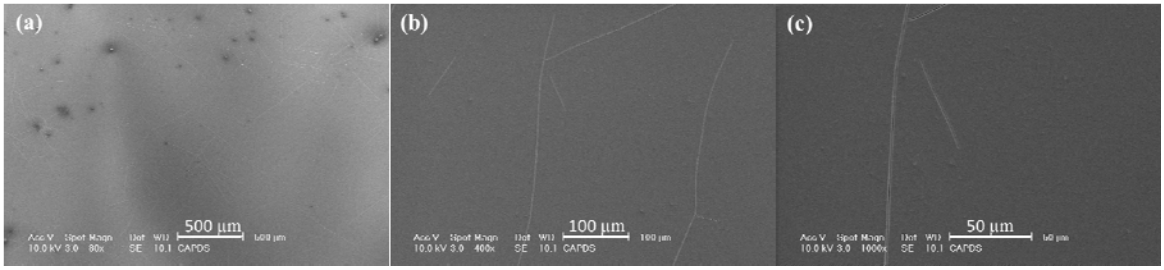

Figure 5.7: (a) CdSe QD-film prepared using layer-by-layer deposition technique, (b) and (c) Cracks formed in the multilayered CdSe QD-film.

5.2 Formation of QD-film by drop-casting of polar CQDs capped with short ligands

The final quantum film prepared with layer-by-layer deposition technique is susceptible to crack formation. One way to address this problem is to use CQDs with shorter length ligands (carrier transport-compatible

ligands). In this regard, solution-phase ligand-exchange is of much interest to get solution of CQDs with short ligand. The solution-phase ligand-exchange method provides a printable, ready to use semiconductor ink which is more compatible with roll to roll manufacturing and large area deposition. Drop-casting is of particular interest since it almost utilizes all of the used colloidal quantum dots.

5.2.1 Mercaptopropionic acid solution-phase ligand-exchange of CdSe quantum dots

The CdSe-OA quantum dots in chloroform were precipitated by adding methanol as non-solvent to the solution. By addition of methanol to 20 mg/ml CdSe in chloroform a precipitate immediately began to form. To get all of the QDs and minimize the loss of QDs, the suspension were centrifuged. The transparent supernatant (methanol and chloroform) was then removed and the sediment was left to dry. The CdSe quantum dots were then redissolved in 2 ml MPA and sonicated for 5 minutes. The mixture was left for three days at room temperature. The quantum dots were then precipitated by adding hexane to the solution. The suspension was centrifuged and the clear supernatant was removed. The final sediment (CdSe-MPA QDs) were dried and then redispersed in a polar solvent (methanol). The FTIR micrograph of CdSe-OA and CdSe-MPA QD-films deposited on ZnO coated glass is depicted in Figure 5.8. The PLQY of the CdSe quantum dots undergoes a considerable reduction during the solution-phase ligand-exchange process.

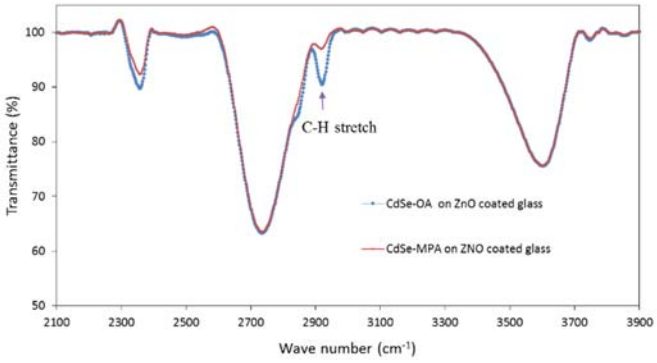

Figure 5.8: Fourier transform infrared (FTIR) micrograph of QD-films deposited on ZnO coated glass. Blue line: CdSe-OA deposited on ZnO coated glass; Red line: CdSe-MPA deposited on ZnO coated glass.

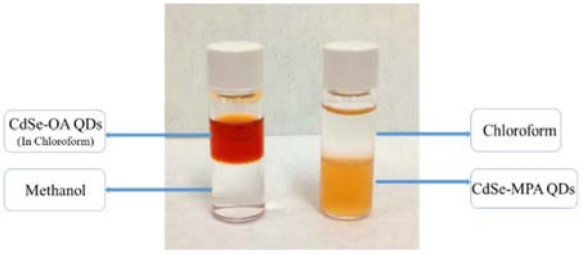

Figure 5.9: CdSe quantum dots with oleic acid ligands dispersed in chloroform and CdSe quantum dots after solution- phase ligand-exchange (mercaptopropionic acid) dispersed in methanol.

5.2.2 Formation of crack-free QD-film in a single-step drop-casting

The CQDs in methanol were bath sonicated prior to use. Then, the sonicated CQDs solutions is filtered using a 450 nanometer size particle filter upon drop-casting onto the samples. A crack-free QD-film is achieved upon single-step drop-casting (Figure 5.10 (a), (b)). Different QD-film thickness is achievable with different concentration of CQDs in solution.

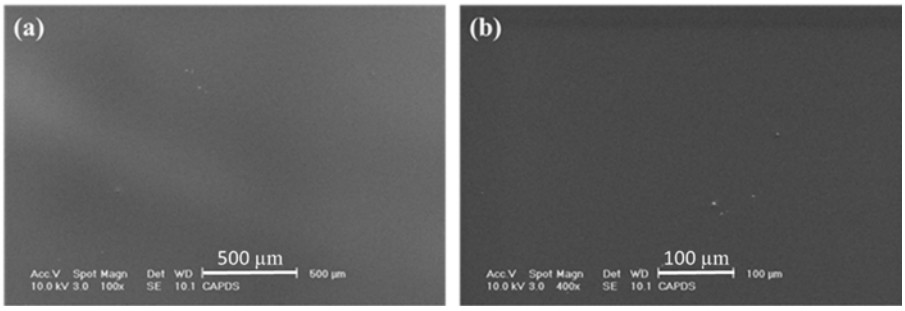

Figure 5.10: QD-film prepared single drop-casting of polar MPA capped QD in methanol.

5.3 Summary

We explored the application of drop-casting in the formation of CdSe QD-film. To increase the conductivity of the CdSe QD-film, the original insulating OA ligands were replaced by shorter, conduction-compatible EDT ligands through solid-phase ligand-exchange process. The drawback of this process is that the resulted QD-film suffers from the formation of micro-cracks. In device fabrication, these cracks short the electronic device. We demonstrated that, one way to solve this problem is to use layer-by-layer deposition technique in the formation of QD-film. In layer-by-layer deposition technique, thick films are prepared from stacking of multiple thinner layers to reduce the overall cracks in the final film. The solid-phase ligand exchange procedure developed here, is applicable to a variety of transport-compatible ligands such as mercaptopropionic acid (MPA).

Solution-phase ligand-exchange is performed on CdSe-OA quantum dots to replace the ligands with polar and charge transport-compatible mercaptopropionic acid (MPA) ligands. Crack-free QD-film is formed by single-step drop-casting of CdSe QDs in methanol. A considerable reduction in PLQY of CQDs is observed after solution-phase ligand-exchange. Another drawback of deposition of QD-film from drop-casting of carrier transport-compatible polar CQDs is that the polar solvent (alcohol) takes some times to evaporate and makes the deposition process slow. We used methanol as solvent of polar CQDs since it has relatively low (~ 65 °C) boiling temperature and it does not evaporate slowly.

Chapter 6
Experimental study of charge transfer dynamics at the QD/ZnO NWs interfaces

Photoluminescence decay lifetime quenching in a sputtered ZnO film (or RIE etched NWs)/QD structure with respect to a control sample can be attributed to electron transfer from the QD layer to the ZnO film (or NW). The same phenomena can be attributed to hole transfer for the excited QDs in contact with a hole transport layer. Due to the possibility of formation of positively charged excitons during the electron transfer processes, and in order to remove the confusion of non-radiative relaxations from the true electron transfer, PL decays in sputtered ZnO film (or RIE etched NWs)/QD/hole transport layer (MoO_3: molybdenum trioxide) structure were studied. The hole can be rapidly removed from QDs with the help of hole transport layer. This way the QDs remained neutral and the PL decay can be attributed to the true electron transfer [156]. Sputtered ZnO film (or RIE etched NWs)/QD/MoO_3 structure is investigated for the first time using PL decay dynamics to gain insight about true electron transfer. After excitation and exciton generation in the QDs, the electrons transfer from QD lowest unoccupied molecular orbital (LUMO) level to the sputtered ZnO film (or RIE etched NW) conduction band (CB), if the driving force is sufficient. The offset between QD LUMO level and ZnO film (or NWs) CB is an important factor for an efficient transfer. As discussed previously in chapter 2, the QD structure (core or core/shell), type (I or II), size, and ligands are the important parameters influencing the carrier transfer efficiency. Among them, ligands are considered the most important factor that significantly influences the position of LUMO levels of QDs [33]. For an efficient transfer, high degree of attachment between QDs and the sputtered ZnO film (or RIE etched NWs) is also required that can be achieved by using an appropriate (polar) ligands.

ZnO film (or NWs)/QD, QD/MoO_3, and ZnO film (or NWs)/QD/MoO_3 structures were used to study electron, hole, and (electron + hole) transfer dynamic respectively. QD layer deposited on a glass substrate was used as control sample (see Figure 6.1). 700 nm sputtered ZnO films with carrier concentration of 5.62×10^{18} cm^{-3} and 500 nm long ZnO NWs formed from the same ZnO film were used for this study. For RIE damage removal, in order to have a surface with less surface trap sites, NWs were treated in 0.1% HCl for 30s after formation. QDs were applied onto the ZnO film or NWs by drop casting of 200 µL colloidal solution of 0.5 mg/mL QD onto a 2×2 cm sample. This condition provides 80 nm QD layer that is thin enough for the light beam ($\lambda_{ex.}$= 380 nm) to pass through the layer to excite QDs at the sputtered ZnO film (or RIE etched NWs)/QD and QD/MoO_3 interfaces. Core CdSe QDs structures with various sizes and

ligands were applied onto ZnO films (or NWs). 50 nm MoO_3 layer was deposited on the ZnO (or RIE etched NWs)/QDs structures using evaporation to act as hole transport layer and help with extraction of holes from QDs.

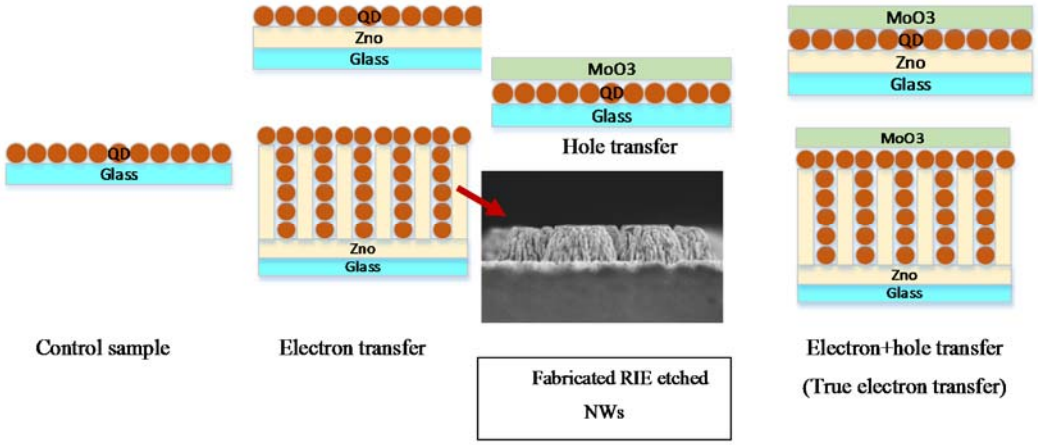

Figure 6.1: Schematic of prepared samples to study electron, hole, and true electron transfer dynamics.

PL spectra were acquired at 380 nm excitation on an Edinburgh Instrument fluorescence spectrometer at room temperature. Decay lifetime measurements were performed upon excitation at 375.4 nm with an elastomeric polymer light-emitting device (EPLED) with 5 MHz pulse repetition frequency, pulse width of 943.3 ps, band width of 10 nm and excitation power of 20 μW using the time correlated single photon counting (TCSPC) method. The raw PL decay data were fitted to decay functions using the "Fluorescence Analysis Software Technology (FAST)" which allowed four decay constants to be obtained by multi-exponential and distribution tail fitting analyses (see Figure 6.2).

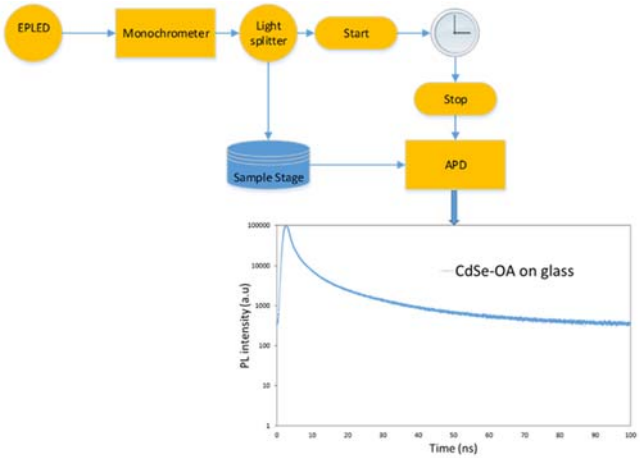

Figure 6.2: Schematic diagram of set-up for TRPL measurement using TCSPC technique. The wavelength of our EPLED is at 375.4 nm and the pulse width of the generated excitation light is 943.3 ps.

6.1 Electron transfer from the excited QDs to sputtered ZnO film (or RIE etched NWs)

Electron transfer from the excited QDs to sputtered ZnO film (or RIE etched NWs) was studied using time-resolved spectroscopic measurements. The quenching in PL decay lifetime of ZnO film (or NWs)/QD structure with respect to a control sample (QD/glass) is an indication of electron transfer from QDs to Sputtered ZnO film (or RIE etched NWs) with characteristic time constant τ_{eT} (see Figure 6.3(a)). At fast excitation rates (which is a function of QD absorption cross section and the pump pulse repetition rate), the second exciton (pulse) is produced before the resulting electron-hole recombines (see Figure 6.3(b)). This phenomena result in creation of positively charged excitons (a positive trion) (see Figure 6.4(c)). This trion result in additional quenching in PL decay lifetime spectra due to non-radiative Auger recombination process which can be confused with that of true electron transfer. Trion decays via the Auger process occurs very fast (in picosecond time range) which is unlikely to be interfere with the slow relaxation lifetimes (in nanosecond range) we are detecting with our system. The slow decay lifetime components presenting here are attributed to the electron transfer.

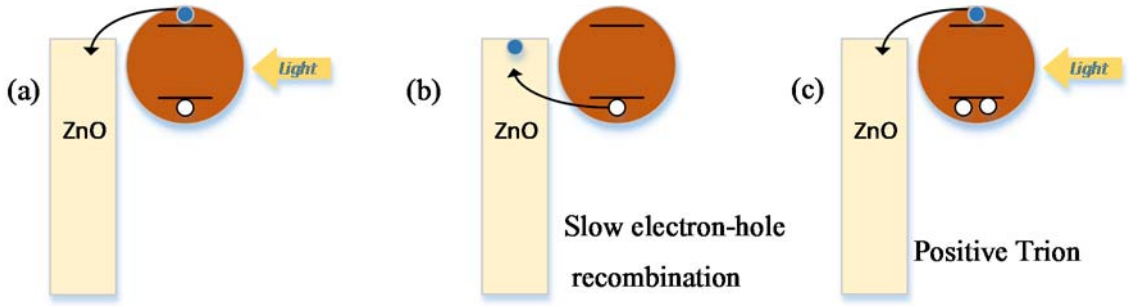

Figure 6.3: (a) Electron transfer from excited QDs to the ZnO film (or NWs), (b) remaining hole in QDs when electron-hole recombination is slow compared to the excitation rate, (c) generation of positively charged exciton (a positive trion) when the next photon is absorbed.

The decay lifetime quenching via electron transfer was studied and compared at the interface of ZnO film/QD and ZnO NW/QD structures with respect to a control sample. The results of this study for three different CdSe QDs with oleic acid (OA) ligand and emissions at 460 nm (QD 460), 540 nm (QD 540)), and 580nm (QD 580) are presented in Figure 6.4(a-c) respectively. The results indicate that the electron transfer is more pronounced in ZnO NW/QD structures. Higher degree of quenching was achieved in structures with QD 460 and QD 580.

6.2 Hole transfer from the excited QDs to MoO_3 film

To study the hole transfer, the PL decay at the interface of QD and MoO_3 hole transport layer (QD/MoO_3 structures) was studied. Figure 6.5(a), (b) show the PL decay in such structure prepared using QD 540 and QD 580 respectively. Quenching in PL decay of QD/MoO_3 structure with respect to a control sample can be attributed to hole transfer from QD layer to MoO_3 hole transport layer. The results also demonstrate that the transfer rate is size dependent.

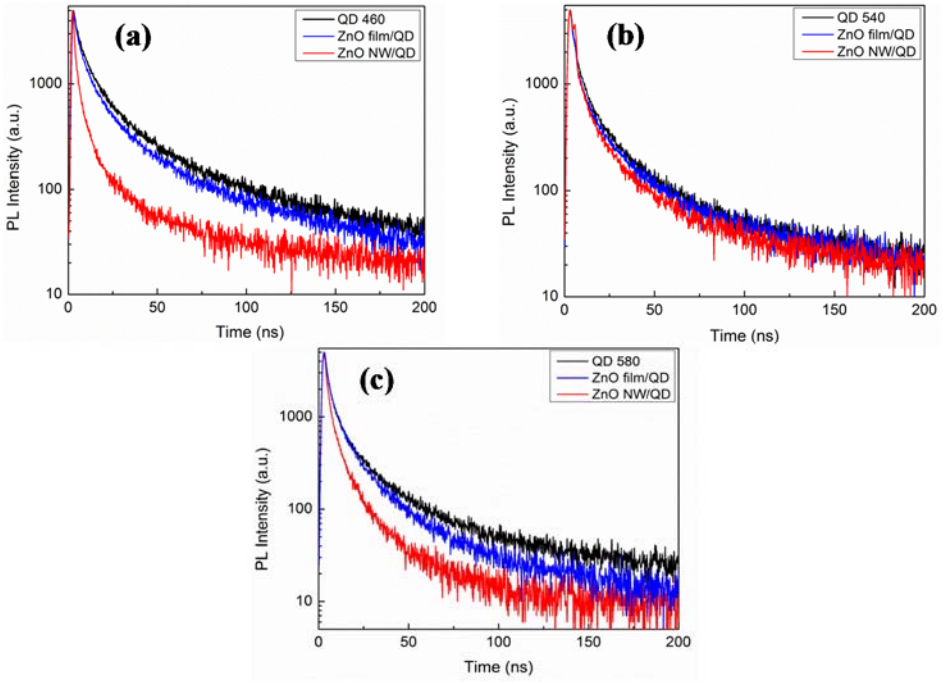

Figure 6.4: PL decay (electron transfer) in sputtered ZnO film/QD and RIE etched ZnO NW/QD structures for (a) QD 460, (b) QD 540, and (c) QD 580. CdSe QDs with OA ligand were used.

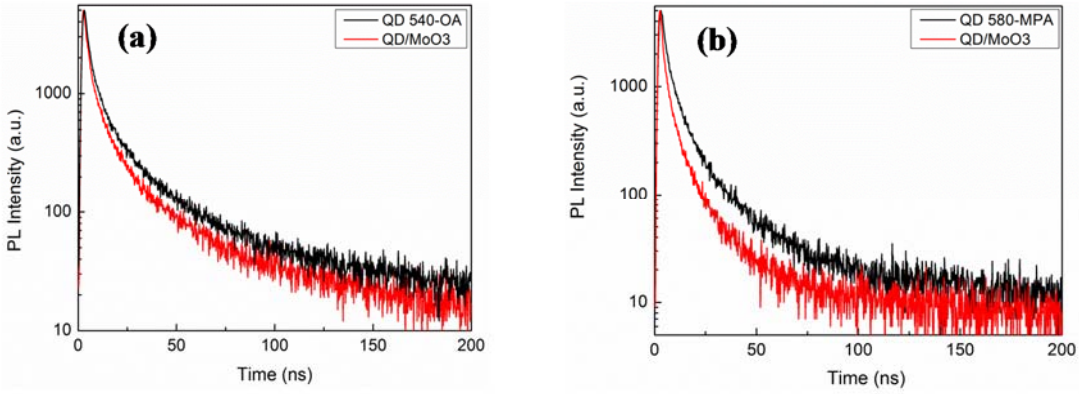

Figure 6.5: PL decay (hole transfer) in QD-film/MoO_3 structure for (a) QD 540, and (b) QD 580. CdSe QDs with OA ligand were used.

6.3 Electron and hole transfer in sputtered ZnO film (or RIE etched NWs)/QD/MoO_3 structures: true electron transfer

As discussed earlier, Auger recombination due to creation of trions happens in ZnO film (or NWs)/QD system. Although the limitation in our measurement set up wouldn't allow to detect the Auger process and its related time constant, in order to eliminate any possibility for confusion of the electron transfer with this non-radiative process, decay in sputtered ZnO film (or RIE etched NWs)/QD/MoO_3 structures was studied. In this structure, the created holes via excitation of QDs with the first pulse rapidly removed from the QDs and transfer to MoO_3 layer. The next pulse only excites the neutral QDs; as a result the decay of excitons can be attributed to the true electron transfer with no contribution of other non-radiative recombination pathways In this case, the measurement yields the true electron transfer time constant (τ_{eT}) (See Figure 6.6).

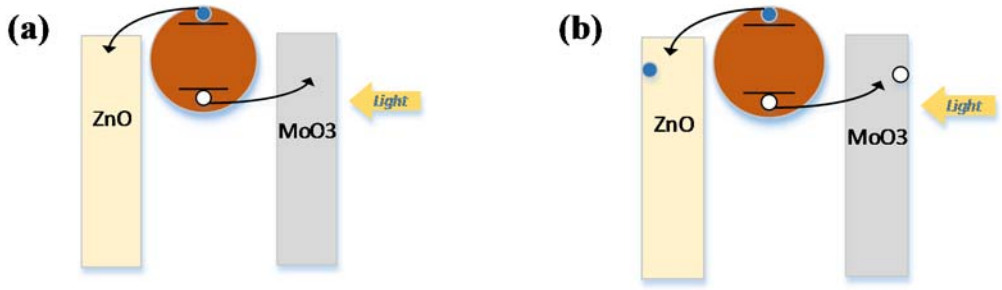

Figure 6.6: True electron transfer from excited QDs to the ZnO film (or NWs) in ZnO film (or NWs)/QD/MoO_3 system. (a) The hole rapidly removed from the QD with the help of MoO_3 hole transport layer, (b) the next absorbed photon excites a neutral exciton.

Figure 6.7(a), (b) compares PL decays corresponded to electron, hole and (electron+hole) transfers in ZnO film/QD, QD/MoO_3, and ZnO film/QD/MoO_3 structures for QD 580 and QD 540 with OA ligand, respectively. Carrier transfer time constants extracted from multi-exponential tail fitting analysis in ZnO film/QD, QD/MoO_3, and ZnO film/QD/MoO_3 structures and their corresponded average lifetimes are reported in Table 6-1, Table 6-2 for QD 580 and QD 540 respectively. The average lifetime was calculated from the equation (6–1). Transfer rates can be calculated from equation (6–2). Lifetime histograms, obtained from multi-exponential and distribution tail fitting analyses for these structures, are also shown in Figure 6.8 for QD 580 and Figure 8 for QD 580.

$$< \tau >= \frac{\sum_{i=1}^{4} \beta \tau_i^2}{\sum_{i=1}^{4} \beta \tau_i} \qquad (6\text{–}1)$$

$$k = \frac{1}{< \tau_{sample} >} - \frac{1}{< \tau_{control} >} \qquad (6\text{–}2)$$

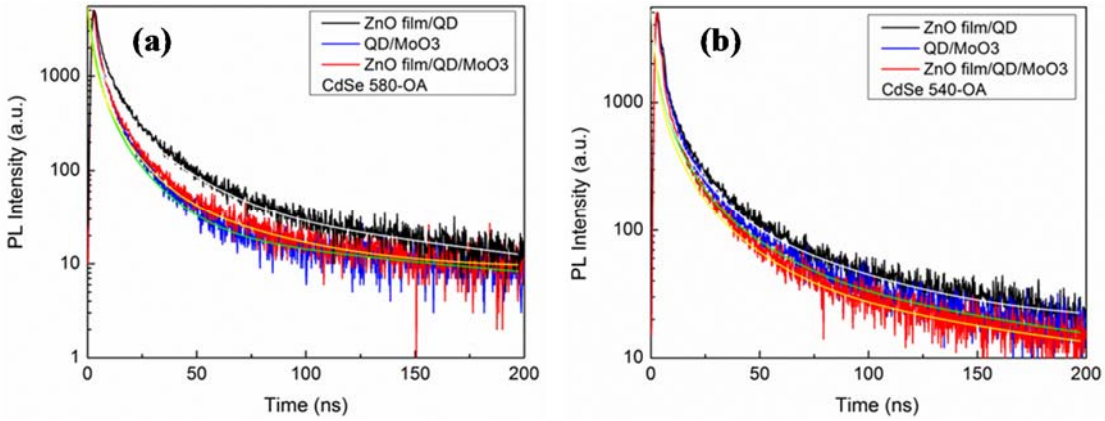

Figure 6.7: PL decays in (a) QD 580 nm, (b) QD 540 nm with OA ligands, due to electron, hole and true electron transfer in sputtered ZnO film/QD, QD/MoO_3 and sputtered ZnO film/QD/MoO_3 structures.

Table 6-1: Carrier transfer time constants extracted from multi-exponential tail fitting analysis for QD 580 in sputtered ZnO film/QD, QD/MoO_3 and ZnO film/QD/MoO_3 structures.

QD 580-OA	B_1	τ_1 (ns)	B_2	τ_2(ns)	B_3	τ_3(ns)	B_4	τ_4(ns)	χ^2	$<\tau>$(ns)
ZnO film/QD	3663.8875	1.976	1584.5173	7.040	525.1083	21.989	46.3040	196.723	1.181	54.8
QD/MoO3	4007.2131	1.750	1524.9570	5.176	393.2932	15.352	22.3613	145.522	1.149	25.6
ZnO film/QD/MoO3	3372.9355	1.250	1668.7786	3.603	728.3242	10.781	88.7389	41.328	1.305	12.1

B: Pre-exponential factor, τ (ns): PL decay lifetime component, χ2: Fit quality was assessed by χ2<1.3, <τ> (ns): Average lifetime.

In Figure 6.7 (a) more quenching in QD/MoO_3 with respect to ZnO film/QD demonstrates that the hole transfer rate in QD 580 is higher (shorter average lifetime) than the electron transfer rate (longer average lifetime). Charged excitons might be the reason for this extra quenching. In ZnO film/QD/MoO_3 structure, neutral excitons produce the true electron transfer time constant (τ_{eT}) (see Table 6-1and Figure 6.8).

As shown in Figure 6.7 (b), the closer rate of electron and hole transfer in ZnO film/QD and QD/MoO_3 structures, when QD 540 were used, provides an efficient true electron transfer (reduced transfer time constant) in ZnO film/QD/MoO_3 structure (see Table 6-2 and Figure 6.9). The larger QD LUMO offset with ZnO CB, in QD 540 as compared to QD 580, likely provides comparable electron and hole transfer rates to ZnO film and MoO_3 respectively (Figure 6.11 (a)).

In RIE etched ZnO NW/QD/MoO_3 structure, there is a chance for the excited electrons to trap in surface trap sites at the interface of ZnO NW/QDs, which causes a non-efficient transfer process. In QDs with OA-ligand, this effect is more pronounced for bigger size QDs (QD580) with low LUMO level (see Figure 6.10 (a) and Figure 6.11 (b)). Transfer process is more efficient in smaller size QDs (QD540) when the band offset between QD LUMO level and from ZnO NW CB is larger (see Figure 6.10 (b) and Figure 6.11 (b)).

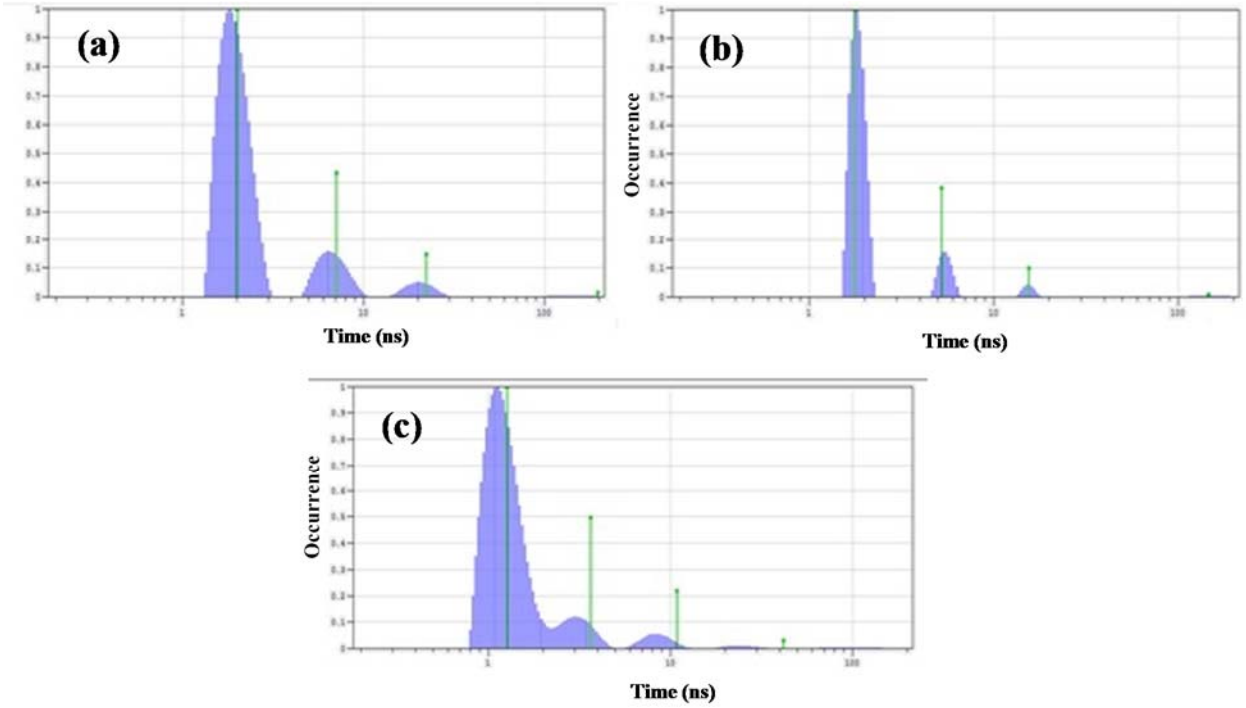

Figure 6.8: Lifetime histograms obtained from multi-exponential (green lines) and distribution fitting analyses (Gaussian tails) for QD 580 in (a) sputtered ZnO film/QD, (b) QD/MoO_3 and (c) sputtered ZnO film/QD/MoO_3 structures.

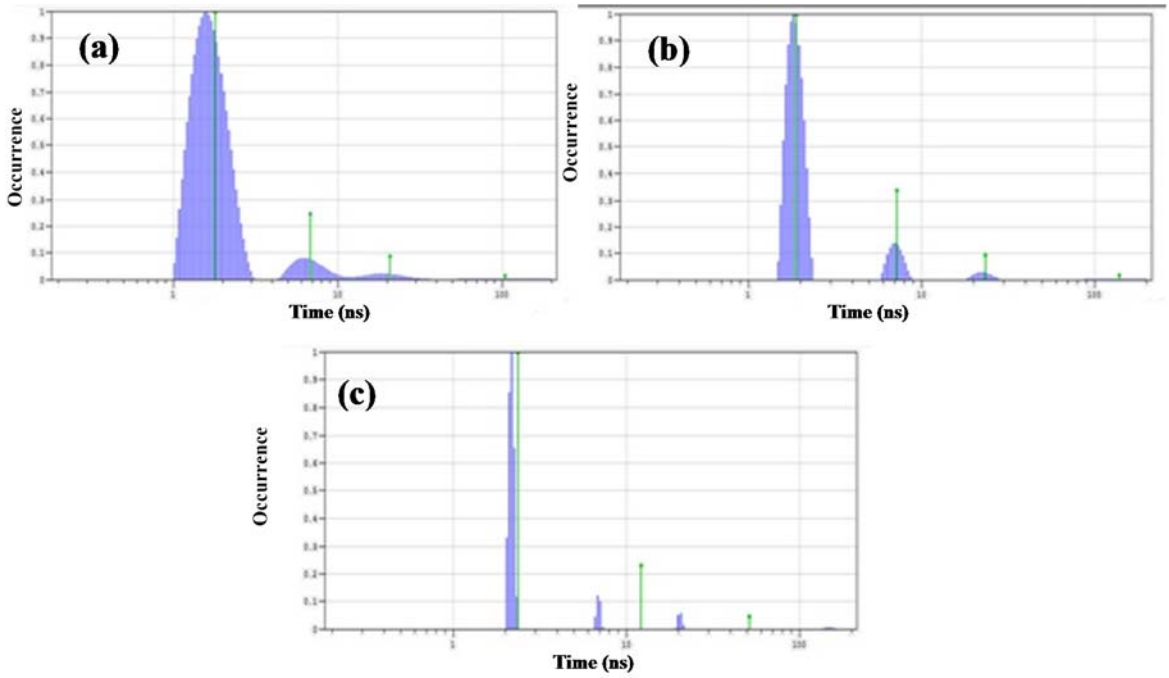

Figure 6.9: Lifetime histograms obtained from multi-exponential (green lines) and distribution fitting analyses (Gaussian tails) for QD 540 in (a) sputtered ZnO film/QD, (b) QD/MoO_3 and (c) sputtered ZnO film/QD/MoO_3 structures.

Table 6-2: Carrier transfer time constants extracted from multi-exponential tail fitting analysis for QD 540 in sputtered ZnO film/QD, QD/MoO_3 and ZnO film/QD/MoO_3 structures.

QD 540-OA	B_1	τ_1 (ns)	B_2	τ_2(ns)	B_3	τ_3(ns)	B_4	τ_4(ns)	χ^2	$<\tau>$(ns)
ZnO film/QD	4223.9604	2.337	967.2195	12.051	185.0825	50.962	-	-	1.315	32.8
QD/MoO3	3922.9165	1.859	1323.3571	7.117	360.5189	23.219	52.4820	138.069	1.108	39.5
ZnO film/QD/MoO3	4238.5054	1.768	1026.4418	6.728	357.7357	20.539	47.6998	103.576	1.169	27.1

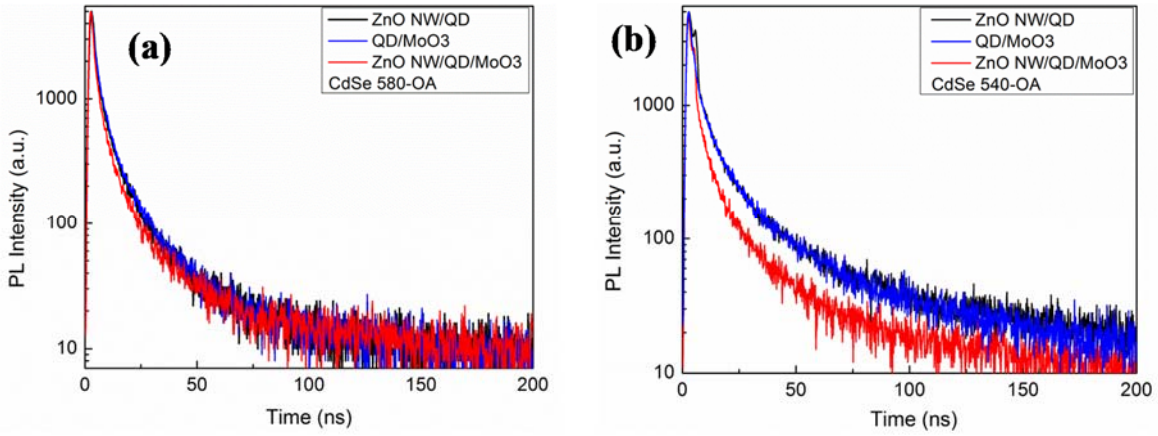

Figure 6.10: Decays in (a) QD 580nm, (b) QD 540nm with OA ligands, due to electron, hole and true electron transfer in RIE etched ZnO NW/QD, QD/MoO_3 and RIE etched ZnO NW/QD/MoO_3 structures.

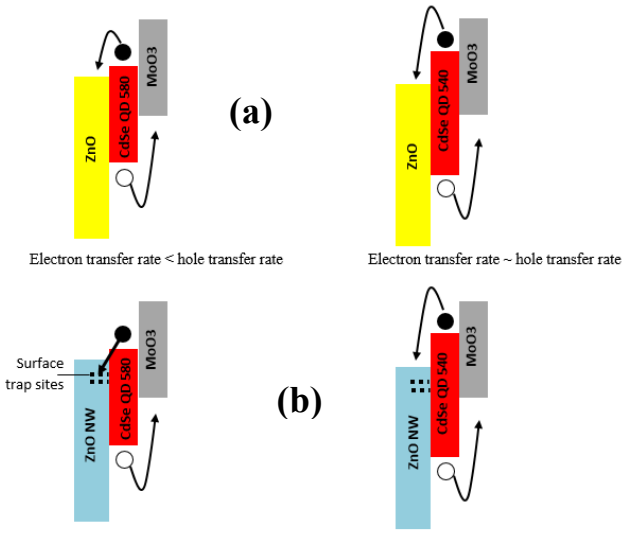

Figure 6.11: Conceptual band diagrams in a) ZnO film/QD/MoO_3, b) ZnO NW/QD540/MoO_3 for two QD sizes (QD 580 and QD 540).

For QD 540 with OA ligand more decay quenching and reduced transfer time constants observed in the ZnO NW/QD/MoO_3 with respect to ZnO film/QD/MoO_3 structure. Results are presented in Figure 6.12 and Table 6-3. This is an indication of higher electron transfer rate in structures with NWs

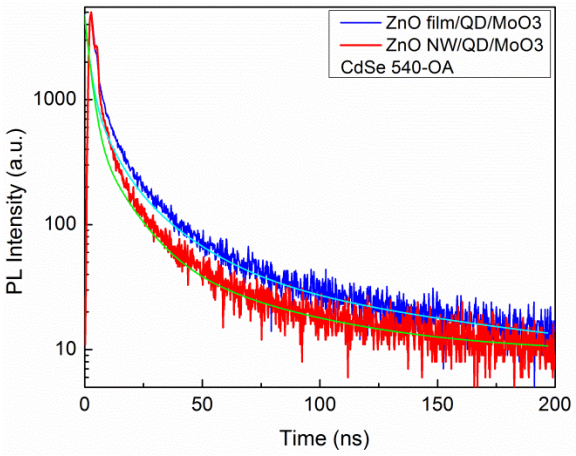

Figure 6.12: Electron transfer in sputtered ZnO film/QD/MoO_3 and RIE etched ZnO NW/QD/MoO_3. QD 540 with OA ligand was used.

Table 6-3: Electron transfer time constants extracted from multi-exponential tail fitting analysis for sputtered ZnO film/QD 540/MoO_3 and RIE etched ZnO NWQD 540/MoO_3 structures.

QD 540-OA	B_1	τ_1 (ns)	B_2	τ_2(ns)	B_3	τ_3(ns)	B_4	τ_4(ns)	χ^2	$<\tau>$(ns)
ZnO film/QD/MoO3	4238.5054	1.768	1026.4418	6.728	357.7357	20.539	47.6998	103.576	1.169	27.1
ZnO NW/QD/MoO3	480.2749	2.975	4542.2700	2.975	675.5540	15.702	81.2160	75.229	3.680	21.2

6.4 Effect of size on electron transfer efficiency

The transfer efficiency between QDs and sputtered ZnO film (or RIE etched NWs) can be enhanced by selecting appropriate size for QD. In the ZnO film/QD structure when QD with OA ligand was used, the transfer rate decrease as the QD size decreases (see Figure 6.13 (a)). In ZnO NW/QD structure the highest quenching observed for QDs with smallest size (QD 460) (see Figure 6.13 (b)).

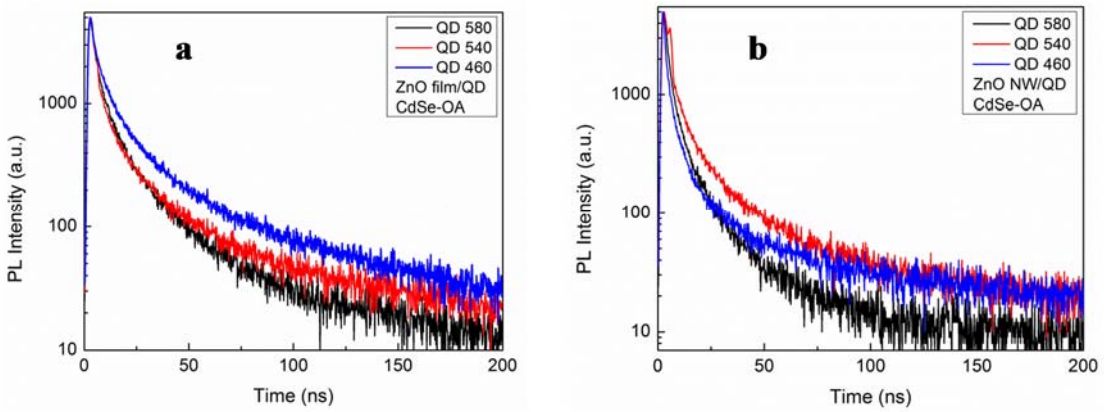

Figure 6.13: Electron transfer in (a) sputtered ZnO film/QD and (b) RIE etched ZnO NWs/QD structures for different size QDs. QDs with OA ligand was used.

6.5 Effect of ligand on electron transfer efficiency

Figure 6.14 demonstrate that the electron transfer is more effective in RIE etched ZnO NW/QD/MoO_3 structure than sputtered ZnO film/QD/MoO_3 when QD 580 with ethanedithiol (EDT) ligand was used. The true electron transfer is more pronounced in ZnO NW/QD/MoO_3 structure formed with EDT-ligated QDs with respect to the same structure formed with OA-ligated QDs describing that the type of ligand plays a major role for an effective transfer process (see Figure 6.14 (b) and Figure 6.10 (a)).

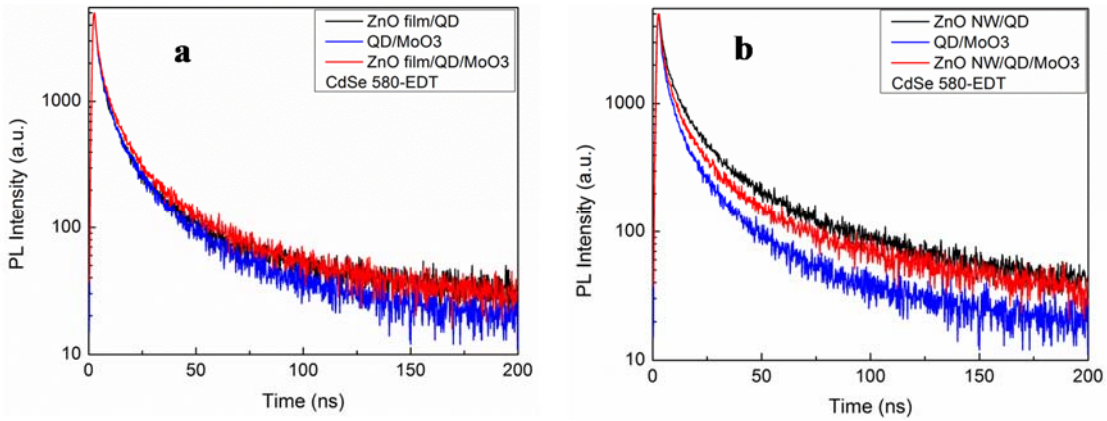

Figure 6.14: PL decays in QD 580nm with EDT ligand, due to electron, hole and true electron transfer in (a) sputtered ZnO film/QD/MoO_3 and RIE etched ZnO NW/QD/MoO_3 structures.

Selection of appropriate ligand is a key to engineer the sputtered ZnO film (or RIE etched NWs)/QD interface for achieving effective attachment of QDs onto the sputtered ZnO film (or RIE etched NWs) as well as operational band alignment between the two materials. Organic compounds of the ligands provide a potential barrier for the carriers to transfer from the QD layer to the adjacent ZnO film (or NWs). As a result using QDs with short ligands is required for efficient transfer.

Effects of different ligands on carrier transfer in ZnO film/QD/MoO_3 and ZnO NW/QD/MoO_3 structures were studied for QD 580 and results are presented in Figure 6.15 (a), (b) respectively. The electron transfer time constants for ZnO film/QD/MoO_3 and ZnO NWs/QD/MoO_3 structures are reported in Table 6-4 and Table 6-5 respectively. Hydrophobic long octadecylamine (ODA), medium size OA and short EDT ligands as well as short hydrophilic mercaptopropionic acid (MPA) ligands were used for this study (See Figure 6.16 (a)). The relatively high lifetime quenching with high electron transfer rate (reduced electron transfer time constant) was detected where QD with MPA ligand was attached onto the ZnO films and NWs. MPA is considered as a polar ligand and expectedly should make a strong bond with the hydrophilic surface of the ZnO film (or NWs) (see Figure 6.16 (b)). The high electron transfer rate in this structure can also be attributed to the effective band alignment between ZnO and MPA-ligated QDs [33]. The short length of MPA ligand also reduces the potential barrier at the ZnO film (or NWs)/QD interface. The electron transfer in QDs with OA and EDT ligands are considerable as well. However, the QDs with long ODA ligands are not showing an effective transfer.

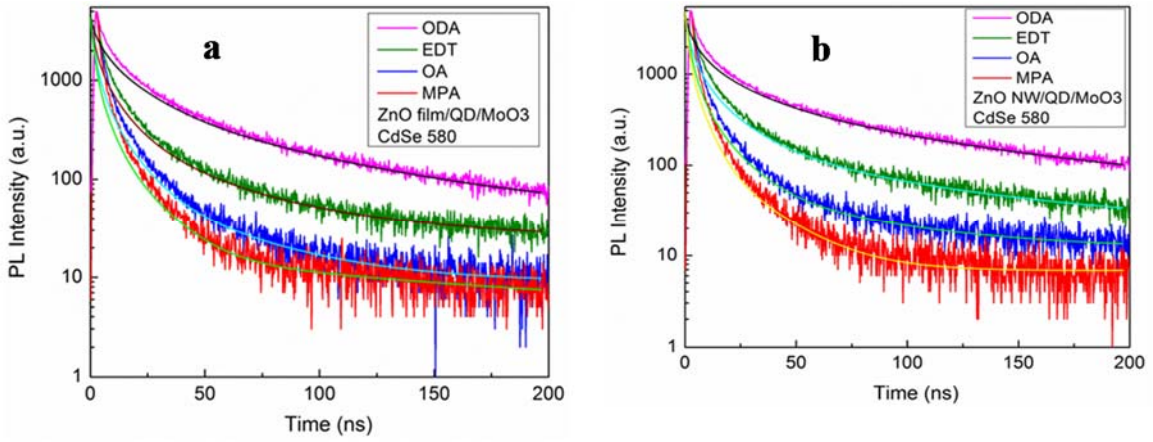

Figure 6.15: Effect of different QD ligands on electron transfer in (a) sputtered ZnO film/QD/MoO_3 and (b) RIE etched ZnO NW/QD/MoO_3 structures. QD 580 was used.

Table 6-4: Electron transfer time constants extracted from multi-exponential tail fitting analysis in sputtered ZnO film/QD/MoO_3 structure using QD 580 with different ligands.

ZnO film/QD580/MoO3	B_1	τ_1 (ns)	B_2	τ_2(ns)	B_3	τ_3(ns)	B_4	τ_4(ns)	χ^2	$<\tau>$(ns)
ODA	1681.6320	1.160	1721.6305	4.719	1505.3551	16.894	548.8305	67.957	1.037	41.3
EDT	3440.3533	1.485	1682.3253	6.485	484.7012	19.926	117.9139	64.184	1.125	22.8
OA	3372.9355	1.250	1668.7786	3.603	728.3242	10.781	88.7389	41.328	1.305	12.1
MPA	25531.6016	1.299	2580.3	4.087	481.6097	13.314	16.2763	97.365	1.163	6.3

Table 6-5: Electron transfer time constants extracted from multi-exponential tail fitting analysis in RIE etched ZnO NW/QD/MoO_3 structure using QD 580 with different ligands.

ZnO NW/QD 580/MoO3	B_1	τ_1 (ns)	B_2	τ_2(ns)	B_3	τ_3(ns)	B_4	τ_4(ns)	χ^2	$<\tau>$(ns)
ODA	1979.2932	1.273	1715.8801	5.252	1174.5419	18.739	537.2963	81.153	0.990	51.9
EDT	2848.3760	1.242	1730.8693	4.787	862.9648	15.722	166.0277	72.769	1.111	30.3
OA	4899.0273	1.509	1129.7659	6.405	110.9104	28.234	-	-	1.412	8.99
MPA	5006.5000	1.223	1170.6306	4.925	134.1551	18.822	-	-	1.453	5.79

Figure 6.17 (a), (b) shows the effectiveness of short polar MPA ligand in decay quenching and electron transfer in ZnO/QD/MoO_3 and ZnO NWs/QD/MoO_3 structures respectively. Figure 6.18 demonstrate that the long non-polar ODA ligands results in minimal quenching in decay and poor transfer efficiency.

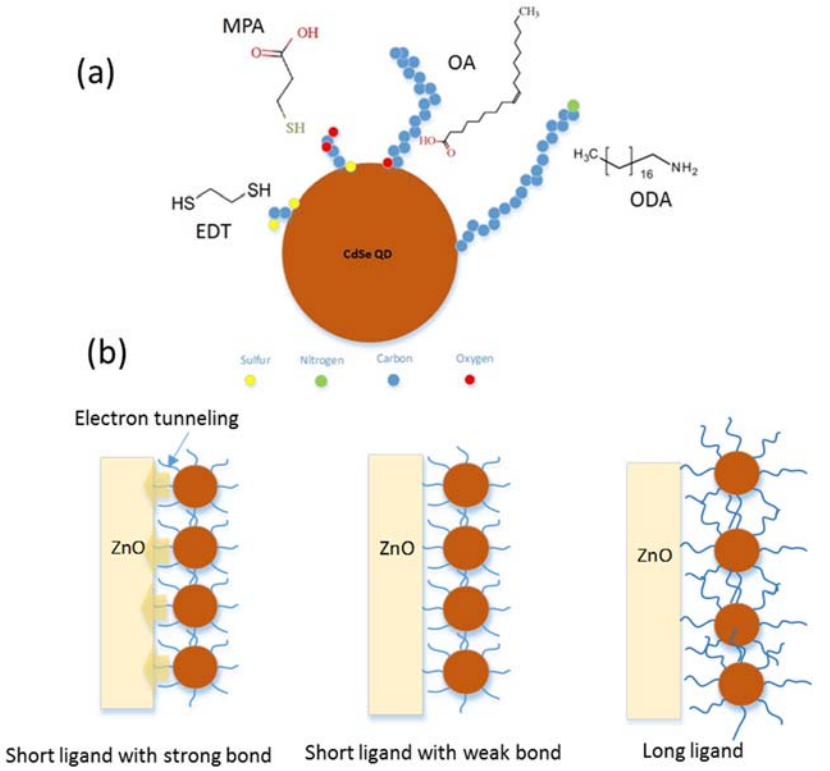

Figure 6.16: Conceptual diagram showing a) QD with different ligand lengths, b) degree of attachment of QDs to ZnO film (or NWs) depending on creation of strong or weak bonds.

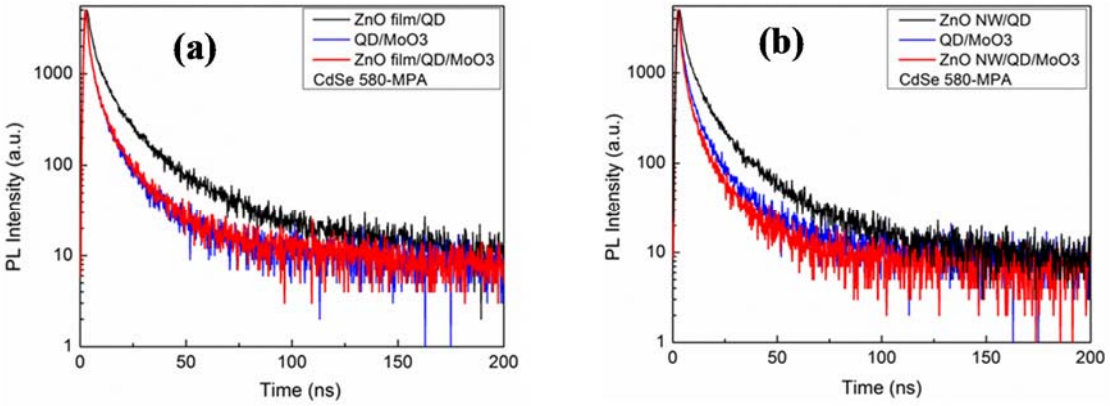

Figure 6.17: PL decays in QD 580nm with MPA ligand, due to electron, hole and true electron transfer in (a) Sputtered ZnO film/QD/MoO_3 and RIE etched ZnO NW/QD/MoO_3 structures.

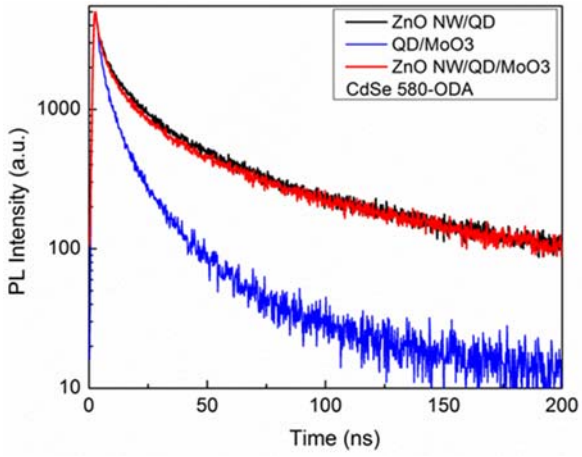

Figure 6.18: PL decays in QD 580nm with ODA ligand, due to electron, hole and true electron transfer in RIE etched ZnO NW/QD/MoO_3 structures.

6.6 Summary

Electron and hole transfer at the interface of sputtered ZnO film (or RIE etched NWs)/QD and QD/MoO_3 structures were studied. When the generated electron hole recombination is slow in comparison to transfer rate, the electron transfer can be confused with non-radiative Auger process. True electron transfer in a neutral exciton were measured when the hole extracted from the QDs by the help of MoO_3 layer in ZnO/CQD/MoO_3 structure. Effect of QD size and ligand on electron transfer in such structure were also explored. The most effective electron transfer was observed for QDs having large band offset relative to conduction band of ZnO. The short polar ligand also result in highest decay quenching with reduced electron transfer time constant indicating efficient transfer rate.

Chapter 7
Design concepts and theoretical analysis of QD-film and QD-film/ZnO heterojunction

QD-films are still a fairly new concept in condensed matter. There is a lack of fundamental knowledge and physical framework to describe the behavior of QD-films. The relationship between the properties of QD-films' building blocks (CQDs), such as quantum yield, band gap, size, geometry and properties of ligands; and their physical properties are not fully understood and yet to be quantified. Improving the performance of electronic devices that incorporate QD-film requires more knowledge and physical frameworks. In this section, we elucidate the properties of CQDs that affect the properties of QD-film. We also qualitatively describe the effect of CQDs properties on the properties of QD-semiconductor heterojunction diode.

7.1 Carrier transport models for quantum dot films

Charge carrier transport mechanisms in nanocrystal solids are not yet fully understood. The physical descriptions developed to formulate carrier transport in bulk materials are not directly applicable to quantum dot thin films. The effects of localized energy states, nanoparticle inter-spacing, quantum confinement effects and organic/inorganic passivation layers (ligand/shell) in charge transport need further investigation. In QD-films, charge transport is often viewed as a sequence of interparticle carrier transport between localized energy states of neighboring quantum dots. In this type of material, charge carrier transport is generally described by the mechanisms such as hopping, tunnelling and band-like transport. The mechanisms are investigated in detail below:

7.1.1 Hopping transport mechanism in quantum dot solids

Hopping is a thermally activated mechanism. In hopping mechanism, charge carriers gain enough thermal energy from the environment to jump over the potential energy barrier and go to energy states/trap states in a neighboring nanoparticle. Variations in nanoparticle size distribution, disturbs the alignment between energy states of neighboring nanoparticles. These alignments are desirable for charge transport (Figure 7.1(a), (b)). The conductivity in temperature-dependent hopping mechanism is described by [157, 158]:

$$\sigma = \sigma_0 \exp\left(-\left({}^{T_0}/_{T}\right)^{p}\right) \qquad (7\text{–}1)$$

Where σ_0 is temperature independent pre-exponential factor and T_0 is the activation temperature. Activation temperature depends on nanoparticle spacing and the dielectric constant of the spacer material (ligand).

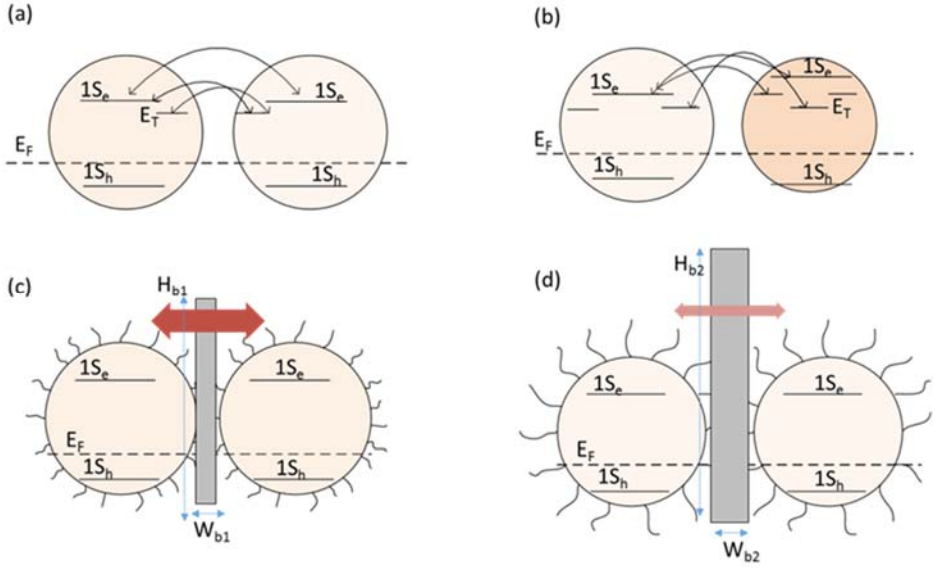

Figure 7.1: (a) Transport mechanism based on hopping of carriers for equal-sized particles. (b) Variation in CQD size distribution produces misalignment between energy states. The smaller the QD, the higher the trap density. Carriers can also hop to trap states and recombine with oppositely charged carriers. (c) Tunnelling between neighboring nanoparticles with shorter ligands, narrower interparticle spacing and shorter barrier height (H_{b1}). (d) Tunnelling between neighboring QDs with longer ligands and wider interparticle spacing. The probability of tunnelling (red double arrows) increases for narrower barrier widths and shorter barrier heights.

7.1.2 Tunnelling transport mechanism in quantum dot solids

Tunnelling is a quantum mechanical phenomena that explains the passage of carriers through thin energy barriers. Tunnelling is a temperature independent mechanism. The tunnelling efficiency or transmission coefficient ($0 < \tau < 1$) is associated with the geometry of the barrier, including its height, shape and width (Figure 7.1(c), (d)). For a rectangular barrier with height (H_b) and width (W_b), tunnelling efficiency is given by [159, 160]:

$$\tau \sim \exp\left(-\frac{2W_b}{\hbar}\sqrt{2m_c H_b}\right) \qquad (7\text{–}2)$$

Where $\hbar$ is the reduced Planks constant and m_c is the mass of carrier. Here, there is an assumption of the presence of an empty energy state behind the potential barrier, which has an energy level that matches the charge carrier's initial energy level. Variations in nanoparticle size distribution induces misalignments in the energy levels of two neighboring nanoparticles. In such case, more complicated considerations are required.

7.1.3 Band-like transport mechanism in quantum dot solids

There have been some reports on the observation of band-like transport mechanism in ordered, densely packed arrays of nanocrystals [161]. The possibility of band-like transport in QD-films is attributed to the formation of conduction and valence bands (or mini-bands). These mini-bands are formed in QD-films with narrow interparticle spacing (see Figure 7.2).

Mobility in densely packed QDs with band-like transport can be related to particle size and interparticle spacing. Using equations (18-21) in reference [162] mobility can be related to the centre to centre distance (b) and the diameter of the QDs ($2a$) by the following equation:

$$\mu \propto \left(\frac{b}{2a}\right)^{\frac{11}{2}} \sqrt{\frac{U_0}{K_B T}} \qquad (7\text{–}3)$$

Where U_0 is the depth of the potential and K_B is Boltzman constant. Depth of the potential (U_0) is determined by the properties of the ligand.

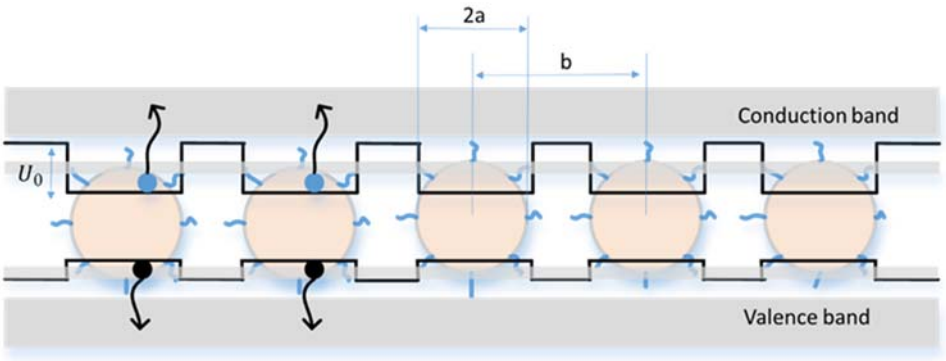

Figure 7.2: Band like transport in densely packed ordered array of QDs (QD-film).

7.2 Photoluminescence and quantum yield of conductive quantum dot films

At room temperature, carrier transport in QD-film is dominated either by hopping or band-like transport. Conversely, at low temperatures, carrier transport is dominated by temperature independent tunneling. Variations in size distribution of CQDs, adversely affects the transport mechanism. Broadening of photoluminescence spectra is an indication of inhomogeneous size distribution. Full width half maximum (FWHM) of photoluminescence spectra (PL) of quantum dots in solution is a good representation of size distribution. Narrower FWHM, indicates more homogeneity in the size distribution of CQD solution. Hence,

CQD solutions with narrower FWHM are favorable for device applications and formation of highly conductive QD-film.

As highlighted in chapter 2, size distribution of CQDs is determined during the "size focusing" step in the synthesis process. Narrow FWHM in the PL emission can be achieved by terminating the process during "size focusing" step. More homogeneous size distribution of CQDs requires analytical centrifuging.

Photoluminescence quantum yield (PLQY) can be defined as the ratio of radiative recombination over all of the recombination:

$$PLQY(T) = \frac{K_{RR}}{K_{RR} + \sum K_{NR}} \qquad (7–4)$$

Where K_{RR} represents radiative recombination rate and $\sum K_{NR}$ represents the sum of all other non-radiative recombination rates.

PLQY is used to assess the quality of CQDs in solution. PLQY is higher for CQDs with longer ligands; because the non-radiative recombination centres are better passivated in CQDs with longer ligands. However, longer length ligands are not charge carrier transport-compatible and often yield rather nonconductive QD-film. The PLQY of solid phase quantum films built using short ligand QDs, is lower than the PLQY of their CQDs building blocks monodispersed in solution [163]. In QD-films made of short ligand-CQDs, the charge carriers can hop or tunnel to neighboring nanocrystals. If the QDs are densely packed, mini-bands are formed and charge carriers can be transported to neighboring particle through band-like transport. These transported charge carriers can undergo non-radiative recombination, hence quenching the photoluminescence of the film. The quenching is higher in more conductive quantum films. In this regard, a decrease in PLQY of CQDs from solution to solid phase can be considered as an indirect sign of a more conductive QD-film.

7.3 Uncovering parameters affecting operation of QD-semiconductor heterojunction

Figure 7.4 (a), shows a typical representation of the heterojunction diode between QD-film and ZnO thin film. Two distinct regions are distinguished:

1- Quantum dots in the interface of ZnO and QD-film and interface of MoO_3 and QD-film

2- Quantum dots in space charge region

The following subsections elaborate on the role of each region in determining the operation and performance of the CQD heterojunction device.

7.3.1 Quantum dots in the interface of ZnO-QD film and MoO_3-QD film: carrier transfer dynamics

Carrier transfer in the heterojunction between two bulk materials, is very fast. Carrier transfer is much slower at the interface of CQDs and other semiconductors.

At the CQD-ZnO heterojunction, charge carriers (electrons) in the quantum dots transfer to the conduction band of ZnO. At the CQD-MoO_3 interface, charge carriers (holes) transfer to the valence band of MoO_3.

Higher rates of carrier transfer translates to lower resistance ($R_{S\text{-interface}}$). Carrier transfer dynamics between CQDs and semiconductor interface is usually assessed by using the time resolved photoluminescence (TRPL) method (chapter 6).Two examples of measured carrier transfer, that were described in detail in chapter 6, at the interface of CQD- sputtered ZnO film (or RIE etched NWs) and CQD-MoO_3 corresponding to electron and hole transfer are shown in Figure 7.3. For easiness these figures are reproduced from chapter 6.

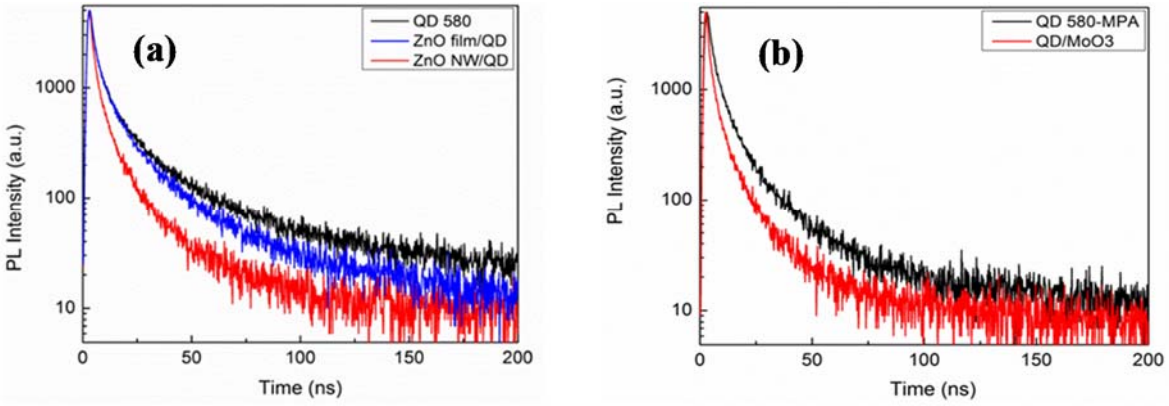

Figure 7.3: PL decay in (a) CQD-sputtered ZnO film and RIE etched ZnO NWs, (b) CQD-MoO_3.

The difference between the energy bands of two materials plays an important role in determining charge carrier transfer rate. For instance, the higher the energy difference between the LUMO ($1S_e$) of QD and the conduction energy band of ZnO, the higher the carrier transfer rate at the ZnO/QD-film interface (Figure 7.5). This difference is controlled by the differences in the electron affinities of the ZnO and CQD film. The electron affinity of CQDs is affected by variety of factors such as passivation (inorganic and organic

passivation), quantum dots sizes and surface properties. The charge transfer rate is also affected by the spacing between CQDs and ZnO surface, which is often determined by ligand length.

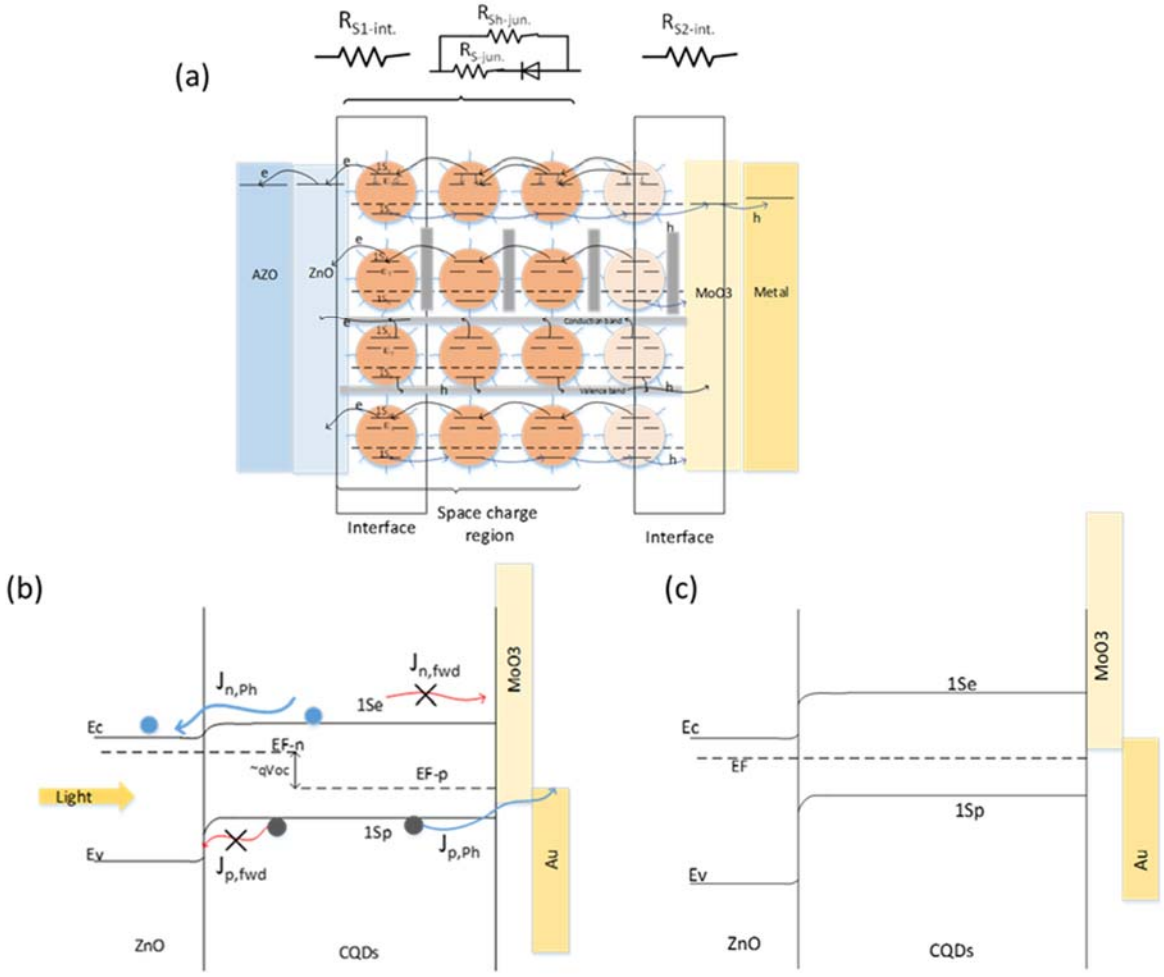

Figure 7.4: (a) Two different regions in the quantum dot-ZnO heterojunction. The effect of carrier transfer rate is modeled as $R_{S\text{-interface}}$. Different carrier transport mechanisms are depicted in the schematic (hopping, tunneling and band like transport). The behavior of the CQD-ZnO heterojunction diode can be modeled by Schottky diode equation. (b) Qualitative energy band diagram of CQD heterojunction under photovoltaic operation at voltages close to open circuit voltage ($V \sim V_{OC}$). $E_{F\text{-}n}$ and $E_{F\text{-}P}$ represent the electron and hole quasi-fermi levels, E_C and E_V are conduction band and valence band edges, $J_{n,Ph}$ and $J_{P,Ph}$ are electron and hole photocurrent. $J_{n,fwd}$ and $J_{P,fwd}$ are electron and hole current in the forward bias direction.(c) Qualitative energy band diagram of CQD heterojunction at equilibrium (zero bias). E_F represents the fermi level.

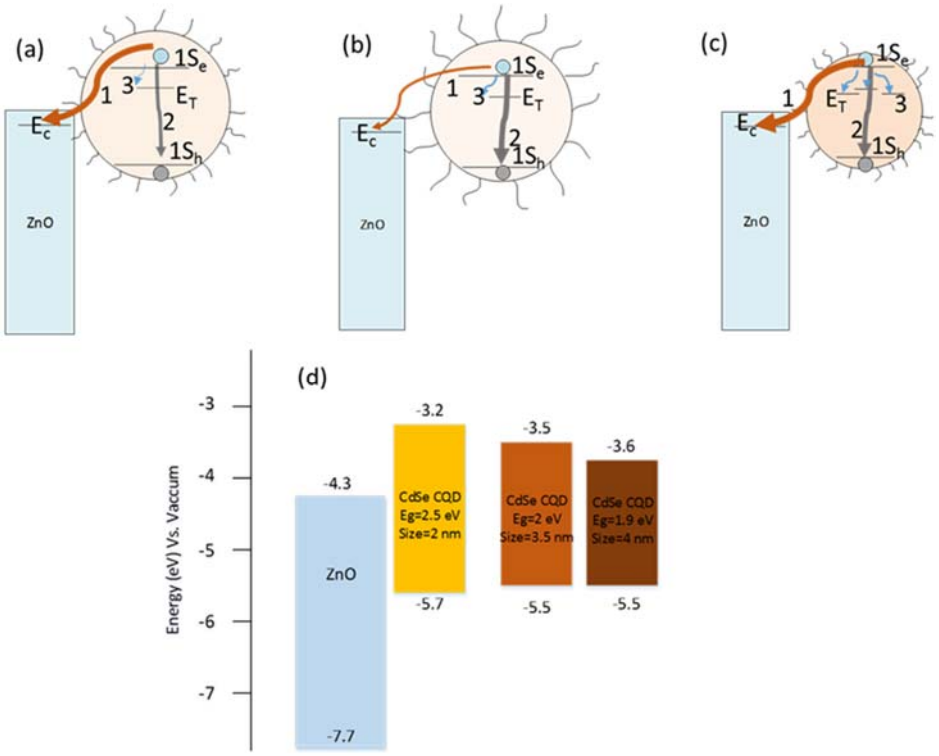

Figure 7.5: Depiction of carrier transfer between CQDs and ZnO. Three competing mechanisms (brown and grey arrows): (1) carrier transfer, (2) self-quenching and recombination with holes, (3) recombination with traps, at QD-ZnO interface. (a) CQD with shorter ligands. The rate of carrier transfer is high. (b) CQDs with longer ligands and longer spacing between QD and ZnO. The carrier transfer rate is lower compared to (a). (c) CQD with smaller size. The energy difference between conduction band of ZnO (E_c) and lowest energy state of electrons ($1S_e$) in QD is higher, therefore the transfer rate is higher. Decreasing the size also increases trap state density and provides alternative recombination routes (blue lines). (d) The effect of size on energy states of CdSe CQDs.

Carrier transfer rate is expected to be higher for short length ligands. However, as described in chapter 2, ligands affect the electron affinity and band gap of the CQDs. The change in the energy difference between $1S_e$ of CQDs and conduction band edge of ZnO caused by ligands, affects the carrier transfer rate in CQDs-ZnO interface. Quantum dots in the space charge region: Schottky diode approximation for quantum dot-semiconductor heterojunction

As described in chapter 6, the QD's electron transfer in a neutral exciton, when the hole is extracted from CQDs by the help of MoO_3 layer in sputtered ZnO/CQD/MoO_3 structure is shown in Figure 7.6. For easiness this figures are reproduced here from chapter 6.

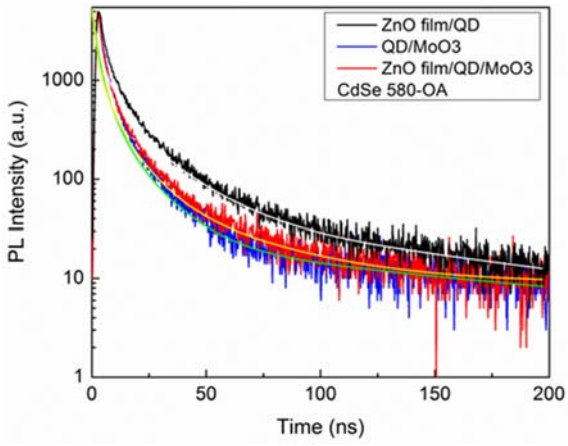

Figure 7.6: PL decay in sputtered ZnO/CQD/MoO_3 structure. The hole is extracted from the QDs by the help of MoO_3.

Effects of CQD size and ligands on electron transfer in RIE etched ZnO NWs/CQD/MoO_3 were also explored as described in chapter 6. In this structure the most effective electron transfer was observed for smaller size CQDs (see Figure 7.7(a)). The MPA short polar ligand also resulted in highest decay quenching with reduced electron transfer time constant indicating the high transfer rate (see Figure 7.7 (b) and Table 7-1). For easiness these figures and the table are reproduced again here from chapter 6.

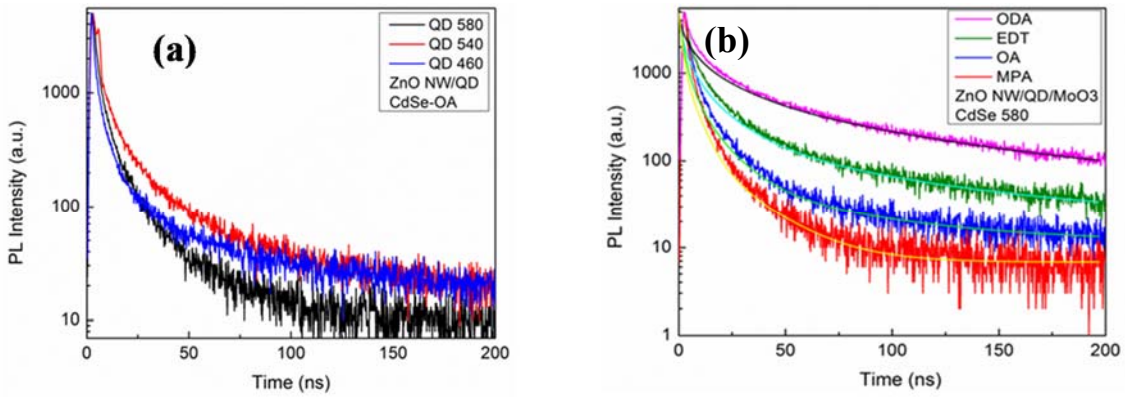

Figure 7.7: PL decays in RIE etched NWs/CQD/MoO_3 structure for CQDs with different (a) sizes and (b) ligands.

Table 7-1: Electron transfer time constants extracted from multi-exponential tail fitting analysis in RIE etched ZnO NWs/CQD/MoO_3 structure using different CQD ligands.

ZnO NW/QD 580/MoO3	B_1	τ_1 (ns)	B_2	τ_2(ns)	B_3	τ_3(ns)	B_4	τ_4(ns)	χ^2	$<\tau>$(ns)
ODA	1979.2932	1.273	1715.8801	5.252	1174.5419	18.739	537.2963	81.153	0.990	51.9
EDT	2848.3760	1.242	1730.8693	4.787	862.9648	15.722	166.0277	72.769	1.111	30.3
OA	4899.0273	1.509	1129.7659	6.405	110.9104	28.234	-	-	1.412	8.99
MPA	5006.5000	1.223	1170.6306	4.925	134.1551	18.822	-	-	1.453	5.79

7.3.2 Quantum dots in the space charge region: Schottky diode approximation for quantum dot-semiconductor heterojunction

At the interface of QD-film and ZnO, space charge region is formed. In the ideal case, the width of the space charge region is larger on the QD-film side than the ZnO side. The diode behavior of this heterojunction can be approximated by the Schottky diode equation:

$$J_D = \frac{R_{ShJunc.}}{R_{SJunc.} + R_{ShJunc.}} \left\{ J_0 \left[exp\left(\frac{e\left(V_D - J_D R_{SJunc.}\right)}{nKT} \right) - 1 \right] \right\} + \frac{V_D}{R_{ShJunc.}} + J_{sc} \qquad (7\text{–}5)$$

Where J_D and V_D represent device current and voltage, $R_{SJunc.}$ and $R_{ShJunc.}$ represent junction series and shunt resistance and n is the ideality factor of the diode. J_0 is the saturation current of the diode and is given by:

$$J_0 = J_{00} T^2 \exp\left(\frac{-E_\mu}{nKT}\right) \qquad (7\text{–}6)$$

In this equation, E_μ is the mobility band gap of free charge carriers and J_{00} is the reduced saturation current.

Three physical models are used to describe current in a Schottky diode (equation (7-5)):

1- Direct band-to-band recombination

2- Trap assisted recombination (based on Schokley-Read-Hall recombination model)

3- Majority carrier emission over the height of the barrier

Experiments show that the QD diode current is controlled by trap-assisted recombination (SRH model) [164]. In this regard, J_D would be:

$$J_D = e \int_0^d U_{SRH}\left(n, p, n_i, N_T, E_T, \beta_n, \beta_p\right) dx \qquad (7\text{–}7)$$

Where n and p are the free electron and hole concentrations, n_i is the intrinsic carrier concentration, N_T is the density of traps, E_T is trap state activation energy and β_n, β_p are capture coefficient of traps for electrons and holes, respectively.

By comparing the solution for equation (7-7) and Schottky diode current in equation (7-5), the reduced current can be related to the capture coefficient of traps (β) and trap density by the following equation [165]:

$$\frac{d\log(J_{00})}{dE_g} = \frac{d\log(\beta)}{dE_g} + \frac{d\log(N_T)}{dE_g} \qquad (7\text{–}8)$$

Experimental reports show that trap state density increases as quantum dot size decreases [165, 166]. So far, there are no established theoritical frame-works to explain this behavior. The increase in trap density associated with reducing the quantum dot size is often related to an increase in truncated crystalline structure and the formation of facets on QDs surfaces.

Capture coefficient of traps is related to carrier mobility (μ) by [165]:

$$\beta \propto \frac{KT}{e}\mu \qquad (7\text{–}9)$$

Experimental results show that carrier mobility in QD-films is dramatically increases by decreasing the size of the nanoparticles [167]. Mobility is also inversly related to the interparticle spacing in QD-films. This is consistant with both hopping transport mechanism and band-like transport mechanism models. Therefore, the capture coefficient of traps (β) increases when the size of quantum dots are decreased. This means that decreasing the size of CQDs increases the reduced saturation current (J_{00}). As a result, the saturation current of the diode (J_0) increases.

On the other hand, reducing the size of CQDs causes trap density to increase. The increase in trap density; decreases shunt resistance ($R_{ShJunc.}$).

In the Schottky diode model, series resistance is inversly related to mobility. Increasing mobility, decreases series resistance. Therefore, it is expected that decreasing the size of quantum dots produces a decrease in series resistance. However, decreasing QD sizes increases the trap density, resulting in increasing the series resistance!

It can be seen that an increase in trap state density occurs with decreasing nanoparticle size (increase of band gap); this compensates for the effects of increaing mobility.

7.4 Summary:

Carrier transport mechanism in QD-film at room temperature is described by hopping and band like transport model. Charge carrier transport in QD-film is affected by nanoparticle size, inter particle spacing, ligand, trap states density and size distribution homogeneity. Size distribution homogeneity is reflected in FWHM of CQDs PL emission. CQD PLQY also provides information about conductivity of the QD-film. The PLQY of conductive QD-film is lower than PLQY of CQDs in solution.

The electrical and optical properties of QD-films are tunable through quantum confinement effect by controlling the size of their CQD building blocks. Decreasing the size of CQDs leads to an increase of

mobility in the QD-film. However, the increase in mobility does not directly result in lower series resistance and higher shunt resistances of the QD-semiconductor heterojunction diode. This is because when the size of nanoparticles decreases, the density of trap states increases. The complicated relationship between trap state density and QD size adds difficulty to the non-trivial task of optimizing QD-semiconductor diode's parameters. To leverage the advantage of CQDs' size-dependent property in QD-films, more insight is required on the behavior of trap states density with respect to size of QDs. Therefore, fabrication methods and passivation techniques of CQDs should be further developed to lower the density of trap states in QD-film.

Chapter 8
Design development and critical analysis of solar cells with quantum dot film and ZnO nanowires

In this chapter, we discuss details on the different designs for fabrication of heterojunction QD solar cells that make use of the developed materials as their building blocks. This includes heterojunctions formed at the interface of CQDs/ZnO film and CQDs/ZnO NWs in the planar and nanowire based devices. We also assess the AZO-ZnO interface for an ohmic junction.

8.1 Planar heterojunction quantum dot solar cell

Figure 8.1 represents the structure of planar quantum dot solar cell. QD-film layer is sandwiched between metal/AZO/ZnO/QDs/MoO_3/metal. The heterojunction is formed between QD-film and zinc oxide wide band gap material. In this heterojunction structure, zinc oxide has the role of n-type material and QD-film has the role of p-type material. The band energy location of QD-film relative to the conduction and valence band of ZnO should be chosen in such a way that assures the formation of staggered (type II) heterojunction (Figure 8.2). In this structure in the solar cell operation, electrons from the conduction band of quantum dots (QD-film) will be transferred to the conduction band of zinc oxide which afterwards will be collected by the AZO electrode (cathode). On the other hand, the holes will flow in the direction of the internal electric field towards the anode (metal contact).

In this design, a thin layer (~10 nm) of molybdenum trioxide (MoO_3) is used as an electron blocking layer (EBL) as well as a hole transport layer (HTL) between the QD-film and the anode electrode. This layer prevents recombination of electrons and holes in the anode electrode. The zinc oxide (ZnO) layer also acts as an electron transport layer (ETL) as well as hole blocking layer (HBL).

The CdSe colloidal quantum dots are used to form the QD-film. Other types of quantum dots (such as PbS, PbSe and CIS) can also be used as building blocks of the QD-film. In a general sense, it is possible for the device to work in two different regimes: excitonic regime [168] and charge carrier regime (p-n junction model) [169].

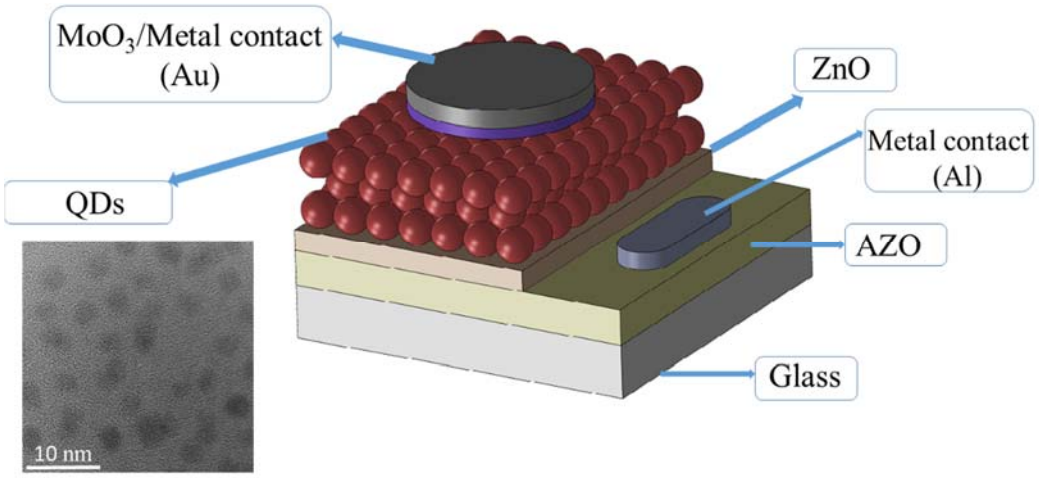

Figure 8.1: Schematic of a planar QD/ZnO heterojunction solar cell.

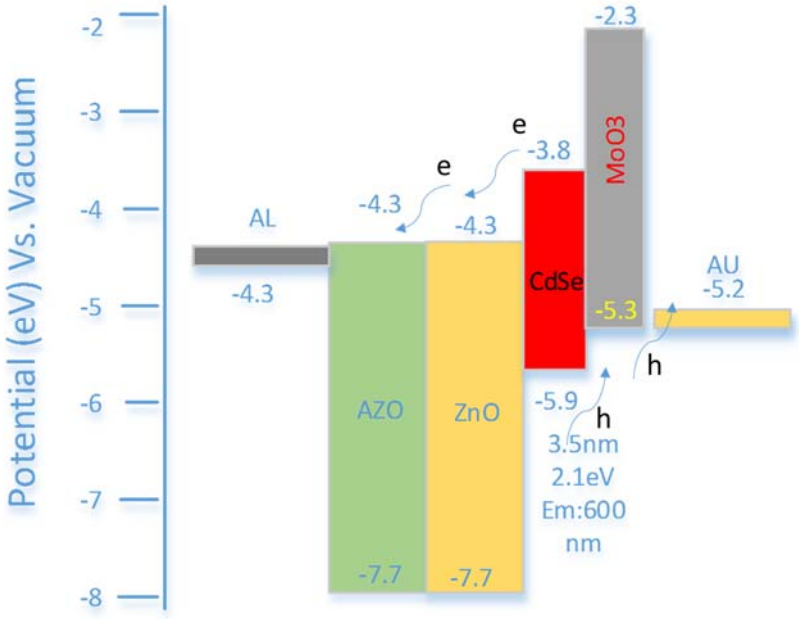

Figure 8.2: Relative location of energy bands for AZO, ZnO, CdSe quantum dots, MoO_3 and metal contact. The alignment between ~ 3.5 nm size CdSe quantum dots and ZnO is representative of a type II heterojunction. CdSe quantum dots with the size of ~ 3.5 nm have PL emission peak at 620 nm. Electron affinities, energy levels and band gap energy values are adopted from [170-173]

The junction between wide band gap semiconductor (ZnO) and QD-film is a type II heterojunction. In a typical p-n junction model (homojunction), the diffusion of majority carriers to the opposite side of the junction, establishes "depletion region". The width of the depletion region, W, can be derived from:

$$W = \left[\frac{2\varepsilon kT}{q^2}\left(ln\left(\frac{N_A N_D}{n_i^2}\right)\left(\frac{1}{N_A}+\frac{1}{N_D}\right)\right)\right]^{1/2} \qquad (8\text{–}1)$$

Where ε, k, T, q, n_i, N_A and N_D are the permittivity, Boltzmann's constant, temperature, elementary charge, intrinsic carrier density, acceptor density and donor density respectively. The depletion region is not equally distributed on both sides. The spread of the depletion region is wider in the lightly doped semiconductor. The depletion region's width expanding into the QD-film (p-type material:W_{p0}) is given by:

$$W_{p0} = \frac{1}{N_A}\sqrt{\frac{2\varepsilon V_{bi}}{q\left(\frac{1}{N_A}+\frac{1}{N_D}\right)}} \qquad (8\text{–}2)$$

Where V_{bi} is the built in potential. V_{bi} reflects the potential change along the depletion region. V_{bi} is derived from:

$$V_{bi} = \frac{kT}{q} ln\left(\frac{N_A N_D}{n_i^2}\right) \qquad (8\text{–}3)$$

As depicted in Figure 8.3 (b), in the p-n junction model, there would be two regions: depletion region and quasi neutral region. In depletion region carrier transport relies on carrier drift, on the other hand, in the quasi-neutral region it relies on carrier diffusion. The depletion width in QD-film is reported to be in the range of 65±5 nm [2].In depletion region the drift length, l_{drift} is a function of built in electric field E, carrier mobility μ and carrier life time τ:

$$l_{\text{drift}} = \mu \times E \times \tau \qquad (8\text{–}4)$$

In the quasi-neutral region, the (minority) carrier diffusion length $l_{diffusion}$ depends on diffusion coefficient D and carrier mobility μ:

$$l_{diffusion} = \sqrt{D \times \tau} \qquad (8\text{–}5)$$

Charge carriers transport in the quasi-neutral region, where there is no electric field, is inefficient. Particularly in the QD-film side, the charge carriers are prone to recombine in the trap states on the quantum dot sites. The carrier diffusion length in QD-film is reported to be in the range of 10-100 nm [2, 174, 175].

In the excitonic regime, absorbed photons in the QD-film create excitons. Excitons should diffuse to the ZnO-quantum dot film interface to dissociate and produce collectable charge carriers. Excitons have a short lifetime and a short diffusion length. For CdSe and CdSe/CdS QD-films, the exciton diffusion lengths are in the range of 43 and 19-24 nm respectively [176, 177]. As a result, only excitons generated in the vicinity of the ZnO-quantum dot film interface (in the order of exciton diffusion length (l_{exiton})) have a chance to be collected before annihilation.

Excitons generated in the QD-film far away from the ZnO-quantum dot film's interface (>l_{exiton}) have a minor chance to be dissociated and produce charge carriers. Instead, these coupled electron-hole pairs (excitons) are prone to recombination. As depicted in Figure 8.3, this region has been referred as "dead zone", due to the fact that generated excitons in this region are annihilated and absorbed photons energy is wasted.

It is possible that these two regimes (excitonic and charge carrier) co-exist in the QD-film layer. In this essence, we have two regions in the QD-film:

- The first region is the region with high charge collection probability. The "high charge collection" region in QD-film consists of the depletion region (W_{p0}) + carrier diffusion length ($l_{diffusion}$) + exciton diffusion length (l_{exiton}). Internal electric field formed in the depletion region, sweeps photo generated minority carriers across the junction and separates electrons and holes. Up to a distance given by the exciton diffusion length away from the depletion region, excitons diffuse towards the depletion region and dissociate in the presence of the internal electric field.
- The second region, is the region with very low charge collection probability. Beyond W_{p0} +$l_{diffusion}$+ l_{exiton} from the junction, the photogenerated excitons will most likely recombine. This region is referred as "dead zone" in the picture.

The depletion region's width at the QD-film side (W_{p0}) is proportional to the ratio of carrier concentration in the p-type QD-film (N_A) to that in the n-type ZnO (N_D). The smaller this ratio ($\frac{N_A}{N_D}$) is, the more is the depletion region's spread in QD-film and the wider is the "high charge collection region".

Considering the fact that most of the photogenerated excitons/carriers in the dead zone region are lost, for higher efficiency device, it is desirable to minimize the width of "dead zone" and maximize the width of "high charge collection region". This can be done by maximizing the spread of the depletion region inside the QD-film (fully depleted QD-film). For efficient charge collection, the thickness of QD-film should not

exceed the sum of depletion width, minority-carrier diffusion length and exciton diffusion length. This limits the practical thickness of QD-film and light-absorbing layer to < 300 nm [174].

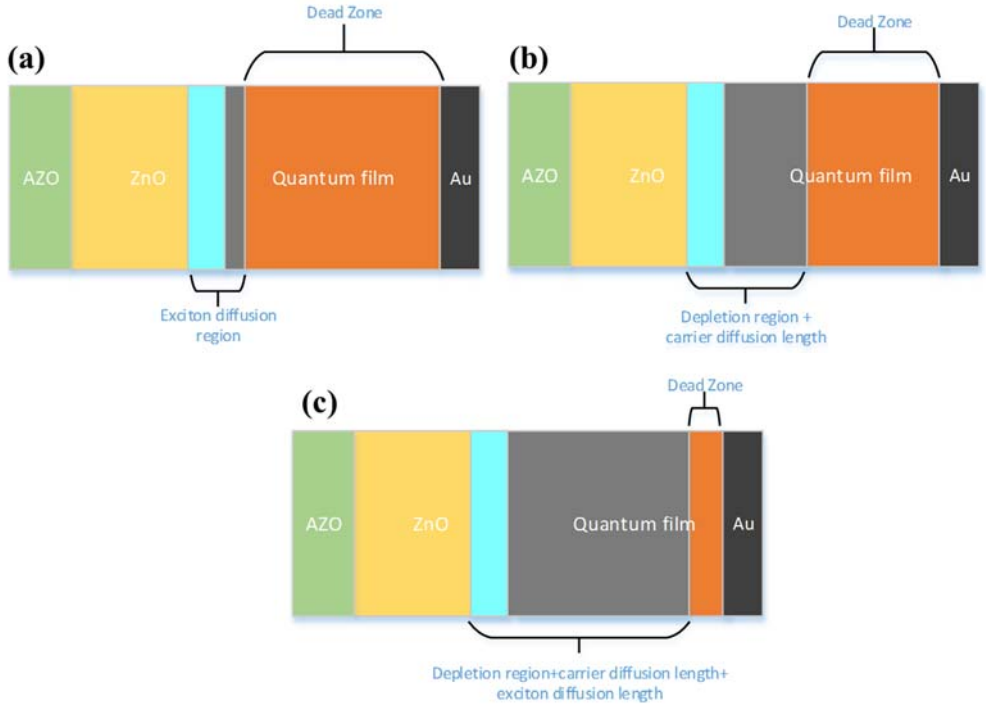

Figure 8.3: (a) ZnO-quantum dot film at excitonic regime. Only excitons within the exciton diffusion length from ZnO-quantum dot film interface are successfully dissociated and produce collectable charge carriers, (b) ZnO-quantum dot film junction and the formation of depletion region and charge carrier regime (p-n junction model).The gray area represents the region with high charge collection probability, (c) Excitonic regime and charge carrier regime in a typical working device. In an ideal device, the aim is to reduce the "dead zone" area and have a "fully depleted device". For efficient charge collection, the thickness of QD-film should not exceed the sum of depletion width, minority-carrier diffusion length and exciton diffusion length.

As described in chapter 2, carrier concentration/doping density (N_A) in QD-film depends on the ratio of hole trapping states to electron trapping states on the surface of quantum dots. As a result, control over N_A is a very complicated task that depends on many parameters such as: deposition condition, type of ligands, level of surface passivation, type of solvent and others.

Therefore, there is a minimum control over carrier concentration (N_A) in QD-film. Thus, controlling $\frac{N_A}{N_D}$ ratio is reduced to controlling carrier concentration in ZnO.

Limited absorption depth

The optical transmission of CdSe-CQDs on glass for a QD-film layer with thickness of ~ 700 nm is depicted in Figure 8.4. The absorbance and photoluminescence of the same layer is depicted in Figure 8.5.

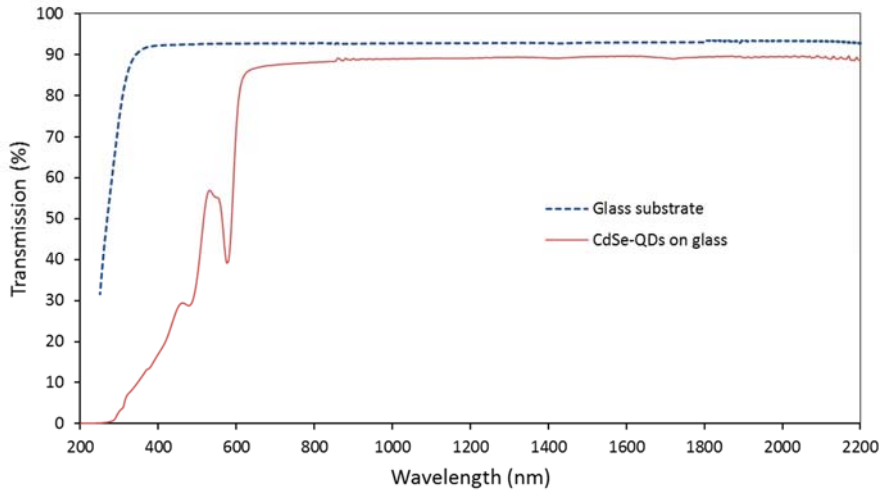

Figure 8.4: Optical transmission intensity of corning glass substrate (blue dashed line), and CdSe QDs deposited on glass substrate (red line). The thickness of the film is ~ 700 nm.

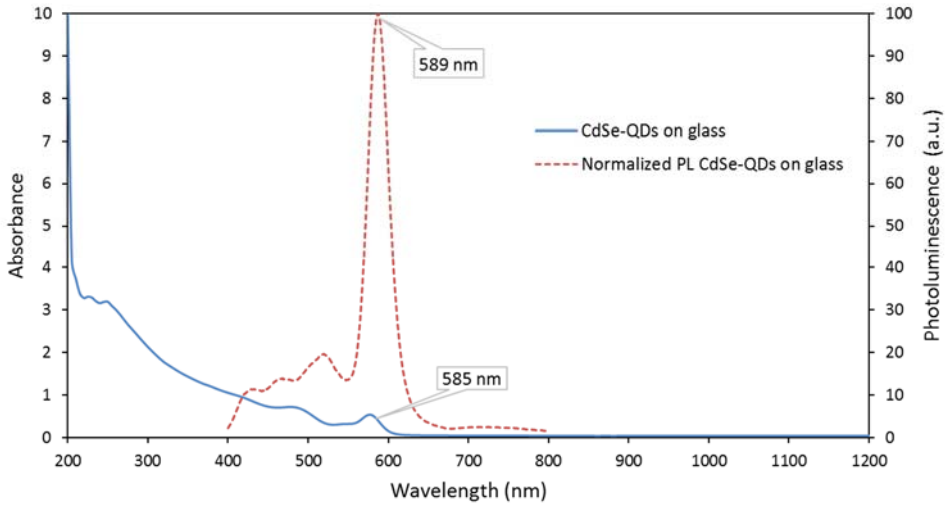

Figure 8.5: Absorbance and Photoluminescence of CdSe QD-film deposited on glass substrate. For PL measurement, wavelength of excitation light is 380 nm and optical filter with cut off wavelength at 395 is used.

Using the Beer-Lambert's law, the absorption length of the CdSe QD-film at different wavelength is calculated. The results are plotted in Figure 8.6. The absorption length is a measure that shows how much thickness of the material is required for ~ 63% of the light to be absorbed. According to this plot, the absorption length at wavelength of 530 nm is around 1000 nm (~ 1 μm). The absorption length at first absorption peak of CdSe CQDs (λ_{abs} at 585 nm) is ~ 600 nm.

For proper light absorption, the thickness of CQD absorber layer should be above 1 μm. On the other hand for better carrier collection the thickness of CQD absorber layer should be smaller than the depletion width (~ 300 nm). One way to address this problem (absorption-charge collection compromise), is to make optical path and charge collection path (electrical path) orthogonal.

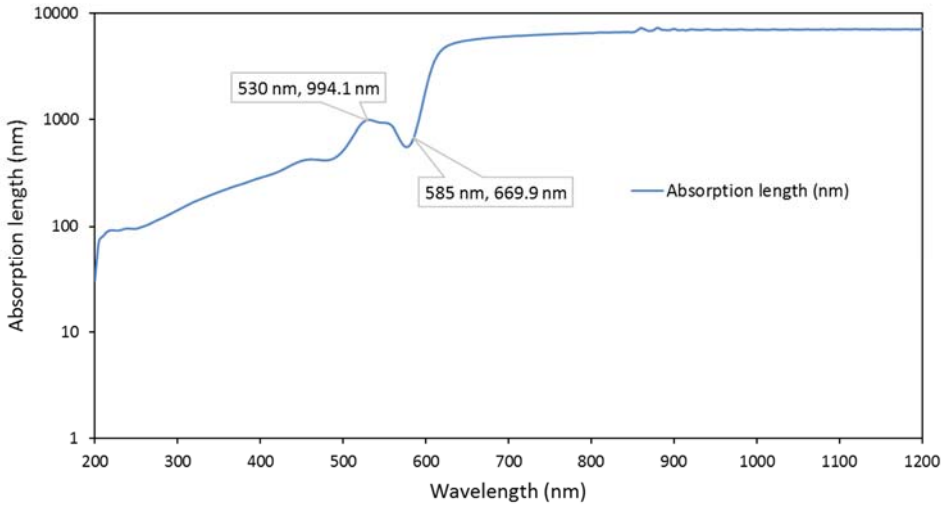

Figure 8.6: The calculated absorption length (nm) for the core CdSe QD-film. The emission peak of the core CdSe quantum dots is at 589 nm. The absorption length for light with wave length of 530 nm is around 1000 nm.

8.2 Nanowire heterojunction quantum dot solar cell

The configuration of the nanowire (bulk) heterojunction quantum dot solar cell employing arrays of ZnO nanowires is depicted in Figure 8.7. The ZnO nanowires fabricated with top-down method (described in chapter 4) are used in this design. However, ZnO nanowires developed with the bottom-up method can also be used.

The advantage of this design is that it inherently separates the optical and electrical path. Therefore, bypasses the absorption-charge collection compromise we talked about in the previous section.

Since the top-down method is used for the formation of ZnO nanowires, the carrier concentration in the ZnO nanowires can be approximated using the Hall effect measurement values presented in chapter 3, Table 3-5. The diameter of the nanowires can be controlled by changing the diameter of silica nanospheres used as the nanomask layer. It is also possible to control the separation of the nanowires by controlling the separation of silica nanospheres in the nanomask. If the mirroring effect of the metal back contact is taken into account, the optical path would be doubled. Array of nanowires with a height of 600-700 nm will

provide an optical path of ~1200-1400 nm, which matches the absorption length (~1000 nm at λ=530 nm) for CdSe quantum dot as depicted in Figure 8.6.

Another advantage of the NW structure is the enhancement of the effective area (effective junction area) of the solar cell device. For our device with the array of ZnO nanowires prepared with top-down method, the SEM micrograph of the silica sphere nanomask described in chapter 4 (Figure 4.3) suggests that the silica spheres are packed with hexagonal close packing (hcp) structure.

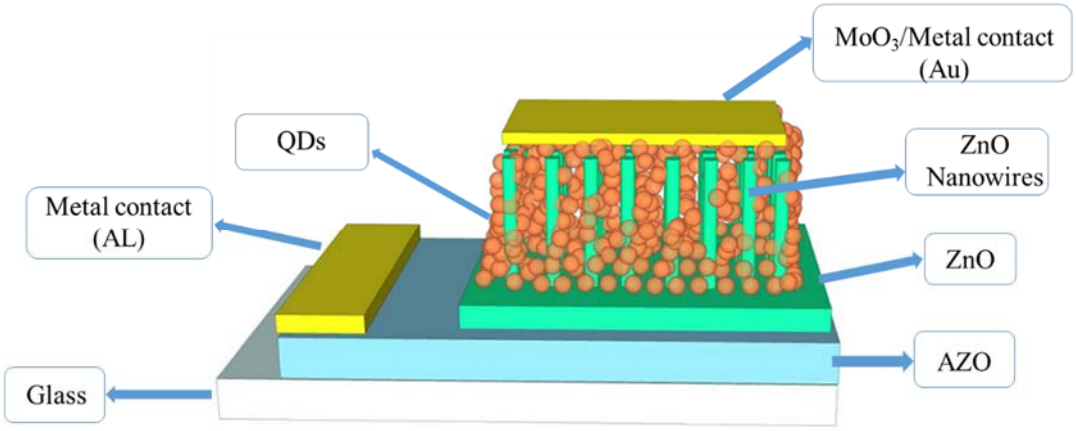

Figure 8.7: Schematic of a NW CdSe QD/ZnO-nanowire heterojunction solar cell.

The unit cell of this hcp structure is depicted in Figure 8.8. In this micrograph, D represents the diameter of the silica spheres/ ZnO nanopillars, S is the spacing of silica spheres/nanopillars and L is the side of the hexagonal unit cell. For H as the height of nanopillars/nanowires, the increase in effective area (effective surface factor) can be calculated by:

$$\eta_{area} = \frac{Total\ area\ of\ the\ surface}{Planar\ surface} = \frac{\frac{3L^2\sqrt{3}}{2} + 3\pi D \times H}{\frac{3L^2\sqrt{3}}{2}} \qquad (8\text{–}6)$$

If the diameter of ZnO nanowires is 500 nm (D=500 nm), and the spacing of the nanowires is 300 nm (S=300 nm) and the height of nanowires is 700 nm (H=700 nm, which is approximately the absorption length at λ=585 nm, see Figure 8.6) the effective surface factor would be η_{area}= 3.59. This means that for the above mentioned nanowire/nanopillar configuration, the effective area is ~3.6 fold higher than planer structure. This figure of merit is directly proportional to height of the nanowires. The ZnO nanowires fabricated with top-down method are preferred in this design. However, ZnO nanowires developed with bottom-up methods such as hydrothermal method can also be used. The advantage of top-down method is that it provides ordered structure and equal size for the nanowires array. In the hydrothermal method the

grown nanowires have random orientation and inhomogeneous dimension. In particular, the height of the grown nanowires vary in hydrothermally fabricated ZnO nanowires. This imposed uncertainty in length of nanowires might result in shortening of devices (low QD-film thickness) or high series resistance (high QD-film thickness) in the device (see Figure 8.9 (a)).

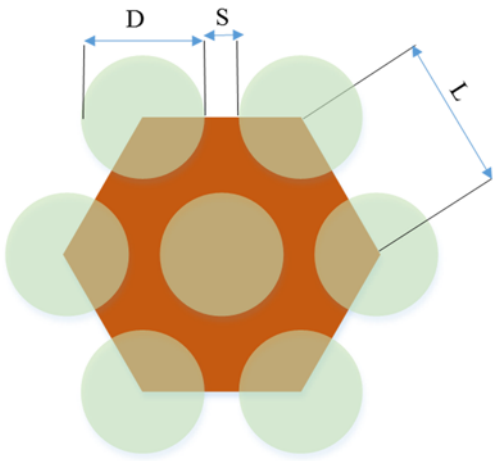

Figure 8.8: The unit cell of hexagonal close packing configuration of circles on the surface which represents the silica nanospheres in the nanomask layer. This also represents the top view of the ZnO nanopillars. D is the diameter of the spheres, S is the spacing between the spheres and L is the side of the hexagonal unit cell (L=D+S).

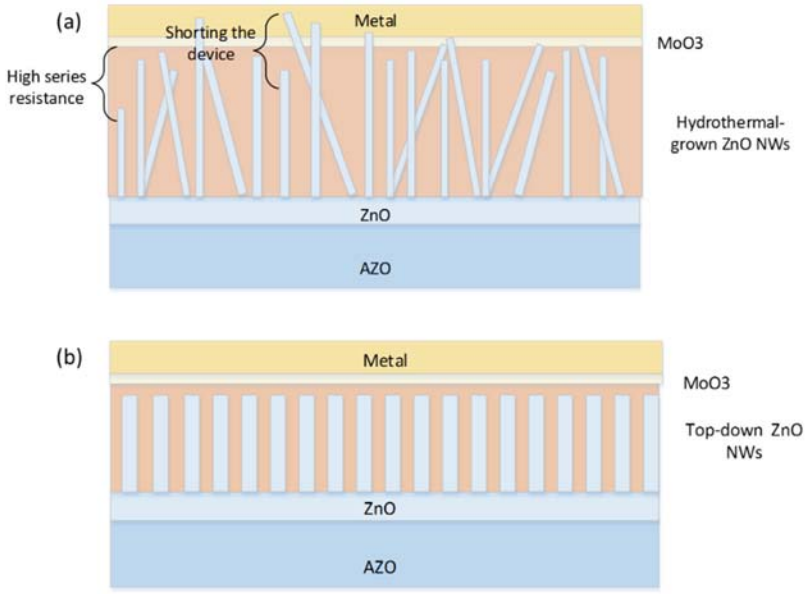

Figure 8.9: (a) Schematics of CQD solar cell fabricated with hydrothermally grown QDs. The variation in length of NWs may result in shortening of fabricated devices or high series resistance in the device. (b) CQD solar cell fabricated with ordered array of ZnO nanowires fabricated with top-down method.

8.3 Assessment of AZO-ZnO interface

In all of the above mentioned structures AZO forms a junction with ZnO. In these solar cell designs, ideally we want an ohmic junction/contact between AZO (cathode) and ZnO (wide band gap semiconductor). As there is a possibility for formation of a non-ohmic junction between AZO and ZnO, the AZO-ZnO junction should be assessed and if necessary optimized for the formation of a proper ohmic contact. The AZO-ZnO junction has been assessed using dark I-V measurement. Figure 8.10 illustrates the structure of our sample to study AZO-ZnO junction.

The sample is prepared by depositing ~800 nm thick AZO at a temperature of 250 °C, sputtering pressure of 0.5 mTorr and power of 150 W on corning glass. Then ~800 nm ZnO is deposited on top of AZO at a temperature of 250 °C, sputtering pressure of 0.5 mTorr and power of 150 W on corning glass. Finally, aluminum contacts have been deposited on both AZO and ZnO thin films. Aluminum forms an ohmic junction/contact with both AZO and ZnO.

The dark I-V profile of the junction is presented in Figure 8.10. This I-V curve is an indication of an ohmic junction between AZO-ZnO. Similar results is found for the junction between AZO (prepared at 250 °C) and ZnO prepared at room temperature.

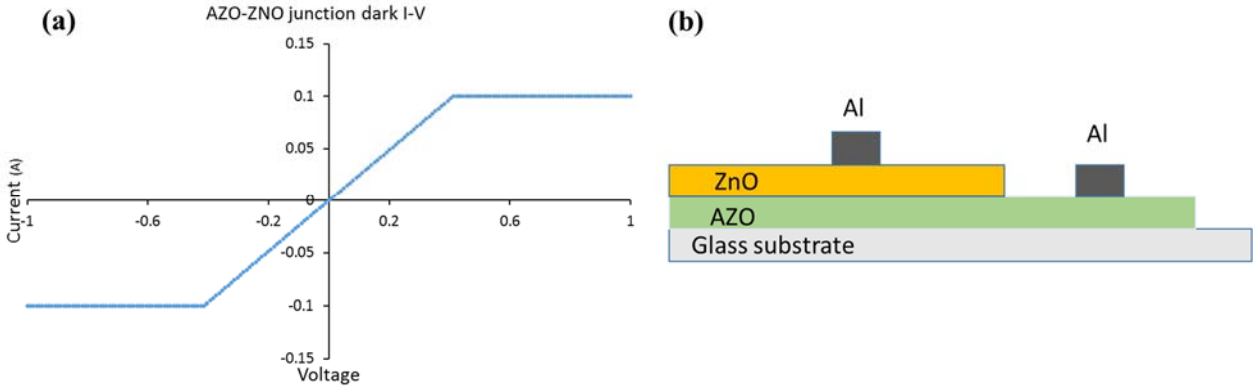

Figure 8.10: (a) Dark I-V plot of AZO-ZnO junction which indicates that the junction is ohmic, (b) Schematic representing structure of the sample made to assess AZO-ZnO junction. The current compliance of the I-V measurement system (measurement limitation) is 100 mA (the flat line in the dark I-V plot).

8.4 Summary

In this chapter, we discussed different QD solar cell designs that employs the developed materials as their building blocks. The planar heterojunction QD solar cell discussed herein is based on heterojunction between the CdSe QD-film and ZnO thin film. On the other hand, the NW heterojunction quantum dot solar cell employs top-down zinc oxide nanowires to form heterojunction with QD-film. We showed that the optical absorption length of the core CdSe QD-film is in the range of ~ 1000 nm. We also discussed that for efficient charge collection, the depletion region should span all over the QD-film layer. It demonstrates that there is a contradiction of higher thickness for high light absorption and lower thickness for higher charge collection. This means that in planar QD solar cell devices, there is an optimum thickness which limits the light absorption and achievable power conversion efficiency. This inherent limitation in planar QD solar cells is relieved in a nanowire heterojunction structure where charge collection and optical path are orthogonal. We also showed that the nanowire structure has the advantage of having higher effective junction area. The AZO-ZnO interface has also been assessed and optimized to achieve an ohmic junction.

Chapter 9

Experimental realization of QD solar cells and device characterization

The results from our studies presented in the previous chapters were implemented for fabrication of advanced QD solar cells. This chapter outlines the experimental steps taken towards integration of CdSe quantum film, sputtered ZnO film and RIE etched nanowires for fabrication of planar and nanowire QD solar cell devices. To form conductive QD-film, two methods were used; (a) layer-by-layer replacement of nonpolar ligands with short polar ones using solid-phase ligand exchange; and (b) single-step drop-casting from dispersion of QDs with short polar ligands. Finally, the characteristics of the fabricated devices were highlighted.

9.1 Generic flow chart of device fabrication

Fabrication steps for realization of the solar cell devices is presented in Figure 9.1. For device fabrication AZO was sputtered on the RCA cleaned glass substrate. Aluminum contact deposited through shadow masks on the AZO film. For planar and nanowire devices ZnO film and nanowires were formed respectively. Quantum films were formed through single-step drop-casting and L-B-L deposition. Finally, the MoO_3 and gold were deposited to form a hole transport layer and the top contact.

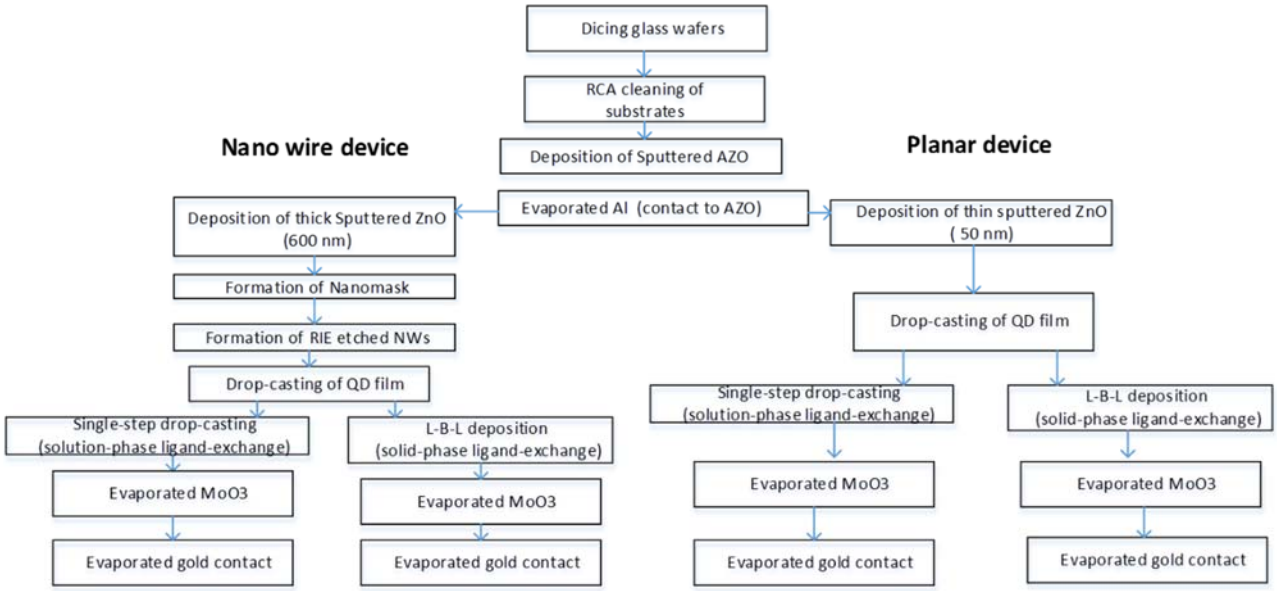

Figure 9.1: Generic flow chart of the devices fabrication.

9.2 Shadow masks for film deposition

Three different shadow masks have been designed and made for deposition of AZO, ZnO and metal/MoO_3 layers. The shadow masks are made on 4 inch stainless steel disks to hold five 22 mm×22 mm samples (corning glass substrates). The schematic of the masks are presented in Figure 9.2.

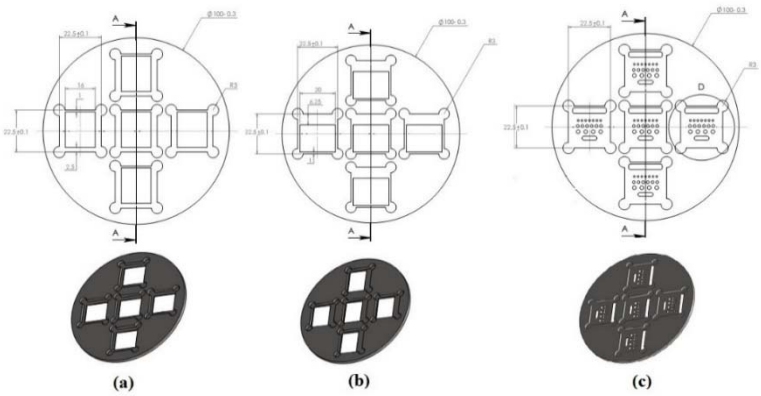

Figure 9.2: Different shadow masks used for deposition of different layers in the colloidal quantum dot solar cell devices: (a) Shadow mask for deposition of AZO, (b) Shadow mask for deposition of ZnO, (c) Shadow mask for deposition of metal/MoO_3 contacts.

9.3 Deposition conditions used for solar cell fabrication

The AZO layer has been deposited based on the process developed in chapter 3. A 750 nm thick AZO is RF sputtered on glass substrate at 250 °C, in 0.5 mTorr pressure and power of 150 W. The ZnO layer has been deposited in a similar way. The deposition temperature is set to 250 °C for high carrier concentration in the films (see Table 3-5). ZnO films with 50 nm and 600 nm thickness are prepared for planar and nanowire devices, respectively (see Figure 9.3). MoO_3 (7-35 nm) has been deposited by thermal evaporation in Intel Vac. evaporation tool at a rate of 1 A°/s. Gold contact (~200 nm) has been deposited on MoO_3 by thermal evaporation at a rate of 1 A°/s in bench top thermal evaporation tool (Cressington coating system). Aluminum (Al) contact has been made in Intel Vac. evaporation tool using electron beam evaporation at a rate of 10 A°/s.

Figure 9.3: Image of fabricated planar CdSe QD-heterojunction solar cells. There are 18 cells with different active area (metal pad area) on the samples.

9.4 Device packaging for measurement and characterization

As discussed in chapter 2 of this report, the high surface to volume ratio in quantum dots makes them susceptible to degradation in air, which adversely would affect the performance of QD solar cell devices. To protect the quantum dots during measurements from oxidation and degradation, a sealed measurement pack has been designed and implemented. As shown in Figure 9.4 (a), the sealed pack consist of two stainless steel disks which are placed on front and back side of a ring with a Viton oring. The pack is then tightened and sealed with clamps. On the front disk, a square opening is machined and a piece of quartz substrate is sealed (with gorilla glue) around the opening window. On the backside disk, eight holes were drilled aligned with the metal contacts (pads). Spring probes (Mouser electronics, S-00-J-1.6-G D/C SS SPG) shielded with plastic shrinks (McMaster Carr, 7496K81) were plugged to these holes and then sealed to provide the electrical contacts to the solar cell's electrodes. The sealed measurement pack is then tested for any leakage using helium gas with LACO leak detector. The leaking rate below 1.5×10^{-3} atm. cc/sec is recorded for the sealed measurement pack. This sealed measurement pack is used to address poor air stability of quantum dots during illuminated, EQE and dark I-V measurements (see Figure 9.5).

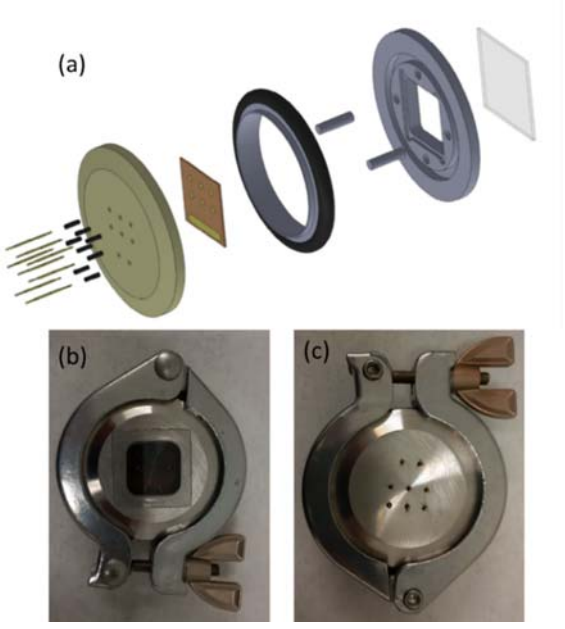

Figure 9.4: (a) Exploded view of the schematic of sealed measurement pack, (b) and (c) Photos of the sealed measurement pack used to characterize the air-sensitive devices.

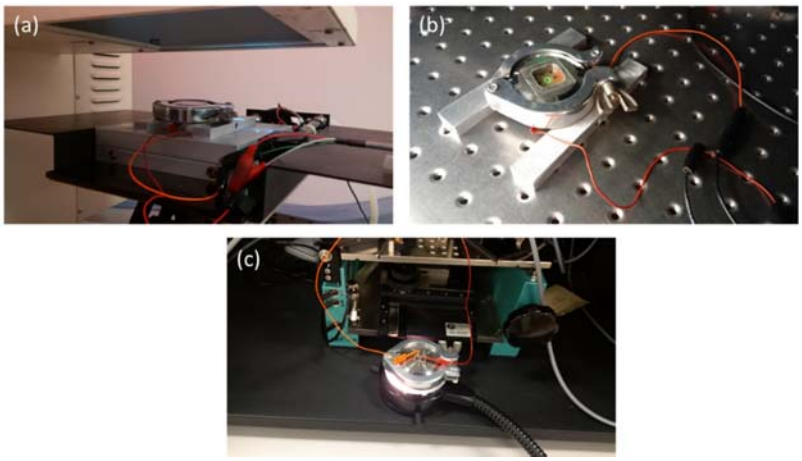

Figure 9.5: QD Solar cells in sealed pack with different set ups used for (a) Illuminated I-V measurement (simulated AM 1.5), (b) EQE measurement and (c) dark I-V measurement. The set up for dark I-V measurements is also used for illuminated I-V measurements.

9.5 Characteristics of fabricated devices: planar and nanowire QD-heterojunction structures

In chapter 5, we described development of two methods for deposition of QD-film: (a) layer-by-layer (L-B-L) drop-casting technique to deposit crack free, thick QD-films by stacking of thin layers; (b) single-step drop-casting technique. In layer-by-layer technique, each layer undergoes solid-phase ligand-exchange (EDT or MPA treatment) to form a conductive QD-film. In single-step drop-casting technique, QD-film is formed via deposition of CQDs capped with transport-compatible ligands from solution. These two methods were used in fabrication of planar and nanowire QD-heterojunction solar cell devices. CQDs with absorption at 588nm (size ~ 3.5 nm) were used for formation of QD-film.

9.5.1 Planar devices fabricated with single-step drop-cast QD-film

To fabricate the planar device, CdSe CQDs with absorption wave-length of 588 nm capped with MPA and EDT short polar ligands dispersed in methanol purchased from commercial supplier were used. Single-step drop-casting technique was used to form 80 nm quantum film on the surface of 50 nm sputtered ZnO as described in chapter 5. 10 nm hole transport MoO_3 and 200 nm gold contact layers were deposited to complete the device. The active area of the device (area of metal pad) is ~ 0.071 cm^2. Figure 9.6 shows the dark I-V characteristics and diode behavior of the fabricated devices. Although the dark current is poor, there is 10 fold improvement in the I_{ON}/I_{OFF} ratio of the device fabricated with CdSe QD-film with EDT ligand with respect to the device fabricated with MPA capped QDs.

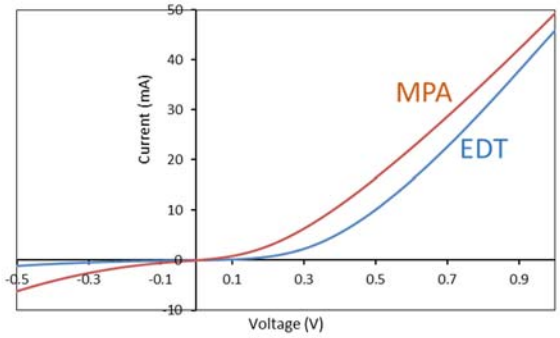

Figure 9.6: Dark I-V characteristic of QD solar cell device prepared with single-step drop-casting of CdSe-MPA (red) and CdSe-EDT (blue).

We also measured the illuminated I-V characteristic of these devices as shown in Figure 9.7. Due to the series, shunt resistances, non-efficient absorption in thin QD-film and thin MoO_3 thickness, no considerable short circuit current is measured.

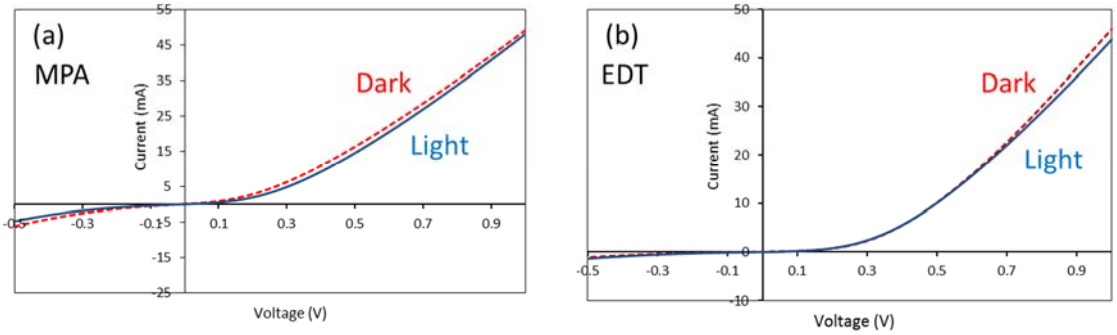

Figure 9.7: (a) I-V characteristic of QD solar cell device prepared with single-step drop-casting of CdSe-MPA, (b) I-V characteristic of QD solar cell device prepared with single-step drop-casting of CdSe-EDT.

External quantum efficiency (EQE) measurement was also performed on these devices as shown in Figure 9.8. Due to the above mentioned problems as well as calibration errors the response of the cells are poor. Also the light used in the EQE system has weak intensity in the blue spectrum which results in low signal to noise ratio in this range. Nevertheless there is some indications of the sensitivity of the devices in the absorption range of the QDs.

Nanowire based QD solar cells also were fabricated using this method. However the IV results from these devices showed high series and shunt resistances. The length of the RIE etched nanowires and the concentration of QD solution needs to be adjusted to achieve a working device.

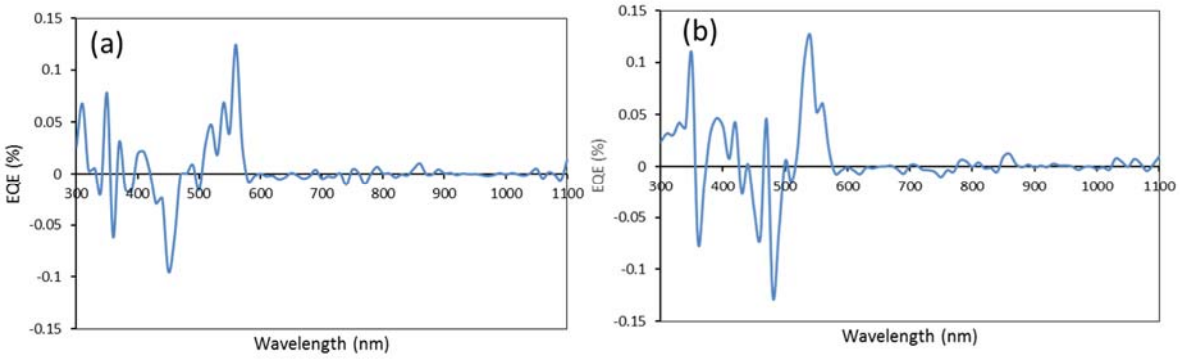

Figure 9.8: External quantum efficiency (EQE) of a planar solar cell prepared via drop-casting of quantum dots capped with (a) MPA ligands and (b) EDT ligands.

9.5.2 Nanowire and planar devices fabricated with layer-by-layer drop-cast QD-film

CdSe-OA CQDs dispersed in chloroform were deposited on the surface of RIE etched ZnO nanowires to conformally cover the surface of the nanowires. 200 µl of 1 mg/mL CQDs dispersed in chloroform were used. Figure 9.9 (a-c) and Figure 9.9 (d) repreesents the cross section high resolution SEM (HRSEM) image of the RIE etched NWs before and after the QD coverage.

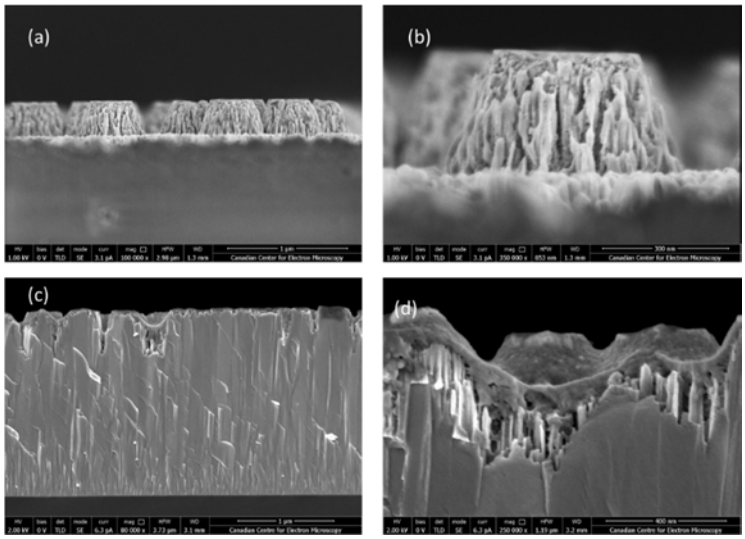

Figure 9.9: Cross sectional high resolution SEM (HRSEM) of (a) ZnO nanopillar/nanowires prepared with nanomasking and RIE of ZnO, (b) High magnification HRSEM image of ZnO nanopillars, (c) CdSe-QDs deposited on ZnO nanopillars/nanowires prepared with top-down method on thick ZnO layer. The thickness of the ZnO layer is 2.2 µm. The quantum dots are drop-casted from 1 mg/ml of CdSe-OA solution in chloroform, (d) High magnification of CdSe-OA coated ZnO nanopillars.

Quantum dot-nanowire devices are prepared with L-B-L drop-casting method. The deposition cycle (dispensing of CQDs followed by EDT treatment) is repeated four times for full coverage of 400 nm NWs

as described in chapter 5. Figure 9.10 shows the I-V characteristics of the fabricated nanowire QD solar cell. The diode behavior of the device fabricated with this method is better than the same structure fabricated with single-step drop-casting. However, the diodic behavior is still poor.

The illuminated I-V (photocurrent) was still not possible. This is probably due to presence of high surface trap density in the nanowires which is hindering any photocurrent. This could be over come by surface treatment of the nanowires as described in chapter 4. The high series resistance of the device can be due to the not fully conformal QD-film and the contact issues. Moreover, the non-optimized nanowire length and distribution of recombination centres due to the surface trap sites added to the device shunt resistance.

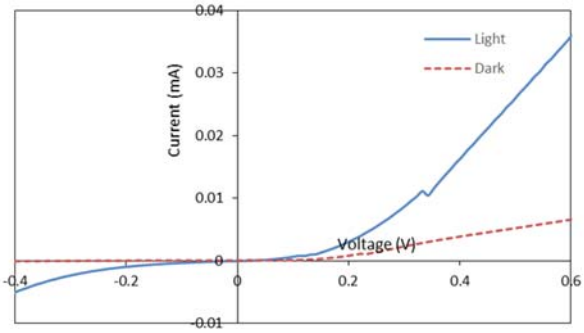

Figure 9.10: I-V characteristics of a nanowire quantum dot solar cell prepared by L-B-L drop-casting and EDT treatment of 3.5 nm size CdSe-OA QDs. The contact area is 0.0314 cm^2.

Figure 9.11 represents I-V characteristics of planar device fabricated after MPA treatment (solid-phase ligand-exchange) of QD-films. 70 nm QD-film, 10 nm MoO_3 followed by 200 nm gold were deposited to complete the device with the active area of ~ 0.071 cm^2 .

As shown in Figure 9.11(a) the diode behavior of this device is improved comparing to the similar one fabricated with single-step drop-casting. However, this device still did not yield any photocurrent. (See Figure 9.11(b)). Application of L-B-L drop-casting method reduces the number and the size of the micro cracks. However, the presence of sub micrometer size cracks in the final film has not yet completely resolved.

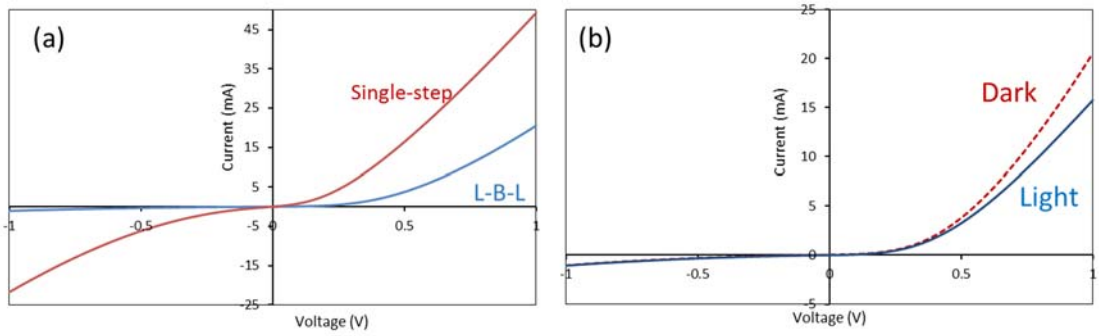

Figure 9.11: (a) Dark I-V characteristics of planar QD solar cell prepared by single-step drop-casting and L-B-L deposition of MPA ligated QD-film, (b) I-V characteristics of QD planar solar cells with MPA ligand prepared with L-B-L method.

Another sets of planar devices were fabricated by QD-film formation via L-B-L deposition of EDT treated QDs through solid-phase ligand-exchange. Figure 9.12 demonstrates the dark I-V characteristics of the QD solar cell prepared by this method. The thicknesses of the QD layer, MoO_3 and gold layers are 170 nm, 35 nm and 200 nm respectively. The diodic behavior of this device is improved as compared to the similar device fabricated by single-step drop-casting.

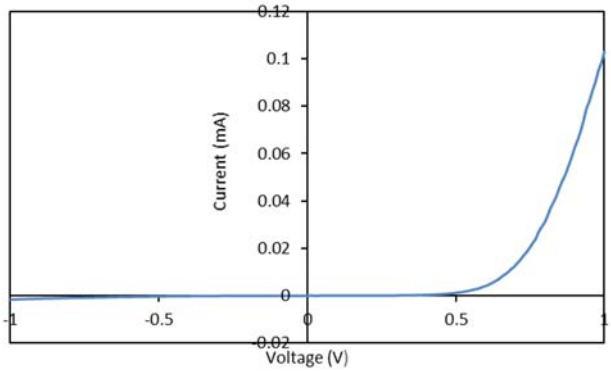

Figure 9.12: Dark I-V characteristic of planar QD solar cell prepared with L-B-L deposition technique and EDT treatment. The thickness of QD layer is 170 nm.

Following this experience, to improve the device performance, more devices with different thicknesses of QD, MoO_3 layers were fabricated and characterized. Figure 9.13 shows the I-V characteristics of the device fabricated with 170 nm QD-film and a 7 nm MoO_3 layer with the active area of 0.3 cm^2. The device shows sensitivity to light. Nevertheless, still device suffers from some series and shunt resistance. This device shows I_{sc}=2.33 mA, V_{OC}=335.8 mV and power conversion efficiency of η=2.3% at 100 mW/cm^2 solar irradiance.

The thickness of MoO_3 has a profound effect on the performance and I-V characteristics of the QD PV devices. MoO_3 is assumed to be a hole transport material and generally exhibits poor electron mobility. For a thin MoO_3 layer, electron carriers in QD-film can tunnel through the MoO_3 layer and recombine with holes in the metal contact. This parasitic carrier recombination at anode electrode, is responsible for the S-shape of the I-V curve (Figure 9.13). The relatively thick QD-film results in an acceptable short circuit current.

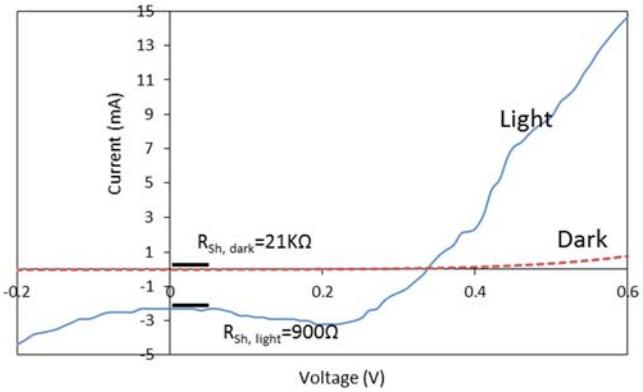

Figure 9.13: I-V characteristics of a planar quantum QD cell prepared by L-B-L drop-casting and EDT treatment of 3.5 nm size CdSe-OA QDs. The thickness of CdSe QD-film is 170 nm and the thickness of MoO_3 is 7 nm. The contact area is 0.3 cm^2.

Another sets of device fabricated with 80 nm of QD-film and 35 nm MoO_3 layer with the same contact area presented above. I-V characteristics of this device is presented in Figure 9.14. This device shows I_{sc}=0.14 mA, V_{OC}= 774 mV, FF=60.9% and power conversion efficiency of η=0.21% at 100 mW/cm^2 solar irradiance.

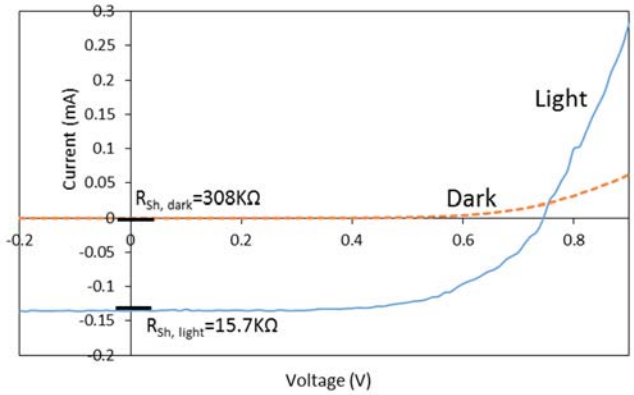

Figure 9.14: I-V characteristics of a planar quantum dot solar cell prepared by L-B-L drop-casting and EDT treatment of 3.5 nm size CdSe-OA QDs. The thickness of CdSe QD-film is 80 nm and the thickness of MoO_3 is 35 nm. The contact area is 0.3 cm2.

Increasing the thickness of MoO_3 decreases the tunneling current of electrons and reduces the probability of electron-hole recombination at the surface of the metal contact. However, the adverse effect of thick MoO_3 is the reduction of current because thick MoO_3 blocks the hole transport to the metal contact (MoO_3 is not a conductor). The reciprocal of the slope at V=0 is used to calculate the shunt resistance (R_{sh}). By increasing the thickness of MoO_3 from 7nm to 35 nm, the illuminated shunt resistance has increased (from 900 to 15.7 KΩ). The thick MoO_3 layer and thin QD-film likely resulted in low short circuit current in this device. To achieve a better device performance the thickness of the MoO_3 and QD-film needs to be optimized.

9.6 Summary

CdSe quantum film, sputtered ZnO film and RIE etched nanowires were employed for fabrication of planar and nanowire QD solar cell devices. To form conductive QD-film, two methods were used; (a) single-step drop-casting from CQDs solutions with short polar ligands; (b) layer-by-layer replacement of nonpolar ligands with short polar ones using solid-phase ligand exchange. For the devices fabricated with the first method, we used solutions of CQDs with MPA and EDT ligands to form the QD-film. Another set, of devices fabricated with the second method, where the OA-ligands of the QD-film were exchanged with MPA and EDT ligands. The fabricated devices were measured and their characteristics were highlighted. Overall, the diode behavior of the devices fabricated with EDT-ligated QD-film was improved as compared to their counterparts having MPA-ligands. Moreover, the devices fabricated with L-B-L QD-films shows better performance than the ones used drop casted QD-films. However, the presence of high series and low shunt resistances results in low device performance. The high series resistance can be due to the presence of cracks in the QD-film, non-optimized QD-film thickness and the contact problems. The low shunt resistance of the solar cell device can be attributed to the parasitic resistance of the MoO_3 layer and the recombination in trap sites in both QD-film, MoO_3/QD-film interface and nanowire surfaces.

Chapter 10
Conclusion and future work

10.1 Conclusion

In this research, alternative materials and simple processes were developed for the cost effective fabrication of QD-heterojunction solar cell devices. The research focus was on development of TCO and wide band gap semiconductor based on ZnO, top-down etched ZnO nanowires with silica sphere nanomasking and QD-films. The developed materials also were employed for the fabrication of planar and nanowire QD-heterojunction solar cells and the characteristics of the fabricated devices were highlighted.

We reported on achieving a very high transparent (~85% in visible range) AZO layer with one of the lowest reported resistivity ($\rho = 2.94 \times 10^{-4}$ Ω.cm) using RF sputtering technique at low deposition temperature of 250 °C. Similarly, ZnO wide band gap semiconductor films were developed. By adjusting the deposition temperature, carrier concentration is controlled in the range of 2.1×10^{17}-5.6×10^{18} cm^{-3}, while carrier mobility is tuned in the range of 2.2-30 $cm^2V^{-1}s^{-1}$.

Ordered arrays of ZnO nanowires also were fabricated combining top-down RIE etching and nanosphere silica masking. The effect of plasma etching parameters and surface treatments on the structural and surface properties of the ZnO NWs were investigated.

A high throughput drop-casting process was next developed for the formation of light absorbing QD-film to replace the widely used input-intensive spin-coating technique. QD-films with low cracks were formed with single-step drop casting of CQDs from solution (solution-phase ligand-exchange) and Layer-by-layer (L-B-L) replacement of long ligands with short charge transport-compatible ones (solid-phase ligand-exchange). We concluded that each approach has some advantages and disadvantages over another. The first approach results in a decrease in the PLQY of CQDs while the latter results in development of some micro-cracks in the QD-film.

Charge carrier dynamics also were studied at the CQDs and ZnO interface using photoluminescence decay analyses in order to optimize the selection of CQDs for efficient electron transfer which leads to a better working device. For the first time, the electron transfer in a ZnO/CQD/MoO_3 structure was investigated to eliminate the effect of Auger process and determine the true electron transfer at the CQD/ZnO interface. Effect of CQD size and ligands on the transfer efficiency was discussed.

Design concepts and theoretical treatment of QD-film/ZnO also was highlighted. Charge carrier transport mechanism in QD-film is described by hoping, tunneling and band like transport model. Charge carrier transport in QD-film is affected by nanoparticle size, inter particle spacing, ligand, trap states density and size distribution homogeneity. This study gives us insight on the parameters effecting the charge carrier transport in QD-film as well as electron transfer at the interface of QD-film/ZnO.

Finally, the applicability of developed materials in the fabrication of planar and nanowire heterojunction QD solar cells was determined. QD solar cell devices with power conversion efficiency as high as η=2.3% at 100 mW/cm^2 solar irradiance is achieved. However, the nanowire devices did not yield any photocurrent. This was attributed to the presence of high density of surface traps caused by RIE damage. The top-down RIE nanowires require further investigation to remove RIE damage and reduce the effects associated with high surface trap density.

10.2 Future work

This section provides some recommendations for further improvements in material quality, process applicability and solar cell performance. The development of third generation solar cell technology is still at an early stage, and considerable effort and research is required to pave the way for fabrication of commercially available, affordable and high-efficiency PV cell devices. Some of the recommended areas to be explored are as follows:

- Improvement of QDs-ZnO nanowires interface: The quality of the interface plays an important role in determining the power conversion efficiency of the device. Traps on the surface of QDs, ZnO and ZnO nanowires provide centers for charge recombination. These recombination centers adversely affect the performance of the solar cell device by reducing the shunt resistance and current density of the QD solar cell device. Further efforts to explore passivation techniques are required to produce a trap free QDs-ZnO interfaces.
- Annihilation of cracks in QD-film through application of QDs with shorter ligands:
  The presence of hairline micrometer and sub-micrometer size cracks in the QD-film is responsible in shortening of approximately 50% of the planar quantum dot PV devices. These cracks are formed due to volume loss, which happens during solid-phase ligand-exchange. The probability of crack formation can be reduced by application of short length ligands.

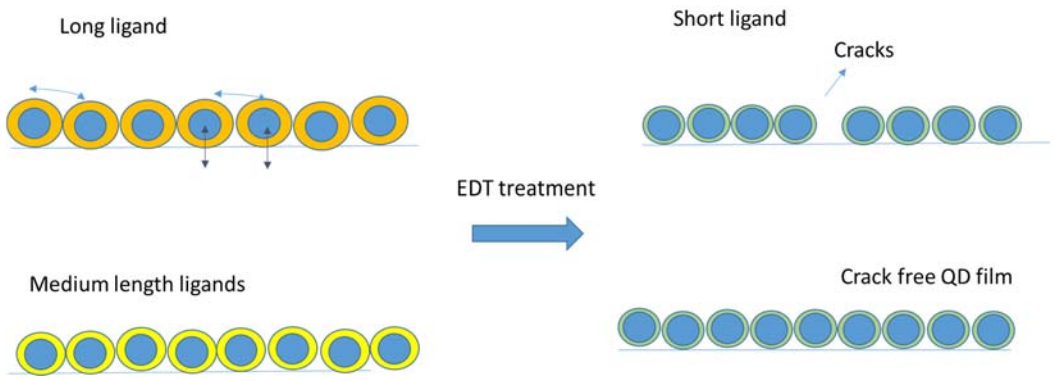

Figure 10.1: Application of shorter length ligands would result in less volume loss and crack free QD-film.

- Application of type II colloidal quantum dots (formation of type II nano-heterojunction in the interface of overcoat and core) for efficient exciton dissociation: Type II core/shell colloidal quantum dots should be employed in the fabrication of the proposed planar and Nanowire (NW) heterojunction quantum dot solar cells. The advantage of core/shell structure is the core surface passivation provided by the overcoat, which results in an expected increase in PLQY. In type II core/shell structure, this increase in PLQY can be coupled with the advantages of forming a nano-heterojunction at the interface of overcoat and core quantum dot. This type II nano-heterojunction can be engineered to be electron confining or hole confining structure (if the QD is anchored to the electron collecting electrode, a type II core/shell structure with hole confinement is favored, and vice versa). In this way, the exciton dissociation occurs at the interface of the core and the overcoat. This efficient exciton dissociation would ultimately yield QD solar cell devices with higher power conversion efficiency.
- P-i-N structure: Application of lowly doped, intrinsic quantum dots as an intrinsic layer (i layer) between n-type ZnO and p-type quantum dot to form p-i-n structure with quantum dots (QD-film) is of great interest. This p-i-n structure can be applied on both planar device and nanowire structures.
- Plasmonic effect with incorporation of metal nanoparticles: Composite materials formed by combining CQDs with colloidal metal nanoparticles, can be used to adjust the overall carrier density on QD-films. Additionally, it can also enhance the absorption of light using plasmonic effect.
- Multicolor (Rainbow) colloidal quantum dot-nanowire solar cell structure: The main focus of this research has been on CdSe quantum dots. The devices (single color) were built with only one color of CdSe colloidal quantum dots (often with emission peaks at ~ 600-630 nm). As it is possible to adjust the light absorption wavelength of quantum dots by controlling their sizes, a combination of

quantum dots with different materials (such as CdSe, CdS, PbS) can also be used. In this way, the final device would stack quantum dots with different colors, organizing them in an orderly manner between ZnO nanowires. This structure advantageously allows all of the sunlight to be absorbed in the proper quantum dots layer (proper color), and generated carriers would have energies close to the edge of the QDs' LUMO/HOMO. Therefore, utilization of both low energy photons, as well as high energy photons, will be maximized.

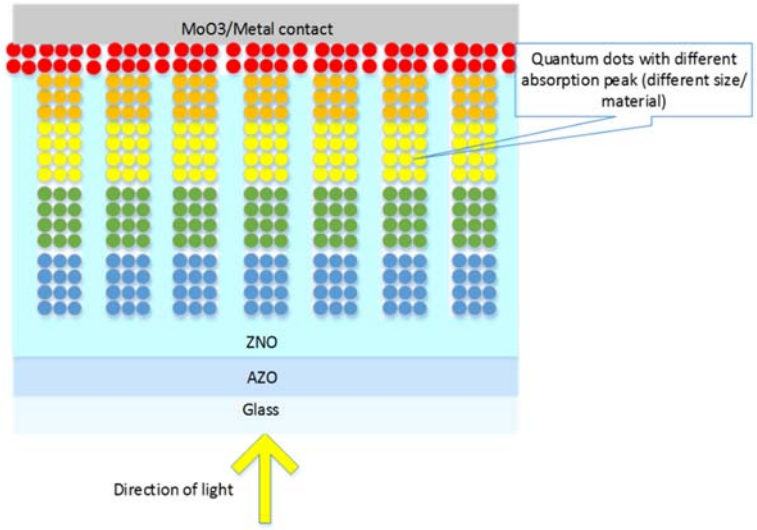

Figure 10.2: Schematic of a rainbow quantum dot solar cell.

Bibliography

[1] M. Graetzel, R. A. J. Janssen, D. B. Mitzi and E. H. Sargent, "Materials interface engineering for solution-processed photovoltaics," *Nature,* vol. 488, pp. 304-312, 2012.

[2] G. I. Koleilat, L. Levina, H. Shukla, S. H. Myrskog, S. Hinds, A. G. Pattantyus-Abraham and E. H. Sargent, "Efficient, stable infrared photovoltaics based on solution-cast colloidal quantum dots," *ACS Nano,* vol. 2, pp. 833-840, 2008.

[3] J. Baxter, Z. Bian, G. Chen, D. Danielson, M. S. Dresselhaus, A. G. Fedorov, T. S. Fisher, C. W. Jones, E. Maginn, U. Kortshagen, A. Manthiram, A. Nozik, D. R. Rolison, T. Sands, L. Shi, D. Sholl and Y. Wu, "Nanoscale design to enable the revolution in renewable energy," *Energy Environ. Sci.,* vol. 2, pp. 559-588, 2009.

[4] E. H. Sargent, "Infrared photovoltaics made by solution processing," *Nat. Photon.,* vol. 3, pp. 325-331, 2009.

[5] G. Conibeer, "Third-generation photovoltaics," *Mater. Today,* vol. 10, pp. 42-50, 2007.

[6] R. Debnath, M. T. Greiner, I. J. Kramer, A. Fischer, J. Tang, D. A. R. Barkhouse, X. Wang, L. Levina, Z. Lu and E. H. Sargent, "Depleted-heterojunction colloidal quantum dot photovoltaics employing low-cost electrical contacts," *Appl. Phys. Lett.,* vol. 97, pp. 023109, July 12, 2010.

[7] V. Celibert, E. Tranvouez, G. Guillot, C. Bru-Chevallier, L. Grenouillet, P. Duvaut, P. Gilet, P. Ballet and A. Million, "MBE growth optimization and optical spectroscopy of InAs/GaAs quantum dots emitting at 1.3 μm in single and stacked layers," *J. Cryst. Growth,* vol. 275, pp. e2313-e2319, 2005.

[8] C. Chang and Y. Lee, "Chemical bath deposition of CdS quantum dots onto mesoscopic TiO_2 films for application in quantum-dot-sensitized solar cells," *Appl. Phys. Lett.,* vol. 91, 2007.

[9] H. Lee, H. C. Leventis, S. -. Moon, P. Chen, S. Ito, S. A. Haque, T. Torres, F. Nüesch, T. Geiger, S. M. Zakeeruddin, M. Grätzel and M. K. Nazeeruddin, "PbS and CdS quantum dot-sensitized solid-state solar cells: "Old concepts, new results"," *Adv. Funct. Mater.,* vol. 19, pp. 2735-2742, 2009.

[10] C. B. Murray, D. J. Norris and M. G. Bawendi, "Synthesis and characterization of nearly monodisperse CdE (E = S, Se, Te) semiconductor nanocrystallites," *J. Am. Chem. Soc.,* vol. 115, pp. 8706-8715, 1993.

[11] J. J. Nairn, P. J. Shapiro, B. Twamley, T. Pounds, R. Von Wandruszka, T. Rick Fletcher, M. Williams, C. Wang and M. Grant Norton, "Preparation of ultrafine chalcopyrite nanoparticles via the

photochemical decomposition of molecular single-source precursors," *Nano Lett.,* vol. 6, pp. 1218-1223, 2006.

[12] S. L. Castro, S. G. Bailey, R. P. Raffaelle, K. K. Banger and A. F. Hepp, "Synthesis and characterization of colloidal CuInS 2 nanoparticles from a molecular single-source precursor," *J Phys Chem B,* vol. 108, pp. 12429-12435, 2004.

[13] Y. Xie, Y. Qian, W. Wang, S. Zhang and Y. Zhang, "A benzene-thermal synthetic route to nanocrystalline GaN," *Science,* vol. 272, pp. 1926-1927, 1996.

[14] B. Li, Y. Xie, J. Huang and Y. Qian, "Synthesis by a solvothermal route and characterization of CuInSe2 nanowhiskers and nanoparticles," *Adv Mater,* vol. 11, pp. 1456-1459, 1999.

[15] E. Lifshitz, I. Dag, I. Litvin, G. Hodes, S. Gorer, R. Reisfeld, M. Zelner and H. Minti, "Optical properties of CdSe nanoparticle films prepared by chemical deposition and sol-gel methods," *Chem. Phys. Lett.,* vol. 288, pp. 188-196, 1998.

[16] X. Peng, L. Manna, W. Yang, J. Wickham, E. Scher, A. Kadavanich and A. P. Alivisatos, "Shape control of CdSe nanocrystals," *Nature,* vol. 404, pp. 59-61, 2000.

[17] J. Ge, Y. Hu, M. Biasini, C. Dong, J. Guo, W. P. Beyermann and Y. Yin, "One-step synthesis of highly water-soluble magnetite colloidal nanocrystals," *Chem. Eur. J.,* vol. 13, pp. 7153-7161, 2007.

[18] H. Chiu, I. Chiang and D. Chen, "Synthesis of NiAu alloy and core-shell nanoparticles in water-in-oil microemulsions," *J. Nanopart. Res.,* vol. 11, pp. 1137-1144, 2009.

[19] G. Philippe, "Colloidal quantum dots," *Comptes Rendus Physique,* vol. 9, pp. 777-787, 10, 2008.

[20] C. B. Murray, C. R. Kagan and M. G. Bawendi, "Synthesis and characterization of monodisperse nanocrystals and close-packed nanocrystal assemblies," *Annu Rev Mater Sci,* vol. 30, pp. 545-610, 2000.

[21] D. V. Talapin, J. Lee, M. V. Kovalenko and E. V. Shevchenko, "Prospects of colloidal nanocrystals for electronic and optoelectronic applications," *Chem. Rev.,* vol. 110, pp. 389-458, 2010.

[22] Y. Xia, P. Yang, Y. Sun, Y. Wu, B. Mayers, B. Gates, Y. Yin, F. Kim and H. Yan, "One-dimensional nanostructures: Synthesis, characterization, and applications," *Adv Mater,* vol. 15, pp. 353-389, 2003.

[23] H. Reiss, "The growth of uniform colloidal dispersions," *J. Chem. Phys.,* vol. 19, pp. 482-487, 1951.

[24] G. H. Carey, A. L. Abdelhady, Z. Ning, S. M. Thon, O. M. Bakr and E. H. Sargent, "Colloidal Quantum Dot Solar Cells," *Chem. Rev.,* 06/24, 2015.

[25] G. Kalyuzhny and R. W. Murray, "Ligand effects on optical properties of CdSe nanocrystals," *J Phys Chem B,* vol. 109, pp. 7012-7021, 2005.

[26] G. K. Soon, Y. Piao, J. Park, S. Angappane, Y. Jo, N. Hwang, J. Park and T. Hyeon, "Kinetics of monodisperse iron oxide nanocrystal formation by "heating-up" process," *J. Am. Chem. Soc.,* vol. 129, pp. 12571-12584, 2007.

[27] S. Baskoutas and A. F. Terzis, "Size-dependent band gap of colloidal quantum dots," *J. Appl. Phys.,* vol. 99, 2006.

[28] H. Choi, J. Ko, Y. Kim and S. Jeong, "Steric-hindrance-driven shape transition in PbS quantum dots: Understanding size-dependent stability," *J. Am. Chem. Soc.,* vol. 135, pp. 5278-5281, 2013.

[29] X. Peng, "Mechanisms for the shape-control and shape-evolution of colloidal semiconductor nanocrystals," *Adv Mater,* vol. 15, pp. 459-463, 2003.

[30] S. K. Batabyal, L. Tian, N. Venkatram, W. Ji and J. J. Vittal, "Phase-selective synthesis of CuInS2 nanocrystals," *J. Phys. Chem. C,* vol. 113, pp. 15037-15042, 2009.

[31] B. Koo, R. N. Patel and B. A. Korgel, "Wurtzite-Chalcopyrite polytypism in $CuInS_2$ nanodisks," *Chem. Mater.,* vol. 21, pp. 1962-1966, 2009.

[32] R. A. Sperling and W. J. Parak, "Surface modification, functionalization and bioconjugation of colloidal Inorganic nanoparticles," *Philos. Trans. R. Soc. A Math. Phys. Eng. Sci.,* vol. 368, pp. 1333-1383, 2010.

[33] P. R. Brown, D. Kim, R. R. Lunt, N. Zhao, M. G. Bawendi, J. C. Grossman and V. Bulovic, "Energy level modification in lead sulfide quantum dot thin films through ligand exchange," *ACS Nano,* vol. 8, pp. 5863-5872, 2014.

[34] T. J. Macdonald and T. Nann, "Quantum Dot Sensitized Photoelectrodes," *Nanomaterials,* vol. 1, pp. 79-88, Dec., 2011.

[35] J. H. Bang and P. V. Kamat, "Quantum Dot Sensitized Solar Cells. A Tale of Two Semiconductor Nanocrystals: CdSe and CdTe," *ACS Nano,* vol. 3, pp. 1467-1476, JUN, 2009.

[36] I. Robel, V. Subramanian, M. Kuno and P. Kamat, "Quantum dot solar cells. Harvesting light energy with CdSe nanocrystals molecularly linked to mesoscopic TiO2 films," *J. Am. Chem. Soc.,* vol. 128, pp. 2385-2393, FEB 22, 2006.

[37] I. Mora-Sero, S. Gimenez, T. Moehl, F. Fabregat-Santiago, T. Lana-Villareal, R. Gomez and J. Bisquert, "Factors determining the photovoltaic performance of a CdSe quantum dot sensitized solar cell: the role of the linker molecule and of the counter electrode," *Nanotechnology,* vol. 19, pp. 424007, Oct. 22, 2008.

[38] Z. Ning, O. Voznyy, J. Pan, S. Hoogland, V. Adinolfi, J. Xu, M. Li, A. R. Kirmani, J. Sun, J. Minor, K. W. Kemp, H. Dong, L. Rollny, A. Labelle, G. Carey, B. Sutherland, I. Hill, A. Amassian, H. Liu, J. Tang, O. M. Bakr and E. H. Sargent, "Air-stable n-type colloidal quantum dot solids," *Nat. Mater.,* vol. 13, pp. 822-828, 2014.

[39] L. Li, A. Pandey, D. J. Werder, B. P. Khanal, J. M. Pietryga and V. I. Klimov, "Efficient synthesis of highly luminescent copper indium sulfide-based core/shell nanocrystals with surprisingly long-lived emission," *J. Am. Chem. Soc.,* vol. 133, pp. 1176-1179, 2011.

[40] Y. Justo, P. Geiregat, K. Van Hoecke, F. Vanhaecke, C. D. M. Donega and Z. Hens, "Optical Properties of PbS/CdS Core/Shell Quantum Dots," *J. Phys. Chem. C,* vol. 117, pp. 20171-20177, Oct. 3, 2013.

[41] S. Kim, B. Fisher, H. Eisler and M. Bawendi, "Type-II quantum dots: CdTe/CdSe (core/shell) and CdSe/ZinTe (core/shell) heterostructures," *J. Am. Chem. Soc.,* vol. 125, pp. 11466-11467, Sep. 24, 2003.

[42] Z. Ning, H. Tian, C. Yuan, Y. Fu, H. Qin, L. Sun and H. Agren, "Solar cells sensitized with type-II ZnSe-CdS core/shell colloidal quantum dots," *Chem. Commun.,* vol. 47, pp. 1536-1538, 2011.

[43] H. Eshet, M. Gruenwald and E. Rabani, "The Electronic Structure of CdSe/CdS Core/Shell Seeded Nanorods: Type-I or Quasi-Type-II?" *Nano Lett.,* vol. 13, pp. 5880-5885, Dec., 2013.

[44] A. R. Denton and N. W. Ashcroft, "Vegard's law," *Phys. Rev. , A,* vol. 43, pp. 3161-3164, March, 1991.

[45] G. I. Maikov, R. Vaxenburg, A. Sashchiuk and E. Lifshitz, "Composition-Tunable Optical Properties of Colloidal IV-VI Quantum Dots, Composed of Core/Shell Heterostructures with Alloy Components," *ACS Nano,* vol. 4, pp. 6547-6556, Nov, 2010.

[46] Z. Pan, K. Zhao, J. Wang, H. Zhang, Y. Feng and X. Zhong, "Near Infrared Absorption of CdSexTe1-x, Alloyed Quantum Dot Sensitized Solar Cells with More than 6% Efficiency and High Stability," *ACS Nano,* vol. 7, pp. 5215-5222, June, 2013.

[47] J. Tang and E. H. Sargent, "Infrared Colloidal Quantum Dots for Photovoltaics: Fundamentals and Recent Progress," vol. 23, pp. 12-29, 2011.

[48] A. Stavrinadis, A. K. Rath, F. Pelayo Garcia de Arquer, S. L. Diedenhofen, C. Magen, L. Martinez, D. So and G. Konstantatos, "Heterovalent cation substitutional doping for quantum dot homojunction solar cells," *Nat. Commun.,* vol. 4, pp. 2981, Dec., 2013.

[49] H. Liu, D. Zhitomirsky, S. Hoogland, J. Tang, I. J. Kramer, Z. Ning and E. H. Sargent, "Systematic optimization of quantum junction colloidal quantum dot solar cells," *Appl. Phys. Lett.,* vol. 101, pp. 151112, Oct. 8, 2012.

[50] K. W. Johnston, A. G. Pattantyus-Abraham, J. P. Clifford, S. H. Myrskog, S. Hoogland, H. Shukla, E. J. D. Klem, L. Levina and E. H. Sargent, "Efficient Schottky-quantum-dot photovoltaics: The roles of depletion, drift, and diffusion," *Appl. Phys. Lett.,* vol. 92, 2008.

[51] D. V. Talapin and C. B. Murray, "Applied physics: PbSe nanocrystal solids for n- and p-channel thin film field-effect transistors," *Science,* vol. 310, pp. 86-89, 2005.

[52] D. Ko, J. J. Urban and C. B. Murray, "Carrier distribution and dynamics of nanocrystal solids doped with artificial atoms," *Nano Lett.,* vol. 10, pp. 1842-1847, 2010.

[53] A. Fischer, L. Rollny, J. Pan, G. H. Carey, S. M. Thon, S. Hoogland, O. Voznyy, D. Zhitomirsky, J. Y. Kim, O. M. Bakr and E. H. Sargent, "Directly deposited quantum dot solids using a colloidally stable nanoparticle ink," *Adv Mater,* vol. 25, pp. 5742-5749, 2013.

[54] M. Shimomura and T. Sawadaishi, "Bottom-up strategy of materials fabrication: A new trend in nanotechnology of soft materials," *Curr. Opin. Colloid Interface Sci.,* vol. 6, pp. 11-16, 2001.

[55] C. Yang, J. Y. Josefowicz and L. Alexandru, "Deposition of ultrathin films by a withdrawal method," *Thin Solid Films,* vol. 74, pp. 117-127, 1980.

[56] C. Jiang and M. A. Green, "Silicon quantum dot superlattices: Modeling of energy bands, densities of states, and mobilities for silicon tandem solar cell applications," *J. Appl. Phys.,* vol. 99, 2006.

[57] K. Sun, Y. Li, M. A. Stroscio and M. Dutta, "Miniband formation in superlattices of colloidal quantum dots and conductive polymers," in *Sensors Based on Nanotechnology 3 - 211th ECS Meeting,* Chicago, IL, 2008, pp. 1-12.

[58] W. A. Tisdale and X. -. Zhu, "Artificial atoms on semiconductor surfaces," *Proc. Natl. Acad. Sci. U. S. A.,* vol. 108, pp. 965-970, 2011.

[59] M. Y. Lee, Y. Li and S. Samukawa, "Miniband Calculation of 3-D Nanostructure Array for Solar Cell Applications," *IEEE Trans. Electron Devices,* vol. 62, pp. 3709-3714, 2015.

[60] K. Ellmer, "Resistivity of polycrystalline zinc oxide films: Current status and physical limit," *J. Phys. D,* vol. 34, pp. 3097-3108, 2001.

[61] I. Hamberg and C. G. Granqvist, "Evaporated Sn-doped In2O3 films: Basic optical properties and applications to energy-efficient windows," *J. Appl. Phys.,* vol. 60, pp. R123-R160, 1986.

[62] K. Ellmer and R. Mientus, "Carrier transport in polycrystalline transparent conductive oxides: A comparative study of zinc oxide and indium oxide," *Thin Solid Films,* vol. 516, pp. 4620-4627, 2008.

[63] J. R. Bellingham, W. A. Phillips and C. J. Adkins, "Intrinsic performance limits in transparent conducting oxides," *J. Mater. Sci. Lett.,* vol. 11, pp. 263-265, 1992.

[64] D. Song, A. G. Aberle and J. Xia, "Optimisation of ZnO:Al films by change of sputter gas pressure for solar cell application," *Appl. Surf. Sci.,* vol. 195, pp. 291-296, 2002.

[65] J. Müller, B. Rech, J. Springer and M. Vanecek, "TCO and light trapping in silicon thin film solar cells," *Sol. Energy,* vol. 77, pp. 917-930, 2004.

[66] S. Calnan and A. N. Tiwari, "High mobility transparent conducting oxides for thin film solar cells," *Thin Solid Films,* vol. 518, pp. 1839-1849, 2010.

[67] T. Minami, "Transparent conducting oxide semiconductors for transparent electrodes," *Semicond Sci Technol,* vol. 20, pp. S35-S44, 2005.

[68] S. Das and T. L. Alford, "Optimization of the zinc oxide electron transport layer in P3HT:PC61BM based organic solar cells by annealing and yttrium doping," *RSC Adv.,* vol. 5, pp. 45586-45591, 2015.

[69] L. Sun, W. Shen, W. Chen, X. Bao, N. Wang, X. Dou, L. Han and S. Wen, "Simple solution-processed titanium oxide electron transport layer for efficient inverted polymer solar cells," *Thin Solid Films,* vol. 573, pp. 134-139, 2014.

[70] B. O'Regan and M. Graetzel, "Low-cost, high-efficiency solar cell based on dye-sensitized colloidal TiO2 films," *Nature,* vol. 353, pp. 737, 1991.

[71] D. A. R. Barkhouse, R. Debnath, I. J. Kramer, D. Zhitomirsky, A. G. Pattantyus-Abraham, L. Levina, L. Etgar, M. Grätzel and E. H. Sargent, "Depleted bulk heterojunction colloidal quantum dot photovoltaics," *Adv Mater,* vol. 23, pp. 3134-3138, 2011.

[72] X. Lan, J. Bai, S. Masala, S. M. Thon, Y. Ren, I. J. Kramer, S. Hoogland, A. Simchi, G. I. Koleilat, D. Paz-Soldan, Z. Ning, A. J. Labelle, J. Y. Kim, G. Jabbour and E. H. Sargent, "Self-assembled, nanowire network electrodes for depleted bulk heterojunction solar cells," *Adv Mater,* vol. 25, pp. 1769-1773, 2013.

[73] Q. Zhang and G. Cao, "Nanostructured photoelectrodes for dye-sensitized solar cells," *Nano Today,* vol. 6, pp. 91-109, 2011.

[74] S. J. Pearton, D. P. Norton, K. Ip, Y. W. Heo and T. Steiner, "Recent progress in processing and properties of ZnO," *Prog Mater Sci,* vol. 50, pp. 293-340, 2005.

[75] S. M. Gupta and M. Tripathi, "A review of TiO2 nanoparticles," *Chin. Sci. Bull.,* vol. 56, pp. 1639-1657, 2011.

[76] H. M. Chen, C. K. Chen, Y. Chang, C. Tsai, R. Liu, S. Hu, W. Chang and K. Chen, "Quantum dot monolayer sensitized ZnO nanowire-array photoelectrodes: True efficiency for water splitting," *Angew. Chem. Int. Ed.,* vol. 49, pp. 5966-5969, 2010.

[77] K. S. Leschkies, T. J. Beatty, M. S. Kang, D. J. Norris and E. S. Aydil, "Solar cells based on junctions between colloidal Pbse nanocrystals and thin ZnO films," *ACS Nano,* vol. 3, pp. 3638-3648, 2009.

[78] A. G. Pattantyus-Abraham, I. J. Kramer, A. R. Barkhouse, X. Wang, G. Konstantatos, R. Debnath, L. Levina, I. Raabe, M. K. Nazeeruddin, M. Grätzel and E. H. Sargent, "Depleted-Heterojunction Colloidal Quantum Dot Solar Cells," *ACS Nano,* vol. 4, pp. 3374-3380, 2010.

[79] B. D. Yuhas and P. Yang, "Nanowire-Based All-Oxide Solar Cells," *J. Am. Chem. Soc.,* vol. 131, pp. 3756-3761, 2009.

[80] Z. Fan, H. Razavi, J. Do, A. Moriwaki, O. Ergen, Y. Chueh, P. W. Leu, J. C. Ho, T. Takahashi, L. A. Reichertz, S. Neale, K. Yu, M. Wu, J. W. Ager and A. Javey, "Three-dimensional nanopillar-array photovoltaics on low-cost and flexible substrates," *Nat. Mater.,* vol. 8, pp. 648-653, 2009.

[81] R. Yan, D. Gargas and P. Yang, "Nanowire photonics," *Nat. Photon.,* vol. 3, pp. 569-576, 2009.

[82] T. Kuykendall, P. Ulrich, S. Aloni and P. Yang, "Complete composition tunability of InGaN nanowires using a combinatorial approach," *Nat. Mater.,* vol. 6, pp. 951-956, 2007.

[83] B. Mandl, J. Stangl, T. Mårtensson, A. Mikkelsen, J. Eriksson, L. S. Karlsson, G. Bauer, L. Samuelson and W. Seifert, "Au-free epitaxial growth of InAs nanowires," *Nano Lett.,* vol. 6, pp. 1817-1821, 2006.

[84] J. Zhu, Z. Yu, G. F. Burkhart, C. Hsu, S. T. Connor, Y. Xu, Q. Wang, M. McGehee, S. Fan and Y. Cui, "Optical absorption enhancement in amorphous silicon nanowire and nanocone arrays," *Nano Lett.,* vol. 9, pp. 279-282, 2009.

[85] W. A. Nositschka, C. Beneking, O. Voigt and H. Kurz, "Texturisation of multicrystalline silicon wafers for solar cells by reactive ion etching through colloidal masks," *Sol Energ Mater Sol Cells,* vol. 76, pp. 155-166, 2003.

[86] C. L. Haynes and R. P. Van Duyne, "Nanosphere lithography: A versatile nanofabrication tool for studies of size-dependent nanoparticle optics," *J Phys Chem B,* vol. 105, pp. 5599-5611, 2001.

[87] C. Chang, M. Shiao, S. Chen, C. Tsai, J. Kao and D. Chiang, "Zinc oxide column rod array prepared by inductively coupled plasma-reactive ion etching technology," in *Optical Interference Coatings,* 2010, pp. WA7.

[88] K. J. Nordheden, B. A. Pathak and J. L. Alexander, "ICP etching of ZnO in BCl_3/SF_6 gas mixtures," in *Zinc Oxide Materials and Devices IV,* San Jose, CA, 2009, .

[89] K. J. Nordheden, "Plasma etching of ZnO: A review," in *Quantum Sensing and Nanophotonic Devices,* San Jose, CA, 2004, pp. 228-233.

[90] J. C. Park, J. K. Kim, T. G. Kim, D. W. Lee, H. Cho, H. S. Kim, S. J. Yoon and Y. Jung, "Dry etching of SnO_2 and ZnO films in halogen-based inductively coupled plasmas," *Int. J. Mod. Phys. B,* vol. 25, pp. 4237-4240, 2011.

[91] J. Lee, K. Chang, K. Kim, W. Choi and S. Park, "Dry etching of ZnO using an inductively coupled plasma," *J. Electrochem. Soc.,* vol. 148, pp. G1-G3, 2001.

[92] J. S. Park, H. J. Park, Y. B. Hahn, G. Yi and A. Yoshikawa, "Dry etching of ZnO films and plasma-induced damage to optical properties," *J Vac Sci Technol B Microelectron Nanometer Struct,* vol. 21, pp. 800-803, 2003.

[93] V. Wood and V. Bulovic, "Colloidal quantum dot light-emitting devices." *Nano Reviews,* vol. 1, 2010, 2010.

[94] Y. Shirasaki, G. J. Supran, M. G. Bawendi and V. Bulovic, "Emergence of colloidal quantum-dot light-emitting technologies," *Nature Photonics,* vol. 7, pp. 13-23, 2013.

[95] A. Zaban, O. I. Micic, B. A. Gregg and A. J. Nozik, "Photosensitization of nanoporous TiO2 electrodes with InP quantum dots," *Langmuir,* vol. 14, pp. 3153-3156, 1998.

[96] K. S. Leschkies, R. Divakar, J. Basu, E. Enache-Pommer, J. E. Boercker, C. B. Carter, U. R. Kortshagen, D. J. Norris and E. S. Aydil, "Photosensitization of ZnO nanowires with CdSe quantum dots for photovoltaic devices," *Nano Lett.,* vol. 7, pp. 1793-1798, 2007.

[97] P. V. Kamat, "Quantum dot solar cells. Semiconductor nanocrystals as light harvesters," *J. Phys. Chem. C,* vol. 112, pp. 18737-18753, 2008.

[98] S. Emin, S. P. Singh, L. Han, N. Satoh and A. Islam, "Colloidal quantum dot solar cells," *Sol. Energy,* vol. 85, pp. 1264-1282, 2011.

[99] N. Greenham, X. Peng and A. Alivisatos, "Charge separation and transport in conjugated-polymer/semiconductor-nanocrystal composites studied by photoluminescence quenching and photoconductivity," *Phys. Rev. B,* vol. 54, pp. 17628-17637, Dec. 15, 1996.

[100] N. Greenham, X. Peng and A. Alivisatos, "A CdSe nanocrystal MEH-PPV polymer composite photovoltaic," *Future Generation Photovoltaic Technologies,* pp. 295-301, 1997.

[101] S. M. Thon and E. H. Sargent, "Colloidal quantum dot photovoltaics," in *Thin Film Solar Technology III,* San Diego, CA, 2011, .

[102] K. W. Johnston, A. G. Pattantyus-Abraham, J. P. Clifford, S. H. Myrskog, D. D. MacNeil, L. Levina and E. H. Sargent, "Schottky-quantum dot photovoltaics for efficient infrared power conversion," *Appl. Phys. Lett.,* vol. 92, 2008.

[103] X. Mai, H. J. An, J. H. Song, J. Jang, S. Kim and S. Jeong, "Inverted Schottky quantum dot solar cells with enhanced carrier extraction and air-stability," *J. Mater. Chem. A,* vol. 2, pp. 20799-20805, 2014.

[104] A. W. Walker, O. Theriault, J. F. Wheeldon and K. Hinzer, "The effects of absorption and recombination on quantum dot multijunction solar cell efficiency," *IEEE J. Photovoltaics,* vol. 3, pp. 1118-1124, 2013.

[105] K. Emery, M. Meusel, R. Beckett, F. Dimroth, A. Bett and W. Warta, "Procedures for evaluating multijunction concentrators," in *28th IEEE Photovoltaic Specialists Conference, PVSC 2000,* 2000, pp. 1126-1130.

[106] X. Wang, G. I. Koleilat, J. Tang, H. Liu, I. J. Kramer, R. Debnath, L. Brzozowski, D. A. R. Barkhouse, L. Levina, S. Hoogland and E. H. Sargent, "Tandem colloidal quantum dot solar cells employing a graded recombination layer," *Nature Photonics,* vol. 5, pp. 480-484, 2011.

[107] O. Christensen, "Quantum efficiency of the internal photoelectric effect in silicon and germanium," *J. Appl. Phys.,* vol. 47, pp. 689-695, 1976.

[108] M. C. Beard, "Multiple exciton generation in semiconductor quantum dots," *J. Phys. Chem. Lett.,* vol. 2, pp. 1282-1288, 2011.

[109] R. D. Schaller, M. Sykora, J. M. Pietryga and V. I. Klimov, "Seven excitons at a cost of one: Redefining the limits for conversion efficiency of photons into charge carriers," *Nano Lett.,* vol. 6, pp. 424-429, 2006.

[110] A. J. Nozik, "Nanophotonics: Making the most of photons," *Nat. Nanotechnol.,* vol. 4, pp. 548-549, 2009.

[111] O. E. Semonin, J. M. Luther, S. Choi, H. Chen, J. Gao, A. J. Nozik and M. C. Beard, "Peak external photocurrent quantum efficiency exceeding 100% via MEG in a quantum dot solar cell," *Science,* vol. 334, pp. 1530-1533, 2011.

[112] M. C. Beard, J. M. Luther, O. E. Semonin and A. J. Nozik, "Third generation photovoltaics based on multiple exciton generation in quantum confined semiconductors," *Acc. Chem. Res.,* vol. 46, pp. 1252-1260, 2013.

[113] J. Kong, H. T. Soh, A. M. Cassell, C. F. Quate and H. Dai, "Synthesis of individual single-walled carbon nanotubes on patterned silicon wafers," *Nature,* vol. 395, pp. 878-881, 1998.

[114] K. M. Yu, W. Walukiewicz, J. Wu, W. Shan, J. W. Beeman, M. A. Scarpulla, O. D. Dubon and P. Becla, "Diluted II-VI oxide semiconductors with multiple band gaps," *Phys. Rev. Lett.,* vol. 91, pp. 246403/1-246403/4, 2003.

[115] K. W. J. Barnham, I. Ballard, J. P. Connolly, N. J. Ekins-Daukes, B. G. Kluftinger, J. Nelson and C. Rohr, "Quantum well solar cells," *Phys E,* vol. 14, pp. 27-36, 2002.

[116] A. W. Walker, O. Theriault and K. Hinzer, "The dependence of multijunction solar cell performance on the number of quantum dot layers," *IEEE J. Quantum Electron.,* vol. 50, pp. 198-203, 2014.

[117] A. Martí, E. Antolín, C. R. Stanley, C. D. Farmer, N. López, P. Díaz, E. Cánovas, P. G. Linares and A. Luque, "Production of photocurrent due to intermediate-to-conduction-band transitions: A demonstration of a key operating principle of the intermediate-band solar cell," *Phys. Rev. Lett.,* vol. 97, 2006.

[118] M. Vörös, G. Galli and G. T. Zimanyi, "Colloidal Nanoparticles for Intermediate Band Solar Cells," *ACS Nano,* vol. 9, pp. 6882-6890, 2015.

[119] F. Auzel, "Upconversion and Anti-Stokes Processes with f and d Ions in Solids," *Chem. Rev.,* vol. 104, pp. 139-173, 2004.

[120] B. Sadeghimakki, Z. Gao and S. Sivoththaman, "Proof of down-conversion by CdSe/ZnS quantum dots on silicon solar cells," in *40th IEEE Photovoltaic Specialist Conference, PVSC 2014,* 2014, pp. 2262-2266.

[121] S. Gardelis and A. G. Nassiopoulou, "Evidence of significant down-conversion in a Si-based solar cell using $CuInS_2$/ZnS core shell quantum dots," *Appl. Phys. Lett.,* vol. 104, 2014.

[122] Z. Deutsch, L. Neeman and D. Oron, "Luminescence upconversion in colloidal double quantum dots," *Nat. Nanotechnol.,* vol. 8, pp. 649-653, 2013.

[123] Y. Huang, S. Gao and M. Liu, "Research of Film Uniformity on Vacuum Coating by Magnetron Sputtering with Multi-Sites," *Mechatronics and Information Technology, Pts 1 and 2,* vol. 2-3, pp. 1082-1087, 2012.

[124] E. G. Birgin, I. Chambouleyron and J. M. Martínez, "Estimation of the Optical Constants and the Thickness of Thin Films Using Unconstrained Optimization," *J. Comput. Phys.,* vol. 151, pp. 862-880, 1999.

[125] R. Andrade, E. G. Birgin, I. Chambouleyron, J. M. Martinez and S. D. Ventura, "Estimation of the thickness and the optical parameters of several stacked thin films using optimization," *Appl. Opt.,* vol. 47, pp. 5208-5220, 2008.

[126] C. Agashe, O. Kluth, G. Schöpe, H. Siekmann, J. Hüpkes and B. Rech, "Optimization of the electrical properties of magnetron sputtered aluminum-doped zinc oxide films for opto-electronic applications," *Thin Solid Films,* vol. 442, pp. 167-172, 2003.

[127] T. Minami, T. Miyata, Y. Ohtani and Y. Mochizuki, "New transparent conducting Al-doped ZnO film preparation techniques for improving resistivity distribution in magnetron sputtering deposition," *Jpn J Appl Phys Part 2 Letter,* vol. 45, pp. L409-L412, 2006.

[128] T. Minami, T. Miyata, Y. Ohtani and T. Kuboi, "Effect of thickness on the stability of transparent conducting impurity-doped ZnO thin films in a high humidity environment," *Physica Status Solidi Rapid Res. Lett.,* vol. 1, pp. R31-R33, 2007.

[129] T. Minami, "Present status of transparent conducting oxide thin-film development for Indium-Tin-Oxide (ITO) substitutes," *Thin Solid Films,* vol. 516, pp. 5822-5828, 2008.

[130] H. P. Klug and L. E. Alexander, *X-Ray Diffraction Procedures for Polycrystalline and Amorphous Materials.* New York: Wiley Interscience, 1974.

[131] I. Sieber, N. Wanderka, I. Urban, I. Dörfel, E. Schierhorn, F. Fenske and W. Fuhs, "Electron microscopic characterization of reactively sputtered ZnO films with different Al-doping levels," *Thin Solid Films,* vol. 330, pp. 108-113, 9/30, 1998.

[132] J. H. Choi, H. Tabata and T. Kawai, "Initial preferred growth in zinc oxide thin films on Si and amorphous substrates by a pulsed laser deposition," *J. Cryst. Growth,* vol. 226, pp. 493-500, 2001.

[133] Y. S. Choi, J. W. Kang, D. K. Hwang and S. J. Park, "Recent advances in ZnO-based light-emitting diodes," *IEEE Trans. Electron Devices,* vol. 57, pp. 26-41, 2010.

[134] C. H. Ahn, Y. Y. Kim, D. C. Kim, S. K. Mohanta and H. K. Cho, "A comparative analysis of deep level emission in ZnO layers deposited by various methods," *J. Appl. Phys.,* vol. 105, 2009.

[135] N. H. Alvi, K. ul Hasan, O. Nur and M. Willander, "The origin of the red emission in n-ZnO nanotubes/p-GaN white light emitting diodes," *Nanoscale Res. Lett.,* vol. 6, pp. X1-7, 2011.

[136] A. Djurišić and Y. H. Leung, "Optical Properties of ZnO Nanostructures," *Small,* vol. 2, pp. 944-961, 2006.

[137] E. Guziewicz, I. A. Kowalik, M. Godlewski, K. Kopalko, V. Osinniy, A. Wójcik, S. Yatsunenko, E. Lusakowska, W. Paszkowicz and M. Guziewicz, "Extremely low temperature growth of ZnO by atomic layer deposition," *J. Appl. Phys.,* vol. 103, 2008.

[138] S. Lin, J. Huang and D. Lii, "The effects of r.f. power and substrate temperature on the properties of ZnO films," *Surf Coat Technol,* vol. 176, pp. 173-181, 2004.

[139] E. M. Bachari, G. Baud, S. Ben Amor and M. Jacquet, "Structural and optical properties of sputtered ZnO films," *Thin Solid Films,* vol. 348, pp. 165-172, 1999.

[140] M. M. Rahman, M. K. R. Khan, M. R. Islam, M. A. Halim, M. Shahjahan, M. A. Hakim, D. K. Saha and J. U. Khan, "Effect of Al Doping on Structural, Electrical, Optical and Photoluminescence

Properties of Nano-Structural ZnO Thin Films," *Journal of Materials Science and Technology,* vol. 28, pp. 329-335, 201204, 2012.

[141] A. Kongkan, K. Tvrdy, K. Takechi, M. Kuno and P. V. Kamat, "Quantum Dot Solar Cells. Tuning Photoresponse through Size and Shape Control of CdSe−TiO2 Architecture," *J. Am. Chem. Soc.,* vol. 130, pp. 4007-4015, 2008.

[142] B. Farrow and P. V. Kamat, "CdSe quantum dot sensitized solar cells. Shuttling electrons through stacked carbon nanocups," *J. Am. Chem. Soc.,* vol. 131, pp. 11124-11131, 2009.

[143] M. Abdellah, K. Žídek, K. Zheng, P. Chábera, M. E. Messing and T. Pullerits, "Balancing electron transfer and surface passivation in gradient CdSe/ZnS core-shell quantum dots attached to ZnO," *J. Phys. Chem. Lett.,* vol. 4, pp. 1760-1765, 2013.

[144] K. T. Kuo, D. M. Liu, S. Y. Chen and C. C. Lin, "Core-shell CuInS2/ZnS quantum dots assembled on short ZnO nanowires with enhanced photo-conversion efficiency," *J. Mater. Chem.,* vol. 19, pp. 6780-6788, 2009.

[145] H. Kim, J. W. Bae, K. Kim, S. Park, T. Seong and I. Adesida, "Inductively-coupled-plasma reactive ion etching of ZnO using BCl 3-based plasmas and effect of the plasma treatment on Ti/Au ohmic contacts to ZnO," *Thin Solid Films,* vol. 447-448, pp. 90-94, 28 April 2002 through 2 May 2002, 2004.

[146] M. G. Mauk, "Silicon solar cells: Physical metallurgy principles," *JOM,* vol. 55, pp. 38-42, 2003.

[147]*Bangs Laboratories Silica Microspheres product data sheet*. Available: http://www.bangslabs.com/sites/default/files/imce/docs/PDS%20702%20Web.pdf.

[148] K. Bandopadhyay and J. Mitra, "Zn interstitials and O vacancies responsible for n-type ZnO: what do the emission spectra reveal?" *Rsc Advances,* vol. 5, pp. 23540-23547, 2015, 2015.

[149] C. Lee, "Fabrication methods and luminescent properties of ZnO materials for light-emitting diodes," *Mater.,* vol. 3, pp. 2218-2259, 2010.

[150] D. Liu, Y. Lv, M. Zhang, Y. Liu, Y. Zhu, R. Zong and Y. Zhu, "Defect-related photoluminescence and photocatalytic properties of porous ZnO nanosheets," *J. Mater. Chem. A,* vol. 2, pp. 15377-15388, 2014.

[151] K. Vanheusden, C. H. Seager, W. L. Warren, D. R. Tallant and J. A. Voigt, "Correlation between photoluminescence and oxygen vacancies in ZnO phosphors," *Appl. Phys. Lett.,* pp. 403, 1995.

[152] S. Sambasivam, D. P. Joseph, S. Asiri Naidu, K. N. Hui, K. S. Hui and B. C. Choi, "Intense violet–blue emission and paramagnetism of nanocrystalline Gd3+ doped ZnO ceramics," *J. Adv. Ceram.,* vol. 4, pp. 300-306, 2015.

[153] E. G. Bylander. Surface effects on the low energy cathodoluminescence of zinc oxide. *J. Appl. Phys. 49(3),* pp. 1188-1195. 1978.

[154] R. Ranjusha, R. Sreeja, P. A. Mini, K. R. V. Subramanian, S. V. Nair and A. Balakrishnan, "Electrical and optical characteristics of surface treated ZnO nanotubes," *Mater. Res. Bull.,* vol. 47, pp. 1887-1891, 2012.

[155] H. Zeng, G. Duan, Y. Li, S. Yang, X. Xu and W. Cai, "Blue luminescence of ZnO nanoparticles based on non-equilibrium processes: Defect origins and emission controls," *Adv. Funct. Mater.,* vol. 20, pp. 561-572, 2010.

[156] N. S. Makarov, H. McDaniel, N. Fuke, I. Robel and V. I. Klimov, "Photocharging artifacts in measurements of electron transfer in quantum-dot-sensitized mesoporous titania films," *J. Phys. Chem. Lett.,* vol. 5, pp. 111-118, 2014.

[157] A. Zabet-Khosousi and A. -. Dhirani, "Charge transport in nanoparticle assemblies," *Chem. Rev.,* vol. 108, pp. 4072-4124, 2008.

[158] Y. Wang, C. Duan, L. Peng and J. Liao, "Dimensionality-dependent charge transport in close-packed nanoparticle arrays: From 2D to 3D," *Sci. Rep.,* vol. 4, 2014.

[159] D. J. Griffiths, *Introduction to Quantum Mechanics.* Upper Saddle River, NJ: Pearson Prentice Hall, 2005.

[160] M. S. Kang, "*Electrical transport in semiconductor nanocrystal assemblies*," 2011.

[161] J. Choi, A. T. Fafarman, S. J. Oh, D. Ko, D. K. Kim, B. T. Diroll, S. Muramoto, J. G. Gillen, C. B. Murray and C. R. Kagan, "Bandlike transport in strongly coupled and doped quantum dot solids: A route to high-performance thin-film electronics," *Nano Lett.,* vol. 12, pp. 2631-2638, 2012.

[162] A. Shabaev, A. L. Efros and A. L. Efros, "Dark and photo-conductivity in ordered array of nanocrystals," *Nano Lett.,* vol. 13, pp. 5454-5461, 2013.

[163] J. Zhang, J. Tolentino, E. R. Smith, J. Zhang, M. C. Beard, A. J. Nozik, M. Law and J. C. Johnson, "Carrier transport in PbS and PbSe QD films measured by photoluminescence quenching," *J. Phys. Chem. C,* vol. 118, pp. 16228-16235, 2014.

[164] W. Yoon, J. E. Boercker, M. P. Lumb, D. Placencia, E. E. Foos and J. G. Tischler, "Enhanced open-circuit voltage of PbS nanocrystal quantum dot solar cells," *Sci. Rep.,* vol. 3, 2013.

[165] D. Bozyigit, W. M. M. Lin, N. Yazdani, O. Yarema and V. Wood, "A quantitative model for charge carrier transport, trapping and recombination in nanocrystal-based solar cells," *Nat. Commun.,* vol. 6, 2015.

[166] A. Veamatahau, B. Jiang, T. Seifert, S. Makuta, K. Latham, M. Kanehara, T. Teranishi and Y. Tachibana, "Origin of surface trap states in CdS quantum dots: Relationship between size dependent photoluminescence and sulfur vacancy trap states," *Phys. Chem. Chem. Phys.,* vol. 17, pp. 2850-2858, 2015.

[167] N. Yazdani, D. Bozyigit, O. Yarema, M. Yarema and V. Wood, "Hole mobility in nanocrystal solids as a function of constituent nanocrystal size," *J. Phys. Chem. Lett.,* vol. 5, pp. 3522-3527, 2014.

[168] J. J. Choi, Y. -. Lim, M. B. Santiago-Berrios, M. Oh, B. -. Hyun, L. Sun, A. C. Bartnik, A. Goedhart, G. G. Malliaras, H. D. Abruña, F. W. Wise and T. Hanrath, "PbSe Nanocrystal Excitonic Solar Cells," *Nano Lett.,* vol. 9, pp. 3749-3755, 2009.

[169] J. Gao, J. M. Luther, O. E. Semonin, R. J. Ellingson, A. J. Nozik and M. C. Beard, "Quantum dot size dependent J - V characteristics in heterojunction ZnO/PbS quantum dot solar cells," *Nano Lett.,* vol. 11, pp. 1002-1008, 2011.

[170] K. Zheng, K. Žídek, M. Abdellah, W. Zhang, P. Chábera, N. Lenngren, A. Yartsev and T. Pullerits, "Ultrafast charge transfer from CdSe quantum dots to p-type NiO: Hole injection vs hole trapping," *J. Phys. Chem. C,* vol. 118, pp. 18462-18471, 2014.

[171] J. Jasieniak, M. Califano and S. E. Watkins, "Size-dependent valence and conduction band-edge energies of semiconductor nanocrystals," *ACS Nano,* vol. 5, pp. 5888-5902, 2011.

[172] V. Stevanovic, S. Lany, D. S. Ginley, W. Tumas and A. Zunger, "Assessing capability of semiconductors to split water using ionization potentials and electron affinities only," *Phys. Chem. Chem. Phys.,* vol. 16, pp. 3706-3714, 2014.

[173] H. Huang and J. Huang, *Organic and Hybrid Solar Cells.* Springer International Publishing, 2014.

[174] X. Lan, S. Masala and E. H. Sargent, "Charge-extraction strategies for colloidal quantum dot photovoltaics," *Nat. Mater.,* vol. 13, pp. 233-240, 2014.

[175] D. Zhitomirsky, O. Voznyy, S. Hoogland and E. H. Sargent, "Measuring charge carrier diffusion in coupled colloidal quantum dot solids," *ACS Nano,* vol. 7, pp. 5282-5290, 2013.

[176] E. M. Y. Lee and W. A. Tisdale, "Determination of exciton diffusion length by transient photoluminescence quenching and its application to quantum dot films," *J. Phys. Chem. C,* vol. 119, pp. 9005-9015, 2015.

[177] A. C. Arango, D. C. Oertel, Y. Xu, M. G. Bawendi and V. Bulovic, "Heterojunction photovoltaics using printed colloidal quantum dots as a photosensitive layer," *Nano Lett.,* vol. 9, pp. 860-863, 2009.